Beiträge zur analytischen und numerischen Homogenisierung in der Materialmodellierung

Habilitationsschrift

von Dr.-Ing. Rainer Glüge

geb. am 16.4.1980 in Magdeburg

zur Verleihung des akademischen Grades

Doktor Ingenieur habilitatus
(Dr.-Ing. habil.)

genehmigt von der Fakultät für Maschinenbau der

Otto-von-Guericke-Universität Magdeburg am 3.2.2016

Gutachterinnen / Gutachter:

Prof. Dr.-Ing. Albrecht Bertram (Universität Magdeburg)

Prof. Dr.-Ing. Thomas Böhlke (Karlsruher Institut für Technologie)

Prof. Dr.-Ing. Jörg Schröder (Universität Duisburg-Essen)

Inhaltsverzeichnis

1 Vorwort

Die Skalenkopplung via Homogenisierung und Lokalisierung ist ein umfangreiches Forschungsgebiet, nicht nur aus Sicht der Mechanik. Man denke allein an die milliardenschweren Forschungsvorhaben zum menschlichen Gehirn, die 2013 von der Europäischen Kommission beschlossen worden (`www.humanbrainproject.eu`). Hier werden ca. 100 Milliarden verschaltete Neuronen simuliert, in der Hoffnung, dass auf der Makro-Ebene Phänomene wie Intelligenz erscheinen. Derartige Emergenzen treten in Physik, Chemie, und Biologie auf. Daher werden Methoden zur Skalenüberbrückung in vielen Bereichen benötigt.

Die Skalenkopplung ist aber auch aus ganz praktischer Sicht ein aktuelles Forschungsgebiet. In der Industrie werden zur Optimierung von Prozessen und Produkten möglichst genaue Materialgesetze benötigt. Diese können nur unter Berücksichtigung der auf Mikroebene ablaufenden physikalischen Vorgängen formuliert werden. Da industrielle Anwendungen allerdings auf einer wesentlich größeren Längenskala ablaufen, gehen in diese jedoch nur die gemittelten, effektiven Materialeigenschaften ein. Somit ist eine Skalenkopplung zwischen Makro- und Mikroebene auch im allgemeinen Maschinenbau von Relevanz. Allein an der Universität Magdeburg wurden mehrere Graduiertenkollegs in Folge zum Thema *Micro-Macro-Interactions in Structured Media and Particle Systems* realisiert (Bertram und Tomas, 2008).

Die vorliegende Arbeit gibt einen groben Überblick über unterschiedliche Homogenisierungsmethoden, wobei vereinfachend zwischen numerischen und analytischen Methoden unterschieden wurde. Es werden jeweils die Beiträge des Autors zu beiden Teilgebieten vergleichend eingeflochten.

2 Einleitung

Fast alle Materialien, die in technischen Strukturen oder Prozessen zum Einsatz kommen, weisen eine Mikrostruktur auf. So besitzen beispielsweise metallische Werkstoffe eine Kornstruktur, Holz eine Faserstruktur, und Beton eine Zement-Matrix mit Zuschlags-Einschlüssen.

Für die genaue Vorhersage des Verhaltens eines Bauteils unter Belastung oder bei einem Umformprozess ist die Berücksichtigung der Mikrostruktur von großer Bedeutung. Im Gegensatz zu rein phänomenologischen Materialmodellen erlaubt die Einbeziehung der Mikrostruktur eine physikalisch motivierte, genauere Berücksichtigung der auf Mikroebene stattfinden Prozesse.

Allerdings ist dies aufgrund des Skalenunterschiedes nicht ohne weiteres möglich. In aller Regel sind die Bauteilabmessungen deutlich größer als die Heterogenitäten in der Mikrostruktur. Die numerischen Methoden, die zur Lösung eines Randwertproblems eine Diskretisierung des Bauteils verwenden, würden bei Berücksichtigung der Mikrostruktur eine allzu feine Diskretisierung erfordern, was zu inakzeptablen numerischen Kosten führt.

Hier schafft die Homogenisierung Abhilfe. Ihre Aufgabe ist es, für eine Mikrostruktur und die auf der Mikroebene verwendeten Materialmodelle ein *effektives Materialmodell* für die Makroebene zu ermitteln, auf welcher dieses dann verwendet werden kann. Außerdem kann eine Umkehrung der Homogenisierung, was als Lokalisierung bezeichnet wird, erfolgen. Diese erlaubt es, die Entwicklung der Mikrostruktur bei auf der Makroebene vorgegebenen Prozessen zu verfolgen, was beispielsweise für die Vorhersage von Rissinitiierung benötigt wird. Insgesamt ergibt sich eine Interaktion zwischen Makro- und Mikroebene, welche nur mit Hilfe entsprechender Werkzeuge rechnerisch zugänglich ist, nämlich der Homogenisierung und der Lokalisierung.

Die Methoden der Homogenisierung lassen sich grob in analytisch und numerisch einteilen. Vor dem massenhaften Aufkommen von leistungsfähigen Rechnern in den

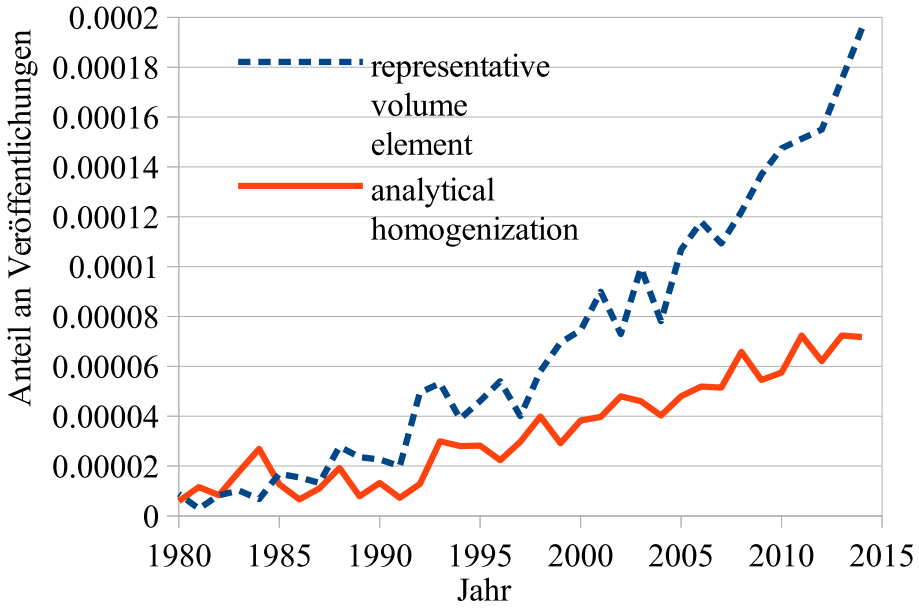

Abbildung 1: Jährliche Anzahl an Publikationen mit *representative volume element* und *analytical homogenization* in Titel, Zusammenfassung oder Schlüsselwörtern bezogen auf die (ungefähre) Gesamtanzahl an jährlichen Publikationen. (Daten von Scopus.com).

1980er Jahren waren analytische Methoden praktisch die einzigen Werkzeuge, die zum Abschätzen des effektiven Materialverhaltens zur Verfügung standen. Bevor Näherungslösungen von komplexen Randwertproblemen allgemein verfügbar wurden, wurden Homogenisierungsaufgaben durch restriktive Annahmen, wie z. B. einem homogenen Verzerrungsfeld (Taylor, 1938; Voigt, 1889) oder einem homogenen Spannungsfeld (Sachs, 1928; Reuss, 1929) in Kombination mit einfachen Materialmodellen soweit vereinfacht, bis geschlossene Ausdrücke als Abschätzungen der effektiven Materialeigenschaften angegeben werden konnten. Analytische Methoden stoßen jedoch sehr schnell an ihre Grenzen. Möchte man die spezifische Anordnungen der Heterogenitäten oder komplexeres Materialverhalten einbeziehen, können in aller Regel keine geschlossenen effektiven Materialgesetze angegeben werden. Daher erfreut sich die numerische Homogenisierung mittels der Methode des repräsentativen Volumenelementes (RVE) großer Beliebtheit (Hill, 1952; Hashin, 1983; Suquet, 1987; Nemat-Nasser, 1999; Miehe, 2002; Schröder, Balzani und Brands, 2011). Hier wird durch geeignete Randbedingungen eine mittlere Deformation auf einen repräsentativen Materialausschnitt aufgebracht, siehe Abb. 3. Die Lösung des Randwertproblems mit anschließender Mittelung liefert dann einen Zusammenhang zwischen effektiven Spannungen und effektiven Dehnungen. Inzwischen werden jährlich mehr als doppelt so viele Veröffentlichungen zu und mit numerischer Homogenisierung wie zu analytischer Homogenisierung publiziert, siehe Abb. 1.

Im Gegensatz zur analytischen Homogenisierung liefert die RVE-Methode kein effektives Materialgesetz in Form von Gleichungen, sondern einen Satz diskreter Werte, z. B. tabellarisch effektive Spannungen und Dehnungen für verschiedene Versuche. Die Destillation eines effektiven Materialgesetzes aus diesen ist wiederum mit einigem Aufwand verbunden.

Im Allgemeinen werden jedoch phänomenologische Materialmodelle an die RVE-Rechnungen angepasst. Auch dieser Modellierungsaufwand kann numerisch umgangen werden, nämlich durch eine parallele Diskretisierung auf beiden Skalen. Dies wird als FE^2-Methode, Mehrgittermethode oder simultane Mehrskalensimulation bezeichnet, Feyel (1999) und Özdemir, Brekelmans und Geers (2008). Sie ist mit erheblichem numerischen Aufwand verbunden.

Daher gehen seit einiger Zeit die Bemühungen dahin, den numerischen Aufwand möglichst klein zu halten. Hierfür gibt es zahlreiche Ansatzpunkte, wie die Optimierung der zugrundeliegenden RVE (z. B. Huet (1990), Hazanov und Huet (1994), Fritzen und Böhlke (2010a), Schröder, Balzani und Brands (2011), Glüge, Weber und Bertram (2012) und Glüge (2013)

Ein weiterer Ansatzpunkt ist, die benötigte Anzahl der RVE-Rechnungen zu reduzieren. Dies ist möglich, indem z. B. der Raum aller RVE-Zustände (Phasenraum) diskretisiert wird, und die Ergebnisse der RVE-Rechnungen in einer Datenbasis abgelegt werden. Für Simulationen auf Makroebene braucht dann nur zwischen den Datenpunkten interpoliert zu werden (Dolzmann, 1999; Ghosh, Lee und Raghavan, 2001). Allerdings steigt der a priori Aufwand bei großen Zustandsräumen dramatisch, wenn z. B. die Materialantwort vom Deformationspfad abhängig ist. Daher wird vermehrt daran gearbeitet, bei einer gleichzeitigen Mehrskalensimulation nur relevante Ausschnitte des Zustandsraumes zu diskretisieren, was als adaptive Tabellierung bezeichnet wird (Pope, 1997; Arsenlis, Barton, Becker und Rudd, 2006; Klusemann und Ortiz, 2015). Hierfür werden vorrangig effiziente numerische Methoden benötigt, z. B. zum schnellen Finden von Daten in einer sehr großen Datenbasis, zur effizienten Diskretisierung des Zustandsraumes oder zur möglichst effizienten Interpolation. Aus Sicht der Materialmodellierung gibt es hier wenig zu tun.

Weiterhin gibt es gemischte Methoden, bei welchen effektive Materialgleichungen z. B. in Form von Entwicklungsgleichungen für effektive innere Variablen analytisch hergeleitet, aber numerisch ausgewertet werden. Als Beispiel seien hier die tensoriellen Fourier-Koeffizienten einer Kristallorientierungs-Verteilungsfunktion genannt (Böhlke, 2001; Kalisch und Bertram, 2013).

3 Grundlagen der Homogenisierung

3.1 Skalenabstand

Jeder Homogenisierungsbemühung geht eine Identifikation der Skalen voraus, zwischen denen vermittelt werden soll. Damit eine Homogenisierung sinnvoll ist, muss ein ausreichender Skalenabstand zwischen den Ebenen vorliegen (Hill, 1952; Hashin, 1983). Die Ebene großer Längen wird im folgenden als Makroebene, die Ebene kleiner Längen als Mikroebene bezeichnet. Sämtliche Fluktuationen auf der Makroebene in den Belastungen, geometrischen Störungen und Randbedingungen müssen von deutlich größerer Abmessung sein als die Inhomogenitäten auf der Mikroebene. Als Beispiel kann wieder ein Polykristall verwendet werden. So sind normale Korngrößen um 100 μm angesiedelt, während die Bauteilabmessungen in der Regel im cm oder m-Bereich liegen.

In aller Regel wird aufgrund von Hashins Mikro-Mini-Makro-Prinzip (Hashin, 1983) ein großer Skalenabstand benötigt. Das Prinzip besagt, dass die Heterogenitäten bereits auf einer Mesoebene (Mini) nur noch durch ihre statistischen Eigenschaften wirken. Dann kann auf der Mesoebene das effektive Materialgesetz verwendet werden. Dieses soll an jedem materiellen Punkt auf der Makroebene angewendet werden können. Daher muss zwischen der Makroebene und der Mesoebene ebenfalls ein ausreichender Skalenabstand liegen. Insbesondere bei der RVE-Methode ist dieses Prinzip wichtig, da das RVE auf der Mesoebene angesiedelt ist. Allerdings kann

auch bei einem geringen Skalenabstand durch Homogenisierung zumindest der Erwartungswert und die Standardabweichung des effektiven Verhaltens ermittelt werden (Jöchen und Böhlke, 2009).

3.2 Lokale Beschreibung der Mikrostruktur

Fluktuation eines Feldes. Die Heterogenität einer Mikrostruktur wird durch die Abhängigkeit eines Materialparameters vom betrachteten materiellen Punkt beschrieben. Zusätzlich können die Materialeigenschaften lokal von einer zeit- oder prozessabhängige Zustandsvariable abhängen. Beispielsweise hängt die elastisch anisotrope Steifigkeit eines Kristalls von der Kristallorientierung ab. In einem Polykristall aus isomorphen Kristalliten würde man dann die lokale Schwankung der Steifigkeit auf eine Zustandsvariable, nämlich die Kristallorientierung, zurückführen.

Stückweise homogene Felder. Viele Mikrostrukturen sind bereichsweise homogen. Dementsprechend sind die Materialparameter bereichsweise homogen, und es gibt scharfe Grenzflächen im Material. Dann kann die Mikrostruktur gut mit der Indikatorfunktion beschrieben werden (Dvorak, 2013). Man hat dann eine begrenzte Anzahl von Phasen, für die jeweils eine Indikatorfunktion die am Punkt vorliegende Phase anzeigt. Ein Beispiel hierfür ist die Elastizität eines plastisch undeformierten Polykristalls.

Eine Besonderheit bei stückweise homogenen Feldern ist, dass die Mikrostruktur vollständig durch die Lage der Grenzfläche und der Information über die an der Grenzfläche benachbarten Phasen gegeben ist. Dies kann bei der analytischen Homogenisierung ausgenutzt werden, siehe Abschnitt 6.3.

Kontinuierlich schwankende Felder. Im Gegensatz dazu steht das kontinuierliche Variieren eines Feldes, bei welchem ein Zurückführen auf Indikatorfunktionen nicht praktikabel ist. Als Beispiel dient hier die Plastizität eines Polykristalls. Kann man nach dem Erstarren der Schmelze sicher problemlos von homogenen Orientierungen in den Körnern ausgehen, so ist dies nach einer plastischen Deformation nicht mehr der Fall.

Dimensionsreduktion durch Diskretisierung. Man kann durch Dimensionsreduktion numerisch Näherungslösungen mit hinreichender Genauigkeit ermitteln. Hier gibt es verschiedene Methoden:

- Diskretisierung des Raumes und der Zeit und numerisches Lösen des Randwertproblems mittels geeigneter numerischer Methoden für ein RVE, wobei die Entwicklung der Zustandsvariablen an jedem Kollokationspunkt (Integrationspunkte in der FEM) mit einem numerischen Zeitintegrationsverfahren verfolgt wird (Vollfeldsimulation). Dies ist sehr rechenaufwendig.
- Eine räumliche Diskretisierung der Mikrostruktur in verschiedene Zellen. In jeder Zelle wird eine homogene Zustandsvariable angenommen, deren Entwicklung verfolgt wird (*Transformation Field Analysis* (TFA), Dvorak (1992)).
- Eine Diskretisierung des Zustandsraumes, wie sie z. B. in Kalidindi (1998) für den Orientierungsraum vorgeschlagen wurde. Ähnlich der TFA-Methode wird der Zustandsraum in eine endliche Anzahl von Zellen geteilt, denen Volumenfraktionen zugeordnet werden.
- Eine Verfeinerung der beiden letztgenannten Methoden ist die Darstellung mit Moden. Diese dienen als Basen, die linear kombiniert werden, wobei der

Faktor vor dem Modus als Komponente bezeichnet wird. Dies ist eine Verallgemeinerung der TFA-Methode (Nonuniform TFA (NTFA), Michel und Suquet (2003) und Fritzen und Böhlke (2010b)). Einerseits kann die Ortsabhängigkeit der Zustandsvariable durch geeignete Moden besser wiedergegeben werden als durch stückweise homogenen Gebiete. Andererseits können Zustände durch eine geeignete Linearkombination von ausgewählten Basiszuständen oft hinreichend gut approximiert werden. Ein Beispiel hierfür ist die Superposition von Texturkoeffizienten (Böhlke, Risy und Bertram, 2006).

Leider sind die Methoden der Dimensionsreduktion nicht unproblematisch. Bei der NTFA wird durch die Linearkombination von Moden eine Linearität in den Materialgleichungen vorausgesetzt, wodurch diese nur auf einfache Materialgleichungen anwendbar ist. Außerdem ist die Identifikation geeigneter Moden recht schwierig, und nicht ohne Vollfeldsimulationen möglich. Es können auch nicht beliebig viele Moden zur Genauigkeitssteigerung verwendet werden, da sonst die Umkehrung der Homogenisierung (die Lokalisierung) nicht eindeutig ist, und somit auch nicht die Entwicklung der einzelnen Komponenten verfolgt werden kann.

Bei der Diskretisierung des Zustandsraumes gibt es ähnliche Probleme. So ist nicht a priori klar, welche Moden den Verlauf der Entwicklung am besten beschreiben können, und wieviele Moden überhaupt dafür benötigt werden. Beispielsweise kann eine scharfe initiale Textur möglicherweise mit wenigen Texturkomponenten genau beschrieben werden, für die Verfolgung der Texturentwicklung sind diese möglicherweise aber nicht ausreichend. Weitere Probleme ergeben sich beim Übergang vom vollen auf den diskreten Zustandsraum, bei dem ein beliebiger Zustand optimal durch die Überlagerung von Moden approximiert werden soll. Hierfür wurden z. B. von Böhlke (2005) spezielle Methoden für die Orientierungsverteilungsfunktion entwickelt. Letztere Methode zielt auf eine optimale Repräsentation des Zustandsraumes durch eine endliche Anzahl von Texturkoeffizienten ab. Ähnliche Optimierungen lassen sich auch auf die räumliche Verteilung der Inhomogenitäten anwenden. So schlagen z. B. Schröder, Balzani und Brands (2011) eine Maximierung der Repräsentativität eines RVE über der räumlichen Anordnung der Phasen vor.

3.3 Statistische Beschreibung der Mikrostruktur

Aufgrund des großen Skalenabstandes sind nicht einzelne Heterogenitäten für das effektive Materialverhalten verantwortlich, sondern deren statistische Eigenschaften. Diese werden durch Wahrscheinlichkeitsdichtefunktionen ermittelt. Letztere sind ein Standardwerkzeug zur Beschreibung statistischer Eigenschaften. Hierbei wird bereits eine klare Abgrenzung von diskreten Phasen impliziert, da als Voraussetzung eine klare Einteilung der Mikrostruktur in endlich viele Phasen benötigt wird. Die Korrelationsfunktionen erlauben es, die statistischen Eigenschaften verschiedener Mikrostrukturen zu vergleichen.

Die 1-Punkt-Korrelation $p_{n1}(\mathbf{x})$ gibt die Wahrscheinlichkeit an, mit welcher die Phase n an einem beliebigen Punkt $\mathbf{x}$ im Material vorgefunden wird. Die 2-Punkt-Korrelation $p_{n2}(\mathbf{x}_1, \mathbf{x}_2)$ gibt die Wahrscheinlichkeit an, mit welcher die Phase n simultan an den beliebigen Punkten $\mathbf{x}_1$ und $\mathbf{x}_2$ vorgefunden wird, und so weiter. Die 1-Punkt-Korrelation entspricht also der Volumenfraktion, bei der 2-Punkt-Korrelation ist durch die relative Lage der Punkte $\mathbf{x}_1$ und $\mathbf{x}_2$ zueinander schon eine Information über die Morphologie der Mikrostruktur enthalten.

Die statistische Homogenität der Mikrostruktur ist gegeben wenn eine Translationsinvarianz der Korrelationsfunktionen vorliegt, wenn also $p_{ni}(\mathbf{x}_1 + \mathbf{c}, \mathbf{x}_2 + \mathbf{c} ... \mathbf{x}_i + \mathbf{c}) = p_{ni}(\mathbf{x}_1, \mathbf{x}_2 ... \mathbf{x}_i) \forall \mathbf{c} \in \mathcal{V}$ gilt. Dies wird in aller Regel angenommen. Statistische Isotropie liegt vor, wenn die Korrelationsfunktionen invariant unter Anwendung aller orthogonalen Transformationen $\mathbf{Q}$ auf die Argumente sind, wenn also

$p_{ni}(\mathbf{Q}\mathbf{x}_1, \mathbf{Q}\mathbf{x}_2 ... \mathbf{Q}\mathbf{x}_i) = p_{ni}(\mathbf{x}_1, \mathbf{x}_2 ... \mathbf{x}_i)$ gilt (Dvorak, 2013). Weitere Eigenschaften von Korrelationsfunktionen und deren Zusammenhang mit der Mikrostruktur sind in Milton (2002) zu finden.

Im Allgemeinen sind die höheren Korrelationsfunktionen analytisch schwierig zu bestimmen, und man beschränkt sich auf die ersten beiden Korrelationsfunktionen und stark idealisierte Mikrostrukturen, siehe z. B. Torquato und Stell (1985) und Lu und Torquato (1990). Auch experimentell lassen sich die höheren Wahrscheinlichkeitsdichten schwer ermitteln, da hierfür eine große 3D-Aufnahme der Mikrostruktur erstellt und numerisch analysiert werden muss. Lediglich 1, 2 und 3-Punkt-Korrelationsfunktionen lassen sich bei Annahme statistischer Isotropie noch durch Oberflächenaufnahmen gewinnen (Berryman, 1988).

Der experimentelle und analytische Aufwand ist also beachtlich (Tewari, Gokhale, Spowart und Miracle, 2004; Gokhale, 2004). Hinzu kommt noch, dass die Wahrscheinlichkeitsdichten zwar rein konzeptionell ein vollständiges Erfassen der statistischen Eigenschaften einer Mikrostruktur gewährleisten, sie jedoch recht unpraktisch bei der Kopplung mit Material- oder Bilanzgleichungen sind. In Milton (2002), Kapitel 15, ist ausgeführt, wie die Korrelationsfunktionen höherer Ordnung in die Terme einer Reihenentwicklung eines effektiven Materialmoduls (Steifigkeit oder Leitfähigkeit) eingehen. Trotz des einfachen Settings (lineares Materialgesetz, kleine Dehnungen) ergeben sich sehr komplexe Ausdrücke, die sich nur für idealisierte Mikrostrukturen oder reduzierte Korrelationsfunktionen auswerten lassen. Daher wird bei der analytischen Homogenisierung oft ein anderer Weg eingeschlagen, nämlich die Verwendung von Grundlösungen (siehe Abschnitt 6.2)

3.4 Skalenkopplung

In der geometrisch nichtlinearen Kontinuumsmechanik steht eine Vielzahl an Spannungs- und Verzerrungsmaßen zur Verfügung. Bei der Homogenisierung muss angegeben werden, welches Maß auf der Makroebene durch eine Volumenmittelung auf der Mikroebene gegeben ist. Nemat-Nasser (1999) hat eindrücklich dargestellt, dass die Wahl der Variablen für die Mikro-Makro-Kopplung prinzipiell beliebig ist, aber aus praktischen Gründen bestimmte Kombinationen verschiedene Vor- und Nachteile haben. So sind die ersten Piola-Kirchhoff-Spannungen $\mathbf{P}$ und die materielle Zeitableitung des Deformationsgradienten $\dot{\mathbf{F}}$ bei weitem die günstigste Wahl. Die Gründe hierfür sind in Glüge, Weber und Bertram (2012) Abschnitt 2.3 zusammengefasst. Andere Variablen können prinzipiell auch für die Kopplung verwendet werden, was allerdings erhebliche Konsequenzen für die Auswertung der Hill-Mandel-Bedingung hat, die die zulässigen Randbedingungen für RVE einschränkt (siehe Abschnitt 5.3). Hill selbst schlug anfänglich die Verwendung der Cauchy-Spannungen $\boldsymbol{\sigma}$ und des räumlichen Geschwindigkeitsgradienten $\mathbf{L}$ vor und erst später die ersten Piola-Kirchhoff-Spannungen und die materielle Rate des Deformationsgradienten (Hill, 1967; Hill, 1984).

4 Homogenisierung und Konvexifizierung

Dieser Abschnitt ist mit dem Zusammenhang der Homogenisierung zu anderen, auf den ersten Blick nicht verwandten Problemen der Materialmodellierung befasst.

Die Lösung eines ratenunabhängigen mechanischen Randwertproblems entspricht in aller Regel der Lösung $\mathbf{u}(\mathbf{x})$ eines Systems von partiellen Differentialgleichungen im Ort $\mathbf{x}$ mit spezifischen Randwerten. Es wird verlangt, dass das inkrementelle Randwertproblem zu jedem Zeitpunkt von genau einem Geschwindigkeitsfeld gelöst wird Bigoni (2000). Existieren mehrere Lösungen zum sogenannten Geschwindigkeitsproblem, liegt ein Bifurkation vor, und die Lösung des Randwertproblems ist

uneindeutig. In aller Regel wird dieses Problem auf hinreichende lokale, vom spezifischen Randwertproblem unabhängige Kriterien zurückgeführt. Dabei handelt es sich um verschiedene Elliptizitätsbegriffe (Gilbarg und Trudinger, 2001), welche spezifische mathematische Eigenschaften partieller Differentialgleichungen sind.

Für gewöhnlich werden allerdings nicht die Differentialgleichungen selbst, sondern den Differentialgleichungen zugeordnete Variationsaufgaben numerisch gelöst. Hier wird ein Funktional $W = \int_\Omega w(\mathbf{u}(\mathbf{x}), \mathbf{u}(\mathbf{x}) \otimes \nabla, \ldots)\mathrm{d}V$ über der unbekannten Funktion $\mathbf{u}(\mathbf{x})$ minimiert. Kern dieser Variationsformulierungen ist das (möglicherweise inkrementelle) Material-Potenzial $w(\ldots)$, dessen Existenz in aller Regel aus thermodynamischen Gründen vorausgesetzt wird (Hackl, 1997; Celigoj, 1998). In diesem Fall ist eine Lösung gegeben, wenn das Funktional unterhalbstetig ist. Dies wurde von Morrey (1952) auf den Begriff der Quasikonvexität des Materialpotenzials zurückgeführt.

Da das Materialpotenzial im Zentrum der Materialmodellierungs-Bemühungen steht, wird die Existenz einer Lösung für beliebige Randwertprobleme an der Quasikonvexität des Materialpotenzials festgemacht. Quasikonvexität ist im Allgemeinen schwer zu beweisen oder zu widerlegen. Grund hierfür ist, dass sie nichtlokale, integrale Eigenschaft, ist (siehe z. B. Schröder (2010b)).

Daher wird Sie meist durch lokale Konvexitätsforderungen, nämlich durch die Untermenge der polykonvexen und die Übermenge der Rank-1-konvexen Funktionen approximiert. Die Entwicklung verschiedener Konvexitätsforderungen wurde hauptsächlich von Ball (1977) initiiert, und stellt ein komplexes und aktuelles Forschungsgebiet dar, siehe z. B. Schröder (2010a) für eine detailliertere Darstellung. Während Polykonvexität Quasikonvexität impliziert, impliziert Rank-1-Konvexität Quasikonvexität *nicht*. Das prominente Gegenbeispiel wurde von Šverák (1992) gegeben. Es erfüllt allerdings nicht das Prinzip der materiellen Objektivität (Bertram und Svendsen, 2001), und ist daher für die Materialmodellierung wenig relevant. Ob objektive Materialpotenziale existieren, die Rank-1-konvex, aber nicht quasikonvex sind, ist unbekannt. Trotz intensiver Suche (Aubert, 1995) wurde bisher keines gefunden, weswegen Rank-1-Konvexität aus Ingenieurssicht hinreichen dürfte. Allerdings kann man Rank-1-Konvexität selbst bei etablierten elastischen Gesetzen nicht als gegeben annehmen. Beispielsweise zeigen Bertram, Böhlke und Šilhavý (2007), dass isotrope elastische Energien, die quadratisch in den verallgemeinerten Dehnungen sind (Seth, 1964), nicht Rank-1-konvex sein können. Deren Rank-1-konvexe Bereiche wurden in Glüge und Kalisch (2012) diskutiert.

Ein Mangel an Quasikonvexität macht sich durch das Auftreten vieler lokaler Minima von W, oder W minimierende Familien von Verschiebungsfeldern $\mathbf{u}(\mathbf{x})$ bemerkbar. All diesen ist gemein, dass die Lösungen $\mathbf{u}(\mathbf{x})$ nur C_0-stetig sind (Carstensen, 2005). Es stellen sich Grenzflächen ein, an welchen der Gradient von $\mathbf{u}$ einen Sprung in Richtung der Grenzflächennormalen aufweist. Die abgegrenzten Gebiete werden als Phasen bezeichnet. Die Lage der Phasen im Gebiet ist im Allgemeinen nicht eindeutig. So gibt es anstatt eines eindeutigen Feldes $\mathbf{u}(\mathbf{x})$ als Lösung des Randwertproblems eine Familie von Lösungen, die nur die Volumenanteile der Phasen gemeinsam haben, nicht aber deren räumliche Anordnung.

Die Rank-1-Konvexität ist eng an die Möglichkeit einer sprunghaften Dehnungslokalisierung gekoppelt. Sie schließt genau diejenigen Lokalisierungsmoden aus, die kinematisch zulässig sind, nämlich Rank-1-Sprünge des Deformationsgradienten. Daher reduziert Sie aus Sicht des Ingenieurs die Menge zulässiger Materialpotenziale genau um diejenigen, die im Rahmen der kinematischen Kompatibilität des Verschiebungsfeldes Dehnungslokalisierungen als Lösungen des Variationsproblems zeigen könnten.

Nun ist ein Phasenzerfall genau das, was man in vielen Materialien beobachtet. Beispiele sind martensitische Umwandlungen, Zwillingsbildung, aber auch Dehnungslokalisierungen in der Metall- und Polymerplastizität.

Die Frage nach einer Eindeutigkeit der Lösung ist also keine rein mathematische, sondern auch eine physikalische. Ein nicht-quasikonvexes Materialpotenzial kann durchaus der Ausgangspunkt einer mikromechanischen Modellierung sein (Glüge, 2010). Die Frage ist vielmehr, wie man das schlecht gestellte Randwertproblem umgeht. Hierfür gibt es mindestens zwei Möglichkeiten:

- Reduktion der gesuchten Lösung um die lokale Auflösung des Phasenzerfalls:
  - Das Ersetzen des Materialpotenzials durch dessen Poly-, Quasi- oder Rank-1-konvexe Hülle.
- Einbeziehen weiterer physikalischer Informationen:
  - Das Erweitern des Problems um Trägheitsterme (dynamische Regularisierung).
  - Das Erweitern des Materialverhaltens um eine Ratenabhängigkeit (viskose Regularisierung).
  - Das Erweitern des Materialpotenzials um einen Gradiententerm (kapilare Regularisierung).

In erstem Fall werden weniger, im zweiten Fall mehr physikalische Informationen verwendet.

Aus Sicht der Homogenisierung sind beide Methoden interessant, wobei erstere sicher die direktere ist: *Das Bestimmen einer Poly- Quasi oder Rank-1-konvexen Hülle entspricht der analytischen Homogenisierung eines Materials, welches durch Phasenzerfall Mikrostrukturen ausbilden kann*[1]. Dementsprechend können alle Konvexifizierungsmethoden, ob numerisch oder analytisch (siehe z. B. Aranda und Pedregal (2001), Bartels, Carstensen, Hackl und Hoppe (2004), Hackl und Kochmann (2008), Bartel und Hackl (2009) und Roubíček (2011) und viele andere) als Homogenisierungsmethoden für eine spezielle Materialklasse aufgefasst werden. Umgekehrt können numerische Homogenisierungen, die aufgrund eines Mangels an Konvexität mit Hilfe einer der genannten Regularisierungen (siehe Abschnitt 4.2) erfolgen, als Algorithmen zur Iteration einer konvexen Hülle angesehen werden. Beispiele für den direkten Zusammenhang zwischen Homogenisierung und Konvexifizierung sind Bartel und Hackl (2010) und Bartel, Kiefer, Buckmann und Menzel (2015).

Quasikonvexe Hüllen können nur in den seltensten Fällen angegeben werden (ein Beispiel für kleine Deformationen ist Khan und Hackl (2012)), weswegen eher Poly- oder Rank-1-Konvexität gefordert wird. Die Schwierigkeiten bei der Bestimmung einer Rank-1-konvexen Hülle kann man erahnen, wenn man sich die aus der Forderung nach Rank-1-Konvexität resultierenden Ungleichungen für isotrope, elastische Materialien anschaut. Deren kompakteste Form kann in Dacorogna (2005) gefunden werden. Auch für inkompressible isotrope elastische Materialien lassen sich (gerade) noch geschlossene Ungleichungen angeben (Zee und Sternberg, 1983). Für anisotrope elastische Materialien sind hingegen keine geschlossenen Ungleichungen bekannt, die exakt Rank-1-Konvexität sichern. Stattdessen ist es in diesem Fall sinnvoller, sich auf polykonvexe Materialpotenziale zu beschränken, für welche von Schröder und Neff (2003) und Schröder (2010a) Konstruktionsregeln angegeben sind.

4.1 Informationsreduktion durch Konvexifizierung

Bei ersterer Maßnahme handelt es sich also grob gesagt um ein Vereindeutigen der Lösung durch Mittelung über denjenigen Parameter, der die Lösungsfamilie des Originalproblems beschreibt, nämlich die Ortsabhängigkeit des Phasenzerfalls. Sie wird durch die Volumenintegration in der Definition der Quasikonvexität eliminiert,

[1] Die Konvexifizierung eines nichtkonvexen Materialpotenzials wird auch als Relaxierung bezeichnet.

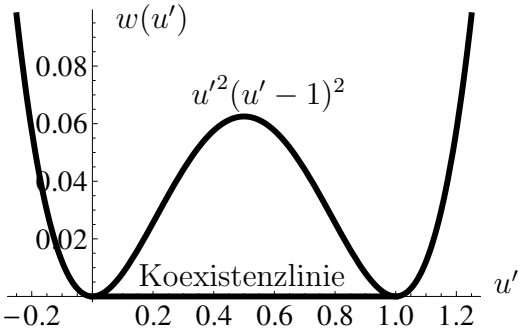

Abbildung 2: Die elastische Energie $w(u'(x)) = u'(x)^2(u'(x)-1)^2$ (Gleichung 1 mit $E = 2$) und deren konvexe Hülle.

so wie sie bei einer Homogenisierung durch Volumenmittelung eliminiert wird. Man bezeichnet den kleinstmöglichen Wert des Funktionals W für die Lösungsfamilie als den Gamma-Grenzwert Γ. Die Theorie der Gamma-Konvergenz für Funktionale ist eng mit der Quasikonvexifizierung des Materialpotenzials verwandt, allerdings ist sie von großer mathematischer Abstraktheit (Braides, 2002).

Beispiel. Gegeben sei ein Zugstab der Länge l_0 mit der elastischen Energie

$$w(u'(x)) = \frac{E}{2}u'(x)^2(u'(x)-1)^2, \tag{1}$$

siehe Abbildung 2. Die Randbedingungen seien $u(0) = 0$ und $u(l_0) = \Delta l$. Die Lösung des elastostatischen Randwertproblems (ohne Neumann-Randbedingungen) ist durch Minimieren des Funktionals

$$W = \int_0^{l_0} \frac{E}{2}u'(x)^2(u'(x)-1)^2 \mathrm{d}x. \tag{2}$$

über $u(x)$ gegeben.

Man erkennt leicht, dass $u' = 0$ und $u' = 1$ die lokalen Minima der Funktion $w(u')$ sind, und w an ihnen den Wert Null annimmt. Erlaubt man C_0-stetige Lösungen für $u(x)$, so kann man für Werte von Δl zwischen 0 und l_0 beliebige Zusammenstückelungen linearer Segmente mit den Anstiegen 0 und 1 konstruieren, so dass $W = 0$ gilt. Es muss lediglich sichergestellt werden, dass

$$\int_0^{l_0} u'(x)\mathrm{d}x = \Delta l \tag{3}$$

gilt, also dass ein Anteil von $\Delta l/l_0$ den Anstieg 1, und der Rest $(1 - \Delta l/l_0)$ den Anstieg 0 hat. Wo genau im Stab die Segmente liegen ist unerheblich. Damit ist das Variationsproblem nicht eindeutig lösbar.

Weiterhin ist es nicht möglich, im Intervall $0 \leq \Delta l \leq l_0$ kleinere Werte als $W = 0$ zu erzielen. Somit ist der Wert 0 für W der Γ-Grenzwert. Ersetzt man die Ausgangsenergie durch die konvexe Hülle

$$\overline{w}(u') = \begin{cases} u'^2(1-u'^2) \text{ wenn } u' < 0 \text{ oder } u' > 1 \\ 0 \text{ anderenfalls} \end{cases} \tag{4}$$

erhält man diesen automatisch, ohne über eine lokale Verteilung des Phasenzerfalls nachdenken zu müssen. Somit entspricht $\overline{w}$ der elastischen Energie des effektiven Materials. Die lineare Verbindung der beiden Minima wird in der Thermodynamik treffend als Koexistenzlinie bezeichnet (Ortin, 1997), da hier beide Phasen gleichzeitig vorliegen. Aufgrund der Einfachheit des Problems ist $W(\Delta l)$ durch $l_0\overline{w}(\Delta l/l_0)$ gegeben.

Was im Eindimensionalen recht einfach ist, wird im Dreidimensionalen und für realistische Materialpotenziale sehr kompliziert, siehe die oben genannten Publikationen zur Konvexifizierung.

4.2 Informationszuwachs durch genauere physikalische Betrachtung

Im Gegensatz dazu stellen die weiteren Maßnahmen eine Modifikation des Problems durch genauere physikalische Betrachtungen dar, man hat also anstatt eines Informationsverlustes eine Informationszuwachs in Form einer räumlichen Auflösung des Phasenzerfalls. Die physikalischen Zusatzinformationen helfen bei der Auswahl einer Lösung des ansonsten schlecht gestellten Problems, wobei streng betrachtet natürlich nicht das Ausgangsproblem gelöst wird. Da die Phasenanordnung a priori unbekannt ist, werden spezielle numerische Methoden benötigt, welche die sich einstellenden und eventuell beweglichen Diskontinuitäten berücksichtigen. Bei der FEM ist z. B. eine Neuvernetzung (Miehe und Schröder, 1994), Netzanpassung (Kaczmarczyk, Nezhad und Pearce, 2014) oder die Aufnahme von Diskontinuitäten in die Formfunktionen (erweiterte FEM, siehe z. B. Melenk und Babuska (1996) und Schröder und Löblien (2005)) möglich.

Die Ergänzung des Ausgangsproblems um physikalische Zusatzinformationen wird am besten an einem Beispiel von Abeyaratne und Knowles (2006) deutlich, welche einen Zugstab mit nichtkonvexer eindimensionaler elastischer Energie betrachten, ähnlich dem obigen Beispiel. Als Lösung sind prinzipiell auch beliebige Zusammenstückelungen der Phasen möglich. Abeyaratne und Knowles (2006) wählen durch Erheben weiterer physikalischer Randbedingungen eine Lösung aus: Ein Stabende wird als als Störstelle identifiziert, an welchem daher die Phasenumwandlung startet. Weiterhin ist es energetisch nicht sinnvoll, mehr Grenzflächen als nötig (also eine) einzubauen, womit eine Lösung festgelegt ist. Deren Bewegung ist durch die Dynamik (siehe nächster Abschnitt) festgelegt.

Im Allgemeinen möchte man jedoch nicht durch Diskussion des spezifischen Randwertproblems eine Lösung suchen. Im folgenden werden allgemein anwendbare Regularisierungsmethoden andiskutiert.

4.2.1 Ergänzung um eine Zeitabhängigkeit

Dynamische Regularisierung. Das Erweitern des Problems um eine Zeitãbhängigk̃eit ist physikalisch sinnvoll. Allein das Hinzunehmen der Massenträgheit verwandelt das schlecht gestellte globale Minimierungsproblem in eine Sequenz gut gestellter globaler inkrementeller Minimierungsprobleme, deren Zeitintegration die gewünschte Auswahl einer Lösung des Ausgangsproblems liefert. Man spricht in diesem Fall von der dynamischen Regularisierung, siehe z. B. Needleman (1989). Allerdings verleidet im allgemeinen die kleine Zeitschrittweite, die wegen der in Festkörpern meist hohen Schallgeschwindigkeit recht niedrig ist, eine effiziente numerische Behandlung.

Viskose Regularisierung. Populärer ist daher das Einbeziehen einer Viskosität. Sie liefert entweder analytisch via eines Grenzüberganges zu Null (Bianchini und Bressan, 2005; Knees, Rossi und Zanini, 2013) oder numerisch als Sequenz inkrementeller Probleme die Auswahl einer Lösung des Ausgangsproblems. Insbesondere letztere

Variante wird zur Simulation vieler Phänomene mit Entfestigung, Risswachstum, Dehnraten-Entfestigung, Schädigung oder Phasenumwandlungen verwendet, siehe jeweils Dias da Silva (2004), Knees, Mielke und Zanini (2007), Böhlke, Bondár, Estrin und Lebyodkin (2009), Chaboche, Feyel und Monerie (2001), Glüge, Bertram, Böhlke und Specht (2010) und Wang und Khachaturyan (1997). Das wohl bekannteste Beispiel ist die ratenabhängige Fließregel von Hutchinson (1976). Einerseits verwandelt sie das Algebro-Differenzialgleichungssystem idealer Plastizität in ein leichter handhabbares System gewöhnlicher Differenzialgleichungen (Simo und Hughes, 1998), andererseits wird durch die Viskosität eine vom Randwertproblem abhängige minimale Dicke für Lokalisierungen induziert, welche die Netzabhängigkeit von FE-Lösungen reduziert (Needleman, 1988). Daher ist es nicht verwunderlich, dass sich viskose Fließregeln wie die von Hutchinson für die Simulation der Einkristallplastizität mit der Finiten Elemente Methode (CPFEM– crystal plasticity finite element method) durchgesetzt haben. Einige solcher Fließregeln sind in Roters (2011) aufgeführt.

4.2.2 Ergänzung um einen Gradiententerm

Dehnungsgradienten. Die Einschränkung des Lösungsraums auf C_1-stetige Verschiebungsfelder entfernt die Möglichkeit des Phasenzerfalls mit scharfen Grenzflächen. Sie ist nur sinnvoll, wenn gleichzeitig eine energetische Berücksichtigung des Dehnungsgradienten, da anderenfalls die geglätteten Sprünge nur durch unendlich scharfe glatte Übergänge ersetzt werden, was eher einer mathematischen Umformulierung entspricht. Genügt diese Erweiterung des Materialpotenzials wiederum bestimmten mathematischen Forderungen, ist das gradientenerweiterte Randwertproblem gut gestellt. Physikalisch kann der Gradientenbeitrag zum Materialpotenzial als Grenzflächenenergie (Carstensen, 2005) gedeutet werden. Durch diese werden unendlich feine Phasenmischungen energetisch unattraktiv. Man spricht in diesem Fall von einer *kapilaren Regularisierung*, siehe z. B. Zimmer (2006). Die Wirkung einer derartige Gradientenerweiterung zu einer nichtkonvexen elastischer Energie ist beispielsweise in Rudraraju, Van der Ven und Garikipati (2014) illustriert.

Phasenfeldmethode. Anstatt den Gradienten des Verschiebungsfeldes als Indikator für einen Phasenübergang zu verwenden, werden oft Phasenfelder eingeführt (Idesman, Levitas und Stein, 2000; Lapczyk, Rajagopal und Srinivasa, 2000; Provatas und Elder, 2010). Dabei handelt es sich um Indikatorfunktionen, die die an einem materiellen Punkt vorherrschende Phase anzeigen. Allerdings werden nur glatte Übergänge zwischen den Phasen zugelassen. Die Gradienten der Phasenfelder leisten dabei einen Beitrag zur freien Energie, was die Schärfe des Phasenüberganges und letztlich auch die Feinheit des Phasenzerfalls begrenzt. Letzterer kann physikalisch wieder als Grenzflächenenergie interpretiert werden. Gleichzeitig kann über die Entwicklungsgleichung für die Phasenfelder eine Grenzflächenkinetik implementiert werden, siehe hierzu z. B. Hildebrand und Miehe (2010). Die Phasenfeldmethode hat ihren Ursprung in der Modellierung freier Oberflächen (Fix, 1983; Langer, 1986) bei Erstarrungsvorgängen, und damit verbundenem Dendritenwachstum (Emmerich, Kassner, Ihle und Weiss, 2000). Diese Ansätze sind meist auf zwei Phasen beschränkt, weshalb nur eine Art von Grenzfläche mit einer kinetischen Beziehung und einer Energie ausgestattet werden muss. Bei Zwillingsbildung oder martensitischen Umwandlungen müssen allerdings erstmal zwischen allen möglichen Phasenkombinationen unabhängig solche Beziehungen eingeführt werden, was den Modellierungsaufwand und den numerischen Aufwand erhöht. Oft sind solche Untersuchungen daher auf wenige Phasen und zweidimensionale Gebiete beschränkt (z. B. Schmitt, Kuhn, Müller und Bhattacharya (2014)).

In jedem Fall enthält die mit Hilfe einer der Regularisierungen ermittelte Lösung Detailinformationen zur Phasenverteilung. Aus dieser können leicht via Volumenmittelung effektive Größen ermittelt werden, weswegen die aufgeführten Methoden häufig zusammen mit der RVE-Methode verwendet werden. Beispielsweise wurde aus dem in Glüge, Bertram, Böhlke und Specht (2010) entwickelte Mikromodell für Zwillingsbildung in Einkristallen mit Hilfe von RVE-Rechnungen ein effektives Materialverhalten ermittelt (Glüge, 2011). Als Regularisierung wurde die häufig verwendete Viskosität gewählt (siehe Abschnitt 4.2.1). Andere Autoren wie z. B. Wang, Jin und Khachaturyan (2004) und Apel, Laschet, Böttger und Berger (2014) haben gezeigt, dass ebenso die Ergänzung um einen Gradientenbeitrag in Zusammenhang mit einem repräsentativen Materialausschnitt verwendet werden kann.

5 Numerische Homogenisierung mit der RVE-Methode

Das Verfolgen der Entwicklung eines repräsentativen Materialausschnittes ist ein pragmatischer Ansatz. In aller Regel ist dies nur mit einer geeigneten Diskretisierung und numerischen Methoden möglich. Je größer der repräsentative Materialausschnitt gewählt wird, umso besser wird das effektive Materialverhalten approximiert.

5.1 Skalenabstand bei RVE: Hashins Prinzip

Wie bereits geschrieben ist die RVE-Methode nur bei großen Skalenabständen zwischen Mikro und Makro anwendbar, da das RVE auf der Zwischenebene (meso) angesiedelt ist, und sowohl zur Mikro- als auch zur Makroebene ein ausreichender Skalenabstand vorhanden sein muss.

5.1.1 Skalenabstand Mikro zu Meso

Zur Quantifizierung des notwendigen Skalenabstandes gibt es zahlreiche Studien, beispielsweise Drugan und Willis (1996), Elvin (1996), Gusev (1997), Ostoja-Starzewski (1998), Ren und Zheng (2002), Nygards (2003), Kanit, Forest, Galliet, Mounoury und Jeulin (2003), Ren und Zheng (2004), Houdaigui, Forest, Gourgues und Jeulin (2007), Glüge, Weber und Bertram (2012), Glüge (2013) und Dirrenberger, Forest und Jeulin (2014). Die notwendige Größe des RVE im Verhältnis zu den Inhomogenitäten hängt stark von der Mikrostrukturmorphologie, den Materialeigenschaften, dem akzeptierbaren Fehler, der Art des Materialverhaltens um das es geht (z. B. elastisch oder plastisch, siehe z. B. Gitman, Askes und Sluys (2007)) und den verwendeten RVE-Randbedingungen ab (siehe Abschnitt 5.4). Für einfache Homogenisierungsaufgaben, z. B. die Ermittlung der elastischen Eigenschaften eines isotrop partikelverstärkten Materials, kann das Verhältnis von RVE-Volumen zu Partikelvolumen so kleine Werte wie 8 annehmen (Drugan und Willis, 1996). Bei anisotropen elastischen Homogenisierungsaufgaben steigt die benötigte RVE-Größe ungefähr linear mit dem Anisotropiegrad und invers quadratisch mit dem akzeptierbaren Fehler (Nygards, 2003). Houdaigui, Forest, Gourgues und Jeulin (2007) ermittelte zum Beispiel eine benötigte Anzahl von 445 Körnern pro RVE für die Bestimmung der elastischen Eigenschaften von polykristallinem Kupfer mit einem zulässigen Fehler von 1%, wobei bereits von optimalen Randbedingungen und der näherungsweise gültigen Ergodizitätshypothese (siehe Abschnitt 5.5) Gebrauch gemacht wurde. Werden zusätzlich die plastischen Eigenschaften betrachtet, steigt der Aufwand nochmal erheblich. Beispielhaft sei wieder ein isotrop partikelverstärktes

Material genannt. Reicht bei kubischen RVE für die elastischen Eigenschaften ein Verhältnis zwischen RVE- und Partikelvolumen von ca. 16 aus, benötigt man bei den plastischen Rechnungen mindestens einen Wert von 64 (Glüge, Weber und Bertram, 2012).

5.1.2 Skalenabstand Meso zu Makro

Detaillierte Untersuchungen hierzu sind in Jöchen und Böhlke (2009) und Böhlke, Jöchen, Kraft, Löhe und Schulze (2010) am Beispiel von Mikrobauteilen zu finden. Bei diesen ist kein ausreichender Skalenabstand zwischen Korngröße und Bauteilabmessung gegeben, was sich in statistischen Schwankungen der Bauteileigenschaften widerspiegelt. Deren Erwartungswert kann via Homogenisierung zumindest abgeschätzt werden.

5.2 Trägheits- und Massenkräfte

Die lokale Impulsbilanz für einfache Materialien enthält drei Summanden, nämlich die Divergenz des Spannungstensors, eine eingeprägte Massenkraftdichte und die Trägheitskraftdichte,

$$\operatorname{div}\left(\mathbf{T}(\mathbf{E})\right) = \rho\ddot{\mathbf{u}} - \rho\mathbf{b}. \tag{5}$$

Die statische Materialmodellierung ist allein mit der Funktion $\mathbf{T}(\mathbf{E})$ befasst, wobei $\mathbf{E}$ ein dem Verschiebungsfeld zugeordnetes Verzerrungsmaß ist. Daher müssen Massen- und Trägheitskräfte bei der Ermittlung effektiver Materialgesetze durch Homogenisierung ausgeschlossen werden. Anderenfalls erhält man effektive Materialgesetze, in welchen die Größe des RVE und dem RVE überlagerte Starrkörperbewegungen auftreten. Man findet hierzu auch Argumentationen der Art, dass das RVE klein ist (Länge l), und somit Volumenkräfte (von der Ordnung l^3) gegenüber Oberflächenkräften (von der Ordnung l^2) vernachlässigbar sind. Dies steht im Widerspruch zum Wunsch nach einem möglichst großen Skalenabstand zwischen Meso- und Mikroebene, also einem möglichst großen, repräsentativem RVE.

Eine andere Perspektive ergibt sich, wenn man an den dynamischen Materialeigenschaften eines Komposites interessiert ist, wie zum Beispiel der Dispersion von elastodynamischen Wellen. In diesem Fall wird die Massenträgheit als Materialeigenschaft aufgefasst. Die Unterschiede zur statischen Materialmodellierung sind erheblich. Bei der dynamischen Homogenisierung werden in aller Regel lineares Materialverhalten und kleine Deformationen vorausgesetzt. Anstatt eines effektiven Materialgesetzes wird ein effektiver Differential-Operator als Funktion der Phasenanordnung gesucht (Willis, 2011; Willis, 2012), der Orts- und Zeitableitungen enthält. Die Entwicklung eines mathematischen Rahmens zur Homogenisierung elastodynamischer/elektromagnetischer Wellen wurde von (Willis, 1980b; Willis, 1980a) initiiert. Zur Zeit hat die dynamische Homogenisierung nicht die Reife der statischen Homogenisierung, und bedarf der mathematischen und physikalischen Weiterentwicklung (Nassar, He und Auffray, 2015).

In diesem Zusammenhang sind zwei Sonderfälle zu nennen, nämlich die Ausbreitung von Wellen in Laminaten und in periodischen Mikrostrukturen. Die Elastodynamik von Laminaten ist besser erforscht als der allgemeine dreidimensionale Fall, da sie mathematisch einfacher und technologisch von großer Relevanz ist, siehe z. B. Nayfeh (1995). Für periodische Mikrostrukturen und Wellenlängen weit größer als die Inhomogenitäten lässt sich ein quasistatischer Grenzwert angeben, bei welchem die Struktur des Hookeschen Gesetzes erhalten bleibt, allerdings mit komplexen Steifigkeiten (Milton, 2002).

5.3 Hill-Mandel-Bedingung

Die Hill-Mandel-Bedingung sagt, dass die Spannungsleistung der effektiven Größen gleich dem Volumenintegral der Spannungsleistung über dem RVE entsprechen muss (Hill, 1963). Sie ist somit nichts anderes als die Forderung nach Energieerhaltung beim Skalenübergang. Ihre Einhaltung ist notwendig, aber nicht hinreichend dafür, dass das RVE bei Vergrößerung gegen das effektive Materialverhalten konvergiert. Ein Beleg hierfür ist, dass homogene Randspannungen die Hill-Mandel-Bedingung erfüllen, RVE dieser Art aber zu unrealistischen, nadelförmigen Lokalisierungen neigen, bei deren Auftreten die gemittelten Größen keine Aussagekraft über das wahre effektive Materialverhalten haben (Inglis, Geubelle und Matous, 2008; Fritzen, Forest, Böhlke, Kondo und Kanit, 2012).

Die Hill-Mandel-Bedingung kann nicht losgelöst von der Skalenkopplung (Abschnitt 3.4) betrachtet werden. Je nach Wahl der kinematischen und dynamischen Größen, die sich auf Makroebene durch ungewichtete Volumenintegrale ergeben sollen, ergeben sich unterschiedliche Schlussfolgerungen.

5.3.1 Interpretation der Hill-Mandel-Bedingung als notwendige Bedingung an die Randbedingungen

Für jede Wahl der Größen für die dynamische und kinematische Kopplung lassen sich Randbedingungen angeben, bei welchen die Hill-Mandel-Bedingung unabhängig von der RVE-Größe, also der Repräsentativität, erfüllt ist (Suquet, 1987; Hazanov, 1998).

Dies ist möglich, da die im RVE umgesetzte Spannungsleistung aufgrund der Abwesenheit von Massen- und Trägheitskräften identisch zur Leistung der Randspannung ist. Man kann die reduzierte Gleichgewichtsbedingung $\mathbf{P} \cdot \nabla_0 = \mathbf{o}$ (erste Piola-Kirchhoff-Spannungen $\mathbf{P}$) und die Deformations-Verschiebungs-Beziehung $\dot{\mathbf{F}} = \dot{\mathbf{x}} \otimes \nabla_0$ verwenden, um das Volumenintegral über die Spannungsleistung mit dem Gaußschen Integralsatz in ein Integral über die Randspannungen und Randgeschwindigkeiten umzuschreiben. Gleichzeitig lassen sich die effektiven Spannungen und Dehnungen ebenfalls durch Oberflächenintegrale angeben, so dass letztlich sowohl die Makro-Spannungsleistung als auch das Integral über die Mikro-Spannungsleistung *durch die Randbedingungen* ausgedrückt werden können. Hier ist die Wahl der Größen für die Skalenkopplung von entscheidender Bedeutung. Nur für die ersten Piola-Kirchhoff-Spannungen und den Deformationsgradienten ergeben sich einfach auswertbare Integrale. Das Skalarprodukt der effektiven Spannung und der effektiven Dehnrate muss laut der Hill-Mandel-Bedingung für alle möglichen Zustände der Leistung der äußeren Kräfte entsprechen. Hieraus lassen sich Forderungen an die Randbedingungen auf einem RVE ableiten.

In Glüge (2013) wird gezeigt, dass die Gleichheit bei der Wahl der ersten Piola-Kirchhoff-Spannungen und der materiellen Rate des Deformationsgradienten für die dynamische und kinematische Kopplung für eine bestimmte Klasse von Randbedingungen gewährleistet ist, in welcher auch die gebräuchlichen klassischen Randbedingungen (iso-strain, iso-stress und periodisch, siehe Abschnitt 5.4) liegen.

5.3.2 Interpretation der Hill-Mandel-Bedingung als Konvergenzkriterium für RVE

Geht man davon aus, dass die Randbedingungen am RVE *nicht* von vornherein die Gleichheit der volumengemittelten Spannungsleistung und der Spannungsleistung aus der effektiven Spannung und der effektiven Dehnrate sicherstellt, kann man die näherungsweise Erfüllung der Hill-Mandel-Bedingung als Qualitätsmerkmal für das RVE deuten. Je größer das RVE ist, umso besser gleichen sich statistische Schwankungen aus, und umso geringer ist der Unterschied zwischen Makro-Spannungsleistung

und dem Volumenmittel der Mikro-Spannungsleistung. Dies ist in der Tat Hills ursprüngliche Interpretation (Hill, 1952). Sie findet in statistischen Theorien als Ergodizitätsannahme Anwendung (Kröner, 1972; Arminjon, 1991).

Es sei angemerkt, dass beide Interpretationen der Hill-Mandel-Bedingung möglich sind, und lediglich die Wahl der Variablen für die Skalenkopplung zusammen mit der Wahl der Randbedingungen darüber entscheidet, welche Interpretation angewendet werden muss. In aller Regel muss von der ersten Deutung ausgegangen werden, da meist klassische Randbedingungen, zusammen mit kleinen Deformationen oder der Skalenkopplung via $\mathbf{P}$ und $\dot{\mathbf{F}}$ bei großen Deformationen verwendet werden.

5.4 Randbedingungen

Die Randbedingungen sind bei RVE über nichtperiodische Mikrostrukturen artifiziell. Sie stellen dann eine Störung dar, die nur durch große RVE reduziert werden kann, da das Volumen kubisch und der Rand nur quadratisch mit der charakteristischen Länge des RVE wächst.

Die klassischen, mit der Hill-Mandel-Bedingung verträglichen Randbedingungen auf RVE sind:

- Randverschiebungen aus global vorgeschriebenen effektiven Verzerrungen (iso-strain), $\mathbf{u} = \overline{\mathbf{H}} \cdot \mathbf{x}_0$,
- Randspannungen aus global vorgeschriebenen effektiven Spannungen (iso-stress), $\mathbf{t} = \overline{\mathbf{P}} \cdot \mathbf{n}_0$,
- periodische Randbedingungen $\mathbf{u}^+ - \mathbf{u}^- = \overline{\mathbf{H}} \cdot (\mathbf{x}_0^+ - \mathbf{x}_0^-)$, $\mathbf{t}^+ + \mathbf{t}^- = \mathbf{o}$ für gekoppelte Randpunkte $+$ und $-$, mit $\mathbf{n}_0^+ - \mathbf{n}_0^- = \mathbf{o}$.

Es sei angemerkt, das letztere Forderung $\mathbf{t}^+ + \mathbf{t}^- = \mathbf{o}$ oft nicht extra genannt wird, da sie durch die Tatsache impliziert wird, dass sich bei den periodischen Verschiebungsrandbedingungen um *Zwangsbedingungen* handelt, die keinen Beitrag zur Arbeit der äußeren Kräfte leisten. Aus dieser Forderung lässt sich die Antiperiodizität von $\mathbf{t}^{\pm}$ ableiten (Glüge und Weber, 2013).

Von diesen Randbedingungen sind die periodischen Randbedingungen bei weitem am populärsten, da sie einen guten Kompromiss zwischen den steifen iso-strain und den nachgiebigen iso-stress Randbedingungen bilden (Huet, 1990; Hazanov und Huet, 1994). Somit ist der Randeinfluss bei den periodischen Randbedingungen von vornherein moderat, und das RVE konvergiert bei Vergrößerung schneller gegen das effektive Materialgesetz.

Am wenigsten gebräuchlich sind die iso-stress-Randbedingungen. Sie sind nicht nur zu nachgiebig. Das Vorschreiben einer mittleren Spannung erfordert einen Wechsel der unabhängigen Variablen, da Materialgesetze normalerweise die Dehnungen als unabhängige Variable haben. Der Wechsel der unabhängigen Variablen führt auf die unpraktischen kinematisch minimalen Randbedingungen, bei welchen nur die mittlere Dehnung vorgeschrieben wird. Dies bereitet einige Probleme bei der Implementierung (Glüge, 2010). Dazu kommt noch, das die iso-stress Randbedingungen eine beliebige Lokalisierung des RVE gestatten, bei welcher die Repräsentativität des RVE verlorengeht (Inglis, Geubelle und Matous (2008) und Gitman, Askes und Sluys (2007), Abschnitt 5.6)

Weniger populär ist eine Unterraum-Aufteilung der Randbedingungen, bei welchen in einer Richtung iso-stress Randbedingungen, und in der Ebene senkrecht dazu iso-strain-Randbedingungen vorgeschrieben werden, oder umgekehrt. Auch diese Art der Randbedingungen stellt einen Kompromiss zwischen den beiden Extremen reiner iso-stress- und reiner iso-strain Randbedingungen dar. Sie findet allerdings kaum bei

der RVE-Methode Anwendung, da die Wahl der besagten Richtung eine artifizielle Anisotropie induziert. Derartige Annahmen sind nur im Zusammenhang mit spezifischen Umformprozessen sinnvoll. So sind zum Beispiel relaxierte Taylor-Modelle, bei welchen die iso-strain-Bedingung in einer Richtung und die iso-stress-Bedingung senkrecht dazu angenommen wird, für die Texturvorhersage bei Walzprozesse geeignet (Houtte, 1982; Houtte, Delannay und Samajdar, 1999; Van Houtte, Li, Seefeldt und Delannay, 2005).

5.5 Ergodizität

Im Zusammenhang mit der RVE-Methode spricht man von Ergodizität, wenn gilt, dass die Mittelung über sehr viele verschiedene Realisierungen kleinerer RVE gegen den gleichen Mittelwert strebt wie die Mittelung über ein sehr großes RVE. Aufgrund des Randeinflusses, der bei kleinen RVE systematisch größer ist als bei großen RVE, gilt diese Annahme nicht. Toleriert man jedoch eine gewisse Abweichung, kann durch die Realisierung mehrerer kleiner RVE anstatt eines großen RVE der numerische Aufwand reduziert werden (Kanit, Forest, Galliet, Mounoury und Jeulin, 2003), da dieser bei ersterer Methode proportional mit der Anzahl der Realisierungen, bei zweiterer Methode aber überproportional mit der Größe n des linearen Systems, also des RVE-Volumens steigt. Der Aufwand ist bei direkten Lösern wie der Cholesky-Zerlegung von der Ordnung $\mathcal{O}(n^3)$ und, im günstigsten Fall, $K\mathcal{O}(n)$ bei modernen iterativen Lösern wie dem Krylow-Unterraum-Verfahren, mit einer sehr großen Konstanten K.

5.6 Lokalisierung

Bei Lokalisierung des RVE geht die Repräsentativität verloren, da die Lokalisierung auf der RVE-Ebene stattfindet (Gitman, Askes und Sluys, 2007; Glüge, 2013). Demzufolge sind zum Beispiel Simulationen mit Rissausbreitung in RVE, welche vollständig versagen, oder Scherbänder, die sich durch das gesamte RVE ziehen, äußerst kritisch zu betrachten. In diesem Zusammenhang sind die Arbeiten von Kadowaki und Liu (2004), Pelissou, Baccou, Monrie und Perales (2009) und Coenen, Kouznetsova und Geers (2012) zu kritisieren, da diese auch nach einer Lokalisierung von einer Verwertbarkeit der gemittelten Größen ausgehen. Leider kann nicht einmal der Zeitpunkt der Lokalisierung selbst als Eigenschaft des effektiven Materials angesehen werden.

Die Fähigkeit zur RVE-Lokalisierung hängt entscheidend von den Randbedingungen ab. So unterbinden iso-strain Randbedingungen RVE-weite Lokalisierungen, während iso-stress Randbedingungen beliebige Lokalisierungsmoden zulassen. Dieses Verhalten hängt nicht von der RVE-Größe ab. Daher ist keine Konvergenz gegen ein wahres, effektives Materialverhalten bei Vergrößerung des RVE zu erwarten. Da die Randbedingungen artifiziell sind, ist somit auch jede Lokalisierung eine RVE-Eigenschaft, nicht jedoch eine effektive Materialeigenschaft.

Zur Klärung wird vorgeschlagen, strikt zwischen Lokalisierung auf Mikroebene und Makroebene zu unterscheiden.

- Bei Ersterer wächst eine Inhomogenität im RVE. Wird diese zu groß, geht die Repräsentativität des RVE verloren, da der Skalenabstand zur Mikroebene nicht mehr gegeben ist. Man hat beim Wachstum einer Inhomogenität durch die Skalen einen Reduktion und schließlich den Verlust des Skalenabstandes zwischen Mikro- und Makroebene (Gitman, Askes und Sluys, 2007). Somit ist der Homogenisierung mit der RVE-Methode der Boden entzogen. Es existieren für derartige Materialien keine RVE, und die Homogenisierung mittels der

RVE-Methode ist nicht möglich (Gitman, Askes und Sluys, 2007). Im folgenden werden solche Lokalisierungen als skalenübergreifend bezeichnet.

- Bei Letzterer findet die Lokalisierung auf der Makroebene statt, zum Beispiel durch ein entfestigendes effektives Materialgesetz. Ein Beispiel hierfür ist die Einschnürung einer polykristallinen Zugprobe (ohne Reißen), wobei die Zone der Einschnürung wesentlich größer ist als die einzelnen Körner. Bei dieser Art der Lokalisierung bleibt der Skalenabstand zwischen Mikro- und Makroebene erhalten, und die RVE-Methode kann angewendet werden.

Bei periodischen Mikrostrukturen sind die periodischen Randbedingungen nicht a priori artifiziell. Allerdings müssen Lokalisierungen nicht zwangsweise innerhalb des Periodizitätsrahmens auftreten. Wendet man periodische Randbedingungen an, erfasst man nur periodische Lokalisierungsmoden, die in den Periodizitätsrahmen des RVE passen. Durch Zusammenfassen mehrerer Einheitszellen im RVE können dementsprechend mehr Lokalisierungsmoden, aber niemals alle, erfasst werden, siehe hierzu z. B. Miehe, Schröder und Becker (2002) und Coenen, Kouznetsova und Geers (2012).

5.6.1 Lösungsansätze für Materialien mit skalenübergreifender Lokalisierung

Im Folgenden werden einige Methoden zur Handhabung skalenübergreifender Inhomogenitäten dargestellt, wobei die Methoden teilweise ineinander übergehen.

- **Methode der gekoppelten Volumina.** Gitman, Askes und Sluys (2008) erkennen korrekt den Verlust des Skalenabstandes zwischen Meso- und Makroebene, und diskutieren das Problem am Beispiel des Sprödbruchs. Sie schlagen vor, die Volumina kleiner virtueller Materialproben an die Volumina der Gebiete zu koppeln, in denen man das mikrostrukturierte Material durch ein effektives Material ersetzen möchte. Der Ansatz wird als *Coupled-volume approach* bezeichnet. Hintergedanke ist die Verwendung der Mehrskalen-Finite-Elemente Methode. Dabei wird jedem Integrationspunkt auf der Makroebene eine virtuelle Materialprobe zugeordnet. Gitmans Vorschlag ist, dass Materialproben-Volumen an das dem Integrationspunkt zugeordnete Volumen zu koppeln. Auf diese Weise wird das RVE-Volumen als Maß für die RVE-Qualität eliminiert, und man muss keinen Grenzübergang zu unendlich großen RVE durchführen um das effektive Materialverhalten zu bestimmen.

  Bei diesem Ansatz könnte es problematisch sein, dass die Netzfeinheit auf Makroebene die Größe der virtuellen Materialprobe bedingt. Dies wurde von Gitman, Askes und Sluys (2008) untersucht, wobei festgestellt wurde, dass die Netzdichten auf beiden Ebenen aufeinander abgestimmt werden müssen. Ist dies erfolgt, kann die Abhängigkeit der Lösung des Randwertproblems auf Makroebene vom Volumen der virtuellen Materialprobe weitgehend reduziert werden.

  Bei dieser Vorgehensweise handelt es sich eher um eine geschickte Methode, eine Vollfeldsimulation mit Mikrostruktur zu implementieren. Die RVE-Methode dient als Werkzeug, mit dessen Hilfe das große Randwertproblem zerlegt wird.

- **FE^2/Mehrgitter-Methoden.** Die Methode ist dem coupled-volume approach recht ähnlich. Auch hier wird anerkannt, dass die Heterogenitäten und deren mögliches skalenübergreifendes Anwachsen nicht durch ein idealisiertes effektives Materialgesetz dargestellt werden können. Stattdessen wird parallel auf beiden Skalen gerechnet, wobei die Mehrgitter-Methoden ein geeignetes Werkzeug für die Kopplung der Mikro- und Makroebene darstellen. So kann das skalenübergreifende Anwachsen, z. B. eines Risses, von der Keimung

bis zum Bauteilversagen, durch die Skalen verfolgt werden. Arbeiten auf diesem Gebiet konzentrieren sich im wesentlichen auf die effiziente Implementierung dieses numerischen Mehrskalenansatzes (siehe z. B. Miehe und Bayreuther (2007), Loehnert und Belytschko (2007), Kaczmarczyk, Pearce, Bicanic und Souza Neto (2010), Geers, Kouznetsova und Brekelmans (2010) und Bosco, Kouznetsova, Coenen, Geers und Salvadori (2014)). Dabei sind

- das Auffinden einer geeigneten Projektion der Felder von der an Freiheitsgraden wesentlich reicheren Mikroebene auf die Makroebene (Homogenisierung) sowie
- die auf Mikroebene anzuwendenden Randbedingungen (Lokalisierung)

die Hauptprobleme. Insbesondere letzterer Punkt enthält eine gewisse Beliebigkeit, da prinzipiell Annahmen getroffen werden müssen, um die makroskopischen Felder auf die Mikroebene zu extrapolieren. Dies äußert sich in der Tatsache, dass verschiedene Randbedingungen auf die Mikro-Volumenelemente verwendet werden können (meist iso-stress, iso-strain oder periodisch).

- **Skalenübergang mit Gradientenerweiterung.** Kouznetsova, Geers und Brekelmans (2002) sehen im stark inhomogenen Verzerrungsfeld lokalisierender RVE das Hauptproblem. Es wird vorgeschlagen, dieses auf Makroebene nicht nur durch eine mittlere Dehnung, sondern zusätzlich durch einen mittleren Dehnungsgradienten zu beschreiben. Daher ergibt sich auf Makroebene ein Gradienten-Materialgesetz, während auf der Mikroebene klassische Materialmodellierung betrieben wird (Kaczmarczyk, Pearce und Bićanić, 2008; Feyel, 2003). Leider löst diese Vorgehensweise das Problem des Repräsentativitätsverlustes nicht. Sie muss vielmehr als spezielle Mehrgittermethode (siehe oben) angesehen werden.

  In diesem Zusammenhang ist erwähnenswert, dass bereits Gabrio Piola im Jahr 1848 ein um Dehnungsgradienten erweitertes Prinzip der virtuellen Leistung vorschlug, wie es in der aktuellen Forschung vermehrt verwendet wird (Bertram und Forest, 2014; Bertram, 2014). Er sah in diesem die einzige Möglichkeit, interne Wechselwirkungen zu beschreiben, die nicht durch ein Cauchy-Kontinuum beschrieben werden können (dell'Isola, Maier, Perego, Andreaus, Esposito und Forest (2014), Kapitel 5, Abschnitt 3.1). Dies wird durch aktuelle Arbeiten untermauert. Beispielsweise passen Shodja und Tehranchi (2010), Shodja, Zaheri und Tehranchi (2013), Po, Lazar, Seif und Ghoniem (2014) und Seif, Po, Mrovec, Lazar, Elsässer und Gumbsch (2015) die zum Gradiententerm gehörenden Materialparameter an Ergebnisse der Molekularstatik an, und gelangen so zu einer Kontinuumstheorie für Versetzungen. Müller, Scardia und Zeppieri (2015) setzten eine Ebene höher an, hier wird via Homogenisierung eine Gradienten-Kontinuumstheorie ohne Versetzungen aus einer Theorie diskreter Versetzungen ermittelt.

- **Materialklassenabhängige Gültigkeit eines RVE.** In Glüge (2013) wird vorgeschlagen, dass RVE (einschließlich spezifischer Randbedingungen) einem Plausibilitätstest zu unterwerfen. Wird dieser für eine bestimmte Materialklasse bestanden, wird von der Gültigkeit der RVE-Methode ausgegangen. Diese Verallgemeinerung ist nicht weiter problematisch, da man im Falle des Versagens der Methode dies sofort an der RVE-weiten Lokalisierung erkennt.

  Als Test wird vorgeschlagen, dass RVE auf ein homogenes Material mit bekanntem Materialgesetz anzuwenden. Wird das Materialverhalten vom RVE direkt auf die Makroebene weitergeleitet, kann von der Anwendbarkeit der RVE-Methode ausgegangen werden.

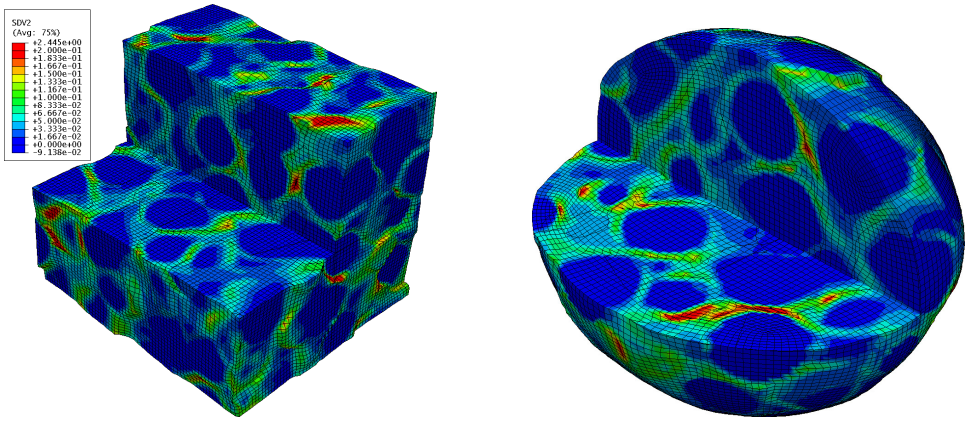

Abbildung 3: Ein würfel- und ein kugelförmiges RVE, aus welchen jeweils ein Viertel rausgeschnitten wurde. Die Farbgebung entspricht der plastischen Deformation eines elasto-plastischen Matrixmaterials, siehe Glüge, Weber und Bertram (2012) für Details.

Auf diese Weise wurde festgestellt, dass z. B. entfestigende Materialien durchaus mit der RVE Methode homogenisiert werden können, wenn die Lokalisierung durch die Randbedingungen unterdrückt wird. Hierfür sind z. B. die iso-strain Randbedingungen und die stochastischen Randbedingungen (siehe Abschnitt 5.7.2) geeignet, als ungeeignet erweisen sich die periodischen und die iso-stress Randbedingungen.

- **Lokalisierungsangepasste Randbedingungen.** Schließlich sei noch die Arbeit von Coenen, Kouznetsova und Geers (2011) und Coenen, Kouznetsova und Geers (2012) erwähnt, welche zur Kopplung der moderat steifen periodischen Randbedingungen mit beliebigen Lokalisierungsmoden sogenannte ,,percolation path" Randbedingungen vorschlägt. Dabei handelt es sich um verschobene periodische Randbedingungen, wobei die Verschiebung der Randpunktkopplungen dynamisch an eine sich entwickelnde Lokalisierung angepasst wird. So wird lediglich der RVE-induzierte Periodizitätsrahmen eliminiert, das eigentliche Problem des Repräsentativitätsverlustes bei Lokalisierung besteht nach wie vor.

5.7 Diskussion eigener Arbeiten

5.7.1 Formoptimierung

Die Form des RVE hat einen wesentlichen Einfluss auf die Qualität der Ergebnisse und die Konvergenz gegen das effektive Materialverhalten. Meist werden würfelförmige RVE verwendet, was unter anderem durch die vorteilhaften periodischen Randbedingungen gerechtfertigt wird. Diese werden aufgrund ihrer positiven Eigenschaften auch bei nichtperiodischen Mikrostrukturen angewendet.

In Glüge, Weber und Bertram (2012) wird gezeigt, dass:

- kugelförmige RVE aufgrund des kleineren Oberfläche/Volumen-Verhältnisses bei Vergrößerung des RVE schneller gegen das effektive Materialverhalten streben,
- kugelförmige RVE im Gegensatz zu würfelförmigen RVE keine artifizielle elastische oder plastische Anisotropie induzieren. Gleichwohl können die zu

den periodischen Randbedingungen bei Würfel-RVE analogen antipodischen Randbedingungen angewendet werden, wodurch die moderate Steifigkeit des Randes erhalten bleibt.

Es scheint eine allgemeine Abneigung gegen RVE zu geben, welche nicht lückenlos den Raum ausfüllen können. Rein formal findet dieses Argument bei der Homogenisierung jedoch keine Anwendung. Konsequenterweise müssten auch alle effektiven Spannungs-Dehnungskurven, die mit Zugproben mit kreisförmigen Querschnitten ermittelt werden, verworfen werden. In der analytischen Homogenisierung werden hingegen kugelförmige RVE verwendet, z. B. das Hollow-Sphere Modell von Gurson (1977).

In einem weiteren Artikel (Glüge und Weber, 2013) wurde gezeigt, dass die Verkleinerung des Randes bezogen auf das Volumen des RVE durch die Kugelform sich unmittelbar positiv auf die numerischen Eigenschaften des resultierenden Randwertproblems auswirkt, da bei antipodischen Randbedingungen eine Verkleinerung der Oberfläche gleichzeitig eine Reduktion numerisch ungünstiger Knotenkopplungen darstellt (siehe auch Fritzen und Böhlke (2010a)).

Allerdings muss eingeräumt werden, dass die Periodizität der Mikrostruktur auch Vorteile bietet. So lassen sich Funktionen in einem periodischem Ausschnitt gut durch periodische Fourier-Reihen approximieren. Dies wird z.B. bei der Analyse statistischer Eigenschaften (Balzani, Brands, Schröder und Carstensen, 2010) oder bei der effizienten Lösung des RVE-Randwertproblems mit Hilfe der Spektralmethode (z.B. in Eisenlohr, Diehl, Lebensohn und Roters (2013)) genutzt.

5.7.2 Verallgemeinerte Randbedingungen

In Glüge (2013) wurde die bisher allgemeinste Klasse von Randbedingungen dargestellt, die mit der Hill-Mandel-Bedingung kompatibel sind. Grob gesagt wird dabei die RVE-Oberfläche in beliebig viele Gebiete unterteilt, und auf jedes einzelne dieser Gebiete werden die iso-stress-Randbedingungen aufgebracht. Die klassischen Randbedingungen ergeben sich durch eine entsprechende Aufteilung der Gebiete, also

- keine Aufteilung → iso-stress Randbedingungen
- Gebiete werden zu Punkten zusammengezogen → iso-strain Randbedingungen
- Gebiete werden zu paarweise gegenüberliegenden Punkten zusammengezogen → periodische oder antipodische Randbedingungen, je nach RVE-Form

Im Gegensatz zum vorher bekannten, diskreten Satz klassischer Randbedingungen erlaubt die gefundene Verallgemeinerung eine

- kontinuierliche Skalierung der Randsteifigkeit zwischen den beiden extremen iso-stress- und iso-strain Randbedingungen, indem die RVE-Oberfläche mehr oder weniger fein partitioniert wird, und
- ein in bestimmten Grenzen unabhängiges Einstellen des Widerstandes gegen homogene und gegen inhomogene Deformationen des RVE.

Insbesondere letzterer Punkt erlaubt eine gewisse Optimierung der Randbedingungen. Durch eine stochastische Aufteilung der Gebiete kann die moderate elastische Steifigkeit der periodischen Randbedingungen beibehalten werden, der Widerstand gegen Lokalisierung allerdings vergrößert werden. Auf diese Weise werden die Vorteile der iso-strain-Randbedingungen und der periodischen Randbedingungen kombiniert, allerdings ohne einen artifiziellen Periodizitätsrahmen einschließlich artifizieller Anisotropie zu induzieren.

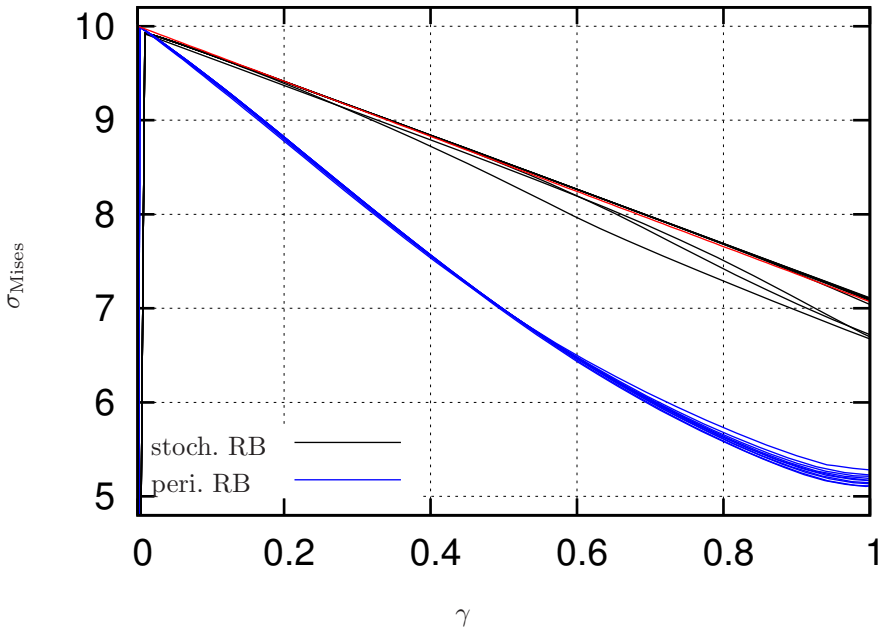

Abbildung 4: Wendet man periodische Randbedingungen auf ein homogenes RVE mit homogenem, entfestigendem Material an, verursacht eine durch Rundungsfehler oder andere minimale Störungen initiierte Lokalisierung eine erhebliche Abweichung vom effektiven Materialverhalten (blaue Kurven). Bei iso-strain Randbedingungen und stochastischen Randbedingungen liegt das vom RVE vorhergesagte Materialverhalten sehr nah am effektiven Materialverhalten.

6 Analytische Homogenisierung

Obwohl numerische Homogenisierung mit der RVE-Methode recht vielseitig einsetzbar ist, sind analytische Lösungen und Abschätzungen nach wie von großer Bedeutung. Die Gründe hierfür sind vielfältig. Einerseits lassen sich an ihnen die mathematischen Eigenschaften der effektiven Materialgesetze besser untersuchen als an diskreten Näherungslösungen, andererseits ist die Auswertung analytischer Lösungen oder Abschätzungen nicht so rechenintensiv wie numerische RVE-Simulationen.

Die Entwicklung analytischer Homogenisierungsmethoden geht bis in das 19. Jahrhundert zurück, und beschäftigte bereits Poisson, Faraday, Maxwell, Rayleigh, und Einstein (Milton, 2002). Dementsprechend existiert eine große Menge an Verzweigungen innerhalb der analytischen Homogenisierungsmethoden, und eine nahezu unüberschaubare Anzahl and Veröffentlichungen zu diesem Thema. Daher werden lediglich einige für die hier vorgestellten Beiträge des Autors relevanten Vorarbeiten angesprochen. Als Einstieg eignen sich die Bücher von Milton (2002), welches einen relativ umfassenden und allgemeinen Zugang bereitstellt, und Gross und Seelig (2011), bei welchem der Fokus bereits auf den mechanischen Eigenschaften wie effektiver Elastizität und Schädigung liegt.

Ein Großteil der Literatur zur analytischen Homogenisierung ist der Ermittlung der elastischen Felder für gegebene Eigendehnungsverteilungen $\varepsilon_{kl}^{\text{eigen}}$ gewidmet,

$$C_{ijkl} u_{k,lj} = C_{ijkl} \varepsilon_{kl,j}^{\text{eigen}} \tag{6}$$

mit den Komponenten der Steifigkeitstetrade $C_{ijkl} = C_{ijlk} = C_{klij}$ bezüglich einer Orthonormalbasis. Sowohl C_{ijkl} als auch $\varepsilon_{kl}^{\text{eigen}}$ sind im Allgemeinen vom Ort abhängig. Als Randbedingungen werden periodische oder im unendlichen abklingende Verschiebungsfelder u_k verwendet. Diese Problemstellung umfasst interessante Phänomene wie elastische Felder um Versetzungen, Risse, Poren, die Dispersion von Wellen in elastischen Medien und vieles mehr, siehe Mura (1987) und Milton (2002). Entwickelt man das Eigendehnungsfeld in eine Fourierreihe, können aufgrund des Superpositionsprinzip in der linearen Elastizität geschlossene Lösungen in Form von Reihen für beliebige Eigendehnungsfelder angegeben werden. Allerdings ist man doch immer auf lineare Elastizität und kleine Deformationen beschränkt. Trotzdem ist der Aufwand beträchtlich, weshalb oft auf Fundamentallösungen beruhende Abschätzungen verwendet werden. Solche können eventuell für einfache Mikrostruktur-Konfigurationen angegeben werden. Beispiele sind die elastischen Felder um einen ellipsoiden Einschluss in einer unendlichen homogenen Matrix (Eshelby, 1957), die effektive kritische Fließspannung für Materialien mit kugelförmige Poren (Gurson, 1977), die effektiven elastischen Eigenschaften eines Laminates (Francfort und Murat, 1986) oder die elastischen Felder um einen würfelförmigen Einschluss (Mura, 1987).

6.1 Effektive elastische Eigenschaften aus den Volumenfraktionen

Insbesondere die Ermittlung der effektiven elastischen Eigenschaften von Kompositen hat sehr die Entwicklung von Abschätzungen und analytischen Lösungen stimuliert.

6.1.1 Voigt, Reuss, Aleksandrov

Die klassischen Abschätzungen von Voigt (1889) und Reuss (1929) erfordern lediglich die Kenntnis der Volumenanteile (1-Punkt-Verteilungsfunktion, siehe Abschnitt 3.3), mit welchen jeweils die Steifigkeiten und die Nachgiebigkeiten der Phasen gewichtet gemittelt werden. In diesem Zusammenhang werden oft die Parallel- und Reihenschaltung von Federn herangezogen, und Zugversuche parallel oder senkrecht in einem Laminat diskutiert (Chen und Lakes, 1993).

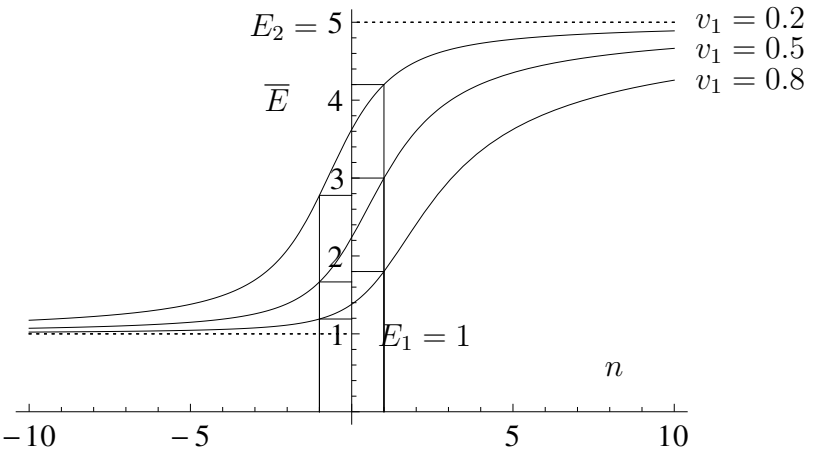

Abbildung 5: Verallgemeinerte Mittelung $\overline{E}$ zweier E-Moduli ($E_1 = 1$, $E_2 = 5$ über dem Exponenten n. Für $n \to \pm\infty$ erhält man jeweils $\max(E_1, E_2)$ und $\min(E_1, E_2)$, unabhängig von den Volumenfraktionen (gestrichelte Linien). Für $n = \pm 1$ erhält man die Voigt- und Reussmittelung. Für $n = 0$ ergibt sich als Grenzwert das geometrische Mittel.

Im Sinne einer verallgemeinerten Mittelung spricht man auch vom arithmetischen (Voigt) und harmonischen (Reuss) Mittelwert der Steifigkeit, bei welchen jeweils direkt die Steifigkeit oder deren Inverse gemittelt wird. Am Beispiel des Elastizitätsmoduls E kann dies

$$\overline{E} = g_{\text{invers}}(\sum v_i g(E_i)) \tag{7}$$

geschrieben werden, mit g als der Identität x^1 (Voigt) oder Inversion x^{-1} (Reuss), sowie den Volumenanteilen v_i. g_{invers} ist die Umkehrfunktion von g, so dass

$$g_{\text{invers}}(g(x)) = x \tag{8}$$

ist, im Gegensatz zum Kehrwert x^{-1}. Daher ist für die Voigt- und Reussmittelung $g = g_{\text{invers}}$. Da das Ergebnis der Mittelung nicht von der Wahl der Maßeinheit der Steifigkeit abhängen darf, muss die Mittelung homogen vom Grad 1 in der Steifigkeit sein. Dies ist nur erfüllt für g homogen vom Grad n, also Funktionen $\{g(x) = x^n,\ g_{\text{invers}} = x^{1/n}\}$ mit $n \in \mathbb{R} \setminus 0$ und $\{g(x) = \ln x,\ g_{\text{invers}}(x) = \exp x\}$. Letzteres ergibt sich als Grenzwert für $n \to 0$. Da $n = \pm 1$ als Extreme ausgezeichnet sind, ist die Wahl $g(x) = \ln x$ natürlich. Man spricht vom geometrischen Mittelwert, siehe Aleksandrov und Aisenberg (1966), Matthies und Humbert (1995) und Böhlke (2001).

6.1.2 Hashin-Shtrikman-Grenzen

Wie bereits diskutiert sind Voigt/Reuss-Abschätzungen extremal in dem Sinne, dass entweder die Verzerrungen oder Spannungen als homogen angenommen werden. Somit stellen sie Grenzen dar, innerhalb welcher das reale effektive Materialverhalten angetroffen wird. Allerdings schließen sie ein recht großes Gebiet ein. Zu engeren Grenzen gelangt man durch die Verwendung von Variationsprinzipien, welche für 1-Punkt-Verteilungen auf die Hashin-Shtrikman-Grenzen (Hashin und Shtrikman, 1963) führen. Für ein zweiphasiges isotropes Material entsprechen diese den exakten Steifigkeiten einer speziellen isotropen Verteilung von kugelförmigen

Einschlüssen in einer Matrix, auf englisch prägnant als *coated sphere assamblage* bezeichnet. Die Grenzen ergeben sich durch Vertauschung der Zuordnung von Matrix- und Einschlussphase. Man kann diese (Hashin-)Struktur als das 3D-Pendant der (Voigt-Reuss-)Laminatstruktur auffassen. Das Laminat kann im Zugversuch so angeordnet sein, dass die steifere Phase in Zugrichtung ununterbrochen trägt (maximale Steifigkeit), oder maximal von der weicheren Phase durchsetzt ist (maximale Nachgiebigkeit). Im Dreidimensionalen entspricht dies der Zuordnung der steiferen oder der weicheren Phase als Matrixmaterial im coated sphere assamblage.

6.2 Analytische Abschätzungen aus Grundlösungen

Wie bereits geschrieben ist die Verwendung von höheren Korrelationsfunktionen zur Ermittelung des effektiven Materialverhaltens eine schwierige Aufgabe von hoher mathematischer Abstraktheit. Wesentlich beliebter ist die Verwendung von Grundlösungen. Hiervon stehen für die lineare Elastizität einige zur Verfügung, wie zum Beispiel die elastischen Felder um Rissspitzen (Griffith, 1920; Irwin, 1957; Guidera und Lardner, 1975), Poren oder Einschlüssen (Eshelby, 1957), Fasern und Lamellen (Hill, 1964; Hashin, 1965; Tartar, 1985; Francfort und Murat, 1986) unter einem entfernten Spannungsfeld. Beispiele für die Abschätzung effektiver Eigenschaften aus der Überlagerung von Grundlösungen sind Li (1994) oder die in Klusemann und Svendsen (2010) und Christensen (1990) kompilierten Ansätze. Im folgenden sollen nur die für die Beiträge des Autors relevanten Aspekte herausgearbeitet werden.

6.2.1 Matrix-Einschluss-basierte selbstkonsistente Abschätzung

Eshelby (1957) gelang erstmals die Berechnung der elastischen Felder um einen elliptischen Einschluss in einer unendlich ausgedehnten Matrix. Bis zu diesem Zeitpunkt konnte lediglich die Homogenität der elastischen Felder innerhalb des Ellipsoides gezeigt werden (Poisson (1826) und Maxwell (1873), formal zwar für Elektromagnetismus, aber die partiellen Differenzialgleichungen entsprechen denen der Elastizitätstheorie). Diese Grundlösung öffnete die Tür für verschiedene Abschätzungen, wie der Abschätzung für schwach konzentrierte (dilute) Einschlussverteilungen und der Matrix-Einschluss-basierten selbstkonsistenten Abschätzung. Der Begriff *selbstkonsistent* wird innerhalb der analytischen Homogenisierung für durchaus unterschiedliche Konzepte verwendet. Hier ist damit der im folgenden beschriebene Ansatz gemeint. Während bei der Abschätzung für schwach konzentrierte Einschlussverteilungen eine Interaktion zwischen den Einschlüssen vernachlässigt wird, wird bei den selbstkonsistenten Methoden für die Matrix das eigentlich zu ermittelnde effektive Materialverhalten eingesetzt. Dies führt in aller Regel dazu, dass die selbstkonsistenten Abschätzungen implizit gegeben sind (Willis, 1977; Christensen, 1990). Es gibt zahllose Variationen dieser Grundidee, einige davon wurden in Klusemann und Svendsen (2010) kompiliert. Eine bemerkenswerte Variante ist der *interaction direct derivative* (IDD) Ansatz (Zheng und Du, 2001; Du und Zheng, 2002), welcher gleichzeitig eine explizite Abschätzung liefert und qualitativ gute Ergebnisse produziert.

Aus diesen Betrachtungen kann man bereits einige Eigenschaften der selbstkonsistenten Abschätzungen folgern. So überrascht es nicht, dass die selbstkonsistenten Abschätzungen bei extremen Volumenfraktionen bis zum Grad 1 mit derjenigen Hashin-Shtrikman-Grenze zusammenfallen, welche die schwächere Auswirkung der Einschlussphase vorhersagt, da die Hashin-Struktur bei extremalen Volumenfraktionen der Prämisse nicht-interagierender Einschlüsse entspricht. Dies wurde ausführlicher in Kalisch und Glüge (2015) besprochen. Man kann ebenfalls erwarten, dass die selbstkonsistenten Abschätzungen nur bei kleinen Volumenfraktionen und bei Matrix-Einschluss-Strukturen gute Ergebnisse liefern.

6.2.2 Laminate

Eine weitere wichtige Grundlösung ist diejenige für die effektiven elastischen Eigenschaften eines Laminates. Obwohl sie deutlich einfacher als die Eshelby-Lösung ist, wurde sie erst von Tartar (1985) und Francfort und Murat (1986) angegeben. Als wesentliche Zutaten benötigt man die Sprungbilanzen für Spannungen und Dehnungen, die Homogenität der elastischen Felder innerhalb der Phasen und die lineare Elastizität der Einzelphasen. Diese Lösung wurde von Glüge und Kalisch (2014) für beliebig viele anisotrope Einzelphasen verallgemeinert.

Auch die Laminat-Grundlösung wurde bereits als Ausgangspunkt für Abschätzungen höherer Ordnung verwendet. Man spricht von Abschätzungen höherer Ordnung, da die Laminatlösung bereits das Ergebnis einer Homogenisierung ist. Solche Methoden werden auch als sequenzielle oder iterierte Abschätzungen bezeichnet, siehe z. B. Braides und Lukkassen (2000), deBotton und Hariton (2002), deBotton (2005), Idiart (2008), Lopez-Pamies und Idiart (2010), Agoras und Ponte-Castañeda (2011), Ponte-Castañeda (2012), Agoras und Ponte-Castañeda (2012) und Idiart und Ponte-Castañeda (2013). Der mehrfachen Homogenisierung liegen notwendigerweise Mikrostrukturen auf mehreren Ebenen zugrunde, wie z. B. eine Kornstruktur im mm-Bereich, deren Körner selbst im μm-Bereich laminiert sind, oder sich durchdringende, überlagerte Laminate mit sehr unterschiedlichen Lamellendicken. Letztere Mikrostrukturen sind eher selten in der Realität anzutreffen. In Kalisch und Glüge (2015) wurde der Versuch unternommen, die Laminat-Grundlösung auf allgemeinere Mikrostrukturen zu erweitern.

6.3 Diskussion eigener Arbeiten

Insgesamt wurden 2 Beiträge zur analytischen Homogenisierung geleistet. In Glüge und Kalisch (2014) wurden

- ein kompakter Ausdruck für die effektive Laminatsteifigkeit mit beliebig vielen anisotropen Konstituenten hergeleitet,
- kompakte Ausdrücke für die Spannungs- und Dehnungskonzentrationstensoren hergeleitet,
- ein ausführlicher Vergleich zu isotropen und anisotropen Lösungen der klassischen Laminattheorie und zu isotropen dreidimensionalen Lösungen vollzogen.

Ersteres Ergebnis ist der Ausgangspunkt für den im zweiten Beitrag (Kalisch und Glüge, 2015) vorgeschlagenen Grenzflächen-Orientierungsverteilungs-Ansatz. Zwar waren schon dreidimensionale Lösungen vorhanden, allerdings waren diese entweder auf zwei Phasen oder Isotropie beschränkt, oder in einer nicht verwertbaren Weise dargestellt. Weiterhin waren die Ergebnisse der klassischen Laminattheorie als Grundlösungen für die Abschätzung eines dreidimensionalen effektiven Materialgesetzes ungeeignet, da diese nur zweiachsige Spannungszustände einschließt. Es konnte gezeigt werden, dass sich die Lösungen der klassischen Laminattheorie als Spezialfälle der dreidimensionalen Lösung ergeben. Weiterhin erlaubt die kompakte und gleichzeitig allgemeine Notation der Konzentrationstensoren die Berechnung der im Laminat wirkenden Spannungen aus den effektiven Spannungen oder den effektiven Dehnungen. Dies kann beispielsweise zur analytischen Homogenisierung der Fließbedingung verwendet werden (in Bearbeitung).

In Kalisch und Glüge (2015) wurde ein analytischer Homogenisierungsansatz vorgeschlagen, der im Kern aus einer Orientierungsmittelung der Laminatlösung über eine Grenzflächenorientierungsverteilung besteht, im folgenden IOD-Ansatz genannt (für *interface orientation distribution*). Letztere ist der Deskriptor der Mikrostruktur, wobei die elastischen Eigenschaften nahe einer Grenzfläche durch die

Laminatlösung approximiert werden. Einen ähnlichen Ansatz verfolgte Richeton und Berbenni (2014). Die Interpretation der Laminatsteifigkeit als Grenzflächensteifigkeit entspricht der Aufweichung der Forderung nach einem Skalenabstand, wie er bei der oben genannten sequenziellen oder iterativen Homogenisierung Voraussetzung ist.

Die Motivation für dieses Vorgehen ist, dass Mikrostrukturen mit gebietsweise homogenen Materialparametern eindeutig durch die Lage der Grenzfläche charakterisiert sind. Gleichzeitig treten an der Grenzfläche die Spannungs- und Dehnungsgradienten auf. Zusätzlich können an der Grenzfläche die Sprungbilanzen ausgewertet, und direkt mit den Materialgesetzen verknüpft werden.

Die Orientierungsmittelung der bei isotropen Phasen transversalisotropen Laminatsteifigkeit kann sowohl analytisch als auch numerisch erfolgen. Dabei wird, bei isotropen Phasen, allein die Anisotropie der Grenzflächenorientierungsverteilung auf die effektive Elastizität übertragen. Somit steht ein analytisches Verfahren zur Abschätzung der Morphologie-induzierten Anisotropie für beliebige Phasenverteilungen zur Verfügung. Allerdings lassen sich auch Mikrostrukturen konstruieren, deren Grenzflächenorientierungsverteilung nichts mit der Morphologie-induzierten Anisotropie zu tun hat, beispielsweise eine anisotrope Anordnung kugelförmiger Einschlüsse. Hier wird deutlich, das es sich nur um eine Abschätzung handelt, die nur für bestimmte Mikrostrukturen gut funktioniert.

Zur Spezifizierung geeigneter Anwendungsfälle wurde die IOD-Mittelung anderen analytischen Abschätzungen sowie den praktisch exakten Lösungen aus RVE-Rechnungen gegenübergestellt. Beim Vergleich zu den analytischen Abschätzungen stellte sich heraus, dass

- die IOD-Abschätzung zwischen den Hashin-Shtrikman-Grenzen liegt,
- zu den selbstkonsistenten Abschätzungen komplementär ist,
- und am besten bei gleichartig verteilten Phasen funktioniert.

Ersteres Ergebnis ist eine typische Eigenschaft von Abschätzungen höherer Ordnung. Interessanter ist die zweite Eigenschaft. Man kann zeigen, dass die selbstkonsistenen Ansätze sich bei extremen Volumenfraktionen an die Hashin-Shtrikman-Grenzen mit dem betragsmäßig kleineren Anstieg anschmiegen, während die IOD-Abschätzungen sich jeweils an die entgegengesetzte Hashin-Shtrikman-Grenze anschmiegen. Dieses Verhalten kann dadurch erklärt werden, dass beim IOD-Ansatz beide Phasen gleich behandelt werden, während die selbstkonsistenten Ansätze grundsätzlich zwischen Matrix- und Einschlussphase unterscheiden. In diesem Sinne implizieren IOD- und selbstkonsistente Ansätze konträre Annahmen, was sich im Rahmen der Hashin-Shtrikman-Grenzen in konträren Ergebnissen zeigt. Beim IOD-Ansatz durchdringen also beide Phasen das Material, wodurch das Einbringen einer Phase einen maximalen Effekt hat, im Gegensatz zu den nicht- oder schwach interagierenden Einschlüsse bei den selbstkonsistenen Ansätzen. Somit stellt der IOD-Ansatz aufgrund der konträren Annahmen über die Phasenverteilung eine komplementäre Ergänzung der Familie der selbstkonsistenten Ansätze dar.

6.3.1 Mögliche Anwendungen des IOD-Ansatzes

Diese Betrachtungen konnten beim Vergleich mit den praktisch exakten Lösungen aus RVE-Rechnungen bestätigt werden. Es wurden kubische RVE mit periodischen Mikrostrukturen mit kubischer und oktaedrischer Grenzflächenorientierungsverteilung untersucht, nämlich sich durchdringende Gitter und verschiedene Anordnungen kubischer und oktaedrischer Einschlüsse. Die beste Übereinstimmung mit dem IOD-Ansatz besteht für Mikrostrukturen, die reich an Grenzfläche sind, und bei welchen beide Phasen das Material durchdringen, z. B. sich durchdringende Gitter. Eine

weitere Anwendungsmöglichkeit sind Matrix-Einschluss-Strukturen, bei welchen die Phase mit der kleineren Volumenfraktion die Matrixphase ist. Zwar entspricht die strukturell eher den Annahmen der selbstkonsistenten Ansatzes, allerdings impliziert dieser, dass die Phase mit der kleineren Volumenfraktion der Einschlussphase entspricht, also das genaue Gegenteil der zu homogenisierenden Mikrostruktur. Da der IOD-Ansatz sich dual zum selbstkonsistenten Ansatz verhält, ist er für solche Strukturen besser geeignet. Dies konnte ebenfalls anhand von RVE-Rechnungen bestätigt werden.

7 Fazit

Homogenisierungsmethoden sind zu wichtigen Werkzeugen der präzisen Vorhersage von Materialeigenschaften geworden. Es ist nicht davon auszugehen, dass die Homogenisierung durch skalenübergreifende Simulationen entbehrlich wird, da der Rechenaufwand hierfür absurd hoch ist. Vielmehr ist eine Weiterentwicklung sowohl der analytischen als auch der numerischen Methoden erstrebenswert und offenbar auch möglich.

Danksagung

Ich möchte mich bei meinem Freund und Kollegen Jan Kalisch für die gute, konstruktive Zusammenarbeit und lange, geduldige Diskussionen bedanken.

Mein Dank gilt auch Prof. Albrecht Bertram, der mir bei meiner Arbeit viel Freiraum ließ, einem in der heutigen Forschungslandschaft selten gewordenen Privileg.

Weiterhin gilt mein Dank Prof. Thomas Böhlke, von dessen Seite wichtige Hinweise zu dieser Arbeit kamen. Ebenso möchte ich bei Prof. Jörg Schröder für die Begutachtung der Arbeit und das Beisteuern kritischer Bemerkungen bedanken.

Insgesamt boten die Graduiertenkollegs 828 und 1554 an der Universität Magdeburg sehr stimulierende Arbeitsumgebungen. Anerkennung gilt allen daran Beteiligten.

8 Literatur

Abeyaratne, R. und J.K. Knowles (2006). *Evolution of Phase Transitions - A Continuum Theory*. Cambridge University Press.

Agoras, M. und P. Ponte-Castañeda (2011). „Homogenization estimates for multi-scale nonlinear composites“. In: *European Journal of Mechanics A/Solids* 30.6, S. 828–843.

— (2012). „Multi-scale homogenization-based modeling of semi-crystalline polymers“. In: *Philosophical Magazine* 92.8, S. 925–958.

Aleksandrov, K. S. und L.A. Aisenberg (1966). „Method of calculating physical constants of polycrystalline metals“. In: *Soviet Physics-Doklady* 11.3, S. 323–325.

Apel, M., G. Laschet, B. Böttger und R. Berger (2014). „Phase field modeling of microstructure formation, DSC curves, and thermal expansion for AgCu brazing fillers under reactive air brazing conditions“. In: *Advanced Engineering Materials* 16.12, S. 1468–1474.

Aranda, E. und P. Pedregal (2001). „On the computation of the rank-one convex hull of a function“. In: *SIAM Journal on Scientific Computing* 22.5, S. 1772–1790.

Arminjon, M. (1991). „Macro-homogeneous strain fields with arbitrary local inhomogeneity“. In: *Archive of Mechanics* 43, S. 191–214.

Arsenlis, A., N.R. Barton, R. Becker und R.E. Rudd (2006). „Generalized in situ adaptive tabulation for constitutive model evaluation in plasticity“. In: *Computer Methods in Applied Mechanics and Engineering* 196.1-3, S. 1–13.

Aubert, G. (1995). „Necessary and sufficient conditions for isotropic rank-one convex functions in dimension 2“. In: *Journal of Elasticity* 39.1, S. 31–46.

Ball, J.M. (1977). „Convexity conditions and existence theorems in nonlinear elasticity“. In: *Archive for Rational Mechanics and Analysis* 63, S. 337–403.

Balzani, D., D. Brands, J. Schröder und C. Carstensen (2010). „Sensitivity analysis of statistical measures for the reconstruction of microstructures based on the minimization of generalized least-square functionals“. In: *Technische Mechanik* 30.4, S. 297–315.

Bartel, T. und K. Hackl (2009). „A micromechanical model for martensitic phase-transformations in shape-memory alloys based on energy-relaxation“. In: *ZAMM - Journal of Applied Mathematics and Mechanics / Zeitschrift für Angewandte Mathematik und Mechanik* 89.10, S. 792–809.

— (2010). „Multiscale modeling of martensitic phase transformations: On the numerical determination of heterogeneous mesostructures within shape-memory alloys induced by precipitates“. In: *Technische Mechanik* 30.4, S. 324–342.

Bartel, T., B. Kiefer, K. Buckmann und A. Menzel (2015). „A kinematically-enhanced relaxation scheme for the modeling of displacive phase transformations“. In: *Journal of Intelligent Material Systems and Structures* 26.6, S. 701–717.

Bartels, C., C. Carstensen, K. Hackl und U. Hoppe (2004). „Effective relaxation for microstructure simulations: algorithms and applications“. In: *Computer Methods in Applied Mechanics and Engineering* 193, S. 5143–5175.

Berryman, J.G. (1988). „Interpolating and integrating three-point correlation functions on a lattice“. In: *Journal of Computational Physics* 75, S. 86–102.

Bertram, A. (2014). „Finite gradient elasticity and plasticity: a constitutive mechanical framework“. In: *Continuum Mechanics and Thermodynamics*, S. 1–20.

Bertram, A., T. Böhlke und M. Šilhavý (2007). „On the rank 1 convexity of stored energy functions of physically linear stress-strain relations“. In: *Journal of Elasticity* 86, S. 235–243.

Bertram, A. und S. Forest (2014). „The thermodynamics of gradient elastoplasticity“. In: *Continuum Mechanics and Thermodynamics* 26, S. 269–286.

Bertram, A. und B. Svendsen (2001). „On material objectivity and reduced constitutive equations“. In: *Archive of Mechanics* 53, S. 653–675.

Bertram, A. und J. Tomas, Hrsg. (2008). *Micro-Macro-Interactions in Structured Media and Particle Systems*. Springer-Verlag Berlin Heidelberg.

Bianchini, S. und A. Bressan (2005). „Vanishing viscosity solutions of nonlinear hyperbolic systems“. In: *Annals of Mathematics* 161, S. 223–342.

Bigoni, D. (2000). „Bifurcation and instability of non-associative elastoplastic solids“. In: *Material instabilities in elastic and plastic solids, CISM courses and lectures no. 414*. Hrsg. von H. Petryk. Springer-Verlag Wien New-York, S. 1–52.

Böhlke, T. (2001). *Crystallographic Texture Evolution and Elastic Anisotropy- Simulation, Modeling and Applications*. Shaker Verlag.

— (2005). „Application of the maximum entropy method in texture analysis“. In: *Computational Materials Science* 32, S. 276–283.

Böhlke, T., G. Bondár, Y. Estrin und M.A. Lebyodkin (2009). „Geometrically non-linear modeling of the Portevin-Le Chatelier effect“. In: *Computational Materials Science* 44, S. 1076–1088.

Böhlke, T., K. Jöchen, O. Kraft, D. Löhe und V. Schulze (2010). „Elastic properties of polycrystalline microcomponents“. In: *Mechanics of Materials* 42.1, S. 11–23.

Böhlke, T., G. Risy und A. Bertram (2006). „Finite element simulation of metal forming operations with texture based material models“. In: *Modelling and Simulation in Materials Science and Engineering* 14, S. 365–387.

Bosco, E., V.G. Kouznetsova, E.W.C. Coenen, M.G.D. Geers und A. Salvadori (2014). „A multiscale framework for localizing microstructures towards the onset of macroscopic discontinuity“. In: *Computational Mechanics* 54.2, S. 299–319.

Braides, A. (2002). *Gamma-Convergence for Beginners*. Oxford lecture series in mathematics and its applications. Oxford University Press.

Braides, A. und D. Lukkassen (2000). „Reiterated homogenization of integral functionals“. In: *Mathematical Models and Methods in Applied Sciences* 10.1, S. 47–71.

Carstensen, C. (2005). „Ten remarks on nonconvex minimisation for phase transition simulations“. In: *Computer Methods in Applied Mechanics and Engineering* 194, S. 169–193.

Celigoj, C. C. (1998). „Finite deformation coupled thermomechanical problems and 'generalized standard materials'“. In: *International Journal for Numerical Methods in Engineering* 42.6, S. 1025–1043.

Chaboche, J.L., F. Feyel und Y. Monerie (2001). „Interface debonding models: a viscous regularization with a limited rate dependency“. In: *International Journal of Solids and Structures* 38, S. 3127–3160.

Chen, C.P. und R.S. Lakes (1993). „Analysis of high-loss viscoelastic composites“. In: *Journal of Materials Science* 28, S. 4299–4304.

Christensen, R.M. (1990). „A critical evaluation for a class of micro-mechanics models“. In: *Journal of the Mechanics and Physics of Solids* 38.3, S. 379–404.

Coenen, E. W. C., V. G. Kouznetsova und M. G. D. Geers (2011). „Enabling microstructure-based damage and localization analyses and upscaling“. In: *Modelling and Simulation in Materials Science and Engineering* 19.7.

— (2012). „Novel boundary conditions for strain localization analyses in microstructural volume elements“. In: *International Journal for Numerical Methods in Engineering* 90, S. 1–21.

Dacorogna, B. (2005). „Necessary and sufficient conditions for strong ellipticity of isotropic functions in any dimensions“. In: *Discrete and Continuous Dynamical Systems–Series B* 1.2, S. 257–263.

deBotton, G. (2005). „Transversely isotropic sequentially laminated composites in finite elasticity“. In: *Journal of the Mechanics and Physics of Solids* 53.6, S. 1334–1361.

deBotton, G. und I. Hariton (2002). „High-rank nonlinear sequentially laminated composites and their possible tendency towards isotropic behavior“. In: *Journal of the Mechanics and Physics of Solids* 50, S. 2577–2595.

dell'Isola, F., G. Maier, U. Perego, U. Andreaus, R. Esposito und S. Forest (2014). *The complete works of Gabrio Piola: Volume I: Commented English Translation*. Advanced Structured Materials. Springer International Publishing.

Dias da Silva, V. (2004). „A simple model for viscous regularization of elasto-plastic constitutive laws with softening“. In: *Communications in Numerical Methods in Engineering* 20, S. 547–568.

Dirrenberger, J., S. Forest und D. Jeulin (2014). „Towards gigantic RVE sizes for 3D stochastic fibrous networks“. In: *International Journal of Solids and Structures* 51.2, S. 359–376.

Dolzmann, G. (1999). „Numerical computation of rank-one convex envelopes“. In: *SIAM Journal on Numerical Analysis* 36.5, S. 1621–1635.

Drugan, W.J. und J.R. Willis (1996). „A micromechanics-based nonlocal constitutive equation and estimates of representative volume element size for elastic composites“. In: *Journal of the Mechanics and Physics of Solids* 44.4, S. 497–524.

Du, D.X. und Q.S. Zheng (2002). „A further exploration of the interaction direct derivative (IDD) estimate for the effective properties of multiphase composites taking into account inclusion distribution“. In: *Acta Mechanica* 157, S. 61–80.

Dvorak, G.J. (1992). „Transformation field analysis of inelastic composite materials“. In: *Proceedings of the Royal Society of London. Series A: Mathematical, Physical and Engineering Sciences* 437.1900, S. 311–327.

— (2013). *Micromechanics of Composite Materials*. Springer.

Eisenlohr, P., M. Diehl, R.A. Lebensohn und F. Roters (2013). „A spectral method solution to crystal elasto-viscoplasticity at finite strains“. In: *International Journal of Plasticity* 46, S. 37–53.

Elvin, A.A. (1996). „Number of grains required to homogenize elastic properties of polycrystalline ice“. In: *Mechanics of Materials* 2.1, S. 51–64.

Emmerich, H., K. Kassner, T. Ihle und A. Weiss (2000). „Dynamic simulations of interface morphologies in free dendritic growth“. In: *Journal of Crystal Growth* 211.1-4, S. 43–48.

Eshelby, J.D. (1957). „The determination of the elastic field of an ellipsoidal inclusion, and related problems“. In: *Proceedings of the Royal Society of London. Series A: Mathematical, Physical and Engineering Sciences* 241, S. 376–396.

Feyel, F. (1999). „Multiscale FE^2 elastoviscoplastic analysis of composite structures“. In: *Computational Materials Science* 16.1-4, S. 344–354.

— (2003). „A multilevel finite element method (FE2) to describe the response of highly non-linear structures using generalized continua“. In: *Computer Methods in Applied Mechanics and Engineering* 192, S. 3233–3244.

Fix, G.J. (1983). „Phase field methods for free boundary problems“. In: *Free Boundary Problems: Theory and Applications*. Hrsg. von A. Fasano und M. Primicerio. Pitman, Boston, S. 580–600.

Francfort, G. und F. Murat (1986). „Homogenization and optimal bounds in linear elasticity“. In: *Archive for Rational Mechanics and Analysis* 94.4, S. 307–334.

Fritzen, F. und T. Böhlke (2010a). „Influence of the type of boundary conditions on the numerical properties of unit cell problems“. In: *Technische Mechanik* 30.4, S. 354–363.

— (2010b). „Three-dimensional finite element implementation of the nonuniform transformation field analysis“. In: *International Journal for Numerical Methods in Engineering* 84, S. 803–829.

Fritzen, F., S. Forest, T. Böhlke, D. Kondo und T. Kanit (2012). „Computational homogenization of elasto-plastic porous metals“. In: *International Journal of Plasticity* 29, S. 102–119.

Geers, M.G.D., V.G. Kouznetsova und W.A.M. Brekelmans (2010). „Multi-scale computational homogenization: Trends and challenges“. In: *Journal of Computational and Applied Mathematics* 234.7, S. 2175–2182.

Ghosh, S., K. Lee und P. Raghavan (2001). „A multi-level computational model for multi-scale damage analysis in composite and porous materials“. In: *International Journal of Solids and Structures* 38.14, S. 2335–2385.

Gilbarg, D. und N.S. Trudinger (2001). *Elliptic Partial Differential Equations of Second Order*. Classics in Mathematics. U.S. Government Printing Office.

Gitman, I.M., H. Askes und L.J. Sluys (2007). „Representative volume: Existence and size determination“. In: *Engineering Fracture Mechanics* 74.16, S. 2518–2534.

— (2008). „Coupled-volume multi-scale modelling of quasi-brittle material“. In: *European Journal of Mechanics - A/Solids* 27.3, S. 302–327.

Glüge, R (2010). „On the elastic energy invariance of twins“. In: *Archive of Mechanics* 62, S. 439–462.

Glüge, R. (2011). „A pseudoelastic model for deformation twinning: Numerical homogenisation and comparison to experiments“. In: *International Journal of Structural Changes in Solids - Mechanics and Applications* 1 (3), S. 29–47.

— (2013). „Generalized boundary conditions on representative volume elements and their use in determining the effective material properties“. In: *Computational Materials Science* 79, S. 408–416.

Glüge, R., A. Bertram, T. Böhlke und E. Specht (2010). „A pseudoelastic model for mechanical twinning on the microscale“. In: *Zeitschrift für Angewandte Mathematik und Mechanik* 90.7-8 (Phase Transitions in Deformable Solids and Structures), S. 565–594.

Glüge, R. und J. Kalisch (2012). „Graphical representations of the regions of rank-one-convexity of some strain energies“. In: *Technische Mechanik* 32, S. 227–237.

— (2014). „The effective stiffness and stress concentrations of a multi-layer laminate“. In: *Composite Structures* 111, S. 580–586.

Glüge, R. und M. Weber (2013). „Numerical properties of spherical and cubical representative volume elements with different boundary conditions“. In: *Technische Mechanik*, S. 97–103.

Glüge, R., M. Weber und A. Bertram (2012). „Comparison of spherical and cubical statistical volume elements with respect to convergence, anisotropy, and localization behavior“. In: *Computational Material Science* 63, S. 91–104.

Gokhale, A. M. (2004). „Experimental measurements and interpretation of microstructural n-point correlation functions“. In: *Microscopy and Microanalysis* 10 (Supplement S02), S. 736–737.

Griffith, A.A. (1920). „The phenomena of rupture and flow in solids“. In: *Transactions of the Royal Society of London A* 221. Reprinted with annotations and corrections, ASM Trans. Q. 61, 871–906 (1968), S. 163–197.

Gross, D. und T. Seelig (2011). *Fracture Mechanics with an Introduction to Micromechanics, Second Edition*. Springer.

Guidera, J.T. und R.W. Lardner (1975). „Penny-shaped cracks“. In: *Journal of Elasticity* 5.1, S. 59–73.

Gurson, A.L. (1977). „Continuum theory of ductile rupture by void nucleation and growth – part I: yield criteria and flow rules for porous ductile media“. In: *Journal of Engineering Materials and Technology* 99, S. 2–15.

Gusev, A.A. (1997). „Representative volume element size for elastic composites: A numerical study“. In: *Journal of the Mechanics and Physics of Solids* 45.9, S. 1449–1459.

Hackl, K. (1997). „Generalized standard media and variational principles in classical and finite strain elastoplasticity“. In: *Journal of the Mechanics and Physics of Solids* 45.5, S. 667–688.

Hackl, K. und D.M. Kochmann (2008). „Relaxed potentials and evolution equations for inelastic microstructures“. In: *IUTAM Symposium on Theoretical, Computational and Modelling Aspects of Inelastic Media*. Hrsg. von B.D. Reddy. Bd. 11. IUTAM Book Series, S. 27–39.

Hashin, Z. (1965). „On elastic behaviour of fibre reinforced materials of arbitrary transverse phase geometry“. In: *Journal of the Mechanics and Physics of Solids* 13.3, S. 119–134.

— (1983). „Analysis of Composite Materials – A Survey“. In: *Journal of Applied Mechanics* 50, S. 481–505.

Hashin, Z. und S. Shtrikman (1963). „A variational approach to the theory of the elastic behaviour of multiphase materials“. In: *Journal of the Mechanics and Physics of Solids* 11.2, S. 127–140.

Hazanov, S. (1998). „Hill condition and overall properties of composites“. In: *Archive of Applied Mechanics* 68.6, S. 385–394.

Hazanov, S. und C. Huet (1994). „Order relationships for boundary condition effects in heterogeneous bodies smaller than the representative volume“. In: *Journal of Mechanics Physics of Solids* 42, S. 1995–2011.

Hildebrand, F. und C. Miehe (2010). „A regularized sharp interface model for phase transformation accounting for prescribed sharp interface kinetics“. In: *Proceedings in Applied Mathematics and Mechanics* 10.1, S. 673–676.

Hill, R. (1952). „The elastic behaviour of a crystalline aggregate“. In: *Proceedings of the Royal Society of London. Series A: Mathematical, Physical and Engineering Sciences* 65, S. 349–354.

— (1963). „Elastic properties of reinforced solids: Some theoretical principles“. In: *Journal of the Mechanics and Physics of Solids* 11.5, S. 357–372.

— (1964). „Theory of mechanical properties of fibre-strengthened materials: I. Elastic behaviour“. In: *Journal of the Mechanics and Physics of Solids* 12.4, S. 199–212.

— (1967). „The essential structure of constitutive laws for metal composites and polycrystals“. In: *Journal of the Mechanics and Physics of Solids* 15, S. 79–95.

— (1984). „On macroscopic effects of heterogeneity in elastoplastic media at finite strain“. In: *Mathematical Proceedings of the Cambridge Philosophical Society* 95 (3), S. 481–494.

Houdaigui, F., S. Forest, A.-F. Gourgues und D. Jeulin (2007). „On the size of the representative volume element for isotropic elastic polycrystalline copper“. In: *IUTAM Symposium on Mechanical Behavior and Micro-Mechanics of Nanostructured Materials*. Hrsg. von Y.L. Bai, Q.S. Zheng und Y.G. Wei. Bd. 144. Solid Mechanics and its Applications. Springer Netherlands, S. 171–180.

Houtte, P. van (1982). „On the equivalence of the relaxed Taylor theory and the Bishop-Hill theory for partially constrained plastic deformation of crystals“. In: *Materials Science and Engineering* 55, S. 69–77.

Houtte, P. van, L. Delannay und J. Samajdar (1999). „Quantitative prediction of cold rolling textures in low-carbon steel by means of the LAMEL model“. In: *Textures and Microstructures* 31, S. 109–149.

Huet, C. (1990). „Application of variational concepts to size effects in elastic heterogeneous bodies“. In: *Journal of Mechanics Physics of Solids* 38, S. 813–841.

Hutchinson, J.W. (1976). „Bounds and self-consistent estimates for creep of polycrystalline materials“. In: *Proceedings of the Royal Society of London. Series A: Mathematical, Physical and Engineering Sciences* 348, S. 101–127.

Idesman, A.V., V.I. Levitas und E. Stein (2000). „Structural changes in elastoplastic material: a unified finite-element approach to phase transformation, twinning and fracture“. In: *International Journal of Plasticity* 16.7, S. 893–949.

Idiart, M. I. (2008). „Modeling the macroscopic behavior of two-phase nonlinear composites by infinite-rank laminates“. In: *Journal of the Mechanics and Physics of Solids* 56.8, S. 2599–2617.

Idiart, M.I. und P. Ponte-Castañeda (2013). „Estimates for two-phase nonlinear conductors via iterated homogenization“. In: *Proceedings of the Royal Society of London. Series A: Mathematical, Physical and Engineering Sciences* 469.2153, S. 1583–1604.

Inglis, H.M., P.H. Geubelle und K. Matous (2008). „Boundary condition effects on multiscale analysis of damage localization“. In: *Philosophical Magazine* 88.16, S. 2373–2397.

Irwin, G.R. (1957). „Analysis of stresses and strains near the end of a crack transversing a plate“. In: *Journal of Applied Mechanics* 24, S. 361–364.

Jöchen, K. und T. Böhlke (2009). „Prediction of the elastic properties of polycrystalline microcomponents by numerical homogenization“. In: *Advanced Engineering Materials* 11.3, S. 158–161.

Kaczmarczyk, L., M.M. Nezhad und C.J. Pearce (2014). „Three-dimensional brittle fracture: configurational-force-driven crack propagation“. In: *International Journal for Numerical Methods in Engineering* 97.7, S. 531–550.

Kaczmarczyk, L., C.J. Pearce und N. Bićanić (2008). „Scale transition and enforcement of RVE boundary conditions in second-order computational homogenization“. In: *International Journal for Numerical Methods in Engineering* 74.3, S. 506–522.

Kaczmarczyk, L., C.J. Pearce, N. Bicanic und E. de Souza Neto (2010). „Numerical multiscale solution strategy for fracturing heterogeneous“. In: *Computer Methods in Applied Mechanics and Engineering* 199.17–20, S. 1100–1113.

Kadowaki, H. und W.K. Liu (2004). „Bridging multi-scale method for localization problems“. In: *Computer Methods in Applied Mechanics and Engineering* 193, S. 3267–3302.

Kalidindi, S.R. (1998). „Incorporation of deformation twinning in crystal plasticity models“. In: *Journal of the Mechanics and Physics of Solids* 46.2, S. 267–290.

Kalisch, J. und A. Bertram (2013). „Fast alternatives to Taylor and Sachs models for rigid perfectly viscoplastic polycrystals“. In: *Technische Mechanik* 33, S. 104–118.

Kalisch, J. und R. Glüge (2015). „Analytical homogenization of linear elasticity based on the interface orientation distribution – a complement to the self-consistent approach“. In: *Composite Structures* 126, S. 398–416.

Kanit, T., S. Forest, I. Galliet, V. Mounoury und D. Jeulin (2003). „Determination of the size of the representative volume element for random composites: statistical and numerical approach“. In: *International Journal of Solids and Structures* 40, S. 3647–3679.

Khan, M.S. und K. Hackl (2012). „Prediction of microstructure in a Cosserat continuum using relaxed energies“. In: *Proceedings in Applied Mathematics and Mechanics* 12.1, S. 265–266.

Klusemann, B. und M. Ortiz (2015). „Acceleration of material-dominated calculations via phase-space simplicial subdivision and interpolation“. In: *International Journal for Numerical Methods in Engineering* 103.4, S. 256–274.

Klusemann, B. und B. Svendsen (2010). „Homogenization methods for multi-phase elastic composites: Comparisons and benchmarks“. In: *Technische Mechanik* 30.4, S. 374–386.

Knees, D., A. Mielke und C. Zanini (2007). „On the inviscid limit of a model for crack propagation“. In: *Mathematical Models and Methods in Applied Sciences* 23.4, S. 565–616.

Knees, D., R. Rossi und C. Zanini (2013). „A vanishing viscosity approach to a rate-independent damage model“. In: *Mathematical Models and Methods in Applied Sciences* 23.4, S. 565–616.

Kouznetsova, V., M. G. D. Geers und W. A. M. Brekelmans (2002). „Multi-scale constitutive modelling of heterogeneous materials with a gradient-enhanced computational homogenization scheme“. In: *International Journal for Numerical Methods in Engineering* 54.8, S. 1235–1260.

Kröner, E. (1972). *Statistical Continuum Mechanics*. Courses and lectures - International Centre for Mechanical Sciences. Springer-Verlag.

Langer, J.S. (1986). „Models of pattern formation in first-order phase transitions“. In: *Directions in Condensed Matter Physics*. Kap. 5, S. 165–186.

Lapczyk, I., K.R. Rajagopal und A.R. Srinivasa (2000). „Deformation twinning during impact of a titanium cylinder- numerical calculations using a constitutive theory based on multiple natural configurations“. In: *Computer Methods in Applied Mechanics and Engineering* 188, S. 527–541.

Li, Guoan (1994). „Effective constitutive behavior of nonlinear solids containing penny-shaped cracks“. In: *International Journal of Plasticity* 10.4, S. 409–429.

Loehnert, S. und T. Belytschko (2007). „A multiscale projection method for macro/microcrack simulations“. In: *International Journal for Numerical Methods in Engineering* 71.12, S. 1466–1482.

Lopez-Pamies, O. und M.I. Idiart (2010). „Fiber-reinforced hyperelastic solids: a realizable homogenization constitutive theory“. In: *Journal of Engineering Mathematics* 68.1, S. 57–83.

Lu, B. und S. Torquato (1990). „Local volume fraction fluctuations in heterogeneous media“. In: *The Journal of Chemical Physics* 93.5, S. 3452–3459.

Matthies, S. und M. Humbert (1995). „On the principle of a geometric mean of even-rank symmetric tensors for textured polycrystals“. In: *Journal of Applied Crystallography* 28.3, S. 254–266.

Maxwell, J.C. (1873). *A Treatise on Electricity and Magnetism*. Clarendon Press.

Melenk, J. M. und I. Babuska (1996). „The partition of unity finite element method: Basic theory and applications“. In: *Computer Methods in Applied Mechanics and Engineering* 39, S. 289–314.

Michel, J.C. und P.M. Suquet (2003). „Nonuniform transformation field analysis“. In: *International Journal of Solids and Structures* 40, S. 6937–6955.

Miehe, C. (2002). „Strain-driven homogenization of inelastic microstructures and composites based on an incremental variational formulation“. In: *International Journal for Numerical Methods in Engineering* 55, S. 1285–1322.

Miehe, C. und C. G. Bayreuther (2007). „On multiscale FE analyses of heterogeneous structures: from homogenization to multigrid solvers“. In: *International Journal for Numerical Methods in Engineering* 71.10, S. 1135–1180.

Miehe, C. und J. Schröder (1994). „Post–critical discontinuous localization analysis of small–strain softening elastoplastic solids“. In: *Archive of Applied Mechanics* 64, S. 267–285.

Miehe, C., J. Schröder und M. Becker (2002). „Computational homogenization analysis in finite elasticity: material and structural instabilities on the micro- and macroscales of periodic composites and their interaction“. In: *Computer Methods in Applied Mechanics and Engineering* 191, S. 4971–5005.

Milton, G.W. (2002). *The Theory of Composites*. Cambridge University Press.

Morrey, C.B. (1952). „Quasi-convexity and the lower semicontinuity of multiple integrals“. In: *Pacific Journal of Mathematics* 2.1, S. 25–53.

Müller, S., L. Scardia und C.I. Zeppieri (2015). „Gradient theorie for geometrically nonlinear plasticity via the homogenization of dislocations“. In: *Analysis and computation of microstructures in finite plasticity*. Hrsg. von S. Conti und K. Hackl. Springer-Verlag, S. 175–204.

Mura, T. (1987). *Micromechanics of Defects in Solids*. Bd. 3. Mechanics of Elastic and Inelastic Solids. Springer Netherlands.

Nassar, H., Q.-C. He und N. Auffray (2015). „Willis elastodynamic homogenization theory revisited for periodic media“. In: *Journal of the Mechanics and Physics of Solids* 77, S. 158–178.

Nayfeh, A.H. (1995). *Wave Propagation in Layered Anisotropic Media: with Application to Composites*. North-Holland Series in Applied Mathematics and Mechanics. Elsevier Science.

Needleman, A. (1988). „Material rate dependence and mesh sensitivity in localization problems“. In: *Computer Methods in Applied Mechanics and Engineering* 67, S. 69–85.

— (1989). „Dynamic shear band development in plane strain“. In: *Journal of Applied Mechanics* 56.1, S. 1–9.

Nemat-Nasser, S. (1999). „Averaging theorems in finite deformation plasticity“. In: *Mechanics of Materials* 31, S. 493–523.

Nygards, M. (2003). „Number of grains necessary to homogenize elastic materials with cubic symmetry“. In: *Mechanics of Materials* 35, S. 1049–1053.

Ortin, J. (1997). „Thermodynamics and kinetics of phasetransitions– an introduction“. In: *Mechanics of solids with phase changes, CISM courses and lectures no.*

368. Hrsg. von M. Berveiller und F.D. Fischer. Springer-Verlag Wien New-York, S. 1–52.

Ostoja-Starzewski, M. (1998). „Random field models of heterogeneous materials“. In: *International Journal of Solids and Structures* 35.19, S. 2429–2455.

Özdemir, I., W.A.M. Brekelmans und M.G.D. Geers (2008). „FE^2 computational homogenization for the thermo-mechanical analysis of heterogeneous solids“. In: *Computer Methods in Applied Mechanics and Engineering* 198, S. 602–613.

Pelissou, C., J. Baccou, Y. Monrie und F. Perales (2009). „Determination of the size of the representative volume element for random quasi-brittle composites“. In: *International Journal of Solids and Structures* 46, S. 2842–2855.

Po, G., M. Lazar, D. Seif und N. Ghoniem (2014). „Singularity-free dislocation dynamics with strain gradient elasticity“. In: *Journal of the Mechanics and Physics of Solids* 68, S. 161–178.

Poisson, S.D. (1826). „Second mémoire sur la théorie de magnétisme“. In: *Mémoires de l'Académie royale des Sciences de l'Institut de France* 5, S. 488–533.

Ponte-Castañeda, P. (2012). „Bounds for nonlinear composites via iterated homogenization“. In: *Journal of the Mechanics and Physics of Solids* 60, S. 1583–1604.

Pope, S.B. (1997). „Computationally efficient implementation of combustion chemistry using in situ adaptive tabulation“. In: *Combustion Theory and Modelling* 1.1, S. 41–63.

Provatas, N. und K. Elder (2010). *Phase-Field Methods in Materials Science and Engineering*. Wiley-VCH.

Ren, Z.Y. und Q.S. Zheng (2002). „A quantitative study of minimum sizes of representative volume elements of cubic polycrystals—numerical experiments“. In: *Journal of the Mechanics and Physics of Solids* 50.4, S. 881–893.

— (2004). „Effects of grain sizes, shapes, and distribution on minimum sizes of representative volume elements of cubic polycrystals“. In: *Mechanics of Materials* 36.12, S. 1217–1229.

Reuss, A. (1929). „Berechnung der Fließgrenze von Mischkristallen auf Grund der Plastizitätsbedingung für Einkristalle“. In: *ZAMM - Journal of Applied Mathematics and Mechanics / Zeitschrift für Angewandte Mathematik und Mechanik* 9.1, S. 49–58.

Richeton, T. und S. Berbenni (2014). „From bicrystals to spherical inclusions: A superposition method to derive analytical expressions of stress fields in presence of plastic strain gradients“. In: *International Journal of Solids and Structures* 51.3–4, S. 794–807.

Roters, F. (2011). *Advanced Material Models for the Crystal Plasticity Finite Element Method*. Habilitationsschrift.

Roubíček, T. (2011). „Approximation in multiscale modelling of microstructure evolution in shape-memory alloys“. In: *Continuum Mechanics and Thermodynamics* 23.6, S. 491–507.

Rudraraju, S., A. Van der Ven und K. Garikipati (2014). „Three-dimensional isogeometric solutions to general boundary value problems of Toupin's gradient elasticity theory at finite strains“. In: *Computer Methods in Applied Mechanics and Engineering* 278, S. 705–728.

Sachs, E. (1928). „Zur Ableitung einer Fließbedingung“. In: *Zeitschrift des Vereines deutscher Ingenieure* 72, S. 734–736.

Schmitt, R., C. Kuhn, R. Müller und K. Bhattacharya (2014). „Crystal plasticity and martensitic transformations - a phase field approach“. In: *Technische Mechanik* 34.1, S. 23–38.

Schröder, J. (2010a). „Anisotropic polyconvex energies“. In: *Poly-, Quasi- and Rank-One Convexity in Applied Mechanics*. Hrsg. von J. Schröder und P. Neff. Bd. 516. CISM International Centre for Mechanical Sciences. Springer Vienna, S. 53–105.

— (2010b). „Quasiconvex envelopes in nonlinear elasticity“. In: *Poly-, Quasi- and Rank-One Convexity in Applied Mechanics*. Hrsg. von J. Schröder und P. Neff. Bd. 516. CISM International Centre for Mechanical Sciences. Springer Vienna, S. 17–51.

Schröder, J., D. Balzani und D. Brands (2011). „Approximation of random microstructures by periodic statistically similar representative volume elements based on lineal-path functions“. In: *Archive of Applied Mechanics* 81 (7), S. 975–997.

Schröder, J. und J. Löblien (2005). „A geometric nonlinear triangular finite element with an embedded discontinuity for the simulation of quasi-brittle fracture“. In: *Computational Mechanics* 36.2, S. 139–157.

Schröder, J. und P. Neff (2003). „Invariant formulation of hyperelastic transverse isotropy based on polyconvex free energy functions“. In: *International Journal of Solids and Structures* 40, S. 401–445.

Seif, D., G. Po, M. Mrovec, M. Lazar, C. Elsässer und P. Gumbsch (2015). „Atomistically enabled nonsingular anisotropic elastic representation of near-core dislocation stress fields in α-iron“. In: *Physiyal Review B* 91 (18), S. 184102.

Seth, B.R. (1964). „Generalized strain measure with applications to physical problems“. In: *Second-Order Effects in Elasticity, Plasticity and Fluid Dynamics*. Hrsg. von M. Reiner und D. Abir. Pergamon Press, Oxford, S. 162–172.

Shodja, H.M. und A. Tehranchi (2010). „A formulation for the characteristic lengths of fcc materials in first strain gradient elasticity via the Sutton–Chen potential“. In: *Philosophical Magazine* 90.14, S. 1893–1913.

Shodja, H.M., A. Zaheri und A. Tehranchi (2013). „Ab initio calculations of characteristic lengths of crystalline materials in first strain gradient elasticity“. In: *Mechanics of Materials* 61, S. 73–78.

Simo, J.C. und T.J.R. Hughes (1998). *Computational Inelasticity*. Springer-Verlag, New York.

Suquet, P.M. (1987). „Homogenization Techniques for Composite Media, Lectures Delivered at the CISM International Center for Mechanical Sciences Udine, Italy, July 1-5, 1985“. In: Bd. 272. Lecture Notes in Physics. Springer-Verlag, Berlin. Kap. Averages, Boundary conditions, S. 199–208.

Šverák, V. (1992). „Rank-one convexity does not imply quasiconvexity“. In: *Proceedings of the Royal Society of Edinburgh: Section A Mathematics* 120 (1-2), S. 185–189.

Tartar, L. (1985). „Estimations fines des coefficients homogénéisés“. In: *Ennio di Giorgi Colloquium: Papers presented at a colloquium held at the H. Poincaré institute in Nov. 1983*. Hrsg. von P. Krée. Pitman Publishing Ltd., S. 168–187.

Taylor, G.I. (1938). „Analysis of plastic strain in a cubic crystal (Reprinted in "The scientific papers of Sir Geoffrey Ingram Taylor", Cambridge University Press 1958)“. In: *Journal of the Institute of Metals* 62, S. 307–324.

Tewari, A., A.M. Gokhale, J.E. Spowart und D.B. Miracle (2004). „Quantitative characterization of spatial clustering in three-dimensional microstructures using two-point correlation functions“. In: *Acta Materialia* 52.2, S. 307–319.

Torquato, S. und G. Stell (1985). „Microstructure of two-phase random media. V. The n-point matrix probability functions for impenetrable spheres“. In: *Journal of Chemical Physics* 82, S. 980–987.

Van Houtte, P., S. Li, M. Seefeldt und L. Delannay (2005). „Deformation texture prediction: from the Taylor model to the advanced LAMEL model“. In: *International Journal of Plasticity* 21.3, S. 589–624.

Voigt, W. (1889). „Über die Beziehung zwischen den beiden Elastizitätskonstanten isotroper Körper“. In: *Annalen der Physik* 274.12, S. 573–587.

Wang, Y. und A.G. Khachaturyan (1997). „Three-dimensional field model and computer modeling of martensitic transformations“. In: *Acta Materialia* 45.2, S. 759–773.

Wang, Y.U., Y.M. Jin und A.G. Khachaturyan (2004). „The effects of free surfaces on martensite microstructures: 3D phase field microelasticity simulation study“. In: *Acta Materialia* 52.4, S. 1039–1050.

Willis, J. R. (2011). „Effective constitutive relations for waves in composites and metamaterials“. In: *Proceedings of the Royal Society of London A: Mathematical, Physical and Engineering Sciences* 467.2131, S. 1865–1879.

Willis, J.R. (1977). „Bounds and self-consistent estimates for the overall properties of anisotropic composites“. In: *Journal of the Mechanics and Physics of Solids* 25.3, S. 185–202.

— (1980a). „A polarization approach to the scattering of elastic waves–II. Multiple scattering from inclusions“. In: *Journal of the Mechanics and Physics of Solids* 28.5-6, S. 307–327.

— (1980b). „Polarization approach to the scattering of elastic waves–I. Scattering by a single inclusion“. In: *Journal of the Mechanics and Physics of Solids* 28.5-6, S. 287–305.

— (2012). „The construction of effective relations for waves in a composite“. In: *Comptes Rendus Mécanique* 340.4-5, S. 181–192.

Zee, L. und E. Sternberg (1983). „Ordinary and strong ellipticity in the equilibrium theory of incompressible hyperelastic solids“. In: *Archive for Rational Mechanics and Analysis* 83 (1), S. 53–90.

Zheng, Q.S. und D.X. Du (2001). „An explicit and universally applicable estimate for the effective properties of multiphase composites which accounts for inclusion distribution“. In: *Journal of the Mechanics and Physics of Solids* 49.11, S. 2765–2788.

Zimmer, J. (2006). „Jog my shape memory: dynamics as a challenge in mathematical materials science“. In: *Philosophical Transactions of the Royal Society of London A* 364, S. 3285–3300.

Reproduktionen der wichtigsten eigenen Beiträge

In R. Glüge, M. Weber und A. Bertram (2012). **Comparison of spherical and cubical statistical volume elements with respect to convergence, anisotropy, and localization behavior**. In: *Computational Material Science* 63, S. 91–104 wurde der Einfluss der geometrischen Form repräsentativer Volumenelemente (RVE) auf die Konvergenzgeschwindigkeit und die Anisotropie untersucht. Hierfür wurden würfel- und kugelförmige RVE bei Anwendung der verschiedenen klassischen Randbedingungen (iso-stress, iso-strain und periodisch) verglichen. Es wurde festgestellt, dass

- die klassischen, periodische Randbedingungen auf würfelförmigen RVE auf nichtperiodische RVE rein mathematisch übertragen werden können, was die antipodischen Randbedingungen auf kugelförmigen RVE liefert,
- kugelförmige RVE aufgrund des besseren Oberfläche-Volumen-Verhältnisses bei Vergrößerung schneller gegen das effektive Materialverhalten konvergieren als würfelförmige RVE,
- kugelförmige RVE mit antipodischen Randbedingungen bei statistisch isotropen, nichtperiodischen Mikrostrukturen keine künstliche Anisotropie induzieren, welche bei würfelförmigen RVE mit periodischen Randbedingungen aufgrund induzierten Periodizitätsrahmens zwangsweise auftritt,
- sich bei kugelförmigen RVE mit antipodischen Randbedingungen aus denselben Gründen Scherbänder frei einstellen können, während diese bei würfelförmigen RVE an den Periodizitätsrahmen gebunden sind.

Computational Materials Science 63 (2012) 91–104

Contents lists available at SciVerse ScienceDirect

Computational Materials Science

journal homepage: www.elsevier.com/locate/commatsci

Comparison of spherical and cubical statistical volume elements with respect to convergence, anisotropy, and localization behavior

R. Glüge *, M. Weber, A. Bertram

Universität Magdeburg, Universitätsplatz 2, D-39106, Germany

ARTICLE INFO

Article history:
Received 29 February 2012
Received in revised form 8 May 2012
Accepted 26 May 2012
Available online 29 June 2012

Keywords:
Representative volume element
Statistical volume element
Shape
Anisotropy
Convergence
Localization

ABSTRACT

The statistical volume element (SVE) technique is commonly used for the estimation of the effective properties of a micro-structured material. Mostly, cubical SVEs with periodic boundary conditions are employed, which result in a better convergence, compared to the uniform boundary conditions. In this work, the possibility of using spherical SVEs is discussed, since their use promises a reduction of the influence of the boundary, and thus a more efficient estimation of the effective material properties. We discuss the applicability of boundary conditions which are similar to the periodic boundary conditions to spherical SVEs. Then we assess the convergence (subject 1) of spherical and cubical SVEs to the effective material behavior for the uniform and periodic boundary conditions, focusing on the elastic and plastic properties of a macroscopically isotropic matrix-inclusion material. It is shown that the spherical SVEs perform indeed better than the cubical SVEs. Also, unlike the spherical SVEs, the cubical SVEs with periodic boundary conditions induce a spurious anisotropy (subject 2), which is quantified for the effective elastic properties. Finally, we examine the effect of the periodicity frame on the localization behavior (subject 3) of cubical SVE, since cubical SVE with periodic boundary conditions are commonly used to estimate macroscale material failure. It is demonstrated that the orientation of the periodicity frame affects the overall SVE response significantly. The latter is not observed for spherical SVE.

1. Introduction

The microscale structure of a material can have a considerable effect on the material properties as perceived on the macroscale. Common examples are polycrystals, which may exhibit a crystallographic (crystal orientation) and morphological (grain shape) texture, fiber or particle reinforced composites, foams and laminates. The process of calculating the effective material properties from the arrangement and the properties of the constituents on a smaller scale is termed as homogenization.

For specific material properties, efficient homogenization methods are at hand, see for example Klusemann and Svendsen [26] for the elastic properties, or Fritzen et al. [13] for the yield limit of porous materials. However, in many cases the analytical homogenization is limited, e.g. for the prediction of the crystallographic texture evolution [5]. Then, one follows commonly the pragmatic approach of the RVE or SVE method, which consists of considering a representative section of the material, define appropriate boundary conditions, and solve the initial- and boundary-value problem, usually with the help of numerical methods such as the finite element method. Then, one is able to extract the volume average of the variable of interest, or examine the effect of different microstructures on the overall material behavior. For an account on numerical homogenization by the SVE/RVE method see, e.g., Zohdi and Wriggers [49]. In this work, we will not distinguish strictly between RVE and SVE, which capture the microstructure identically (RVE) or in an approximate sense (SVE). Here, the two terms are used like synonyms.

When focusing on macroscale stress–strain relations, in contrast to analytical techniques, one does not arrive at a closed-form, but obtains an approximation for a specific deformation path. For a coupling with a large-scale FE application, one may use the FE^2 method [44,9,30,38]. However, this is computationally very expensive, and one is interested in a reduction of the numerical costs. A relatively new approach to this problem is the coupling of the RVE-method with the nonuniform transformation field analysis (NTFA [29,12]). Roughly speaking, the RVE method is used to build a database for different deformation modes, from which the actual stress–strain-relations needed in the macroscale calculation are estimated. However, the NTFA is restricted to the small strain setting.

A more direct reduction of the numerical costs of the FE^2 method is the optimization of the RVE, and to apply it simultaneously to a large-scale constitutive law. Then, the RVE calculations are carried out only when and where it is necessary, e.g., when the

* Corresponding author. Tel.: +49 391 67 12592; fax: +49 391 67 12863.
E-mail address: gluege@ovgu.de (R. Glüge).

0927-0256/$ - see front matter © 2012 Elsevier B.V. All rights reserved.
http://dx.doi.org/10.1016/j.commatsci.2012.05.063

straining is large. Also, the RVE itself should be as representative as possible, but still require an acceptable numerical effort. The problem of determining a RVE with a good balance between representativity and numerical expense, arises. It depends on the material under consideration, and has been subject of many studies, e.g., Kanit et al. [23], Xu and Chen [47], Pelissou et al. [39], Salahouelhadj and Haddadi [41]. Another possibility to increase the ratio representativity/numerical effort is to optimize the material section under consideration [42].

Here, we examine the influence of the shape of the RVE. Usually, cubical RVEs are used. We demonstrate that the use of spherical RVEs is advantageous for two reasons. Firstly, the bias due to specific boundary conditions is weaker, since the surface-to-volume ratio is smaller than for cubical RVEs. Secondly, spherical RVEs do not induce a material-independent anisotropy, unlike cubical RVEs with periodic boundary conditions. The reduction of the shape-induced anisotropy has been discussed by Grasset-Bourdel et al. [16], who considered RVEs with shapes that allow for a complete filling of the space. It was found that a hexagonal arrangement is advantageous, compared to a cubic shape. However, the restriction to shapes that allow for a complete filling of the space appears to be unnecessary, since spherical RVE are used routinely for analytical methods [17,43,8], while in numerical calculations the cubical RVEs predominate. Only few exceptions can be found, e.g., Kim et al. [25] and the authors referred to in this work used non-periodic RVEs.

The outline of this work is as follows: We firstly reproduce the fundamentals of the RVE method (Section 2), followed by a discussion of the possible boundary conditions (Section 3) that may be applied to spherical and cubical RVEs (Section 4). In Section 5 the setup for the numerical experiments is described. In Section 6 we examine the convergence while increasing the RVE size for the elastic and plastic properties of a matrix–inclusion-material, and compare different shapes and boundary conditions. In Section 7 we assess the shape-induced anisotropy of the spherical and cubical RVE with periodic boundary conditions by applying them to an effectively isotropic material. Finally we focus on the peculiarities of the localization behavior of the spherical and cubical RVE (Section 8).

1.1. Notation

Throughout the work a direct tensor notation is preferred. If an expression cannot be represented in the direct notation without introducing new conventions, its components are given with respect to orthonormal base vectors $\boldsymbol{e}_i$, using the summation convention. Vectors are symbolized by lowercase bold letters $\boldsymbol{v} = v_i\boldsymbol{e}_i$, second-order tensors by uppercase bold letters $\boldsymbol{T} = T_{ij}\boldsymbol{e}_i \otimes \boldsymbol{e}_j$ or bold Greek letters. The second-order identity tensor is denoted by $\boldsymbol{I}$. Fourth-order tensors are symbolized like $\mathbb{C}$. The dyadic product is defined as $(\boldsymbol{a} \otimes \boldsymbol{b}) \cdot \boldsymbol{c} = (\boldsymbol{b} \cdot \boldsymbol{c})\boldsymbol{a}$. A dot represents a scalar contraction. If more than one scalar contraction is carried out, the number of dots corresponds to the number of contractions, thus $(\boldsymbol{a} \otimes \boldsymbol{b} \otimes \boldsymbol{c}) \cdot\cdot (\boldsymbol{d} \otimes \boldsymbol{e}) = (\boldsymbol{b} \cdot \boldsymbol{d})(\boldsymbol{c} \cdot \boldsymbol{e})\boldsymbol{a}$, $\alpha = \boldsymbol{A} \cdot\cdot \boldsymbol{B}$ and $\boldsymbol{\sigma} = \mathbb{C} \cdot\cdot \boldsymbol{\varepsilon}$. If only one scalar contraction is carried out, the scalar dot is frequently omitted, e.g., $\boldsymbol{v} = \boldsymbol{F}\boldsymbol{w}$, $\boldsymbol{A} = \boldsymbol{B}\boldsymbol{C}$. $\|\boldsymbol{x}\|$ denotes the Frobenius norm.

The position vector of a material point is denoted by $\boldsymbol{x}(\boldsymbol{x}_0, t)$, where $\boldsymbol{x}_0$ indicates the position vector of the same material point in the reference placement. At $t = 0$, $\boldsymbol{x} = \boldsymbol{x}_0$ holds. The partial derivative of a function with respect to t with $\boldsymbol{x}_0$ kept constant is the material time derivative, indicated by a superimposed dot. The index "0" indicates that a function or derivative is to be evaluated in the reference placement or with respect to $\boldsymbol{x}_0$. Ω denotes the domain of the RVE under consideration. All unweighted volume averages over this domain are evaluated in the reference placement, denoted as $\langle\cdot\rangle := \frac{1}{V_0}\int_{\Omega_0} \cdot \, \mathrm{d}V$. A superimposed bar indicates a macroscale-quantity.

1.2. List of symbols

C_{ijkl}	components of the stiffness tetrad with respect to an orthonormal basis
J	$\det\boldsymbol{F}$
ρ	mass density
Ω	domain of the RVE
∇	nabla operator
$\boldsymbol{b}$	mass-specific force density
$\boldsymbol{n}$	surface normal vector
$\boldsymbol{t}$	traction vector $\boldsymbol{t} = \boldsymbol{\sigma} \cdot \boldsymbol{n}$
$\boldsymbol{u}$	displacement vector, $\boldsymbol{u} = \boldsymbol{x} - \boldsymbol{x}_0$
$\boldsymbol{x}$	position vector
$\boldsymbol{\sigma}$	Cauchy stress tensor
$\boldsymbol{\varepsilon}$	linear strain tensor, $\boldsymbol{\varepsilon} = \frac{1}{2}(\boldsymbol{H} + \boldsymbol{H}^T)$
$\boldsymbol{\tau}$	Kirchhoff stress tensor, $\boldsymbol{\tau} = J\boldsymbol{\sigma}$
$\boldsymbol{D}$	rate of deformation tensor, symmetric part of $\boldsymbol{L}$, $\boldsymbol{D} = \frac{1}{2}(\boldsymbol{L} + \boldsymbol{L}^T)$
$\boldsymbol{F}$	deformation gradient, $\boldsymbol{F} = \boldsymbol{x} \otimes \nabla_0$
$\boldsymbol{H}$	displacement gradient, $\boldsymbol{H} = \boldsymbol{F} - \boldsymbol{I} = \boldsymbol{u} \otimes \nabla_0$
$\boldsymbol{L}$	velocity gradient, $\boldsymbol{L} = \dot{\boldsymbol{x}} \otimes \nabla = \dot{\boldsymbol{F}}\boldsymbol{F}^{-1}$
$\boldsymbol{T}$	first Piola–Kirchhoff stress tensor, $\boldsymbol{T} = \det(\boldsymbol{F})\boldsymbol{\sigma}\boldsymbol{F}^{-T}$
$\mathbb{I}$	fourth order identity on symmetric second order tensors
$\mathbb{P}_1$	first isotropic projector, $\mathbb{P}_1 = \frac{1}{3}\boldsymbol{I} \otimes \boldsymbol{I}$
$\mathbb{P}_2$	second isotropic projector, $\mathbb{P}_2 = \mathbb{I} - \mathbb{P}_1$
$\mathbb{P}_{c2}$	second cubic projector
$\mathbb{P}_{c3}$	third cubic projector
HTBC	homogeneous traction boundary conditions
LDBC	linear displacement boundary conditions
PBC	periodic boundary conditions

2. Basic considerations

2.1. Scale separation

The scale separation requires that $l_{\text{micro}} \ll l_{\text{mini}} \ll l_{\text{macro}}$ [18], where l_{micro} refers to the characteristic size of the heterogeneities, l_{mini} to the RVE size and l_{macro} to the dimensions of the body. $l_{\text{micro}} \ll l_{\text{mini}}$ ensures the representativity of the RVE, while $l_{\text{mini}} \ll l_{\text{macro}}$ is necessary if one wants to consider the RVE as a material point on the macroscale.

2.2. Equilibrium equations

The local balances of linear and angular momentum require

$$\boldsymbol{\sigma} \cdot \nabla = \rho(\ddot{\boldsymbol{x}} - \boldsymbol{b}), \qquad \boldsymbol{\sigma} = \boldsymbol{\sigma}^T, \tag{1}$$

where $\boldsymbol{b}$ is a mass-specific force density. They must hold globally for an RVE Ω,

$$\int_\Omega \boldsymbol{\sigma} \cdot \nabla \mathrm{d}V = \int_\Omega \rho(\ddot{\boldsymbol{x}} - \boldsymbol{b}) \, \mathrm{d}V, \qquad \int_\Omega (\boldsymbol{\sigma} - \boldsymbol{\sigma}^T) \, \mathrm{d}V = \boldsymbol{0}, \tag{2}$$

where the global balance of linear momentum may be transformed by Gauss' theorem and Cauchy's theorem $\boldsymbol{t} = \boldsymbol{\sigma} \cdot \boldsymbol{n}$,

$$\int_{\partial\Omega} \boldsymbol{t} \mathrm{d}A - \int_\Omega \rho(\ddot{\boldsymbol{x}} - \boldsymbol{b}) \, \mathrm{d}V = \boldsymbol{0}. \tag{3}$$

However, the incorporation of inertia and body forces leads to material laws which depend on superimposed rigid body motions.[1] Thus, we may consider only the static balance of linear momentum without body forces when using the RVE method.[2]

2.3. Micro–Macro-coupling

The micro–macro-coupling is obtained by assigning macroscale quantities to unweighted volume averages of the corresponding microscale quantities, where the integral is carried out over the domain occupied by the material. Thus, porous materials require either a treatment of pores by some material law, or need to be excluded from the volume integral. In the latter case, care must be taken when Gauss's theorem is applied. Here we exclude this peculiarities, assuming a space-filling arrangement of micro-constituents. Following Nemat-Nasser [33], *"there is an inherent arbitrariness in the selection of suitable kinematic and dynamical quantities whose overall measures are defined in terms of unweighted volume averages of the corresponding micromeasure"*. To avoid ambiguities, it must be clarified which quantities are used. For several reasons it is advantageous to use the deformation gradient and the first Piola–Kirchhoff stresses,

$$\overline{\boldsymbol{F}} := \langle \boldsymbol{F} \rangle, \qquad \overline{\boldsymbol{T}} := \langle \boldsymbol{T} \rangle. \tag{4}$$

Firstly, $\overline{\boldsymbol{F}}$ and $\overline{\boldsymbol{T}}$ can be defined in terms of surface integrals in the reference placement,

$$\langle \boldsymbol{F} \rangle = \frac{1}{V_0} \int_{\Omega_0} \boldsymbol{x} \otimes \nabla_0 \mathrm{d}V = \frac{1}{V_0} \int_{\partial\Omega_0} \boldsymbol{x} \otimes \boldsymbol{n}_0 \mathrm{d}A, \tag{5}$$

$$\langle \boldsymbol{T} \rangle = \frac{1}{V_0} \int_{\partial\Omega_0} \boldsymbol{t} \otimes \boldsymbol{x}_0 \mathrm{d}A. \tag{6}$$

Relation (5) involves merely Gauss' theorem, while the latter relation is confirmed by reformulating with Cauchy theorem $\boldsymbol{t} = \boldsymbol{T} \cdot \boldsymbol{n}_0$, Gauss' theorem, and the static equilibrium condition without body forces $\boldsymbol{T} \cdot \nabla_0 = \boldsymbol{0}$ (see Section 2.2),

$$\begin{aligned} \langle \boldsymbol{T} \rangle &= \frac{1}{V_0} \int_{\partial\Omega_0} \boldsymbol{t} \otimes \boldsymbol{x}_0 \ \mathrm{d}A = \frac{1}{V_0} \int_{\partial\Omega_0} \boldsymbol{n}_0 \cdot (\boldsymbol{T}^T \otimes \boldsymbol{x}_0) \ \mathrm{d}A \qquad (7) \\ &= \frac{1}{V_0} \int_{\Omega_0} \nabla \cdot (\boldsymbol{T}^T \otimes \boldsymbol{x}_0) \ \mathrm{d}V = \frac{1}{V_0} \int_{\Omega_0} ((\boldsymbol{T} \cdot \nabla) \otimes \boldsymbol{x}_0 + \boldsymbol{T}) \ \mathrm{d}V \\ &= \frac{1}{V_0} \int_{\Omega_0} \boldsymbol{T} \ \mathrm{d}V. \qquad (8) \end{aligned}$$

Secondly, since the reference placement is time-independent, one can interchange the unweighted volume averaging and the material time derivative, i.e. $\dot{\overline{\boldsymbol{F}}} = \langle \dot{\boldsymbol{F}} \rangle = \langle \boldsymbol{F} \rangle^{\cdot} = \dot{\overline{\boldsymbol{F}}}$ and $\dot{\overline{\boldsymbol{T}}} = \langle \dot{\boldsymbol{T}} \rangle = \langle \boldsymbol{T} \rangle^{\cdot} = \dot{\overline{\boldsymbol{T}}}$.

Thirdly, $\boldsymbol{T}$ and $\dot{\boldsymbol{F}}$ are power-conjugate, which allows for a compact expression of the Hill–Mandel condition (Section 2.4). For the foregoing reasons, in this work $\boldsymbol{T}$ and $\boldsymbol{F}$ are taken for the micro–macro-coupling. Then, the macroscopic Cauchy stresses are obtained from $\bar{\boldsymbol{\sigma}} = \bar{J}^{-1} \overline{\boldsymbol{T}} \overline{\boldsymbol{F}}^T$, $\bar{J} = \det \overline{\boldsymbol{F}}$, which is not necessarily equivalent to $\langle \boldsymbol{\sigma} \rangle$. However, for the special case of the micro–macro-coupling in the first Piola–Kirchhoff stresses and the deformation gradient, it follows that $\bar{\boldsymbol{\tau}} = \langle \boldsymbol{\tau} \rangle$ [33].

[1] One can easily find examples which give an effective material behavior that violates the principle of invariance under superimposed rigid body motions [46]. Subject the RVE boundary to an accelerated rigid body motion and take $\overline{\boldsymbol{F}} := \langle \boldsymbol{F} \rangle$ and $\bar{\boldsymbol{\sigma}} := \langle \boldsymbol{\sigma} \rangle$ for the micro–macro-coupling to find that $\overline{\boldsymbol{F}} = \boldsymbol{I}$ holds constantly while $\overline{\boldsymbol{T}}$ depends on the motion.

[2] At this point, it is often argued that the volume integral $\left(\mathcal{O}\left(l_{\mathrm{mini}}^3\right)\right)$ is small compared to the surface integral $\left(\mathcal{O}\left(l_{\mathrm{mini}}^2\right)\right)$ due to the small size of the RVE, in order legitimate the disregard of inertia and body forces. This argument is conflicting with the idea of a possibly large RVE for a better representativity.

2.4. The Hill–Mandel condition

The Hill–Mandel condition, demands the equivalence of the stress power as perceived on the macroscale and on the microscale. For the small strain setting it is sufficient to consider

$$\langle \boldsymbol{\sigma} \cdot \cdot \dot{\boldsymbol{\varepsilon}} \rangle = \langle \boldsymbol{\sigma} \rangle \cdot \cdot \langle \dot{\boldsymbol{\varepsilon}} \rangle. \tag{9}$$

The latter equation is trivially satisfied if $\boldsymbol{\sigma}$ and $\dot{\boldsymbol{\varepsilon}}$ are homogeneous, from which the first interpretation of the Hill–Mandel-condition is derived: The larger the RVE is, the more homogeneous appears the material, i.e. the smaller are the fluctuations, leading to the conclusion that the Hill–Mandel-condition poses requirements on the RVE size [20].

However, the RVE is subjected to some boundary conditions. It was found that the Hill–Mandel-condition is satisfied for specific boundary data a priori [45], independent of the size of the RVE. From this, the second interpretation of the Hill–Mandel-condition arises: The boundary conditions should comply the Hill–Mandel-condition a priori to assure convergence to the effective material law with increasing RVE size. The latter interpretation appears to be widely accepted, since all commonly used boundary conditions a priori fulfill the Hill–Mandel-condition.

Before examining specific boundary conditions, the derivation of Suquet [45], which was originally given in the small strain setting, is reproduced here for the finite strain form of the Hill–Mandel-condition (see also Bertram [2]). The volume average of the volume-specific stress power of the RVE (left handside) must be equivalent to the volume-specific stress power on the macroscale,

$$\langle \boldsymbol{T} \cdot \cdot \dot{\boldsymbol{F}} \rangle = \overline{\boldsymbol{T}} \cdot \cdot \dot{\overline{\boldsymbol{F}}}. \tag{10}$$

Taking $\boldsymbol{F}$ and $\boldsymbol{T}$ for the micro–macro-coupling, the latter equation becomes

$$\langle \boldsymbol{T} \cdot \cdot \dot{\boldsymbol{F}} \rangle = \langle \boldsymbol{T} \rangle \cdot \cdot \langle \dot{\boldsymbol{F}} \rangle. \tag{11}$$

The latter equation can be recast with surface integrals, involving the boundary conditions. Up to Eq. (17), the dependency on $\boldsymbol{x}_0$ and t is written out, since the dependence is of importance for the argumentation. Firstly, the fluctuation part of $\dot{\boldsymbol{F}}$ is defined as

$$\tilde{\dot{\boldsymbol{F}}}(\boldsymbol{x}_0, t) := \dot{\boldsymbol{F}}(\boldsymbol{x}_0, t) - \dot{\overline{\boldsymbol{F}}}(t), \qquad \dot{\overline{\boldsymbol{F}}}(t) := \langle \dot{\boldsymbol{F}}(\boldsymbol{x}_0, t) \rangle. \tag{12}$$

Note that $\dot{\boldsymbol{F}}(\boldsymbol{x}_0, t) = \dot{\boldsymbol{H}}(\boldsymbol{x}_0, t)$, and consequently $\dot{\overline{\boldsymbol{F}}}(t) = \dot{\overline{\boldsymbol{H}}}(t)$ and $\tilde{\dot{\boldsymbol{F}}}(\boldsymbol{x}_0, t) = \tilde{\dot{\boldsymbol{H}}}(\boldsymbol{x}_0, t)$ hold. For the velocity field, one can define the decomposition

$$\dot{\boldsymbol{u}}(\boldsymbol{x}_0, t) := \dot{\boldsymbol{u}}(\boldsymbol{x}_0, t) - \dot{\overline{\boldsymbol{H}}}(t) \cdot \boldsymbol{x}_0, \dot{\boldsymbol{u}}(\boldsymbol{x}_0, t) - \dot{\overline{\boldsymbol{u}}}(\boldsymbol{x}_0, t). \tag{13}$$

Since $\boldsymbol{x}_0$ is not a function of t, the material time derivative and the material gradient $\otimes\nabla_0$ may be interchanged. Applying $\otimes\nabla_0$ to $\dot{\tilde{\boldsymbol{u}}}(\boldsymbol{x}_0, t)$ yields

$$\begin{aligned} \dot{\tilde{\boldsymbol{u}}}(\boldsymbol{x}_0, t) \otimes \nabla_0 &= \dot{\boldsymbol{u}}(\boldsymbol{x}_0, t) \otimes \nabla_0 - \dot{\overline{\boldsymbol{H}}}(t) = \dot{\boldsymbol{H}}(\boldsymbol{x}_0, t) - \dot{\overline{\boldsymbol{H}}}(t) \\ &= \tilde{\dot{\boldsymbol{H}}}(\boldsymbol{x}_0, t), \end{aligned} \tag{14}$$

i.e. $\dot{\tilde{\boldsymbol{u}}}(\boldsymbol{x}_0, t)$ and $\tilde{\dot{\boldsymbol{F}}}(\boldsymbol{x}_0, t)$ are related by

$$\tilde{\dot{\boldsymbol{F}}}(\boldsymbol{x}_0, t) = \dot{\tilde{\boldsymbol{u}}}(\boldsymbol{x}_0, t) \otimes \nabla_0. \tag{15}$$

Note that, unlike $\dot{\overline{\boldsymbol{F}}}(t)$, $\dot{\tilde{\boldsymbol{u}}}(\boldsymbol{x}_0, t)$ does depend on $\boldsymbol{x}_0$. The displacement $\tilde{\boldsymbol{u}}(\boldsymbol{x}_0, t)$ can be viewed as the part of the local displacement that stems from the homogeneous part $\overline{\boldsymbol{H}}$ of the displacement gradient. Although it depends linearly on $\boldsymbol{x}_0$ it is often referred to as the homogeneous part of the local displacement. Inserting the decomposition of $\dot{\boldsymbol{F}}(\boldsymbol{x}_0, t)$ into Eq. (11) yields

$$\langle \boldsymbol{T}(\boldsymbol{x}_0, t) \cdot \cdot \dot{\overline{\boldsymbol{F}}}(t) \rangle + \langle \boldsymbol{T}(\boldsymbol{x}_0, t) \cdot \cdot \tilde{\dot{\boldsymbol{F}}}(\boldsymbol{x}_0, t) \rangle = \langle \boldsymbol{T}(\boldsymbol{x}_0, t) \rangle \cdot \cdot \dot{\overline{\boldsymbol{F}}}(t), \tag{16}$$

where $\dot{\overline{\boldsymbol{F}}}(t)$ can be pulled out of the volume averaging, since it is independent on $\boldsymbol{x}_0$. Then one finds

$$\langle \boldsymbol{T}(\boldsymbol{x}_0,t)\cdot\cdot\dot{\widetilde{\boldsymbol{F}}}(\boldsymbol{x}_0,t)\rangle = 0. \tag{17}$$

One proceeds by using Eq. (15), and considering $\boldsymbol{T}\cdot\cdot(\dot{\tilde{\boldsymbol{u}}}\otimes\nabla_0)$ as one summand of a product rule,

$$\boldsymbol{T}\cdot\cdot\dot{\tilde{\boldsymbol{u}}}\otimes\nabla_0 + (\boldsymbol{T}\cdot\nabla_0)\cdot\dot{\tilde{\boldsymbol{u}}} = (\dot{\tilde{\boldsymbol{u}}}\cdot\boldsymbol{T})\cdot\nabla_0, \tag{18}$$

which allows to write

$$0 = \langle(\dot{\tilde{\boldsymbol{u}}}\cdot\boldsymbol{T})\cdot\nabla_0 - (\boldsymbol{T}\cdot\nabla_0)\cdot\dot{\tilde{\boldsymbol{u}}}\rangle. \tag{19}$$

Here one identifies $\boldsymbol{T}\cdot\nabla_0 = \boldsymbol{0}$ in the second summand as the local balance of linear momentum without inertia and body forces in the reference placement. Therefore, by considering only equilibrium states, this summand is dropped. The remaining summand is transformed by Gauss' theorem and Cauchy's theorem to

$$0 = \frac{1}{V_0}\int_{\partial\Omega_0}\dot{\tilde{\boldsymbol{u}}}\cdot\boldsymbol{T}\cdot\boldsymbol{n}_0\,\mathrm{d}A = \frac{1}{V_0}\int_{\partial\Omega_0}\dot{\tilde{\boldsymbol{u}}}\cdot\boldsymbol{t}\,\mathrm{d}A. \tag{20}$$

By this, the Hill–Mandel-condition is expressed as a surface integral in terms of the traction and displacement, which allows to examine specific boundary conditions with respect to the Hill–Mandel-condition.

3. Boundary conditions on the RVE

The boundary value problem is complete when at each surface point, with respect to a suitable orthogonal basis $\boldsymbol{b}_i$, either u_i, t_i or a mixture of both is prescribed. More general, the boundary conditions may be given implicitly in form of constraints, as it is the case for the periodic boundary conditions.

The boundary conditions to which an RVE may be subjected have been exhaustively discussed, see e.g. Suquet [45]. There are no natural or self-evident boundary conditions for the RVE, except for microstructures with a periodicity, where periodic boundary conditions are reasonable [31]. The most common boundary conditions are the homogeneous traction, linear displacement and periodic boundary conditions. Recent advances focus on the definition of boundary conditions which allow for an arbitrary localization of a RVE [7,36] (percolation path boundary conditions), where the periodic boundary conditions on a cubic RVE serve as the starting point. In this regard, a consideration of spherical RVEs with periodic boundary conditions is helpful. This topic is addressed in Section 8.

3.1. Uniform boundary data

The assumption of homogeneous tractions or linear displacements on the boundary are related to the Sachs/Reuss or Taylor/Voigt estimates, which assume a homogeneous stress or strain field not only on the boundary but in the entire volume. Thus, restricting this extreme assumptions to the RVE boundary gives estimates between these bounds. However, out of the commonly applied boundary conditions, homogeneous traction or linear displacement boundary conditions give bounds for the effective material law that may be obtained from a specific RVE [27,24]. While homogeneous traction boundary conditions give a softer effective material response, the linear displacement boundary conditions overestimate the stresses. In both cases, the Hill–Mandel-condition holds a priori, irrespective of the material law and the RVE size. The uniform boundary conditions have the advantage of an easy implementation.

3.1.1. Linear displacement boundary conditions

These are also termed as uniform strain boundary conditions [45], homogeneous displacement boundary conditions [11], kinematic uniform boundary conditions [23]. Given the average displacement gradient $\dot{\overline{\boldsymbol{H}}}_{\text{impose}}$ at each instant t, the velocity of the boundary points is given by

$$\dot{\boldsymbol{u}} = \dot{\overline{\boldsymbol{H}}}_{\text{impose}}\boldsymbol{x}_0 \quad \text{on } \partial\Omega. \tag{21}$$

One notes that due to the decomposition (13), $\dot{\tilde{\boldsymbol{u}}} = \boldsymbol{0}$ at the boundary, which renders the Hill–Mandel-condition (Eq. (20)) satisfied. The linear displacement boundary conditions correspond to the extremal Taylor and Voigt assumptions.

3.1.2. Homogeneous traction boundary conditions

Given the average stress tensor $\overline{\boldsymbol{T}}_{\text{impose}}$, the surface tractions are prescribed by

$$\boldsymbol{t} = \overline{\boldsymbol{T}}_{\text{impose}}\boldsymbol{n}_0 \qquad \text{on } \partial\Omega. \tag{22}$$

If this is inserted into the Hill–Mandel-condition (Eq. (20)), one notes that $\overline{\boldsymbol{T}}_{\text{impose}}$ can be pulled out of the integral, which leaves

$$0 = \frac{1}{V_0}\overline{\boldsymbol{T}}_{\text{impose}}\cdot\cdot\int_{\partial\Omega_0}\dot{\tilde{\boldsymbol{u}}}\otimes\boldsymbol{n}_0\mathrm{d}A = \frac{1}{V_0}\overline{\boldsymbol{T}}_{\text{impose}}\cdot\cdot\langle\dot{\widetilde{\boldsymbol{F}}}\rangle. \tag{23}$$

With $\langle\dot{\widetilde{\boldsymbol{F}}}\rangle = \boldsymbol{0}$ (Eq. (12)) one notes that the Hill–Mandel-condition is satisfied. The homogeneous traction boundary conditions correspond to the extremal Sachs and Reuss assumptions.

Commonly, material laws are formulated such that the stresses are a function of the motion of the body, although an inversion or even an implicit form is possible [40]. In case of the homogeneous traction boundary conditions, one prescribes the average stress state and obtains the average straining, i.e. it is the other way around. Miehe [31] used Lagrangian multipliers for changing the independent variable from $\boldsymbol{T}$ to $\boldsymbol{H}$. One finds that

$$\dot{\overline{\boldsymbol{H}}}_{\text{impose}} = \frac{1}{V_0}\int_{\partial\Omega_0}\dot{\boldsymbol{u}}\otimes\boldsymbol{n}_0\,\mathrm{d}A, \tag{24}$$

needs to be enforced, instead of Eq. (22). The latter is often termed as kinematic minimal boundary conditions [28], natural boundary conditions [10], weakly enforced kinematic boundary conditions [11] or static uniform boundary conditions [23]. The equivalence of the kinematic minimal boundary conditions to the homogeneous traction boundary conditions can be seen by considering perturbations of a solution of a boundary value problem with kinematic minimal boundary conditions. Suppose that we have imposed $\dot{\overline{\boldsymbol{H}}}_{\text{impose}}$ by Eq. (24), and found a global velocity field $\dot{\boldsymbol{u}}$ which we consider the solution. According to the incremental work minimization principle [37], the stress power attains a minimum state in equilibrium, thus any deviation from this solution must result in an increase of the incremental condensed potential. We denote an infinitesimal deviation from $\dot{\boldsymbol{u}}$ by $\delta\dot{\boldsymbol{u}}$. $\delta\dot{\boldsymbol{u}}$ must be compatible to the boundary conditions, i.e.,

$$\int_{\partial\Omega_0}\delta\dot{\boldsymbol{u}}\otimes\boldsymbol{n}_0\,\mathrm{d}A = \boldsymbol{0}. \tag{25}$$

The stress power change due to $\delta\dot{\boldsymbol{u}}$ is denoted as

$$\delta\dot{w} = \int_{\partial\Omega_0}\boldsymbol{t}\cdot\delta\dot{\boldsymbol{u}}\,\mathrm{d}A. \tag{26}$$

The tractions $\boldsymbol{t}$ can be decomposed into a homogeneous and a fluctuation part,

$$\boldsymbol{t} = \overline{\boldsymbol{T}}\cdot\boldsymbol{n}_0 + \tilde{\boldsymbol{t}}, \qquad \int_{\partial\Omega_0}\tilde{\boldsymbol{t}}\otimes\boldsymbol{n}_0\,\mathrm{d}A = \boldsymbol{0}. \tag{27}$$

We insert this decomposition into the variation of the stress power,

$$\delta\dot{w} = \int_{\partial\Omega_0} (\overline{\boldsymbol{T}} \cdot \boldsymbol{n}_0 + \tilde{\boldsymbol{t}}) \cdot \delta\dot{\boldsymbol{u}} \, \mathrm{d}A \tag{28}$$

$$= \int_{\partial\Omega_0} (\overline{\boldsymbol{T}} \cdot \cdot \, \delta\dot{\boldsymbol{u}} \otimes \boldsymbol{n}_0 + \tilde{\boldsymbol{t}} \cdot \delta\dot{\boldsymbol{u}}) \, \mathrm{d}A. \tag{29}$$

The first summand is zero by definition: We can pull out $\overline{\boldsymbol{T}}$, and the remaining integral is equal to Eq. (25). It remains

$$\delta\dot{w} = \int_{\partial\Omega_0} \tilde{\boldsymbol{t}} \cdot \delta\dot{\boldsymbol{u}} \, \mathrm{d}A. \tag{30}$$

One can see that $\tilde{\boldsymbol{t}} = \boldsymbol{0}$ must hold if $\dot{\boldsymbol{u}}$ is a minimizer of $\dot{w}$. Otherwise it is possible to reduce the stress power by choosing $\delta\dot{\boldsymbol{u}} = \alpha\tilde{\boldsymbol{t}}$, with $\alpha < 0$ (and the corresponding physical unit). This is admissible because of Eq. (27) being in accordance with Eq. (25). Thus, $\delta\dot{w}$ can only be zero for all admissible perturbations of $\dot{\boldsymbol{u}}$ if $\tilde{\boldsymbol{t}} = \boldsymbol{0}$, i.e. the solution in case of kinematic minimal boundary conditions must correspond to a state of homogeneous tractions, as prescribed by the homogeneous traction boundary conditions.

3.2. Mixing of homogeneous traction and linear displacement boundary conditions

Since the linear displacement boundary conditions and homogeneous traction boundary conditions pose bounds, these boundary conditions are sometimes mixed on one RVE, in order to get a better approximation of the real material behavior [25,14]. Two different approaches are possible.

3.2.1. Globally mixed boundary conditions

One may prescribe on all surface points mixed boundary conditions, where with respect to a suitable orthogonal basis a mixture of the components u_i and t_i is prescribed, which are obtained from uniform $\overline{\boldsymbol{H}}_{\text{impose}}\boldsymbol{x}_0$ and $\overline{\boldsymbol{T}}_{\text{impose}}\boldsymbol{x}_0$. For this case the Hill–Mandel-condition holds a priori [19]. This can be seen by decomposing

$$\dot{\boldsymbol{u}} = \dot{\boldsymbol{u}}_{\text{impose}} + \dot{\boldsymbol{u}}_{\text{reaction}} \tag{31}$$

$$\boldsymbol{t} = \boldsymbol{t}_{\text{impose}} + \boldsymbol{t}_{\text{reaction}}, \tag{32}$$

where the relations

$$0 = \dot{\boldsymbol{u}}_{\text{impose}} \cdot \boldsymbol{t}_{\text{impose}} \tag{33}$$

$$0 = \dot{\boldsymbol{u}}_{\text{reaction}} \cdot \boldsymbol{t}_{\text{reaction}} \tag{34}$$

$$0 = \dot{\boldsymbol{u}}_{\text{reaction}} \cdot \dot{\boldsymbol{u}}_{\text{impose}} \tag{35}$$

$$0 = \boldsymbol{t}_{\text{reaction}} \cdot \boldsymbol{t}_{\text{impose}} \tag{36}$$

must hold. With $\dot{\boldsymbol{u}}_{\text{impose}} = \dot{\overline{\boldsymbol{H}}}_{\text{impose}}\boldsymbol{x}_0$ it is clear that $\dot{\boldsymbol{u}}_{\text{impose}}$ does not contribute to $\dot{\tilde{\boldsymbol{u}}}$, i.e.,

$$\dot{\tilde{\boldsymbol{u}}} \cdot \dot{\boldsymbol{u}}_{\text{impose}} = 0, \tag{37}$$

which leads to the conclusion that $\dot{\tilde{\boldsymbol{u}}}$ must be parallel to $\dot{\boldsymbol{u}}_{\text{reaction}}$. Examining the Hill–Mandel-condition leads to

$$0 = \frac{1}{V_0}\int_{\partial\Omega_0} \dot{\tilde{\boldsymbol{u}}} \cdot \boldsymbol{t} \, \mathrm{d}A = \frac{1}{V_0}\int_{\partial\Omega_0} (\dot{\tilde{\boldsymbol{u}}} \cdot \boldsymbol{t}_{\text{impose}} + \dot{\tilde{\boldsymbol{u}}} \cdot \boldsymbol{t}_{\text{reaction}}) \, \mathrm{d}A. \tag{38}$$

Since $\dot{\tilde{\boldsymbol{u}}}$ is parallel to $\dot{\boldsymbol{u}}_{\text{reaction}}$ and due to Eq. (34) the second summand vanishes, and the remainder corresponds to Eq. (23), i.e., the Hill–Mandel-condition is met a priori.

3.2.2. Locally pure homogeneous tractions and linear displacements

Another possibility is to divide the surface into the parts $\partial\Omega_{\boldsymbol{u}}$ and $\partial\Omega_{\boldsymbol{t}}$ where $\dot{\boldsymbol{u}} = \dot{\overline{\boldsymbol{H}}}_{\text{impose}}\boldsymbol{x}_0$ and $\boldsymbol{t} = \overline{\boldsymbol{T}}_{\text{impose}}\boldsymbol{n}_0$ are prescribed, respectively. Then the Hill–Mandel-condition gives (Eq. (20))

$$0 = \frac{1}{V_0}\int_{\partial\Omega_{0\boldsymbol{u}}} [(\dot{\overline{\boldsymbol{H}}}_{\text{impose}} - \dot{\overline{\boldsymbol{H}}})\boldsymbol{x}_0] \cdot [\boldsymbol{T}\boldsymbol{n}_0] \, \mathrm{d}A + \frac{1}{V_0}\int_{\partial\Omega_{0\boldsymbol{t}}} [(\dot{\boldsymbol{H}} - \dot{\overline{\boldsymbol{H}}})\boldsymbol{x}_0] \cdot [\overline{\boldsymbol{T}}_{\text{impose}}\boldsymbol{n}_0] \, \mathrm{d}A. \tag{39}$$

with $\dot{\tilde{\boldsymbol{u}}} = \dot{\boldsymbol{u}} - \dot{\overline{\boldsymbol{H}}}\boldsymbol{x}_0$. Unfortunately, it appears that no constraints can be given that ensure the Hill–Mandel-condition a priori.

3.3. Periodic boundary conditions

The periodic boundary conditions are a compromise between the homogeneous traction boundary conditions and linear displacement boundary conditions in the sense that they distribute the constraints that are needed to complete the boundary value problem equally on $\boldsymbol{t}$ and $\boldsymbol{u}$. The periodic boundary conditions also result in a better convergence to the effective material behavior as the RVE size is increased, which is why they are mostly preferred to the homogeneous traction boundary conditions and the linear displacement boundary conditions. In order to apply the periodic boundary conditions, one needs to form pairs $\boldsymbol{x}_0^+$ and $\boldsymbol{x}_0^-$ of all boundary points, where

$$\boldsymbol{n}_0^+ = -\boldsymbol{n}_0^- \tag{40}$$

must hold. This can be done in a reasonable fashion if the RVE-shape allows to fill the space without gaps by a periodic arrangement of equal RVEs. For 3D problems, mostly cuboid-shaped RVE are used. Regarding the FE method, this is mostly done by a similar node arrangement on opposing surfaces of the RVE, although this restriction can be surmounted [34]. Then, by assigning opposing boundary points to pairs, and enforcing periodic boundary conditions, the principle of sections holds for the opposing RVE surfaces. For homogeneous traction boundary conditions and linear displacement boundary conditions, opposing surfaces are in force equilibrium or kinematically compatible, respectively. This renders the periodic boundary conditions most suitable for periodic microstructures, where it may be sufficient to consider only the smallest possible repeatable unit cell. Given the pairs $\boldsymbol{x}_0^{\pm}$ with $\boldsymbol{n}_0^+ = -\boldsymbol{n}_0^-$ and an imposed average displacement gradient $\dot{\overline{\boldsymbol{H}}}_{\text{impose}}$, the periodic boundary conditions are

$$\dot{\boldsymbol{u}}^+ - \dot{\boldsymbol{u}}^- = \dot{\overline{\boldsymbol{H}}}_{\text{impose}}(\boldsymbol{x}_0^+ - \boldsymbol{x}_0^-) \tag{41}$$

$$\boldsymbol{t}^+ - \boldsymbol{t}^- = \boldsymbol{0}, \tag{42}$$

which are six implicit equations for six degrees of freedom (three on the two surface points $\boldsymbol{x}^{\pm}$), necessary to complete the mixed boundary value problem. Only if $\boldsymbol{n}_0^+ = -\boldsymbol{n}_0^-$ we find that $\dot{\overline{\boldsymbol{H}}}_{\text{impose}} = \dot{\overline{\boldsymbol{H}}}$, which is needed for the verification of the Hill–Mandel-condition. $\dot{\overline{\boldsymbol{H}}}$ is given by Eq. (24). Splitting the surface integral into the minus- and plus-part and using $\boldsymbol{n}_0^+ = -\boldsymbol{n}_0^-$ gives

$$\dot{\overline{\boldsymbol{H}}} = \frac{1}{V_0}\int_{\partial\Omega_0^+} \dot{\boldsymbol{u}}^+ \otimes \boldsymbol{n}_0^+ \, \mathrm{d}A + \frac{1}{V_0}\int_{\partial\Omega_0^-} \dot{\boldsymbol{u}}^- \otimes \boldsymbol{n}_0^- \, \mathrm{d}A \tag{43}$$

$$= \frac{1}{V_0}\int_{\partial\Omega_0^+} (\dot{\boldsymbol{u}}^+ - \dot{\boldsymbol{u}}^-) \otimes \boldsymbol{n}_0^+ \, \mathrm{d}A \tag{44}$$

$$= \frac{1}{V_0}\int_{\partial\Omega_0^+} \dot{\overline{\boldsymbol{H}}}_{\text{impose}}(\boldsymbol{x}_0^+ - \boldsymbol{x}_0^-) \otimes \boldsymbol{n}_0^+ \, \mathrm{d}A \tag{45}$$

$$= \frac{1}{V_0}\dot{\overline{\boldsymbol{H}}}_{\text{impose}}\int_{\partial\Omega_0} \boldsymbol{x}_0 \otimes \boldsymbol{n}_0 \, \mathrm{d}A = \dot{\overline{\boldsymbol{H}}}_{\text{impose}}. \tag{46}$$

For the periodic boundary conditions, the Hill–Mandel-condition holds as well a priori: By subtracting Eq. (13) for the minus-side from the plus-side we obtain

$$\dot{\boldsymbol{u}}^+ - \dot{\boldsymbol{u}}^- = \dot{\overline{\boldsymbol{H}}} \cdot (\boldsymbol{x}_0^+ - \boldsymbol{x}_0^-) + \dot{\tilde{\boldsymbol{u}}}^+ - \dot{\tilde{\boldsymbol{u}}}^-. \tag{47}$$

Given that $\dot{\bar{\boldsymbol{H}}}_{\text{impose}} = \dot{\bar{\boldsymbol{H}}}$, we can use Eq. (41) to summarize to

$$\dot{\boldsymbol{u}}^{+} = \dot{\boldsymbol{u}}^{-}. \tag{48}$$

Then, together with Eq. (42), the Hill–Mandel-condition (Eq. (20)) must hold, since opposing surface points mutually cancel out their contribution to the surface integral.

4. The shape of the RVE

4.1. Non-periodic microstructures

In the case of non-periodic microstructures, the homogenized material response must be approximated by considering possibly large RVE. As the size of the RVE increases, the representativity gets better, and the surface-to-volume ratio tends to zero. Presuming that there is no softening or fracture or other localization-inducing material behavior, the influence of the boundary conditions vanishes (see Section 8).

Considering that the boundary influence is artificial, and therefore preferably small right from the start, spherical RVE appear advantageous. Compared to a cubical RVE of the same volume, one has 19.4% less surface. It is therefore to expect that the spherical RVEs perform better than cubical RVEs.

While one might accept the use of spherical RVE with uniform boundary conditions, the use of periodic boundary conditions on spherical RVE appears prohibitive at first glance. However, the application of periodic boundary conditions is advantageous due to the better convergence. Thus, the periodic boundary conditions are also applied in case of non-periodic microstructures, mostly with cuboid-shaped RVE and periodic microstructures, which motivates their name. However, this periodicity is artificial. It is in fact not necessary to insist on periodically repeatable unit cells. The periodic boundary conditions require merely that the paired surface points have opposing surface normals in the reference placement. The argument that the RVE must have a shape that allows for a complete filling of the space does not enter as an equation. It is merely used to facilitate the assignment of pairs of surface points with opposing surface normals. It is therefore possible to use the periodic boundary conditions with non-periodic volume cells like spheres or ellipsoids, as long as the assignment of pairs of surface points complies with $\boldsymbol{n}_0^{+} = -\boldsymbol{n}_0^{-}$. Of course, the term "periodic" is misleading when the periodic boundary conditions are applied to non-periodic shapes. In that case, it might be better to speak of coupled boundary conditions, although not the boundary conditions itself but the shape of the RVE differs. Thus, we continue to refer to periodic boundary conditions, even if applied to a sphere.

It is worth noting that this assignment of pairs is, in contrast to cubical RVEs, unique for spherical RVEs. However, in contrast to the periodically repeatable unit cells, the opposing surface normals $\boldsymbol{n}^{\pm}$ of arbitrarily shaped RVEs need not remain parallel during the deformation. This has, nonetheless, no effect at all for the argumentation, which is based entirely on $\boldsymbol{n}_0$.

4.2. Periodic microstructures

If the microstructure under consideration is periodic, one can construct arbitrary large material samples from an irreducible unit cell. For many cases, it is sufficient to consider a periodically repeatable unit cell with periodic boundary conditions. Only for some cases this is not sufficient, e.g., if one wants to associate structural instabilities of the RVE with material instabilities of the effective material [32]. Then, one takes a larger, periodically repeatable material section as RVE. In summary, the use of non-periodic RVE shapes is reasonable only in case of non-periodic microstructures.

5. Material and simulation setup

5.1. Material behavior of the matrix and inclusions

The material under consideration is a matrix–inclusion material. The matrix is an isotropic, linearly elastic, perfect plastic von Mises material without hardening. The inclusions with a total volume fraction of 0.3 are spherical, isotropic, linearly elastic particles of equal diameter, distributed uniformly without preferred alignment or pattern. They are considerably stiffer than the matrix material. The material parameters are collected in Table 1.

5.2. Definition of the RVE

The calculations have been carried out using the FE system ABAQUS, which has a Python interface. We created a Python script that reads an input file, from which the FE-model of the RVE is created. The input file contains information regarding the desired shape of the RVE, the material properties, the inclusion volume fraction, the boundary conditions, the element type and the average displacement gradient. The mesh has been generated such that each surface node had an antipode, in order to allow for an easy application of periodic boundary conditions. The meshing has not been adapted to the matrix-inclusion interfaces, i.e., the material assignment is not element-wise, but on the integration point level. The material assignment has been obtained by generating a large cubic sample of the material with randomly located spherical inclusions, with a total volume fraction of 0.3. The inclusions have been generated without intersections. Out of this material section we generated many RVE by randomly assigning the RVE mid-point. Consequently, no periodicity has been introduced by the inclusion distribution. From these RVE we selected the ones which best recovered the inclusion volume fraction, with a maximum absolute deviation of 0.005 from the desired 0.3. The RVE-sizes have been scaled by setting the RVE diameter (spherical RVE) or edge length (cubical RVE) to integer multiples (namely 1, 2, 3, 4, 5) of the inclusion diameter, resulting in the RVE sizes given in Table 2. We maintained a minimum elements-per-inclusion ratio of ≈270 for the purely elastic and of ≈900 for the elastoplastic simulations, using 8-node hexahedral elements with linear shape functions (C3D8) (Fig. 1). No special treatment, like the generation of a periodic microstructure, has been employed for the cubical RVE with periodic boundary conditions.

Table 1
Material parameter for the matrix and the inclusion material.

Parameter	Matrix	Inclusion
Young's modulus E in MPa	5000	50,000
Poisson's ratio ν	0.4	0.3
Flow stress σ_f in MPa	10	–
Volume fraction	0.7	0.3

Table 2
Number of configurations for the different combinations of shape, boundary conditions and size. The volumes of the cubical RVEs differ by a factor of $6/\pi$ from the corresponding spherical RVEs.

$V_{\text{RVE}}/V_{\text{inc}}$	PBC	LDBC	HTBC	$V_{\text{RVE}}/V_{\text{inc}}$	PBC	LDBC	HTBC
1.91	10	10	10	1	10	10	10
15.28	10	10	10	8	10	10	10
51.57	10	10	–	27	10	10	10
122.23	10	10	–	64	10	10	–
238.73	10	10	–	125	10	10	–
Cubical RVE				Spherical RVE			

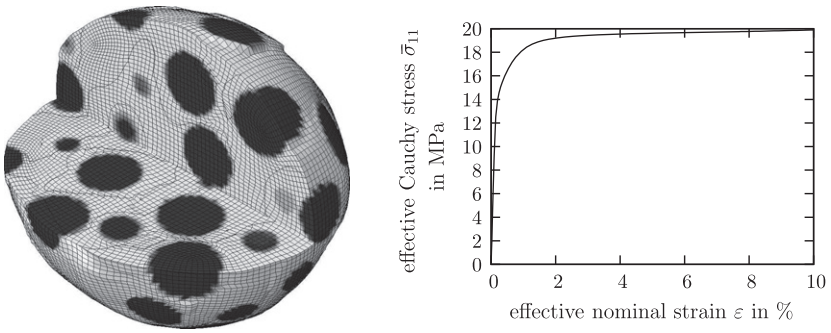

Fig. 1. Deformed spherical RVE with periodic boundary conditions (left), typical effective stress-strain curve (right).

5.3. Incorporation of boundary conditions

For the application of the boundary conditions, three nodes that are not attached to the FE mesh have been created. The nine additional displacement degrees of freedom have been assigned to the components of the average displacement gradient. Then, the boundary conditions have been incorporated by constraint equations, by which the displacement degrees of freedom of the surface nodes are coupled by the discrete versions of Eqs. (21), linear displacement boundary conditions), ((24), homogeneous traction boundary conditions) and ((41) and (42), periodic boundary conditions) to the three additional nodes.

While the linear displacement boundary conditions and the periodic boundary conditions are incorporated relatively simple, the homogeneous traction boundary conditions posed some problems. These have been implemented via the kinematic minimal boundary conditions by constraining the displacements according to the discrete version of Eq. (24). The latter equation involves weight factors that assign an area fraction to the surface nodes, which needed to be determined. This problem has been solved by carrying out a FE simulation of the homogeneous, isotropic elastic RVE, where a small volume change was imposed. The weight factors have been calculated from the absolute values of the resulting surface nodal forces. Secondly, the constraint equations require a careful implementation, due to the appearance of the same degree of freedom in more than one equation and the way that ABAQUS handles constraint equations. The first degree of freedom of an equation cannot appear in a following equation, i.e. an according ordering is necessary. Finally, the resulting constraint equations (involving all surface nodes) are very long, which results in a drastic decrease of the performance of ABAQUS. This issue is discussed elsewhere [15]. For these reasons, one might consider the implementation of homogeneous tractions via the kinematic minimal boundary conditions as unnecessary complicated. However, it is problematic to study the effect of different boundary conditions without expressing them with respect to the same independent variable, in our case $\overline{\boldsymbol{H}}$. Otherwise, one needs to identify iteratively a loading $\overline{\boldsymbol{T}}$ that yields the desired average deformation for every single boundary value problem, which results also in a drastic increase of computational effort. It should be noted that the troubles with long constraint equations are ABAQUS-specific, and efficient treatments for such special linear systems are at hand.[3]

[3] For example, the conjugate gradients method, in conjunction with a sparse matrix storage scheme that does not rely on a small bandwidth, or the substructure technique can be employed. Fritzen and Böhlke (2010), Technische Mechanik 30 (4), to be found at http://www.uni-magdeburg.de/ifme/zeitschrift_tm/2010_Heft4/05_Fritzen.html.

5.4. Extraction of the average stresses

Depending on whether one prescribes the displacements or the forces on the nine additional degrees of freedom, one can prescribe $\overline{\boldsymbol{H}}$, $\overline{\boldsymbol{T}}$ or a mixture of both, and extract the other one. For the extraction or prescription of the stresses, the reference volume of the RVE enters as a factor of proportionality.

6. Rate of convergence for spherical and cubical RVE

6.1. Simulation setup

For the study of convergence, we carried out uniaxial tension tests, in which the nominal strain ε is increased to 10%. The latter is accomplished by imposing

$$\overline{H}_{(\mathrm{uax})ij} = \begin{bmatrix} \varepsilon & 0 & 0 \\ 0 & - & 0 \\ 0 & 0 & - \end{bmatrix}. \tag{49}$$

Not prescribing $\overline{H}_{(\mathrm{uax})22}$ and $\overline{H}_{(\mathrm{uax})33}$ results in zero stress components $\overline{T}_{22}$ and $\overline{T}_{33}$. As characteristic quantities for the statistical evaluation, Young's modulus $E = \bar{\sigma}_{11}/\overline{H}_{11}$ at the onset of the deformation and the Cauchy stress $\bar{\sigma}_{11}$ at 10% of nominal strain have been extracted. Six combinations of RVE shapes and boundary conditions have been considered (cube and sphere with homogeneous traction boundary conditions, linear displacement boundary conditions and periodic boundary conditions). For any of these, at most five different RVE sizes have been taken into account. Then, 10 realizations with different inclusion distributions have been carried out for each of these combinations (see Table 2).

The homogeneous traction boundary conditions did not allow for large RVE sizes due to the inappropriate way that ABAQUS handles long constraint equations. This problem is mostly overcome by applying the homogeneous traction boundary conditions directly in terms of traction vectors, which, however, has the disadvantage that only $\overline{\boldsymbol{T}}$ can be prescribed. Also, the homogeneous traction boundary conditions allow for needle-like localizations [22], which renders them improper for simulations involving large plastic deformations. Thus, for the homogeneous traction boundary conditions, we considered only Young's modulus for small RVE sizes.

6.2. Results

In Fig. 1, a typical stress–strain curve of the macroscale material is depicted, in Fig. 2 the deformed shape with a color map of the equivalent plastic strain is depicted. One can see the onset of

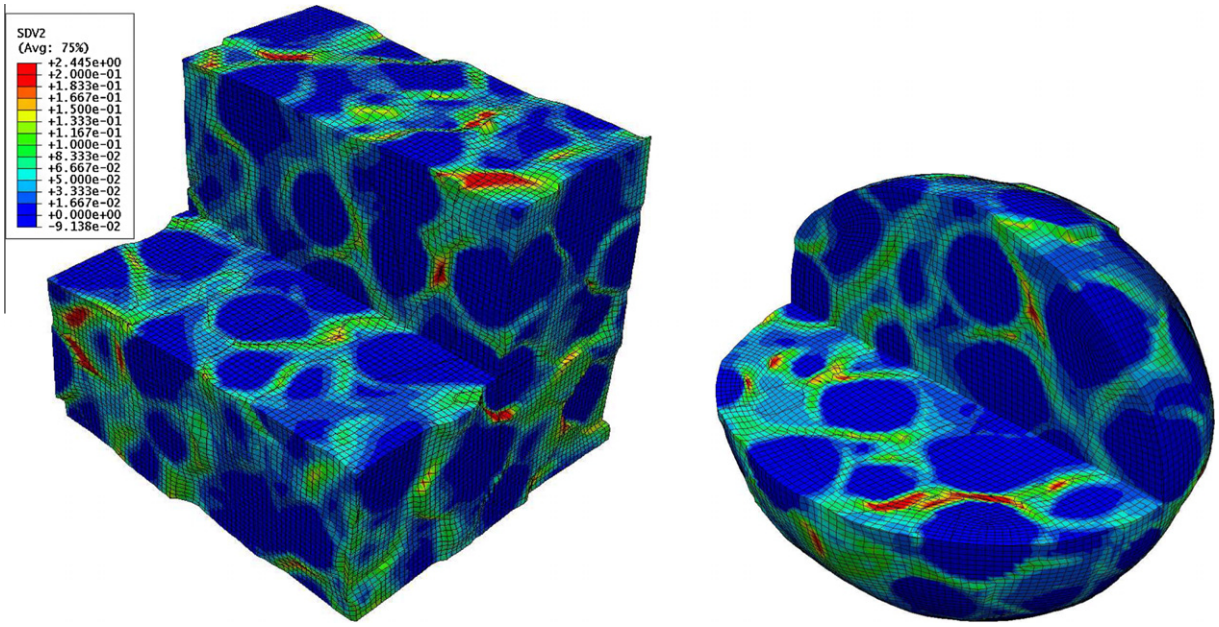

Fig. 2. Deformed cubical and spherical RVE with periodic boundary conditions ($\frac{1}{4}$ cut out). The coloring indicates the equivalent plastic strain from 0 (blue) to 0.2 (red). (For interpretation of the references to color in this figure legend, the reader is referred to the web version of this article.)

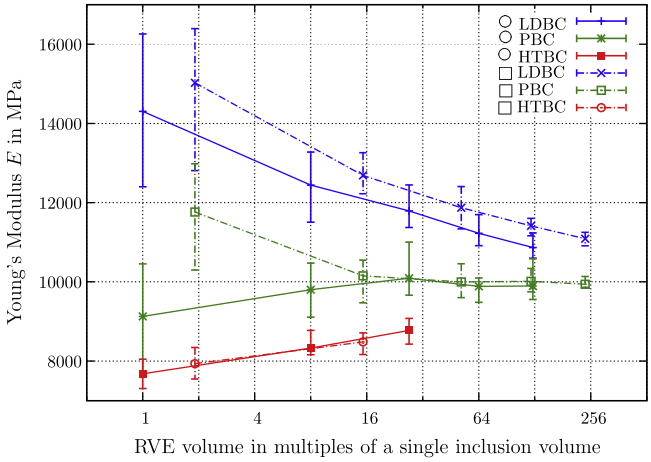

Fig. 3. Convergence of Young's modulus, ensemble min, max and average.

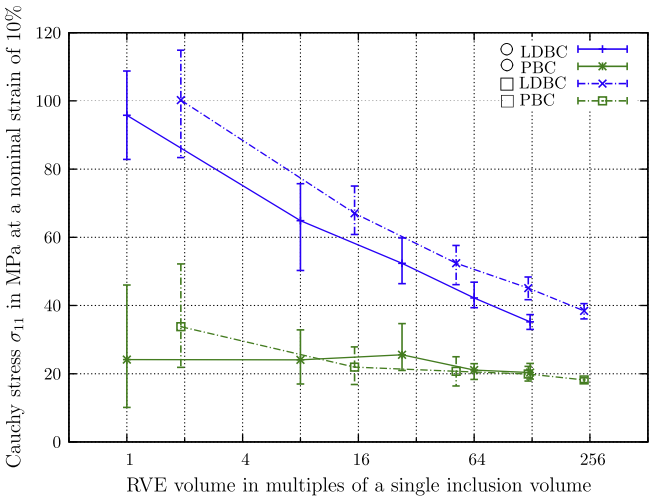

Fig. 4. Convergence of σ_{11} at 10% of nominal strain, ensemble min, max, and average.

plastic flow[4] at $\bar{\sigma}_{11} \approx 12$ MPa, followed by a short stage of effective hardening, before a value of approximately $\bar{\sigma}_{11} = 20$ MPa is approached asymptotically. Unlike the individual microscale materials, the effective material does not exhibit a sharp, but a rather smooth transition from the elastic to the plastic behavior. This is due to the inhomogeneous formation (first deviation from the linear elastic behavior) and growth (stage of effective hardening) of the plastic zones displayed in Fig. 2. The qualitative distinct behavior of the effective material is a result of the microscale-constituents interaction, see e.g. Chawla and Shen [6], who refer to the described behavior as "apparent work hardening".

The results for Young's modulus at $\varepsilon = 0$ and $\bar{\sigma}_{11}$ at $\varepsilon = 10\%$ for the different RVE sizes and boundary conditions is depicted in Figs. 3 and 4. Young's modulus tends to approximately 10 GPa, which is well inside the Reuss-Voigt (6849.3 – 18674.4 MPa) and Hashin–Shtrikman (8484.9 – 13912.1 MPa) bounds.

[4] Here, we locate the onset of effective plastic flow at $\frac{\partial \bar{\sigma}_{11}}{\partial \bar{\varepsilon}_{11}} = 0.5E$, with E being Youngs modulus.

As these figures indicate, the convergence behavior is similar both for the elastic and the plastic properties. In both cases, the results with periodic boundary conditions converge fastest, while the linear displacement boundary conditions predict a stiffer and the homogeneous traction boundary conditions a softer material behavior. Also, there is a gain in the rate of convergence for the spherical RVEs over the cubical RVEs, most notable for the linear displacement boundary conditions: to obtain similar results, one needs cubical RVEs with a volume approximately two to three times that of the corresponding spherical RVEs. This tendency is also observed for the periodic boundary conditions, though less pronounced. Interestingly, the effective Young's modulus displays no systematic difference between spherical and cubical RVE with homogeneous traction boundary conditions.

The graph given by Kanit et al. [23] (Fig. 7) displays a wider scattering compared to our findings. This is due to considering only

RVEs with inclusion volume fractions close to the macroscopic one in this work (see Section 5.2). Therefore, we have a reduced scattering in general. From that it became apparent that the homogeneous traction boundary conditions display a considerably weaker scattering for small RVE sizes than the periodic boundary conditions and linear displacement boundary conditions, independently of the shape of the RVE. For the smallest sphere we have a relative difference $(x_{\max} - x_{\min})/x_{\min}$ that is approximately three to four times smaller than for the periodic boundary conditions and linear displacement boundary conditions (0.101 (HTBC) vs 0.311 (LDBC) and 0.378 (PBC)), while for the smallest cube this difference is slightly less pronounced (0.106 (HTBC) vs 0.28 (LDBC) and 0.26 (PBC)), due to the smaller volume of the sphere.

7. Quantification of the shape-induced anisotropy

The shape-induced elastic anisotropy is determined by imposing mutually orthogonal small strains,

$$\overline{H}_{(1)ij} = \begin{bmatrix} \delta & 0 & 0 \\ 0 & 0 & 0 \\ 0 & 0 & 0 \end{bmatrix}, \quad \overline{H}_{(2)ij} = \begin{bmatrix} 0 & 0 & 0 \\ 0 & \delta & 0 \\ 0 & 0 & 0 \end{bmatrix}, \quad \overline{H}_{(3)ij} = \begin{bmatrix} 0 & 0 & 0 \\ 0 & 0 & 0 \\ 0 & 0 & \delta \end{bmatrix}, \tag{50}$$

$$\overline{H}_{(4)ij} = \begin{bmatrix} 0 & \delta & 0 \\ \delta & 0 & 0 \\ 0 & 0 & 0 \end{bmatrix}, \quad \overline{H}_{(5)ij} = \begin{bmatrix} 0 & 0 & \delta \\ 0 & 0 & 0 \\ \delta & 0 & 0 \end{bmatrix}, \quad \overline{H}_{(6)ij} = \begin{bmatrix} 0 & 0 & 0 \\ 0 & 0 & \delta \\ 0 & \delta & 0 \end{bmatrix}. \tag{51}$$

where δ is small enough to guarantee a purely elastic material response. The components of the stiffness tetrad are then obtained by

$$C_{ij11} = \bar{\sigma}_{ij}/\delta \quad \text{imposing } \boldsymbol{H}_{(1)}, \tag{52}$$
$$C_{ij22} = \bar{\sigma}_{ij}/\delta \quad \text{imposing } \boldsymbol{H}_{(2)}, \tag{53}$$
$$C_{ij33} = \bar{\sigma}_{ij}/\delta \quad \text{imposing } \boldsymbol{H}_{(3)}, \tag{54}$$
$$C_{ij12} = C_{ij21} = \bar{\sigma}_{ij}/\delta \quad \text{imposing } \boldsymbol{H}_{(4)}, \tag{55}$$
$$C_{ij13} = C_{ij31} = \bar{\sigma}_{ij}/\delta \quad \text{imposing } \boldsymbol{H}_{(5)}, \tag{56}$$
$$C_{ij23} = C_{ij32} = \bar{\sigma}_{ij}/\delta \quad \text{imposing } \boldsymbol{H}_{(6)}. \tag{57}$$

Any deviation from elastic isotropy must stem from the RVE itself, since the effective material under consideration is isotropic. We examined five RVE sizes (see Table 2), where the periodic boundary conditions have been used on spherical and cubical RVE. For each model we examined 100 different configurations of the microstructure, of which we extracted the average stiffness tetrad. The latter is weakly anisotropic. The overall anisotropy is quantified by the anisotropy measure a, given by

$$a = \|\mathbb{D} - (\mathbb{P}_1 \cdots \mathbb{D})\mathbb{P}_1 - \frac{1}{5}(\mathbb{P}_2 \cdots \mathbb{D})\mathbb{P}_2\| \tag{58}$$

$$\mathbb{D} = \frac{\ln(\det(\mathbb{C})^{-\frac{1}{6}}\mathbb{C})}{\|\ln(\det(\mathbb{C})^{-\frac{1}{6}}\mathbb{C})\|}, \tag{59}$$

with the first and second isotropic projectors $\mathbb{P}_1 = \frac{1}{3}\boldsymbol{I} \otimes \boldsymbol{I}$ and $\mathbb{P}_2 = \mathbb{I} - \mathbb{P}_1$. The factor 1/5 must be introduced to normalize $\mathbb{P}_2$. In the following, we restrict to symmetric fourth order tensors that map symmetric second order tensors into symmetric second order tensors. By this, we can extend the eigenvalue problem to this tensor space and define the inverse of $\mathbb{C}$ by restricting to positive definite tensors $\mathbb{C}$. The function $a(\mathbb{C})$ is constructed such that

$$a(\mathbb{C}) = a(\alpha\mathbb{C}), \quad \alpha \in \mathbb{R}, \quad \alpha > 0 \tag{60}$$
$$a(\mathbb{C}) = a(\mathbb{C}^{-1}) \tag{61}$$

hold, in order to make a independent of whether the anisotropy of the stiffness $\mathbb{C}$ or the compliance $\mathbb{C}^{-1}$ is evaluated, and to make a independent on the absolute values of the stiffness or compliance. The properties of $a(\mathbb{C})$ are examined in the Appendix. Likewise, we can filter out the cubic anisotropy by

$$a_c = \|\mathbb{D} - (\mathbb{P}_1 \cdots \mathbb{D})\mathbb{P}_1 - \frac{1}{2}(\mathbb{P}_{c2} \cdots \mathbb{D})\mathbb{P}_{c2} - \frac{1}{3}(\mathbb{P}_{c3} \cdots \mathbb{D})\mathbb{P}_{c3}\|, \tag{62}$$

with the cubic eigenprojectors $\mathbb{P}_{c2} = \mathbb{I} - \mathbb{P}_1 - \mathbb{P}_{c3}$ and $\mathbb{P}_{c3} = \sum_{i=1}^{3} \boldsymbol{d}_i \otimes \boldsymbol{d}_i \otimes \boldsymbol{d}_i \otimes \boldsymbol{d}_i$, where $\boldsymbol{d}_i$ is an orthonormal basis that coincides with the cubic anisotropy axes. Here, we presumed that $\boldsymbol{d}_i$ coincides with the edges of the cubical RVEs. Note that $a_c \leqslant a$ holds. Commonly, the cubic anisotropy is quantified by the Zener ratio [48],

$$Z = \frac{2C_{ijij}}{(C_{iiii} - C_{iijj})}, \tag{63}$$

presuming that the components of $\mathbb{C}$ are given with respect to $\boldsymbol{d}_i$. Then, the eigenvalues of a cubic stiffness tetrad are given by $\lambda_1 = C_{1111} + 2C_{1122}$, $\lambda_2 = C_{1111} - C_{1122}$ and $\lambda_3 = 2C_{1212}$ [3]. Thus, one can identify $Z = \lambda_3/\lambda_2$.

Comparing a and a_c, which differ only by the cubic part of the anisotropy that has been removed in a_c, shows that the anisotropy of the cubical RVE is indeed mostly cubic (Fig. 5), with $a/a_c \approx 5 - 10$. The largest anisotropy is encountered for the smallest cubical RVE with periodic boundary conditions, with $a = 0.198$, $a_c = 0.019$ and $Z = 0.765$. For the spherical RVE with periodic boundary conditions, a and a_c do not differ significantly. Comparing a and a_c between cube and sphere, we find a_c in both cases fall-

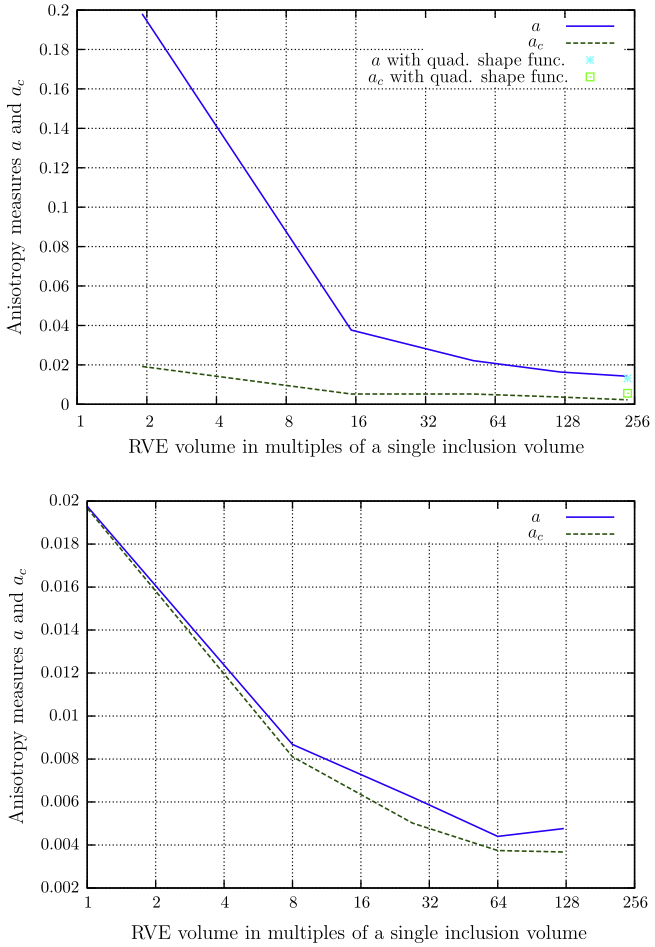

Fig. 5. Anisotropy measures a (filtering out isotropy) and a_c (filtering out cubic anisotropy) for the cubical (upper figure) and the spherical RVE (lower figure).

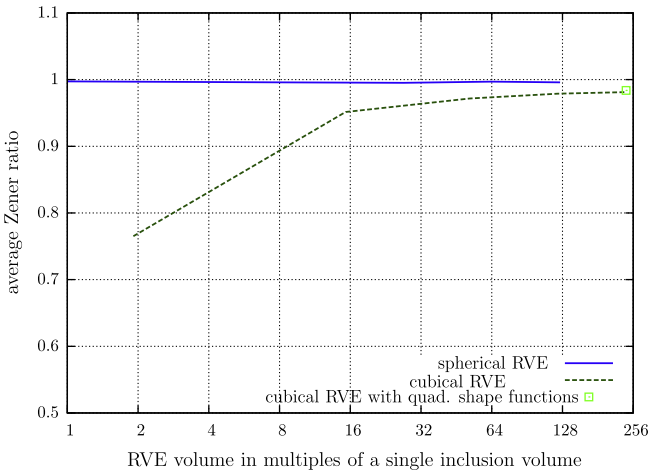

Fig. 6. Zener ratio for spherical and cubical RVE with periodic boundary conditions.

ing from approximately 0.02 for the smallest RVE to approximately 0.005 for the largest RVE. For a, we observe basically the same in case of the sphere, while a starts of at approximately 0.2 for the cubical RVE.

We assessed the influence of the shape functions on the results by repeating the largest RVE calculation with a quadratic hexahedral mesh (Figs. 5 and 6). A slight improvement with respect to the anisotropy has been observed. However, the smallness of the change indicates that the discretization that has been used is sufficient, i.e., the main result is unaffected.

8. Localization behavior

In case of non-quasi-convex incremental stress potentials, structural failure of the RVE may occur. For periodic microstructures, a framework for relating the structural failure of an RVE to a material instability on the macroscale is at hand [32]. For non-periodic microstructures, this issue is still not clear. The reason therefor is twofold:

- While linear displacement boundary conditions prevent localizations to reach the boundary, homogeneous traction boundary conditions allow for an arbitrary deformation of the boundary of the RVE. The periodic boundary conditions, applied to periodically repeatable unit cells, allow for a localization pattern that fits the periodicity frame. Thus, the RVE localization depends on the arbitrary orientation of the periodicity frame. The apparent material should, however, be attained independently on these choices as the size of the RVE is increased.
- As a RVE-wide localization takes place, the representativity of the RVE is lost.

Despite this problems, predictions of macroscopic fracture [1,39], macroscale traction separation laws [35] and forming limit diagrams [21] are obtained by the RVE method, mostly by using cubical RVE with periodic boundary conditions. While most authors demonstrate convergence by considering larger RVE, it is not shown whether the results are sensitive to changes of the RVE shape, the boundary conditions and, in case of periodic boundary conditions, the orientation of the periodicity frame. Just recently, the development of numerical homogenization schemes that overcome the dependence on the orientation of the periodicity frame is approached by Coenen et al. [7], Nguyen et al. [36], who adapt the boundary conditions during the simulation to the specific localization pattern that is encountered. These are termed by Coenen et al. [7] as percolation path boundary conditions.

Since the periodic boundary conditions enjoy some popularity for the prediction of macroscale material failure, this section is dedicated to the study of the localization behavior of spherical and cubical RVE with periodic boundary conditions.

8.1. Simulation setup and material parameters

We start by considering a simple shear deformation with a shear number $\bar{\gamma} = 1$,

$$\overline{\boldsymbol{H}} = \boldsymbol{d} \otimes \boldsymbol{n}, \tag{64}$$

$$\boldsymbol{d} = \cos\alpha \boldsymbol{e}_1 + \sin\alpha \boldsymbol{e}_2, \tag{65}$$

$$\boldsymbol{n} = -\sin\alpha \boldsymbol{e}_1 + \cos\alpha \boldsymbol{e}_2. \tag{66}$$

We applied $\overline{\boldsymbol{H}}$ with $\bar{\gamma}$ growing time-proportional from 0 to 1, with α between 0° and 45°, in steps of 5°, to cubical and spherical RVE with periodic boundary conditions. The material under consideration was the ABAQUS internal, elastic isotropic (E = 5000 MPa, ν = 0.3), von Mises plastic material with σ_{flow} initially at 10 MPa, decaying linearly to 5 MPa at 100% of plastic strain. Beyond 100% of plastic strain, σ_{flow} is constant. The mesh resolution was 20 elements along

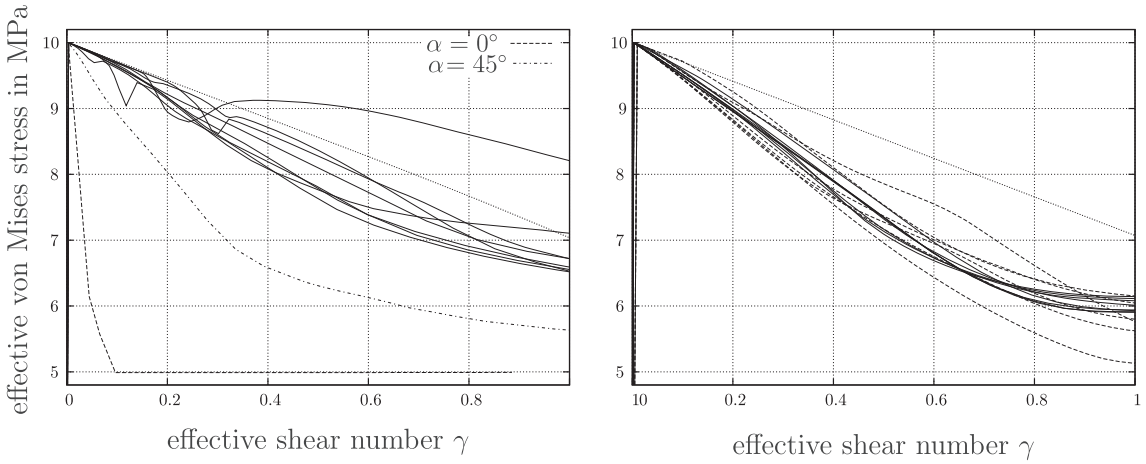

Fig. 7. Von Mises equivalent stress for the shear test in the cubical (left) and spherical (right) RVE with periodic boundary conditions. In the left figure, the dashed lines correspond to the shear directions 0° and 45°. In the right figure, the solid and dashed lines correspond to the cases where the lamination is parallel (eight curves) and perpendicular (six curves) to the effective shear direction, respectively. The dotted lines correspond to the homogeneous deformation of the RVE, enforced by linear displacement boundary conditions.

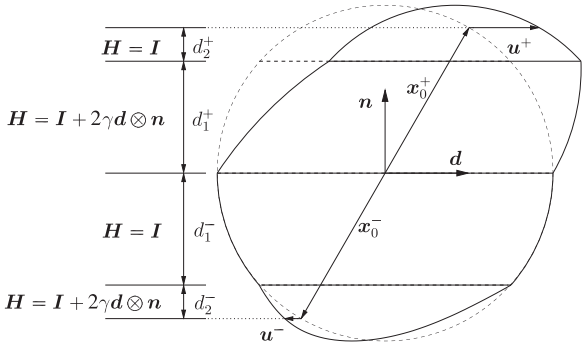

Fig. 8. Schematic figure of a layer decomposition of a spherical RVE, with homogeneously deformed layers.

one edge for the cubical and 20 elements along the diameter for the spherical RVE. We used hexahedral elements with quadratic shape functions (element type C3D20), in order to reduce tendency of a mesh-conform alignment of the shear bands. For a controlled initiation of the localization, in one element the flow stress has been reduced 9 MPa, which has been selected randomly from the list of elements. If the simulations are carried out without perturbing the homogeneous material, the localization is initiated by unavoidable numerical errors.

8.2. Results

The resulting effective equivalent von Mises stress is given in Fig. 7. While the spherical RVEs display only a slight variation, in case of the cubical RVEs a wide variation of the stress–strain curve is observed. The reason therefor is that the localization behavior differs markedly for cubical and spherical RVE.

8.2.1. Behavior of the spherical RVEs

We observed two distinct deformation patterns. These have in common that the sphere is divided into an even number of layers (mostly four layers, at most we observed eight layers). From the resulting odd number of parallel interfaces, one coincides with an equatorial plane, dividing the sphere into two hemispheres. The remaining interfaces are placed symmetrically in the two hemispheres. The layer decomposition takes place either parallel or perpendicular to the effective shear plane $\boldsymbol{n}$. In both cases, the layers alternate between almost undeformed and strongly deformed.

8.2.1.1. Lamination parallel to the effective shear plane. In case of a lamination parallel to the effective shear direction, the deforming layers display an almost homogeneous shearing near the layer interface and the RVE surface, with $\overline{\boldsymbol{H}} = 2\bar{\gamma}\boldsymbol{d}\otimes\boldsymbol{n}$. In the bulk of the layers, a further layer decomposition is observed, see Fig. 9. A sketch with four layers is given in Fig. 8, with the layer thicknesses $d_2^+ = d_2^-$ and $d_1^+ = d_1^-$ and the shear deformation in the first layer on the plus and the second layer on the minus side. One can easily see, by picking two opposing surface points $\boldsymbol{x}_0^\pm$ and calculating the displacements $\boldsymbol{u}^\pm$, that this results in the imposed average deformation and compliance with the periodic boundary conditions,

$$\boldsymbol{u}^+ - \boldsymbol{u}^- = f^+ 2\bar{\gamma}\boldsymbol{d}\otimes\boldsymbol{n}\cdot\boldsymbol{x}_0^+ - f^- 2\bar{\gamma}\boldsymbol{d}\otimes\boldsymbol{n}\cdot\boldsymbol{x}_0^-. \tag{67}$$

The factors $f^\pm$ give fractions of the projected length $(\boldsymbol{n}\cdot\boldsymbol{x}_0)\boldsymbol{n}$ that passes layers that are subjected to the displacement gradient $2\bar{\gamma}\boldsymbol{d}\otimes\boldsymbol{n}$. Due to the described arrangement of the layers we have $f^- = 1 - f^+$. Summarizing with $\boldsymbol{x}_0^- = -\boldsymbol{x}_0^+$ gives

$$\begin{aligned}\boldsymbol{u}^+ - \boldsymbol{u}^- &= f^+ 2\bar{\gamma}\boldsymbol{d}\otimes\boldsymbol{n}\cdot\boldsymbol{x}_0^+ + (1-f^+)2\bar{\gamma}\boldsymbol{d}\otimes\boldsymbol{n}\cdot\boldsymbol{x}_0^+ &(68)\\ &= 2\bar{\gamma}\boldsymbol{d}\otimes\boldsymbol{n}\cdot\boldsymbol{x}_0^+ &(69)\\ &= \bar{\gamma}\boldsymbol{d}\otimes\boldsymbol{n}\cdot\left(\boldsymbol{x}_0^+ - \boldsymbol{x}_0^-\right) = \bar{\boldsymbol{H}}\left(\boldsymbol{x}_0^+ - \boldsymbol{x}_0^-\right). &(70)\end{aligned}$$

8.2.1.2. Lamination perpendicular to the effective shear plane. The overall behavior is quite similar compared to the first case. However, the deformation near the layer interfaces and the RVE surface is less homogeneous. Also, the interfaces undergo a more pronounced bending. Fig. 11 allows for a direct comparison of the two deformation patterns. We did not observe any localization that does not fit into one of these schemes. A variation of the magnitude and the location of the perturbation did not have any notable effect on the effective material behavior. Also, no regularity could be found in which of the two described localization schemes is activated.

8.2.2. Behavior of the cubical RVEs

One can find a large number of cubical RVE with periodic boundary conditions undergoing localization in the literature, e.g., Miehe [30], Böhlke et al. [4], Nguyen et al. [35]. At the onset of localization, we observed the formation of a single shear band of constant thickness, the deformation of which growing time-proportional. However, the shear band has to fit the periodicity frame, and is therefore not necessarily parallel to the imposed effective shear direction. Thus, the effective shear strain is approximated by a shifting between differently oriented shear bands (Fig. 10). The change of the active shear band is accompanied by a stiffening

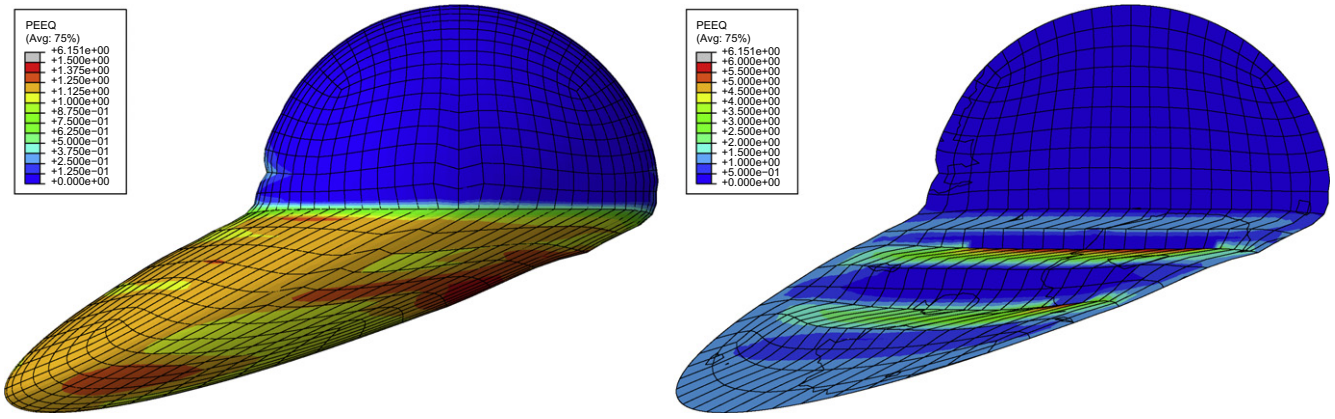

Fig. 9. Localization of the spherical RVE with lamination parallel to the effective shear direction ($\alpha = 0°$) at $\bar{\gamma} = 1$. The color map indicates the equivalent plastic strain between 0 and 1.5 on the left (surface) and 0 and 6 on the right (cut). (For interpretation of the references to color in this figure legend, the reader is referred to the web version of this article.)

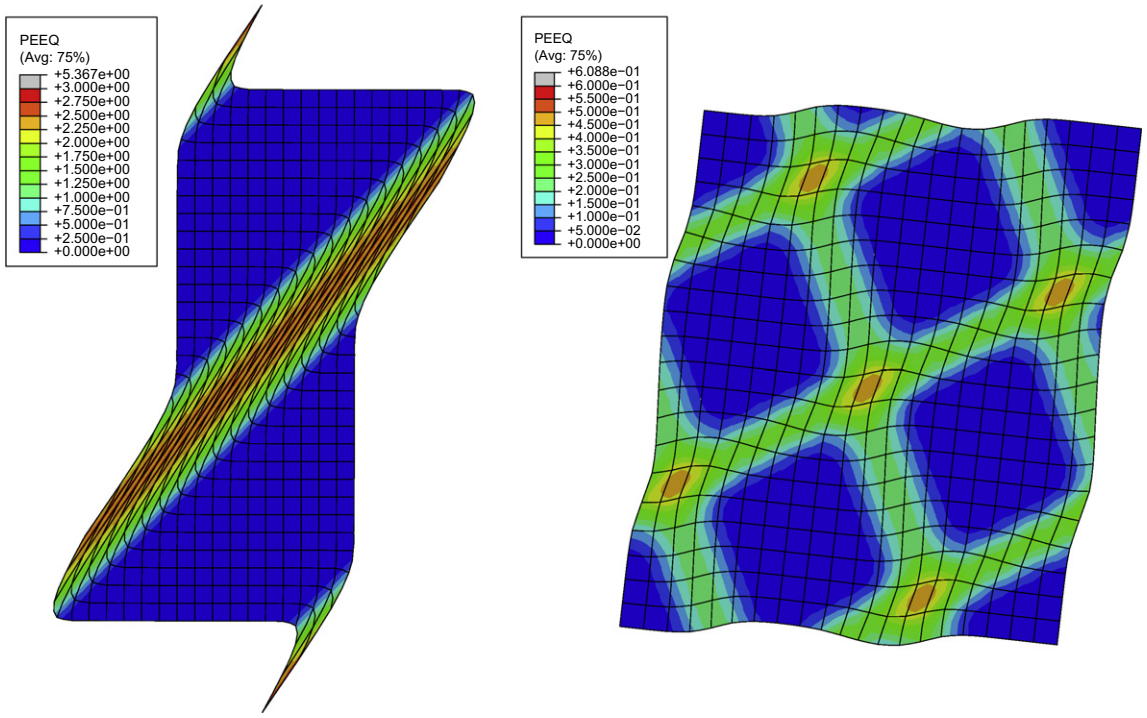

Fig. 10. Localization of the cubical RVE. The color map indicates the equivalent plastic strain. Left: $\bar{\gamma} = 1,\ \alpha = 45^\circ,\ 0 < \varepsilon_{\mathrm{PEEQ}} < 3$. Right: $\bar{\gamma} = 0.216,\ \alpha = 25^\circ,\ 0 < \varepsilon_{\mathrm{PEEQ}} < 0.5$. (For interpretation of the references to color in this figure legend, the reader is referred to the web version of this article.)

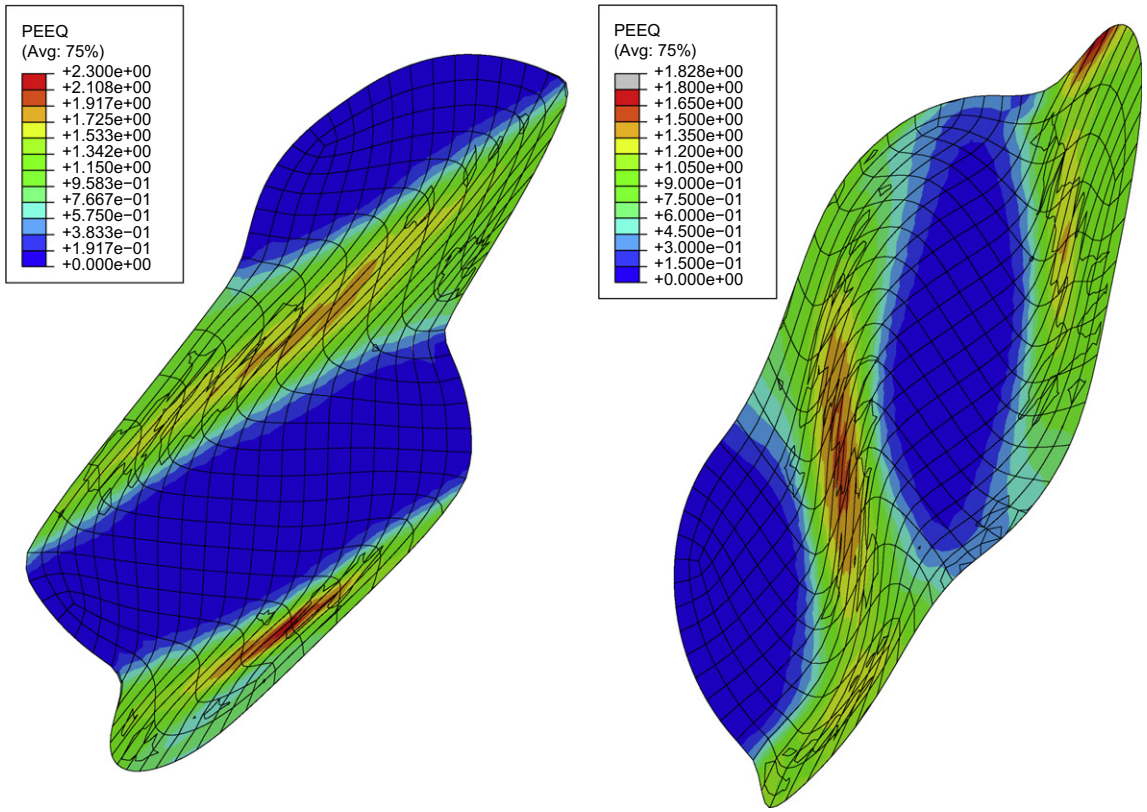

Fig. 11. Cut through localization of the spherical RVE for $\alpha = 30^\circ$ and $\bar{\gamma} = 1$. The color map indicates the equivalent plastic strain, $0 < \varepsilon_{\mathrm{PEEQ}} < 2.3$ on the left and $0 < \varepsilon_{\mathrm{PEEQ}} < 1.8$ on the right. On the left, the lamination is parallel to the effective shear plane, on the right lamination started perpendicular to the effective shear plane, but during the deformation the shear direction changes locally. (For interpretation of the references to color in this figure legend, the reader is referred to the web version of this article.)

effect, which induced the spikes in the stress–strain curves (Fig. 7). The stiffening due to the successive shearing in two different directions exceeds even the response of the homogeneous material. Only in the cases $\alpha = 0°$ and $\alpha = 45°$, a single shear band persisted. Accordingly, the stress–strain curves indicate the softest effective material for this two cases. This is most pronounced for the case $\alpha = 0°$, where the shear band alignment parallel to the mesh interface results in a concentration of the shear band in a single element layer. A variation of the position of the perturbation does not have any effect in case of the cubical RVE, it corresponds to a mere shift of the periodicity frame. Likewise, the magnitude of the perturbation has no notable influence.

8.2.3. Discussion of the localization behavior

It is evident that the orientation of the periodicity frame strongly affects the results in case of the cubical RVE, inducing a scattering of the effective stress strain curve. This is not observed in case of spherical RVE. However, the applicability of the periodic boundary conditions is disputable in both cases. In both cases, even if the perturbation is left out, localization is observed, triggered by numerical round off errors, i.e., stability of the effective material response with respect to small perturbations is not attained. Thus, with the dictum that an RVE should conduct the microscale material behavior "as is" to the macroscale when the material is homogeneous, neither the cubic nor the spherical RVE with periodic boundary conditions give satisfactory results for the softening material. Only the linear displacement boundary conditions satisfy the latter requirement. Then, no difference between cubical and spherical RVE is observed.

9. Summary

We compared the performance of spherical and cubical RVE with different boundary conditions, applied to a macroscopically isotropic matrix–inclusion material with hard elastic inclusions and a soft elastoplastic matrix. It is argued that the periodic boundary conditions are not restricted to periodically repeatable unit cells, although the denomination "periodic" is misleading when applied to non-periodic shapes. Then one should speak more generally of coupled boundary conditions.

We could identify basically two features that distinguish the spherical and the cubical RVE, namely different surface to volume ratio and, in case of periodic boundary conditions, the presence or absence of a periodicity frame. The smaller surface to volume ratio of the spheres result in a smaller influence of the boundary, leading to a better convergence to the effective material behavior. The presence of a periodicity frame in case of the cubical RVE results in a bias of the material anisotropy, which affects the elastic and plastic material properties. To study the convergence and RVE induced anisotropy, we considered macroscopically isotropic matrix-inclusion material.

Considering the rate of convergence to the effective material behavior, for linear displacement boundary conditions, results of similar quality require the cubical RVE to have a volume approximately two to three times that the corresponding spherical RVE. This applies to the elastic and the plastic properties, over the entire range of sizes that has been considered. This behavior is less pronounced for the periodic boundary conditions. It is a result of the smaller surface-to-volume ratio of a sphere compared to a cube of equal volume. For the homogeneous traction boundary conditions, only the elastic properties have been considered, which display almost no difference between spherical and cubical RVE. A comprehensive analysis of the scattering in case of spherical and cubical RVE cannot be delivered, since this requires a much larger amount of data. It is only noted that no clear tendency in favor or against one of the RVE shapes is observed, and that the homogeneous traction boundary conditions appear to result in a reduced scattering of the elastic properties.

Examining the elastic properties of the isotropic macroscale material allows to quantify the spurious cubic anisotropy induced by cubical RVE with periodic boundary conditions. This artificial anisotropy vanishes as the size of the RVE tends to infinity. However, we found that the convergence is quite slow, requiring large RVE. Thus, the cubical shape affects the smallest RVE size which one may consider as sufficiently large to perform sample averaging. If the RVE size is to small, a systematic bias of the anisotropy is induced, which cannot be separated from the effective material properties. This issue can be avoided a priori by using spherical RVE. Other strategies to reduce this effect could be the examination of randomly oriented cubical RVE, where the cubic anisotropy should cancel out in the average, or the application of uniform boundary conditions, which converge slower to the effective material behavior.

Since cubical RVE with periodic boundary conditions that undergo structural failure are commonly used for the prediction of effective material failure and softening, we studied the localization behavior of spherical and cubical RVE with periodic (resp. coupled) boundary conditions. We employed these on a homogeneous, isotropic, softening, elastoplastic material with a small perturbation. It is found that the response of the cubical RVEs depends strongly on the orientation of the periodicity frame. The dependence on the magnitude and position of the perturbation is rather weak. This specific bias is not observed for the spherical RVE, due to the missing periodicity frame. However, the applicability of periodic boundary conditions appears problematic in both cases, since only for linear displacement boundary conditions the material behavior of the quasi homogeneous RVE is conducted "as is" to the macroscale.

In conclusion, the use of spherical RVE is advantageous in case of a random microstructure. For regular microstructures, RVEs that account for the periodicity of the microstructure suit better. In case of localization, the use of spherical instead of cubical RVEs with periodic boundary conditions eliminates the periodicity frame that restricts the localization mode, similarly to the technique proposed by Coenen et al. [7]. However, the use of RVEs that undergo localization for the prediction of effective material failure remains doubtful.

Acknowledgements

We gratefully acknowledge valuable remarks from Jan Kalisch, Felix Fritzen and Thomas Böhlke. Also, we like to express our gratitude to an unknown reviewer for his/her comments.

Appendix A

The requirements (60) and (61) are basically taken care of by mapping $\mathbb{C}$ to $\mathbb{D}$ (Eq. (59)), where only $\mathbb{D}(\mathbb{C}) = -\mathbb{D}(\mathbb{C}^{-1})$ prevents the fulfillment of Eq. (61). However, the minus is taken care of by $a(\mathbb{D}) = a(-\mathbb{D})$ (Eq. (58)).

Specifically, the first mapping to the unimodular part $\mathbb{C}^\circ = \det(\mathbb{C})^{-\frac{1}{6}}\mathbb{C}$ ensures the invariance $a(\mathbb{C}) = a(\alpha\mathbb{C})$. The logarithm $\mathbb{C}^* = \ln \mathbb{C}^\circ$ ensures that inverting $\mathbb{C}$ results merely in a change of sign of the eigenvalues of $\mathbb{C}^*$. Then normalizing $\mathbb{C}^*$ gives $\mathbb{D}$. Due to this normalization, the measure a has the nice property of ranging from 0 (isotropy) to 1 (most anisotropic). This can be seen by noting that

$$\|\mathbb{D} - (\mathbb{P}_1 \cdots \mathbb{D})\mathbb{P}_1 - \frac{1}{5}(\mathbb{P}_2 \cdots \mathbb{D})\mathbb{P}_2\| < 1, \tag{71}$$

since subtracting a projection of a tensor from the tensor itself must result in a tensor with equal or lower norm. One can see that the isotropic part $(\mathbb{P}_1 \cdot\cdot\cdot\cdot \mathbb{D})\mathbb{P}_1 + \frac{1}{5}(\mathbb{P}_2 \cdot\cdot\cdot\cdot \mathbb{D})\mathbb{P}_2$ can indeed be zero: $\mathbb{D} = \sum d_i \mathbb{E}_i$ is traceless due to the logarithm on the unimodular $\mathbb{C}^\circ$, i.e. the eigenvalues d_i sum up to zero. Thus, with the abbreviations

$$\alpha_1 = \mathbb{P}_1 \cdot\cdot\cdot\cdot \mathbb{D} = \sum d_i p_i, \quad p_i = \mathbb{E}_i \cdot\cdot\cdot\cdot \mathbb{P}_1 \tag{72}$$

$$\alpha_2 = \mathbb{P}_2 \cdot\cdot\cdot\cdot \mathbb{D} = \sum d_i (1 - p_i) \tag{73}$$

we have $\alpha_1 + \alpha_2 = \sum d_i = 0$, i.e. if α_1 vanishes the isotropic part of $\mathbb{D}$ is zero. With the restrictions $\mathbb{I} \cdot\cdot\cdot\cdot \mathbb{P}_1 = 1 = \sum p_i$ and all $p_i > 0$ one can find arbitrary many eigenprojectors $\mathbb{E}_i$ such that α_1 vanishes, for example all $p_i = 1/6$.

References

[1] H.Y. Agha, F. Hild, R. Billardon, Microscopic and mesoscopic damage localization, ASTM Special Technical Publication 1315 (1997) 119–130.
[2] A. Bertram, Elasticity and Plasticity of Large Deformations – An Introduction, third ed., Springer Verlag, Berlin, 2012.
[3] T. Böhlke, Crystallographic Texture Evolution and Elastic Anisotropy – Simulation, Modeling and Applications, Shaker Verlag, 2001.
[4] T. Böhlke, G. Bondár, Y. Estrin, M. Lebyodkin, Computational Materials Science 44 (2009) 1076–1088.
[5] T. Böhlke, R. Glüge, B. Klöden, W. Skrotzki, A. Bertram, Modelling and Simulation in Materials Science and Engineering 15 (2007) 619–637.
[6] N. Chawla, Y.-L. Shen, Advanced Engineering Materials 3 (6) (2001) 357–370.
[7] E.W.C. Coenen, V.G. Kouznetsova, M.G.D. Geers, International Journal for Numerical Methods in Engineering 90 (2012) 1–21.
[8] D. Durdban, T. Cohen, Y. Hollander, Mechanics Research Communications 37 (2010) 636–641.
[9] F. Feyel, J.-L. Chaboche, Computer Methods in Applied Mechanics and Engineering 183 (2000) 309–330.
[10] J. Fish, R. Fan, International Journal for Numerical Methods in Engineering 76 (2008) 1044–1064.
[11] F. Fritzen, T. Böhlke, Technische Mechanik 30 (4) (2010) 354–363.
[12] F. Fritzen, T. Böhlke, International Journal for Numerical Methods in Engineering 84 (2010) 803–829.
[13] F. Fritzen, S. Forest, T. Böhlke, D. Kondo, T. Kanit, International Journal of Plasticity 29 (0) (2012) 102–119.
[14] M. Galli, J. Botsis, J. Janczak-Rusch, Computational Materials Science 41 (3) (2008) 312–321.
[15] R. Glüge, Revista chilena de ingeniería 18 (2010) 395–400.
[16] R. Grasset-Bourdel, A. Alzina, N. Tessier-Doyen, N. Schmitt, M. Huger, T. Chotard, Computational Materials Science 50 (2011) 3136–3144.
[17] A. Gurson, Journal of Engineering Materials and Technology 99 (1977) 2–15.
[18] Z. Hashin, Journal of Applied Mechanics 50 (1983) 481–505.
[19] S. Hazanov, C. Huet, Journal of the Mechanics and Physics of Solids 42 (12) (1994) 1995–2011.
[20] R. Hill, Proceedings of the Royal Society of London A 65 (1952) 349–354.
[21] M.F. Horstemeyer, V. Revelli, Stress history dependent localization and failure using continuum damage mechanics concepts, ASTM Special Technical Publication 1315 (1997) 216–237.
[22] H. Inglis, P. Geubelle, K. Matous, Philosophical Magazine 88 (16) (2008) 2373–2397.
[23] T. Kanit, S. Forest, I. Galliet, V. Mounoury, D. Jeulin, International Journal of Solids and Structures 40 (2003) 3647–3679.
[24] Z. Khisaeva, M. Ostoja-Starzewski, Proceedings of the Royal Society of London A 462 (2006) 1167–1180.
[25] S.-J. Kim, J. Choi, M.K. Kwak, Computational Mechanics 31 (2003) 469–478.
[26] B. Klusemann, B. Svendsen, Technische Mechanik 30 (4) (2010) 374–386.
[27] A. Krawietz, Materialtheorie, Springer Verlag, Berlin, 1986.
[28] S. Mesarovic, J. Padbidri, Philosophical Magazine 85 (2005) 65–78.
[29] J. Michel, P. Suquet, International Journal of Solids and Structures 40 (2003) 6937–6955.
[30] C. Miehe, International Journal for Numerical Methods in Engineering 55 (2002) 1285–1322.
[31] C. Miehe, Computer Methods in Applied Mechanics and Engineering 192 (2003) 559–591.
[32] C. Miehe, J. Schröder, M. Becker, Computer Methods in Applied Mechanics and Engineering 191 (2002) 4971–5005.
[33] S. Nemat-Nasser, Mechanics of Materials 31 (1999) 493–523.
[34] V.-D. Nguyen, E. Béchet, C. Geuzaine, L. Noels, Computational Materials Science 55 (0) (2012) 390–406.
[35] V.P. Nguyen, O. Lloberas-Valls, M. Stroeven, L. Sluys, Computer Methods in Applied Mechanics and Engineering 200 (9–12) (2011) 1220–1236.
[36] V.P. Nguyen, M. Stroeven, L.J. Sluys, Engineering Fracture Mechanics 79 (2012) 78–102.
[37] M. Ortiz, E. Repetto, Journal of the Mechanics and Physics of Solids 47 (1999) 397–462.
[38] I. Özdemir, W. Brekelmans, M. Geers, Computer Methods in Applied Mechanics and Engineering 198 (2008) 602–613.
[39] C. Pelissou, J. Baccou, Y. Monrie, F. Perales, International Journal of Solids and Structures 46 (2009) 2842–2855.
[40] K. Rajagopal, Zeitschrift für angewandte Mathematik und Physik ZAMP 58 (2) (2007) 309–317.
[41] A. Salahouelhadj, H. Haddadi, Computational Materials Science 48 (3) (2010) 447–455.
[42] J. Schröder, D. Balzani, D. Brands, Archive of Applied Mechanics 81 (2011) 975–997.
[43] L. Shen, S. Yi , International Journal of Solids and Structures 37 (2000). 3525–3534.
[44] R. Smit, W. Brekelmans, H. Meijer, Computer Methods in Applied Mechanics and Engineering 155 (1998) 181–192.
[45] P. Suquet, Homogenization techniques for composite media, in: Lectures Delivered at the CISM International Center for Mechanical Sciences Udine, Italy, July 1–5, 1985, Lecture Notes in Physics, vol. 272, Springer-Verlag, Berlin, 1987, pp. 199–208 (Ch. Averages, Boundary condition).
[46] B. Svendsen, A. Bertram, Acta Mechanica 132 (0) (1999) 195–207.
[47] X. Xu, X. Chen, Mechanics of Materials 41 (2009) 174–186.
[48] C. Zener, Physical Review 71 (12) (1947) 846–851.
[49] T. Zohdi, P. Wriggers, Introduction to Computational Micromechanics, Lecture Notes in Applied and Computational Mechanics, Springer, 2005.

In R. Glüge und M. Weber (2013). **Numerical properties of spherical and cubical representative volume elements with different boundary conditions**. In: *Technische Mechanik*, S. 97–103 wurde der Einfluss der geometrischen Form von RVE in Kombination mit verschiedenen Randbedingungen auf die numerischen Eigenschaften des mit der Finite-Elemente-Methode gelösten Randwertproblems untersucht. Es wurde festgestellt, dass

- die kugelförmigen RVE nicht nur bezogen auf das RVE-Volumen schneller gegen das effektive Materialverhalten konvergieren, sondern auch aufgrund der Reduktion numerisch ungünstiger Knotenkopplungen bessere numerische Eigenschaften, nämlich eine kleinere Bandweite der globalen Steifigkeitsmatrix, aufweisen,
- dieser Vorteil allerdings durch die im Gegensatz zum würfelförmigen RVE irregulären Vernetzung des kugelförmigen RVE teilweise aufgehoben wird.

TECHNISCHE MECHANIK, 33, 2, (2013), 97 – 103
submitted: December 11, 2012

Numerical Properties of Spherical and Cubical Representative Volume Elements with Different Boundary Conditions

R. Glüge, M. Weber

It has been found that, due to the smaller surface to volume ratio, the spherical representative volume elements (RVE) converge faster to the effective properties than cubical RVEs, in terms of the RVE volume (Glüge et al., 2012). It remains to discuss whether one can actually draw a numerical advantage from this in the finite element calculations, since there are also some drawbacks, for example the necessarily irregular meshing. It has been demonstrated that the boundary conditions, in conjunction with different solution strategies for the linear system that emerges in the FEM, can significantly influence the numerical expense (Fritzen and Böhlke, 2010a). In the light of these results, we examine the numerical properties of spherical and cubical RVEs with linear displacement and periodic (resp. antipodic) boundary conditions.

1 Introduction

The industry requires an ever increasing quality and precision of forming process simulations, while keeping expenses preferably low. This has lead to the incorporation of the microstructural properties like texture and grain structure into material models. Unfortunately, the analytical determination of effective properties from the lower-scale structure (homogenization) is restricted to quite elementary problems. Thus, there is a demand for efficient numerical schemes for the determination of effective properties from representative material samples. In many cases, the representative volume element (RVE) method is used, where a (nearly) representative volume element is subjected to some process, and effective material properties are extracted by averaging. The resulting boundary value problem is mostly tackled by the finite element method (FEM). Then, one can use a set of RVE-results as input for the adaption of an effective material law, e.g., with the nonuniform transformation field analysis (Fritzen and Böhlke, 2010b), or even consider the RVEs as material points in large-scale FE simulations (e.g., Feyel (1999); Ilic and Hackl (2009)). Especially for the multiscale FEM approach, the RVE simulations need to be very efficient from a numerical point of view. The question for an numerically optimized RVE is raised, where one may consider different boundary conditions, RVE sizes, RVE shapes and numerical solution strategies. The answer is not as straight forward as one might think. It is for example well known that periodic boundary conditions (PBC) result in a faster convergence in terms of the RVE size, compared to linear displacement boundary conditions (Kanit et al., 2003; Glüge et al., 2012). However, the node coupling in case of PBC increases the bandwidth of the matrix that appears in the linear system in the FEM, which results in higher numerical costs (Fritzen and Böhlke, 2010a). In this work, we address the questions how the RVE-shape affects the numerical properties, specifically the difference between cube and sphere, and discuss different combinations of RVE shapes, boundary conditions and solution techniques exemplarily for a simple homogenization task. Due to the smaller surface to volume ratio, the boundary influence in spherical RVE is smaller than in cubical RVE, which results in a better convergence to the effective material properties in terms of the RVE volume. However, the reduced RVE volume does not result directly in a numerical advantage. Clearly, since the convergence depends on the material and microstructure under consideration, these issues depend on the materials, the microstructure, and the specific FE implementation. However, the case examined in this work may serve as a representative example.

2 Problem Setup

The benchmark problem is the same that has been used for the analysis of convergence in terms of RVE volume in Glüge et al. (2012), briefly summarized in the following sections.

Parameter	Matrix	Inclusion
Young's modulus E in MPa	5000	50000
Poisson's ratio ν	0.4	0.3
Volume fraction	0.7	0.3

Table 1: Material parameters for the matrix and the inclusion material

2.1 RVE and Boundary Conditions

We consider four RVE setups, namely cubical RVEs with periodic boundary conditions, spherical RVEs with antipodic boundary conditions (ABC), and linear displacement boundary conditions on both types. The latter are

$$\boldsymbol{u} = \overline{\boldsymbol{H}} \cdot \boldsymbol{x}_0 \qquad \text{on } \partial\Omega \tag{1}$$

where the displacement gradient $\overline{\boldsymbol{H}}$ is prescribed on the entire boundary of the domain Ω that is occupied by the RVE. The periodic/antipodic boundary conditions require

$$\boldsymbol{u}^+ - \boldsymbol{u}^- = \overline{\boldsymbol{H}} \cdot (\boldsymbol{x}_0^+ - \boldsymbol{x}_0^-) \tag{2}$$

$$\boldsymbol{t}^+ + \boldsymbol{t}^- = 0 \tag{3}$$

on $\partial\Omega$. The points on the surface are coupled in pairs, where the reference surface normals must satisfy

$$\boldsymbol{n}_0^+ + \boldsymbol{n}_0^- = \boldsymbol{o}. \tag{4}$$

One might consider Eq. (3) basically independent of Eq. (2), since 6 independent equations are needed to complete the boundary value information for two boundary points. However, practically no other choice than Eq. (3) is reasonable. Firstly, static equilibrium requires $\int_{\partial\Omega} \boldsymbol{t} \mathrm{d}A = \boldsymbol{o}$ and $\int_{\partial\Omega} (\boldsymbol{x} \times \boldsymbol{t} - \boldsymbol{t} \times \boldsymbol{x}) \mathrm{d}A = \boldsymbol{o}$, and an equal treatment of all boundary points allows only for the application of Eq. (3). Secondly, Eq. (3) is generally adopted automatically in any FE system when imposing Eq. (2), since the node coupling should not contribute to the internal power. The contribution to the stress power p from the coupled points is

$$p = \dot{\boldsymbol{u}}^+ \cdot \boldsymbol{t}^+ + \dot{\boldsymbol{u}}^- \cdot \boldsymbol{t}^-, \tag{5}$$

which becomes with Eq. (2)

$$p = \underbrace{\dot{\boldsymbol{u}}^+ \cdot (\boldsymbol{t}^+ + \boldsymbol{t}^-)}_{p_{\text{coupling}}} \underbrace{- \boldsymbol{t}^- \cdot \dot{\overline{\boldsymbol{H}}} \cdot (\boldsymbol{x}_0^+ - \boldsymbol{x}_0^-)}_{p_{\text{external}}}, \tag{6}$$

where the first term does not involve the external loading. Since the coupling, as a constraint, should not contribute to the stress power, Eq. (3) follows from $p_{\text{coupling}} = 0$ for all possible deformations. Last but not least, only this choice guarantees compliance with the Hill-Mandel-condition (Glüge et al., 2012).

Applied to a cube, one mostly couples opposing surface points such that a periodicity frame emerges, thus the denomination as *periodic boundary conditions*. However, the periodic coupling may also be shifted in order to rotate the periodicity frame (Coenen et al., 2012) or such that no periodicity frame is induced. On the sphere, the coupling is unique: only antipodic points have opposing surface normals. Interestingly, the coupling equations are the same in all cases. The (non)-periodicity depends on the assignment of pairs of surface points. Therefore, it might be clearer to speak of coupled boundary conditions when one refers to the Eqs. (2) and (3) alone.

2.2 Materials and Microstructure

We used the same material and RVE description as published in Glüge et al. (2012), in order to take advantage of a large set of existing RVE results. The material under consideration is a matrix-inclusion material. The matrix is isotropic and linearly elastic. The inclusions, with a total volume fraction of 0.3 are spherical, isotropic, linearly elastic particles of equal diameter, distributed uniformly without preferred alignment or pattern. They are considerably stiffer than the matrix material. The material parameters are collected in Table 1.

	approx. No. of incl.	total No. of nodes	approx. No. of nodes per incl.	No. of surface nodes	No. of DOF for linear disp. BC	No. of DOF for periodic/antipodic BC
	2.4	4462	1858	962	10500	11943
	4.7	7992	1704	1538	19362	21669
spherical	11.1	17832	1604	2562	45810	49653
RVE	19.2	31478	1639	3650	83484	88959
	28.2	45794	1625	4930	122592	129987
	37.5	59926	1598	5642	162852	171315
	4.6	4916	1072	1538	10134	12441
	9.0	9264	1034	2402	20586	24189
cubical	21.2	21171	998	4268	50709	52656
RVE	36.7	35940	980	6146	89382	98601
	53.8	50656	941	7778	128634	140301
	71.62	68924	962	9602	177966	192369

Table 2: RVE and mesh sizes that have been tested.

2.3 Test Setup

We carried out uniaxial tension tests, in which the effective Young's modulus is to be determined. The latter is accomplished by imposing most components of the average displacement gradient,

$$\overline{H}_{(\mathrm{uax})ij} = \begin{bmatrix} \varepsilon & 0 & 0 \\ 0 & - & 0 \\ 0 & 0 & - \end{bmatrix}. \tag{7}$$

Not prescribing $\overline{H}_{(\mathrm{uax})22}$ and $\overline{H}_{(\mathrm{uax})33}$ results in zero stress components $\overline{T}_{22}$ and $\overline{T}_{33}$ of the effective first Piola-Kirchhoff-stresses, which are stress-power-conjugate to $\dot{\overline{\boldsymbol{H}}}$. Young's modulus is given by

$$E = \overline{T}_{11}/\varepsilon, \tag{8}$$

where ε needs to be small.

2.4 Numerical Setup

For the FE simulations, we employed hexahedral eight-node bricks with linear shape functions for the meshing, which is regular in case of the cubical RVE (see Fig. 1. The microstructure has been accounted for by the Gauss-point-method (Kreikemeier, 2012), where the largest element size has been constrained to one eighth of the inclusion diameter. The inclusions have been dispersed randomly in the RVE, where intersections with the RVE boundary have been allowed, disregarding the periodicity frame. The volume fractions have been ensured by trial and error distributions. To impose an average displacement gradient $\overline{\boldsymbol{H}}$, three additional nodes have been used, the three degrees of freedom (DOF) of which appear in the constraint equations. These equations allow for a linear coupling of arbitrary DOF, which serve for the implementation of the displacement boundary conditions (Eqs. (1) and (2)). The simulations have been conducted on an eight-core Intel I7-950 CPU[1], using the FE system ABAQUS 6.10-2 and its iterative and direct solver. Different RVE-sizes have been examined, the parameters of which are collected in Table 2. One can already notice that the number of nodes per inclusion is approximately 1.7 times larger for the spherical RVE. This is due to the common element size limit. The cube is meshed regularly with cubical elements, while the meshing of the sphere requires smaller and distorted elements. For numerical parameters like tolerances and precisions, ABAQUS default values have been used.

2.4.1 Influence of the Type of Boundary Condition on the Numerical Problem

Firstly, the linear displacement boundary conditions require twice the number of constraint equations, compared to the periodic/antipodic boundary conditions. Presuming that each constraint equation is used to eliminate a DOF,

[1] Linux 3.2.0-33-generic x86-64 GNU/Linux with Intel Fortran 12.0.4

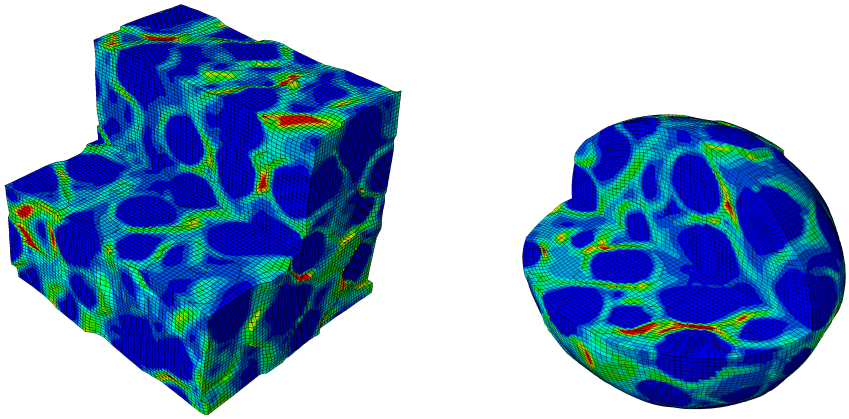

Figure 1: Deformed cubical and spherical RVE with periodic and antipodic boundary conditions, one fourth is cut out. The color map indicates the accumulated plastic strain from 0 (blue) to 0.2 (red).

one has a slightly reduced number of DOF in case of the linear displacement boundary conditions. Secondly, the node coupling for the periodic/antipodic boundary conditions induces an increase of the system matrix bandwidth, see Fritzen and Böhlke (2010a). For some matrix storage schemes and solvers, this can result in a severe decrease of performance.

2.4.2 Influence of the RVE Shape on the Numerical Problem

Taking the cubical RVE as reference, there are two competing effects when going to spherical RVE. Capturing the same volume requires approximately 19% less surface, hence one may expect a corresponding reduction of the number of surface nodes. However, this holds only when both types of RVE are meshed the same way, i.e. both regularly or irregularly. In the present example, the cube is meshed regularly. With hexahedral elements, this is not possible on spherical RVE. With a common maximum permitted element length, one has a higher density of surface points on the sphere. Thus, the overall reduction of surface points is only approximately 8% (see Table 2, largest spherical and third-largest cubical RVE).

3 Results

For most calculations, the iterative solver performes better than the direct solver, regarding the time per iteration as well as memory requirements. Only in case of relatively small FE models the direct solver is slightly faster. The largest ratio $t_{\Delta\text{direct}}/t_{\Delta\text{iterative}}$ (timer per iteration using the direct solver over timer per iteration using the iterative solver) is obtained as approximately 7.5 for the largest cubical RVE with periodic boundary conditions.

3.1 Effect of the Type of Boundary Condition and RVE Shape on the the Solver Performance

Time per iteration Regarding the time per equilibrium iteration, there is no notable difference between spherical and cubical RVE in case of linear displacement boundary conditions. Only the total number of DOF is relevant. Going from linear displacement boundary conditions to periodic/antipodic boundary conditions, a slight decrease of performance is observed for the iterative solver, while the direct solver displays a more pronounced decrease of performance. The results are depicted in Fig. 2. The leading coefficients of the quadratic and linear regressions on the data points (time per iteration in seconds over the number of DOF) are summarized in Table 3. For the direct solver, the leading coefficients in the quadratic regressions differ by a factor of approximately 2.97 for the spherical and by approximately 4.9 for the cubical RVE when going from linear displacement to periodic/antipodic boundary conditions, while for the iterative solver these ratios are with 1.19 for the sphere and 1.09 for the cube close to one.

Memory usage ABAQUS estimates a minimum and an optimum amount of required memory, where for the latter the read and write activity from and to the hard disk is minimized. The memory usage is plotted in Fig. 3

RVE setup	direct	iterative
spherical, LDBC	$0.007199\ 10^{-6}$	$0.78682\ 10^{-3}$
spherical, PBC	$0.021426\ 10^{-6}$	$0.93816\ 10^{-3}$
cubical, LDBC	$0.006468\ 10^{-6}$	$0.83013\ 10^{-3}$
cubical, PBC	$0.031925\ 10^{-6}$	$0.90690\ 10^{-3}$

Table 3: Leading coefficients in the quadratic (direct solver) and linear (iterative solver) regression functions for the CPU time per iteration in seconds over number of DOF for the different RVE setups.

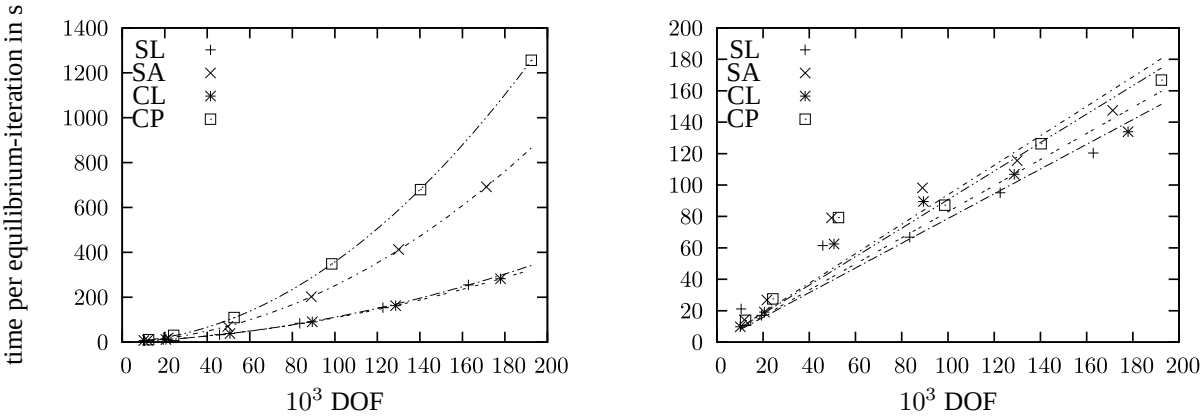

Figure 2: Time per equilibrium iteration over the number of degrees of freedom needed by the direct (left) and iterative (right) solver for the different RVE setups. In the legend, S and C stand for sphere and cube, while L, P and A stand for linear displacement, periodic and antipodic boundary conditions.

for different RVE setups and solvers. The minimum memory requirements are similar for both solver types, and relatively insensitive to the RVE shape.
Iterative solver: It turns out that the memory requirements of the iterative solver are insensitive both to the kind of boundary condition and the shape of the RVE. The ratio of the optimum to the minimum memory usage is rather small, and lies mostly below 1.4.
Direct solver: While insensitive to the RVE shape, the minimum memory requirement is approximately doubled when going from linear displacement to periodic/antipodic boundary conditions. The optimal memory usage depends highly on the boundary conditions and the RVE shape: it is insensitive to the shape of the RVE in case of linear displacement boundary conditions, but sensitive to the RVE shape when periodic/antipodic boundary conditions are used. Similarly to the increase of time per iteration, the node coupling due to periodic/antipodic boundary conditions increases the memory usage. This behaviour is more pronounced for the cubical RVE, since the ratio of coupled DOF to the overall number of DOF is, due to the greater surface to volume ratio, larger than for the spherical RVE. In any case, the optimum memory required is considerably higher than the minimum memory requirement, at least by a factor of 3.5.

3.2 RVE Quality

One can estimate the overall RVE quality by relating the precision of the effective material to the numerical expense. Here, we use the absolute value of the relative deviation of E_{RVE} from the asymptotic Young's modulus E_∞, $|(E_\infty - E_{RVE})|/E_\infty$, as the error estimate. Plotting this measure over the time per iteration gives a clear picture of which RVE/boundary condition/solution technique is most advantageous, see Fig. 4. Each data point is the result of an averaging over 100 RVE simulations with different inclusion distributions. E_∞ has been taken as the average of the results of the largest spherical and cubical RVE.

One sees immediately that the numerical extra-costs of periodic/antipodic boundary conditions instead of linear displacement boundary conditions pay off, regardless of solver type and RVE shape. The convergence is quite fast when PBC/ABC are applied. The advantage of the spherical RVE over the cubical RVE observed in Glüge et al. (2012) is almost cancelled out by the higher munber of nodes per volume, due to the irregular meshing of the sphere. Still, especially for small RVE, the effective properties are estimated more efficiently for spherical RVE.

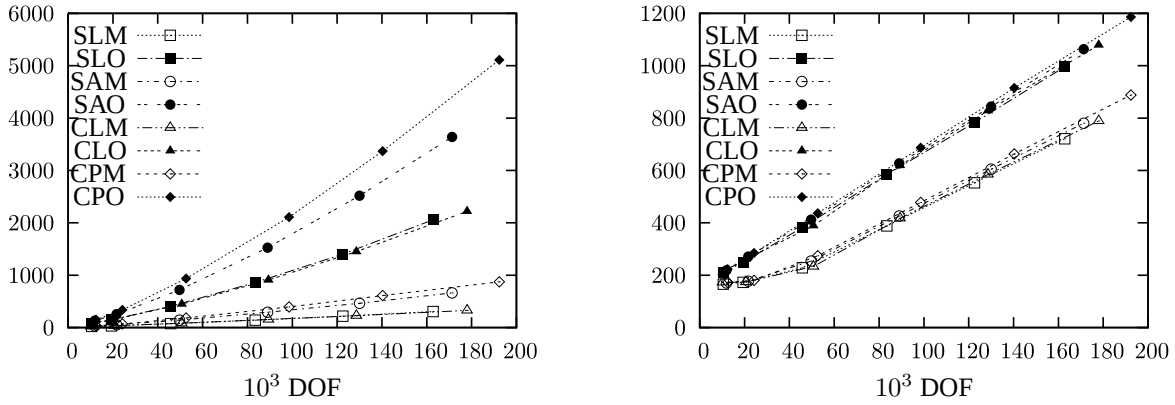

Figure 3: Memory usage over the number of degrees of freedom for different RVE setups for the direct (left) and iterative (right) solver. In the legend, S and C stand for sphere and cube, while L, P and A stand for linear displacement, periodic and antipodic boundary conditions, and M and O stand for the minimum and optimum performance memory requirement.

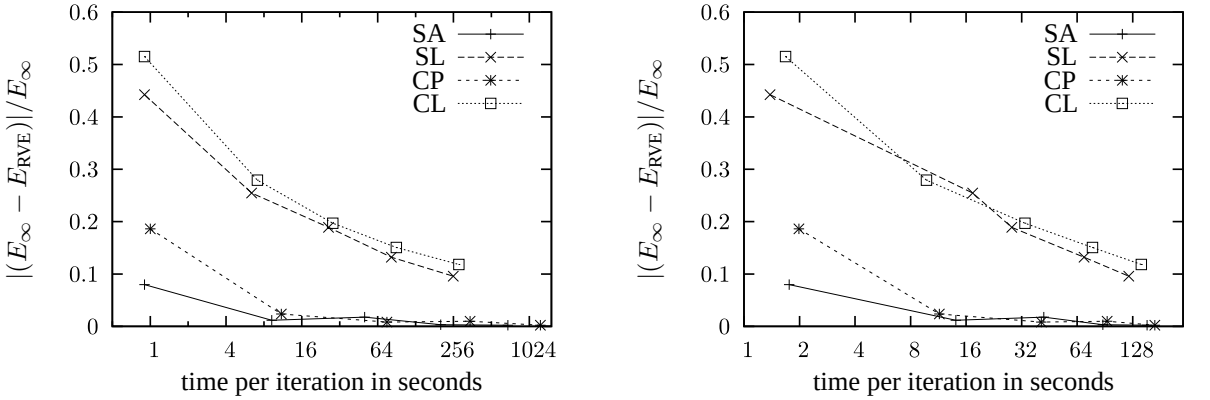

Figure 4: Absolute value of the realtive deviation of the RVE Young's modulus from the asymptotic Young's modulus over the numerical expense. In the legend, S and C stand for sphere and cube, while L, P and A stand for linear displacement, periodic and antipodic boundary conditions.

4 Summary

When addressing the question whether the advantage of spherical RVE in terms of surface to volume ratio results in a reduction of computational time, two specific conclusions can be drawn:

In case of periodic/antipodic boundary conditions and the direct solver, the reduced number of surface points leads to a better performance of spherical RVE compared to cubical RVE with a similar number of DOF, since there are less numerically disadvantageous node adjacencies. This advantage is partially cancelled out due to a necessarily irregular meshing of the sphere, when hexahedral elements are used. With a common maximum element size, the spherical RVE require more nodes per volume (namely by a factor of approximately 1.7).

In most situations, one will use the iterative solver and a microstructure-conform meshing, for which none of these two issues plays a role. However, for the multiscale FEM, one is usually restricted to relatively small RVE, where the direct solver is to prefer, and periodic/antipodic boundary conditions, for obtaining reasonable effective properties at small RVE sizes. Then, it seems appropriate to use spherical RVE with antipodic boundary conditions, both due to better convergence in terms of RVE size and a better performance of the direct solver.

References

Coenen, E. W. C.; Kouznetsova, V. G.; Geers, M. G. D.: Novel boundary conditions for strain localization analyses in microstructural volume elements. *International Journal for Numerical Methods in Engineering*, 90, (2012), 1–21.

Feyel, F.: Multiscale FE^2 elastoviscoplastic analysis of composite structures. *Computational Materials Science*, 16, 14, (1999), 344–354.

Fritzen, F.; Böhlke, T.: Influence of the type of boundary conditions on the numerical properties of unit cell problems. *Technische Mechanik*, 30, 4, (2010a), 354–363.

Fritzen, F.; Böhlke, T.: Three-dimensional finite element implementation of the nonuniform transformation field analysis. *International Journal for Numerical Methods in Engineering*, 84, (2010b), 803–829.

Glüge, R.; Weber, M.; Bertram, A.: Comparison of spherical and cubical statistical volume elements with respect to convergence, anisotropy, and localization behavior. *Computational Material Science*, 63, (2012), 91–104.

Ilic, S.; Hackl, K.: Application of the multiscale FEM to the modeling of nonlinear multiphase materials. *Journal of Theoretical and Applied Mechanics*, 47, 3, (2009), 537–551.

Kanit, T.; Forest, S.; Galliet, I.; Mounoury, V.; Jeulin, D.: Determination of the size of the representative volume element for random composites: statistical and numerical approach. *International Journal of Solids and Structures*, 40, (2003), 3647–3679.

Kreikemeier, J.: Modelling of Phase Boundaries via the GAUSS-Point Method. *Technische Mechanik*, 32, 6, (2012), 658–666.

Address: Otto-von-Guericke–Universität Magdeburg, Universitätsplatz 2, D-39104 Magdeburg
email: gluege@ovgu.de, martin.weber@ovgu.de

In R. Glüge (2013). **Generalized boundary conditions on representative volume elements and their use in determining the effective material properties**. In: *Computational Materials Science* 79, S. 408–416 wurde eine Klasse von Randbedingungen vorgestellt, welche die Hill-Mandel-Bedingung a priori unabhängig, von der RVE-Größe erfüllen. Dabei wird die die RVE-Oberfläche in beliebig viele Gebiete unterteilt, und auf jedes einzelne dieser Gebiete werden die iso-stress-Randbedingungen aufgebracht. Es wurde festgestellt, dass

- sich die klassischen iso-stress, iso-strain und periodischen Randbedingungen als Spezialfälle ergeben,
- durch eine mehr oder weniger feine Teilung der Oberfläche kontinuierlich die künstliche Randsteifigkeit zwischen den extrem steifen iso-strain Randbedingungen und den extrem nachgiebigen iso-stress Randbedingungen skaliert werden kann,
- durch die Art der Oberflächenpartitionierung der Widerstand gegen homogene und inhomogene Deformationen des RVE in gewissen Grenzen unabhängig voneinander eingestellt werden kann.

In der Arbeit wird die RVE-weite Lokalisierung als Verlust der Repräsentativität des RVE interpretiert. Es wird vorgeschlagen,

- die Gültigkeit einer RVE-Konfiguration für eine bestimmte Materialklasse zu überprüfen, indem das RVE auf ein homogenes Material angewendet wird, dessen effektive Materialantwort man daher kennt,
- sowie zwischen skalenübergreifender Lokalisierung und Lokalisierung auf Makroebene zu unterscheiden.

Dabei zeigt sich, dass bei skalenübergreifender Lokalisierung eine Abweichung vom erwarteten Materialverhalten auftritt. Aus diesem Grund wird die oben letztgenannte Eigenschaft dazu verwendet, um die Lokalisierung von RVE möglichst weit hinauszuzögern oder sogar zu unterdrücken, ohne dabei die elastische Steifigkeit des effektiven Materials zu überschätzen. So werden die Vorteile der periodischen und der iso-strain-Randbedingungen kombiniert. Die neu entwickelten Randbedingungen werden als stochastische Randbedingungen bezeichnet, da sie auf der stochastischen Kopplung der Oberflächenpartitionen beruht.

Computational Materials Science 79 (2013) 408–416

Contents lists available at SciVerse ScienceDirect

Computational Materials Science

journal homepage: www.elsevier.com/locate/commatsci

Generalized boundary conditions on representative volume elements and their use in determining the effective material properties

Rainer Glüge *

Universität Magdeburg, Universitätsplatz 2, Magdeburg D-39106, Germany

ARTICLE INFO

Article history:
Received 1 February 2013
Received in revised form 21 May 2013
Accepted 19 June 2013

Keywords:
Representative volume element
Generalized boundary conditions
Stochastic boundary conditions
Localization
Elastic
Plastic

ABSTRACT

When determining an effective stress–strain law by means of the representative volume element (RVE) method, one needs to subject the RVE to the effective strains by appropriate boundary conditions (BC). Usually, classical BC that prescribe a homogeneous stress or strain field at the boundary or a periodic unit cell are used. In this work, we discuss generalized BC, which involve the partitioning of the RVE boundary into n parts. It is demonstrated that the classical BC are contained as special cases, and that the Hill–Mandel-condition holds for all partitionings.

By a more or less fine surface partitioning, the generalized BC allow for a smooth scaling between the extremal cases of homogeneous stress or homogeneous strain BC. Further, by an irregular surface partitioning, one can obtain stochastic BC with an elastic stiffness close to the periodic/antipodal BC, but with a higher resistance against localization. This has been demonstrated by examining a softening example material. A test of plausibility for a RVE is to apply it to a homogeneous microstructure. Then, the microscale material law should be conducted directly to the macroscale. In case of softening microscale materials, this test works only for homogeneous strain BC. For homogeneous stress- and periodic/antipodal BC, localization occurs, accompanied by a drastic deviation from the expected stress–strain curve. From the generalization, one can derive stochastic BC that combine the moderate elastic stiffness of periodic BC with the high resistance against localization of homogeneous strain BC.

1. Introduction

The micro-scale structure of a material can have a considerable effect on the material properties as perceived on the macroscale. It may be the byproduct of a forming or solidification process, be an inseparable part of the material (e.g., fibers of wood), or it may be the result of a material design process (micro-structural reinforced or micro-architectured materials). In order to efficiently examine the micro–macro interaction, one needs fast, reliable and robust homogenization methods. These demands can be accounted for by the representative volume element method. The method consists basically in choosing a representative material sample (step 1), enforcing the average (macro) fields of the independent variable (e.g., the strains, step 2), solving the boundary value problem (step 3), and averaging the fields of the resulting dependent variable (e.g., the stresses, step 4). The method allows to obtain estimates of effective material properties when analytical homogenization is due to the geometric nonlinear setting or complicated interactions between the constituents hardly possible (e.g. [1]). Here, the term "representative" is used in an approximate sense as suggested in [15–17], compared to the strict interpretation of [18].

The present work is concerned with step 2, namely how the average macro-scale field may be imposed most efficiently. Since RVE are something artificial, there are no natural boundary conditions (BC), except for periodic microstructures. Then, the periodicity prescribes a specific self-interaction of the boundaries. Another possibility is to prescribe homogeneous fields on the boundary. Regarding the mechanical material behavior, one may prescribe either homogeneous deformations ($\boldsymbol{u} = \overline{\boldsymbol{H}} \cdot \boldsymbol{x}_0$) or homogeneous stresses ($\boldsymbol{t} = \overline{\boldsymbol{T}} \cdot \boldsymbol{n}_0$), see [14]. The latter BC are extremal in the sense that they result in the stiffest (homogeneous deformations) or softest (homogeneous stresses) possible RVE, while periodic BC lie between these extremes. Although the homogeneous deformation BC require, strictly speaking, a prescribed displacement gradient, we will refer to them in the remainder as homogeneous *strain* BC to emphasis the dual character of the pair stresses/strains and the resulting extremal BC.

Mostly, one of these three classical BC is employed. Due to a more complicated implementation and problems with RVE localization, the homogeneous stress BC are much less popular than the homogeneous strain BC and the periodic BC. Especially the periodic BC are commonly used, even for non-periodic structures, due to the absence of other popular BC that lie between the extremal BC. The reason is that it is not easy to give BC of moderate stiffness that comply with the Hill–Mandel-condition [5], which is a

* Tel.: +49 391 67 12592; fax: +49 391 67 12863.
E-mail address: gluege@ovgu.de

0927-0256/$ - see front matter © 2013 Elsevier B.V. All rights reserved.
http://dx.doi.org/10.1016/j.commatsci.2013.06.038

necessary condition for the RVE to converge to a macroscale material law as the RVE size is increased [14]. To the best knowledge of the author, only two other BC of non-extremal stiffness are known, namely the subspace decomposition of the boundary data, which consists of enforcing homogeneous displacements in one direction and homogeneous tractions perpendicular to this direction (or the other way around, [4]), and the gradual penalization of a deviation from the homogeneously deformed RVE by spring elements [3]. The aim of the present work is to give generalized BC that comply with the Hill–Mandel-condition, and enclose the classical BC (Section 2). From this generalization, one can construct BC that have yet unseen properties. The applicability of the generalized BC is examined for an elasto-plastic matrix inclusion material (Section 3). We demonstrate that elasto-plastic material homogenization can benefit from the properties of the generalization, especially when softening microscale materials are considered (Sections 4 and 5).

1.1. Notation

Throughout the work a direct tensor notation is preferred. Vectors are symbolized by lowercase bold letters, and second-order tensors by uppercase bold letters. The second-order identity tensor is denoted by $\boldsymbol{I}$. A dot represents a scalar contraction. If more than one scalar contraction is carried out, the number of dots corresponds to the number of contractions, e.g., $(\boldsymbol{a}\otimes\boldsymbol{b}\otimes\boldsymbol{c})\cdot\cdot(\boldsymbol{d}\otimes\boldsymbol{e}) = (\boldsymbol{b}\cdot\boldsymbol{d})(\boldsymbol{c}\cdot\boldsymbol{e})\boldsymbol{a}$, $\alpha = \boldsymbol{A}\cdot\cdot\boldsymbol{B}$.

The position vector of a material point is denoted by $\boldsymbol{x}(\boldsymbol{x}_0,t)$, where $\boldsymbol{x}_0$ indicates the position vector of the same material point in the reference placement. At $t = 0$, $\boldsymbol{x} = \boldsymbol{x}_0$ holds. The partial derivative of a function with respect to t with $\boldsymbol{x}_0$ kept constant is the material time derivative, indicated by a superimposed dot. The index "0" indicates that a function or derivative is to be evaluated in the reference placement or with respect to $\boldsymbol{x}_0$. Ω denotes the domain of the RVE under consideration. A bar denotes the unweighted volume average over Ω.

1.2. List of symbols

Ω	domain of the RVE
$\partial\Omega$	RVE boundary
$\partial\Omega_i$	part of $\partial\Omega$
k	number of surface partitions
n	number of discrete points contained in $\partial\Omega_i$, referred to as group size
$n_{\max}$	number of discrete points contained in $\partial\Omega$
u_{abs}	absolute under-determinacy, u_{abs} = No. of vars. − No. of. eqs.
u_{rel}	relative under-determinacy, $u_{rel} = u_{\text{abs}}$/No. of vars.
$\boldsymbol{n}_0$	surface normal vector in the reference placement
$\boldsymbol{t}$	traction vector $\boldsymbol{t} = \boldsymbol{T}\cdot\boldsymbol{n}_0$
$\boldsymbol{u}$	displacement vector, $\boldsymbol{u} = \boldsymbol{x} - \boldsymbol{x}_0$
$\boldsymbol{x}$	position vector
$\boldsymbol{H}$	displacement gradient
$\boldsymbol{T}$	first Piola–Kirchhoff stress tensor

2. Generalized boundary conditions

The generalized BC are given by.

- dividing the surface $\partial\Omega$ of the RVE into k parts $\partial\Omega_i$,
- and constraining $\boldsymbol{u}$ on each $\partial\Omega_i$ by

$$\underbrace{\overline{\boldsymbol{H}}\cdot\int_{\partial\Omega_i}\boldsymbol{x}_0\otimes\mathrm{d}\boldsymbol{A}_0}_{\overline{\boldsymbol{H}}_i} = \int_{\partial\Omega_i}\boldsymbol{u}\otimes\mathrm{d}\boldsymbol{A}_0. \tag{1}$$

In the latter equation, one can consider the left handside as the displacement gradient $\overline{\boldsymbol{H}}_i$ that is imposed on the surface part $\partial\Omega_i$. After fixing an average deformation $\overline{\boldsymbol{H}}$ and a surface partitioning, it can be calculated for each part $\partial\Omega_i$ of the surface.

One can show that the well known homogeneous strain-, homogeneous stress- and periodic BC are contained special cases, resulting from different surface partitionings:

- The **homogeneous strain BC** require an infinitely fine partitioning of the surface, i.e., Eq. (1) must hold pointwise on $\partial\Omega$ instead on average. Thus, we drop the integral,

$$(\overline{\boldsymbol{H}}\cdot\boldsymbol{x}_0)\otimes\mathrm{d}\boldsymbol{A}_0 = \boldsymbol{u}\otimes\mathrm{d}\boldsymbol{A}_0. \tag{2}$$

Comparing coefficients gives

$$\boldsymbol{u} = \overline{\boldsymbol{H}}\cdot\boldsymbol{x}_0, \tag{3}$$

which must hold everywhere on $\partial\Omega$. This corresponds to the well known homogeneous strain BC.

- For **periodic BC**, the partitioning is infinitely fine, but points are coupled pairwise such that

$$\mathrm{d}\boldsymbol{A}_0^+ = -\mathrm{d}\boldsymbol{A}_0^-, \tag{4}$$

holds, where the + and − sign index the two coupled points. Again, the integral is contracted at the two points,

$$\begin{aligned}&(\overline{\boldsymbol{H}}\cdot\boldsymbol{x}_0^+)\otimes\mathrm{d}\boldsymbol{A}_0^+ + (\overline{\boldsymbol{H}}\cdot\boldsymbol{x}_0^-)\otimes\mathrm{d}\boldsymbol{A}_0^-\\ &\quad= (\boldsymbol{u}^+\otimes\mathrm{d}\boldsymbol{A}_0^+) + (\boldsymbol{u}^-\otimes\mathrm{d}\boldsymbol{A}_0^-).\end{aligned} \tag{5}$$

With Eq. (4) one can write

$$\overline{\boldsymbol{H}}\cdot(\boldsymbol{x}_0^+ - \boldsymbol{x}_0^-)\otimes\mathrm{d}\boldsymbol{A}_0^+ = (\boldsymbol{u}^+ - \boldsymbol{u}^-)\otimes\mathrm{d}\boldsymbol{A}_0^+, \tag{6}$$

where a comparison of coefficients gives the well known periodic BC,

$$\overline{\boldsymbol{H}}\cdot(\boldsymbol{x}_0^+ - \boldsymbol{x}_0^-) = \boldsymbol{u}^+ - \dot{\boldsymbol{u}}^-. \tag{7}$$

Further, periodicity requires an RVE shape that allows to fill the space entirely with instances of the RVE, and a corresponding coupling. However, one may as well apply Eqs. (6) and (4) to RVE that do not have such a shape, or employ a non-periodic node coupling.

- **Homogeneous stress BC** are obtained when there is no surface partitioning at all. Then Eq. (1) becomes with Gauss's theorem

$$\overline{\boldsymbol{H}} = \frac{1}{V_0}\int_{\partial\Omega}\boldsymbol{u}\otimes\mathrm{d}\boldsymbol{A}_0. \tag{8}$$

These, sometimes termed as *kinematic minimal BC*, correspond to the homogeneous stress BC. This has been demonstrated by Miehe [8] (Section 2.4.2), using Lagrangian multipliers to enforce the latter equation as a weak constraint. A proof of this statement that relies on the macroscopic stress power is contained in the Appendix.

It is noteworthy that Eq. (8) should always hold, since it is nothing else but the kinematic coupling between the micro- and macroscale [10]. One can see in fact that it holds independently of the surface partitioning. However, if Eq. (8) is the *only* constraint that is imposed on $\partial\Omega$, the resulting stresses on the RVE boundary are homogeneous.

2.1. The Hill–Mandel-condition

The Hill–Mandel condition demands the equivalence of the stress power as perceived on the macroscale to the integral of the stress-power over the RVE. For the large strain setting, it can be written as

$$\int_{\partial\Omega}\dot{\tilde{\boldsymbol{u}}}\cdot\boldsymbol{t}\mathrm{d}A_0 = 0, \tag{9}$$

[14,4], where

$$\dot{\tilde{\boldsymbol{u}}} = \dot{\boldsymbol{u}} - \dot{\overline{\boldsymbol{H}}} \cdot \boldsymbol{x}_0 \tag{10}$$

is denominated as the fluctuation part of $\dot{\boldsymbol{u}}$.

The Hill–Mandel condition is necessary for the validity of the RVE. Only if the BC satisfy it a priori, the RVE can, but must not, converge to the true effective material behavior when its size is increased. A proof for the generalized BC is given in the Appendix.

2.2. Discrete version of the generalized boundary conditions

When implementing the generalized BC into a finite element system, surface areas are represented by discrete points, each of which is equiped with a normal vector, where the absolute length of the latter corresponds to the area associated to the surface point. The discrete version of Eq. (1) is

$$\sum_{j=1,n} \overline{\boldsymbol{u}}_j^i \otimes \boldsymbol{n}_{0j}^i = \sum_{j=1,n} \boldsymbol{u}_j^i \otimes \boldsymbol{n}_{0j}^i, \quad \overline{\boldsymbol{u}}_j^i = \overline{\boldsymbol{H}} \cdot \boldsymbol{x}_{0j}^i, \tag{11}$$

with the number of surface points n belonging to $\partial\Omega_i$. In the remainder, n is referred to as the *group size*. Depending on the group size and the normal vectors $\boldsymbol{n}_{0j}^i$, the system may or may not be under-determined for the degrees of freedom $\boldsymbol{u}_j^i$. One can see that the system is always kinematically under-determined for $n > 3$. For $n = 2$ or $n = 3$, kinematic under-determinacy may occur if the corresponding $\boldsymbol{n}_0^i$ are linearly dependent, as it is the case for the periodic/antipodal BC. When the system is not kinematically under-determined, it results in the homogeneous strain BC $\overline{\boldsymbol{u}}_j^i = \boldsymbol{u}_j^i$. The absolute kinematic under-determinacy is equal to the number of DOF minus the number of linearly independent equations. The number of linearly independent equations is equal to the dimension of span $(\boldsymbol{n}_{01}, \ldots, \boldsymbol{n}_{0n})$ times 3. The relative kinematic under-determinacy u_{rel} is the absolute kinematic under-determinacy over the number of degrees of freedom. Scaling u_{rel} between 0 and 1 corresponds to a smooth transitions between homogeneous strain- and homogeneous stress BC, respectively, see Fig. 1 for an illustration.

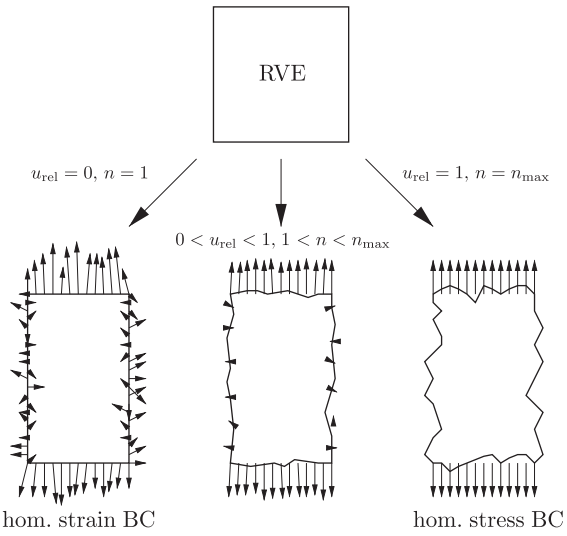

Fig. 1. Scaling between homogeneous stress- and homogeneous strain BC by adjusting u_{rel}. For $u_{\mathrm{rel}} = 0$ we have homogeneous strain BC, resulting in a surface free of displacement fluctuations but large fluctuations in the tractions. For $u_{\mathrm{rel}} = 1$ we have homogeneous stress BC, resulting in a large displacement– and no traction fluctuations. In order to minimize the boundary influence, a choice $0 < u_{\mathrm{rel}} < 1$ is more reasonable, involving moderate fluctuations of the displacements and tractions on the surface. The value $n_{\max}$ corresponds to the overall number of surface points of the discretized domain.

3. Examination of the generalized boundary conditions for a specific material

In order to test the generalized BC, we determine the effective Young's modulus of a matrix-inclusion material. Both constituents are linearly elastic and isotropic. The inclusions, with a total volume fraction of 30%, are spherical, of equal diameter, and distributed uniformly without preferred alignment or pattern. They are considerably stiffer than the matrix material (see Table 1).

Table 1
Material parameters for the matrix and the inclusion materials.

Parameter	Matrix	Inclusion
Young's modulus E in MPa	5000	50,000
Poisson's ratio ν	0.4	0.3
Volume fraction	0.7	0.3

3.1. Definition of the RVE

The calculations have been carried out using the finite element system ABAQUS. We considered spherical and cubical RVE, the meshes of which have been generated such that each surface node has an antipode, in order to allow for an easy application of the periodic/antipodal BC. Although geometrically not interpretable as a self-interacting, embedded unit cell, the spherical RVE with antipodal BC serve well for homogenization [4], since they do not induce an artificial anisotropy, and have the highest possible volume to surface ratio, minimizing the effect of the boundary a priori. The meshing has not been adapted to the matrix-inclusion interfaces, i.e., the material assignment is not element-wise, but on the integration point level. Following [7], the results obtained with a conform meshing of the microstructure are better, but require a more efforts for the mesh generation. In our case, the meshing is relatively coarse, especially the regular meshing of the cubical RVE. There, the maximum allowed element length is encountered everywhere, while this is the case for the spherical RVE only at three perpendicular great circles. This results in a slightly stiffer behavior of the cubical RVE. However, the focus is on the properties of different BC and the qualitative RVE-behavior, which is why we regard a non-conform meshing of the particles as sufficient.

The material assignment has been obtained by generating a large cubic sample of the material with randomly located spherical inclusions. The inclusions have been generated without intersections. Out of this material section, we generated many RVE by randomly assigning the RVE mid-point. From these RVE, we selected the ones which best recovered the inclusion volume fraction, with a maximum deviation of 0.5% from the desired volume fraction of 30%. We maintained a minimum elements-per-inclusion ratio of approximately 270, using 8-node hexahedral elements with linear shape functions (C3D8).

3.2. Incorporation of boundary conditions

For the application of the BC, three nodes that are not attached to the FE mesh have been created. The nine additional displacement degrees of freedom have been assigned to the components of the average displacement gradient. Then, the BC have been incorporated by linear constraint equations, by which the displacement degrees of freedom of the surface nodes are coupled by the discrete versions of Eqs. (3), (7), (8) and (11) to the three additional nodes.

3.3. Distribution of the coupled points

For the classical BC, the treatment is well known. For homogeneous strain- and stress BC all boundary points are treated equally,

and the antipodal and periodic node coupling is unique. Other special cases can be derived from the generalized BC by specifying different surface partitionings. In general, the surface parts are not simply connected. Simply connected surface partitions that are represented in a FE mesh by a fixed number of points contract to points as the mesh discretization becomes finer. Then, the generalized BC convert into the homogeneous strain BC, similar to the case $n = 1$. Thus, we regard only simply non-connected surface areas $\partial\Omega_i$. For a given finite element mesh, all surface points have been assigned to groups of sizes $n = \{2,3,4,5,6,7,8,9,12,16,24,32,48,64,96\}$. The points have been selected randomly. When the division into groups was not possible without a remainder, the remaining points have been added to the last group. The bias due to this larger group of at most $2n - 1$ members is quite small. Due to the random grouping, we refer to this special case as *stochastic BC$_n$* (SBC$_n$), where the group size is indexed. Considering cubical RVE, a special stochastic node coupling has been considered: we shuffled the node coupling of the usual periodic BC such that $\boldsymbol{n}^+ = -\boldsymbol{n}^-$ is maintained, but the periodicity is lost. Here, these BC are referred to as *shuffled periodic BC*.

For the random assignment of surface points to groups of n members, we can give the relative kinematic under-determinacies (see Section 2.2) for spherical and cubical RVE as a function of the group size:

3.3.1. Spherical RVE

In general[1]

$$\operatorname{span}(\boldsymbol{n}_{01},\ldots,\boldsymbol{n}_{0n}) = \begin{cases} n, & \text{if } n = \{1,2,3\}. \\ 3, & \text{if } n > 3. \end{cases} \tag{12}$$

Thus, we have as many equations as degrees of freedom for $n = \{1,2,3\}$, i.e., no kinematic under-determinacy, resulting in homogeneous strain BC. For $n > 3$ we have $u_{\text{abs}} = 3n - 9$ and $u_{\text{rel}} = u_{\text{abs}}/(3n) = 1 - 3/n$. By setting the group size n between 3 and ∞, one can scale u_{rel} between 0 and 1. In practice, $u_{\text{rel}} = 1$ requires an infinitely fine discretization, so this value is approached asymptotically.

3.3.2. Cubical RVE

Determining the kinematic under-determinacy in this case is more involved. We can only give an average, expected value. We firstly need to presume a homogeneous mesh density with a discretization such that the node number is much larger than n. The first assumption is needed to make each of the three surface orientations equally likely, the second assumption allows to neglect ordering-effects, e.g., assigning n nodes from one face to the first group does not affect significantly the probability of picking nodes from this face for the following groups. The probabilities of picking all $\boldsymbol{n}_{0j}$ such that $\operatorname{span}(\boldsymbol{n}_{01},\ldots,\boldsymbol{n}_{0n}) = \{1,2,3\}$ are

$$p_{1\text{D}} = \frac{1}{3^{n-1}}, \tag{13}$$

$$p_{2\text{D}} = 3\left(\frac{2}{3}\right)^n - \frac{6}{3^n}, \tag{14}$$

$$p_{3\text{D}} = 1 - p_{1\text{D}} - p_{2\text{D}}. \tag{15}$$

The expected absolute kinematic under-determinacy is then

$$u_{\text{abs}} = 3n - 3p_{1\text{D}} - 6p_{2\text{D}} - 9p_{3\text{D}}. \tag{16}$$

Dividing by $3n$ gives the expected relative kinematic under-determinacy

$$u_{\text{rel}} = 1 + \frac{3}{n}\left(-1 + \left(\frac{2}{3}\right)^n\right). \tag{17}$$

In this case, u_{rel} scales between 0 and 1 for group sizes between 1 and ∞, respectively.

3.4. Extraction of the average stresses

Depending on whether one prescribes the displacements or the forces on the nine additional degrees of freedom, one can prescribe $\overline{\boldsymbol{H}}$, $\overline{\boldsymbol{T}}$ or a mixture of both, and extract the other one. For the extraction or prescription of the stresses, the reference volume of the RVE enters as a factor of proportionality. For the study of convergence, we carried out uniaxial tension tests by prescribing a small nominal strain ε in direction of $\boldsymbol{e}_1$, zero shear strains with respect to the global coordinate frame, and free lateral straining:

$$\overline{H}_{(\text{uax})ij} = \begin{bmatrix} \varepsilon & 0 & 0 \\ 0 & - & 0 \\ 0 & 0 & - \end{bmatrix}. \tag{18}$$

4. Scaling between homogeneous stress and homogeneous strain boundary conditions

In order to examine the apparent Young's modulus for different RVE setups, simulations with different RVE sizes, shapes and BC have been carried out. Each RVE setup has been examined with 10 inclusion distributions, from which the average Young's modulus has been calculated. By varying n, one can adjust the stiffness of the BC smoothly. For the relative kinematic under-determinacy $u_{\text{rel}} = 0$ ($n = 1$ for cubical and $n = 3$ for spherical RVE), the homogeneous strain BC are obtained, while for $u_{\text{rel}} \to 1$ ($n = n_{\max}$), the homogeneous stress BC are obtained, see Figs. 2–5. Several interesting observations can be made:

- One can scale the elastic stiffness of the stochastic BC almost linearly with the relative kinematic under-determinacy, independently whether spherical or cubical RVE are considered. Thus, for the stochastic BC, u_{rel} appears to be a good measure for the elastic compliance of the BC.
- The apparent Young's modulus determined with periodic BC is quite close to the intersection point of the curves that result from varying the stochastic BC stiffness for different RVE sizes (Figs. 2 and 3).
- For spherical RVE, the effective Young's modulus obtained with antipodal BC practically coincides with the results of the stochastic BC of group size $n = 9$, although the relative kinematic under-determinacy u_{rel} is equal to 1/2 for antipodal BC and equal to 2/3 for the stochastic BC$_9$. This indicates that not only the kinematic under-determinacy, but also the whether the coupling is regular or stochastic is of importance. This optimal group size of $n = 9$ has been found also for cubical RVE, although slightly more scattered (see Fig. 5). The coincidence is most likely due to the fact that for $n = 9$, cubical and spherical RVE have very similar relative kinematic under-determinacies, namely 0.675337 and 2/3, respectively.
- The latter point is underlined by comparing the shuffled-periodic BC to the periodic BC on the cubical RVE. Although having the same relative kinematic under-determinacy of $u_{\text{rel}} = 0.5$, the shuffled periodic BC give a stiffer RVE, see Fig. 5. Thus, for the present RVE, the stochastic coupling induces a stiffening effect.
- As already discussed in [4], the spherical RVE converge faster to the true effective material behavior. This is noticed by considering the range of the effective Young's modulus that is bracketed by the extremal BC, which is approximately 1925 MPa for

[1] Picking by chance three points on a great circle or two opposing points involves sets with zero area measures, which is why the propability also vanishes.

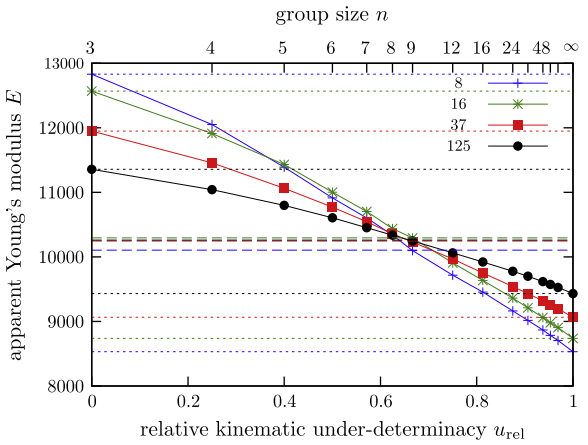

Fig. 2. Variation of the stochastic BC stiffness for four different spherical RVE of different volumes, given in multiples of a single inclusion volume. The dashed horizontal lines represent the results for the homogeneous strain BC (upper), antipodal BC (center) and homogeneous stress BC (lower).

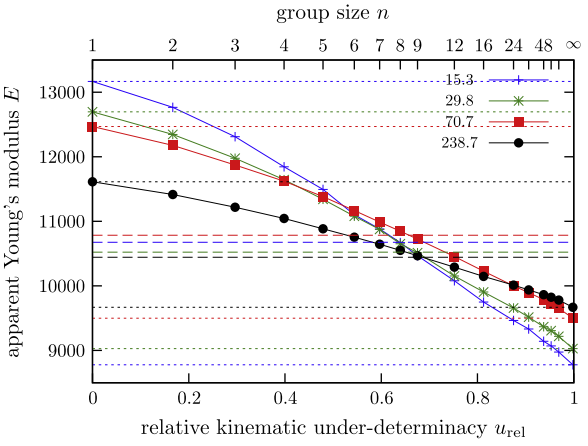

Fig. 3. Variation of the stochastic BC stiffness for four different cubical RVE of different volumes, given in multiples of a single inclusion volume. The dashed horizontal lines represent the results for the homogeneous strain BC (upper), periodic BC (center) and homogeneous stress BC (lower).

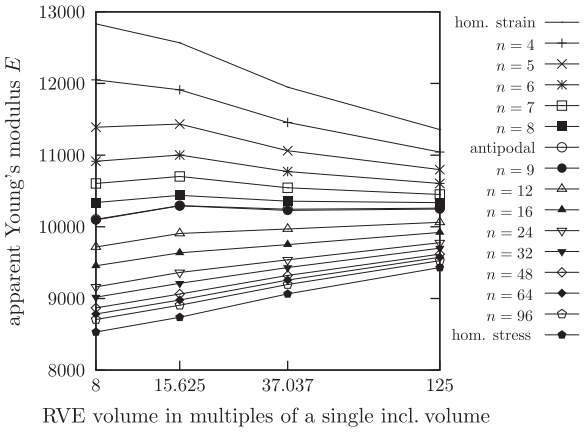

Fig. 4. Variation of the size of the spherical RVE for BC of different stiffnesses. The homogeneous strain BC coincide with the stochastic BC of group size $n = 3$. The periodic BC and the stochastic BC with $n = 9$ practically coincide.

spherical RVE at a volume of 125 times a single inclusion volume, and approximately 1944 MPa for cubical RVE at a volume of approximately 238.7 times a single inclusion volume.

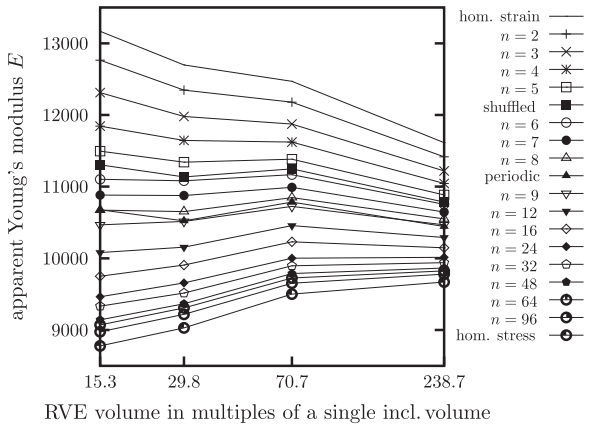

Fig. 5. Variation of the size of the cubical RVE for BC of different stiffnesses. The stiffness of the periodic BC lies between the stiffness of the stochastic BCs with group sizes 8 and 9. The shuffled periodic BC lie between the stochastic BC with group sizes 5 and 6.

5. Resistance against homogeneous and inhomogeneous deformations

The homogeneous stress BC and periodic BC allow for the localization of the deformation in shear bands (periodic BC) or even needle-like pop-out (homogeneous stress BC, see, e.g., [6], Section 6, last paragraph). This holds also for the antipodal BC [4]. Localization of RVE is sometimes interpreted as an indicator for macroscopic material failure [13,2].

A simple criterion for the validity of an RVE is to apply it to a homogeneous material. Then, the microscale material law should be conducted directly to the macroscale. Unfortunately, due to the localization, the periodic/antipodal and homogeneous stress BC fail this test when softening materials are considered [4]. Localization is accompanied by a drastic deviation from the expected stress–strain curve, which is why the extraction of results beyond localization is arguable. Even the onset of localization depends on the RVE setup, and is hence not a material property. Thus, it is questionable whether it can be interpreted as an indicator of macroscale material failure.

In this section, we examine the stochastic BC with respect to this issue. Specifically, since the stochastic BC_9 perform well in the elastic calculations, they are subjected to the test mentioned above. For this purpose, an elastoplastic material with linear softening has been subjected to a shear test by imposing

$$\overline{\boldsymbol{H}} = \overline{\gamma}\boldsymbol{d}\otimes\boldsymbol{n}, \quad \boldsymbol{d}\cdot\boldsymbol{n} = 0, \quad |\boldsymbol{d}| = |\boldsymbol{n}| = 1. \tag{19}$$

We applied $\overline{\boldsymbol{H}}$ with $\overline{\gamma}$, growing time-proportional from 0 to 1. The shear direction $\boldsymbol{d}$ and shear plane normal $\boldsymbol{n}$ have been varied inside the $\boldsymbol{e}_3$-plane. The material under consideration was the ABAQUS internal, elastically isotropic ($E = 5000$ MPa, $\nu = 0.3$), von Mises plastic material with σ_{flow} initially at 10 MPa, decaying linearly to 5 MPa at 100% of plastic strain. Beyond 100% of plastic strain, σ_{flow} is constant.

We used hexahedral elements with quadratic shape functions (element type C3D20), in order to reduce the tendency of a mesh-conform alignment of the shear bands. For a controlled initiation of the localization, in one element the flow stress has been reduced 9 MPa, which has been selected randomly from the list of elements, but not from the surface, in order to avoid problems with the implementation of the boundary conditions. If the simulations are carried out without perturbing the homogeneous material, the localization is initiated by a deviation from the

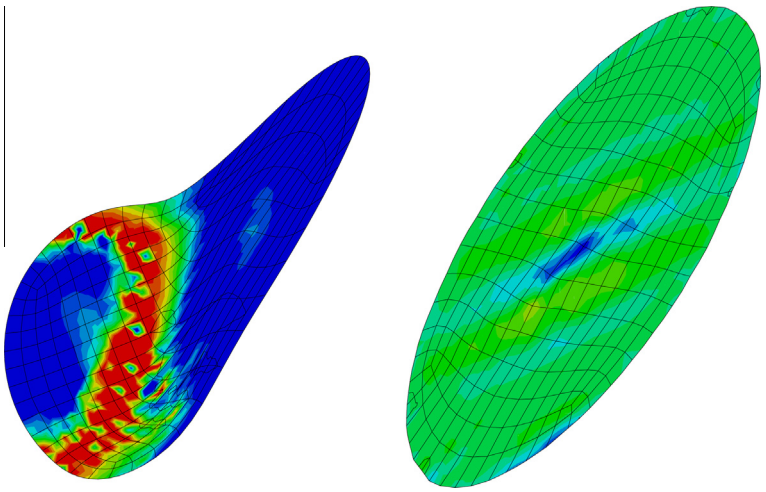

Fig. 6. Equivalent von Mises stress ranging from 5 MPa (blue) to 10 MPa (red) in a center cut through the spherical RVE parallel to the plane spanned by $\boldsymbol{d}$ and $\boldsymbol{n}$, at $\overline{\gamma} = 1$. The shear direction is 25° inclined with respect to the x-direction. On the left figure, antipodal BC are applied, on the right figure, the stochastic BC_9 are applied. (For interpretation of the references to color in this figure legend, the reader is referred to the web version of this article.)

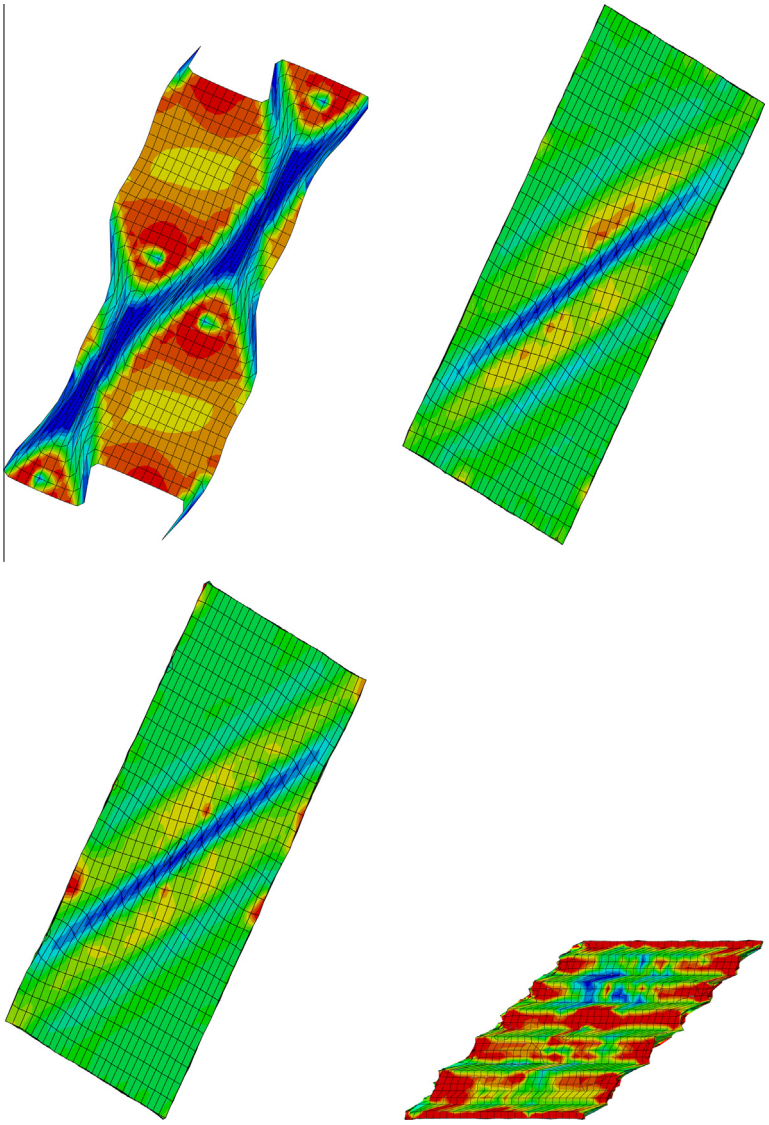

Fig. 7. Equivalent von Mises stress ranging from 5 MPa (blue) to 10 MPa (red) in a center cut through the cubical RVE parallel to the plane spanned by $\boldsymbol{d}$ and $\boldsymbol{n}$, at $\overline{\gamma} = 1$. Except for the lower right figure, the shear direction is 35° inclined with respect to the $\boldsymbol{e}_1$-direction. On the upper left figure, periodic BC are applied, on the upper right figure, the shuffled periodic BC are applied, on the lower left figure, stochastic BC_9 are applied. In the lower right figure, the stochastic BC_9 are applied, but the shear plane is parallel to the surface normal to $\boldsymbol{e}_3$. (For interpretation of the references to color in this figure legend, the reader is referred to the web version of this article.)

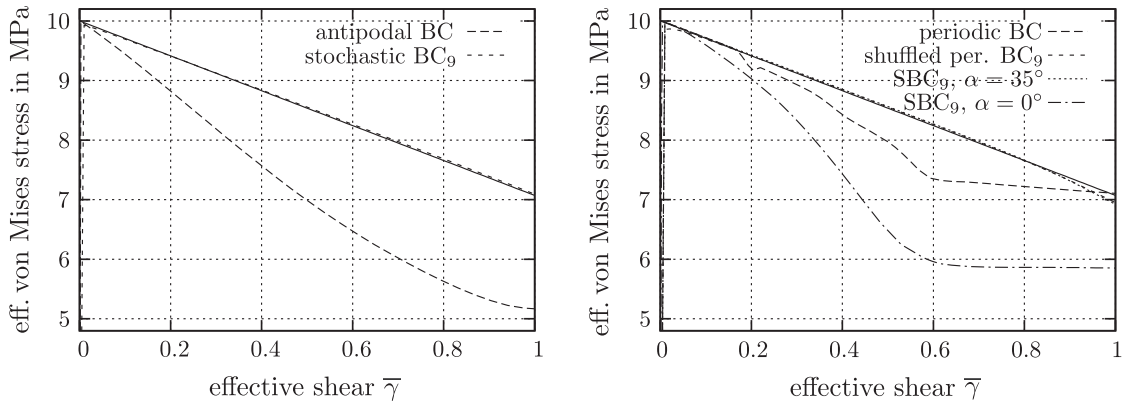

Fig. 8. Effective stress–strain curves from simulations with different BC compared to the microscale material law (solid line), left for the spherical and right for the cubical RVE. One notes that the simulations with antipodal and periodic BC are due to an early localization far off the expected material law, while the simulations with a stochastic node coupling are close to the true effective material law, except for regularly meshed cubical RVE that is sheared parallel to one of the cube's faces.

homogeneous state through unavoidable numerical errors, e.g., due to an iterative solution method or by round-off errors.

5.1. Results

5.1.1. Spherical RVE

It turns out that the stochastic BC_9 with random grouping suppress the localization that is observed when antipodal BC are applied, see Fig. 6. Since the RVE then deforms almost homogeneously, the microscale material law is practically conducted to the macroscale, see Fig. 8. The shear direction has only a weak influence, which is due to regularities in the meshing. For a discussion of the localization behavior of spherical RVE with antipodal BC, see [4].

5.1.2. Cubical RVE

The capability of the stochastic BC to suppress the localization is strongly affected by the meshing. Due to the regular meshing, shear bands align easily when the cube is sheared parallel to its faces. For sufficiently inclined shear directions, the behavior is similar to the spherical RVE: localization could be suppressed by the stochastic BC_9 and the shuffled periodic BC (Fig. 7), leading to a better prediction compared to the results obtained with periodic BC (Fig. 8).

The results depend slightly on the location of the perturbation, but these variations appear neither significant nor systematic. The depicted curves and figures are obtained with a central perturbation.

Apparently, one needs to distinguish a homogeneous and an inhomogeneous deformation resistance: Both, the antipodal/periodic BC and the stochastic BC_9 are equally stiff in the elastic range (see Section 4). However, in case of localization, the stochastic BC_9 practically suppress the localization of the deformation, while with the antipodal/periodic BC localization takes place. This is due to the fact that shear bands are diffused by the stochastic coupling when they reach the boundary. The effect is similar to the blocking of shear bands at the boundary when homogeneous strain BC are applied. It has been demonstrated that the functionality of the RVE is lost at the moment of localization. In this regard, the ability of BC to supress localization is a useful property. However, one may argue that non–quasiconvex incremental potentials should result in strain localization. The discussion eventually leads to the question on which scale localization takes place. To answer this question, one has to look at the specific material.

5.1.3. Localization on the microscale

Considering, for example, crack propagation, localization starts on the microscale and expands continuously into the macroscale. Such phenomena pose conceptual problems regarding the scale separation that is required for the RVE method [19], since inhomogeneities grow through different scales. It appears that for such problems, new homogenization techniques are required, if homogenization is possible at all.

5.1.4. Localization on the macroscale

If the localization zone covers a representative number of microscale-inhomogeneities, one may consider localization as a macroscale phenomenon, as, for example, the necking (but not rupture) of a bar in a tension test. It appears that in this case, the RVE method may be applied. As demonstrated in this work, the inhibition of RVE-localization ensures that even microscale material laws with non-quasiconvex incremental potential are conducted to the macroscale, where they will lead to localization. Still, it is open where a minimum localization size on the macroscale should come from when such a methodology is applied.

6. Summary

We proposed a generalization of the classical BC that involves a partitioning of the RVE surface. This allows to derive BC of smoothly adjustable stiffness, where a finer surface partitioning leads to elastically stiffer RVE. At the same time, the resistance against localization depends on the distribution of the surface parts. Thus, one can adjust the stiffness with respect to homogeneous and inhomogeneous deformations to a certain extend independently. In our FE simulations, we employed a stochastic coupling of surface nodes, varying the fineness of the surface partitioning. This allows us to combine the best properties of different BC: in the elastic range, the stiffness is moderate, which implies a good convergence to the effective elastic properties as the RVE volume is increased. This is as well the case for the classical periodic or antipodal BC. However, due to the avoidance of a regular frame for the RVE, be it periodic or central-symmetric, localization is suppressed quite effectively. Due to the stochastic coupling, shear bands are diffused at the boundary, which has a similar blocking effect like the homogeneous strain BC. As a result, the material law of a homogeneous RVE is conducted directly to the macroscale, even when a softening microscale law is employed. This is clearly an advantage over the regular coupling of surface points. It also shows that one should distinguish between the resistance of the BC against homogeneous and inhomogeneous deformations. The best results have been obtained for the coupling 9 randomly distributed surface points on spherical RVE, although the effect is similar for cubical RVE. However, the regular meshing that was employed in this work basically cancels out the diffusing effect when shearing is parallel to the cube's faces.

A special case are the BC obtained from shuffling randomly the initially periodic coupling of opposing faces. They are also able to suppress shear bands. However, the resistance against homogeneous deformations (elastic stiffness) is slightly higher than for the periodic BC. They are a cheap alternative to the periodic BC, which may be especially interesting for non-periodic microstructures. They allow, for example, for RVEs of moderate stiffness, but without inducing an artificial periodicity. A potential application are hexahedral RVE that are generated from micrographs of non-periodic microstructures.

The shuffled periodic BC are easily obtained from the usual periodic BC. The implementation of the more general stochastic BC is easier for the spherical RVE, since less exception handling is required, compared to cubical RVE.

Appendix A

In this Section, the conformance of the generalized BC with the Hill–Mandel-condition and the equivalence of the kinematic minimal BC to the homogeneous stress BC are demonstrated. The dependence of a field on the position vector $\boldsymbol{x}_0$ is written out. Also, fields that are defined on $\partial\Omega$ are nevertheless indexed by i when attention is restricted to the sub-domains $\partial\Omega_i$.

With a surface partitioning of $\partial\Omega$ into k parts $\partial\Omega_i$, Cauchys theorem $\boldsymbol{t}(\boldsymbol{x}_0) = \boldsymbol{T}(\boldsymbol{x}_0)\cdot\boldsymbol{n}_0(\boldsymbol{x}_0)$ and the split of the displacement field into a fluctuation and a homogeneous part (Eq. (10)), the Hill–Mandel-condition (Eq. (9)) becomes

$$0 = \sum_{i=1,n}\left[\int_{\partial\Omega_i}\boldsymbol{T}_i(\boldsymbol{x}_{0i})\cdot\cdot(\dot{\boldsymbol{u}}_i(\boldsymbol{x}_{0i})\otimes \mathrm{d}\boldsymbol{A}_0) - \int_{\partial\Omega_i}\boldsymbol{T}_i(\boldsymbol{x}_{0i})\cdot\cdot(\dot{\overline{\boldsymbol{H}}}_i\cdot\boldsymbol{x}_{0i}\otimes \mathrm{d}\boldsymbol{A}_0)\right], \tag{20}$$

$$\dot{\overline{\boldsymbol{H}}}_i = \dot{\overline{\boldsymbol{H}}}\cdot\int_{\partial\Omega_i}\boldsymbol{x}_{0i}\otimes \mathrm{d}\boldsymbol{A}_0. \tag{21}$$

Proving that the latter holds for the generalized BC is achieved by demonstrating that the application of the generalized BC (Eq. (1)) on each $\partial\Omega_i$ results in homogeneous stresses on each $\partial\Omega_i$, i.e., $\overline{\boldsymbol{T}}_i = \boldsymbol{T}_i(\boldsymbol{x}_{0_i})$. Then, one can pull $\overline{\boldsymbol{T}}_i$ out of each integral, and the remaining equation is just Eq. (1). The equivalence of kinematic minimal BC (no surface partitioning) to homogeneous stress BC is contained as the special case $k = 1$.

Ortiz and Repetto [11] (Section 2.2, Eq. (13)) showed that boundary value problems with generalized standard materials (GSM) can be rewritten as incremental variational problems. The solution of an incremental boundary value problem is found by minimizing the time integral of the stress power in each time increment. They showed that the resulting variational problem is similar to the variational problems in the elastostatic setting. Its usefulness for homogenization has been demonstrated successfully by Miehe et al. [9]. The restriction to GSMs is a rather weak, since most established material models can be recast in this setting (see [12] for some examples).

Thus, the solution of a boundary value problem minimizes the global stress power $\dot{W}$ at each instant. Its variation with respect to $\dot{\boldsymbol{u}}(\boldsymbol{x}_0)$ must vanish. We denote a variation of $\dot{\boldsymbol{u}}(\boldsymbol{x}_0)$ from the equilibrium state $\dot{\boldsymbol{u}}_{\mathrm{eq}}(\boldsymbol{x}_0)$ by $\delta\dot{\boldsymbol{u}}(\boldsymbol{x}_0)$. The solution, as well as the variation, must be compatible to the BC (Eq. (1)), i.e., on each $\partial\Omega_i$, the prescribed average rate of deformation (Eq. (21)) must remain unaffected:

$$\dot{\overline{\boldsymbol{H}}}_i = \int_{\partial\Omega_i}\dot{\boldsymbol{u}}_{\mathrm{eq}i}(\boldsymbol{x}_{0i})\otimes \mathrm{d}\boldsymbol{A}_0 \tag{22}$$

$$= \int_{\partial\Omega_i}(\dot{\boldsymbol{u}}_{\mathrm{eq}i}(\boldsymbol{x}_{0i}) + \delta\dot{\boldsymbol{u}}_i(\boldsymbol{x}_{0i}))\otimes \mathrm{d}\boldsymbol{A}_0. \tag{23}$$

Hence,

$$\boldsymbol{O} = \int_{\partial\Omega_i}\delta\dot{\boldsymbol{u}}_i(\boldsymbol{x}_{0i})\otimes \mathrm{d}\boldsymbol{A}_0, \tag{24}$$

must hold for the variation from $\dot{\boldsymbol{u}}_{\mathrm{eq}}(\boldsymbol{x}_{0i})$. It is assumed that the overall velocity field $\dot{\boldsymbol{u}}(\boldsymbol{x}_0)$ and its variation is C_1-continuous. With the surface partitioning, the stress power change due to $\delta\dot{\boldsymbol{u}}$ is denoted as

$$\delta\dot{W} = \sum_{i=1,n}\int_{\partial\Omega_i}\boldsymbol{t}_i(\boldsymbol{x}_{0i})\cdot\delta\dot{\boldsymbol{u}}_i(\boldsymbol{x}_{0i})\mathrm{d}A_0. \tag{25}$$

The stress tensor on $\partial\Omega_i$ can be decomposed into a homogeneous and a fluctuation part,

$$\boldsymbol{T}_i(\boldsymbol{x}_{0i}) = \overline{\boldsymbol{T}}_i + \widetilde{\boldsymbol{T}}_i(\boldsymbol{x}_{0i}),\quad \overline{\boldsymbol{T}}_i = \frac{1}{A_{0i}}\int_{\partial\Omega_i}\boldsymbol{T}_i(\boldsymbol{x}_{0i})\mathrm{d}A_0, \tag{26}$$

similar to the decomposition of the displacement gradient (Eq. (10)). It follows that

$$\boldsymbol{O} = \int_{\partial\Omega_i}\widetilde{\boldsymbol{T}}_i(\boldsymbol{x}_{0i})\mathrm{d}A_0 \tag{27}$$

holds. Also, the homogeneous part $\overline{\boldsymbol{T}}_i$ does not depend on $\boldsymbol{x}_{0i}$. With this decomposition, the tractions become

$$\boldsymbol{t}_i(\boldsymbol{x}_{0i}) = \overline{\boldsymbol{T}}_i\cdot\boldsymbol{n}_0(\boldsymbol{x}_{0i}) + \tilde{\boldsymbol{t}}_i(\boldsymbol{x}_{0i})\,. \tag{28}$$

The variation of the stress power is then

$$\delta\dot{W} = \sum_{i=1,n}\int_{\partial\Omega_i}(\overline{\boldsymbol{T}}_i\cdot\boldsymbol{n}_0(\boldsymbol{x}_{0i}) + \tilde{\boldsymbol{t}}_i(\boldsymbol{x}_{0i}))\cdot\delta\dot{\boldsymbol{u}}_i(\boldsymbol{x}_{0i})\mathrm{d}A_0 \tag{29}$$

$$= \sum_{i=1,n}\int_{\partial\Omega_0}(\overline{\boldsymbol{T}}_i\cdot\cdot\delta\dot{\boldsymbol{u}}_i(\boldsymbol{x}_{0i})\otimes\boldsymbol{n}_0(\boldsymbol{x}_{0i}) + \tilde{\boldsymbol{t}}_i(\boldsymbol{x}_{0i})\cdot\delta\dot{\boldsymbol{u}}_i(\boldsymbol{x}_{0i}))\mathrm{d}A_0. \tag{30}$$

The first summand of the latter integral vanishes: Due to its independence of $\boldsymbol{x}_{0i}$, we can pull out $\overline{\boldsymbol{T}}_i$, and the remainder is due to Eq. (24) equal to zero. It remains

$$\delta\dot{W} = \sum_{i=1,n}\int_{\partial\Omega_i}\tilde{\boldsymbol{t}}_i(\boldsymbol{x}_{0i})\cdot\delta\dot{\boldsymbol{u}}_i(\boldsymbol{x}_{0i})\mathrm{d}A_0. \tag{31}$$

We can vary the $\delta\dot{\boldsymbol{u}}_i(\boldsymbol{x}_{0i})$ independently, thus each summand must vanish independently. Choosing

$$\delta\dot{\boldsymbol{u}}_i(\boldsymbol{x}_{0i}) = \alpha\tilde{\boldsymbol{t}}_i(\boldsymbol{x}_{0i}), \tag{32}$$

with a real number $\alpha\neq 0$, shows that we can make $\delta\dot{W}$ nonzero for any $\tilde{\boldsymbol{t}}_i(\boldsymbol{x}_{0i})\neq\boldsymbol{o}$. Thus, for $\delta\dot{W}=0$, $\tilde{\boldsymbol{t}}_i$ must vanish on all $\partial\Omega_i$ independently. A peculiar detail of the proof is to show that the choice Eq. (32) is always admissible, since $\partial\dot{\boldsymbol{u}}$ must comply with Eq. (24). One can see that this requirement does not affect the possibility to choose $\delta\dot{\boldsymbol{u}}_i(\boldsymbol{x}_{0i}) = \alpha\tilde{\boldsymbol{t}}_i(\boldsymbol{x}_{0i})$ by recognizing that

$$\int_{\partial\Omega_i}\tilde{\boldsymbol{t}}_i\otimes\mathrm{d}\boldsymbol{A}_0 = \int_{\partial\Omega_i}\widetilde{\boldsymbol{T}}_i(\boldsymbol{x}_{0i})\cdot(\boldsymbol{n}_0(\boldsymbol{x}_{0i})\otimes\boldsymbol{n}_0(\boldsymbol{x}_{0i}))\mathrm{d}A_0 = \boldsymbol{O}, \tag{33}$$

holds always, analogous to the required Eq. (24). Writing the last integral component-wise over two surface coordinates, say s_1 and s_2, followed by an integration by parts of the inner and the outer integral, converts the latter integral into 4 summands,

$$(\boldsymbol{e}_i\otimes\boldsymbol{e}_k)\cdot\cdot\int_{\partial\Omega}\tilde{\boldsymbol{t}}\otimes\mathrm{d}\boldsymbol{A}_0 = n_j n_k\iint\widetilde{T}_{ij}\mathrm{d}s_1\mathrm{d}s_2 \tag{34}$$

$$-\int\frac{\mathrm{d}(n_j n_k)}{\mathrm{d}s_2}\iint\widetilde{T}_{ij}\mathrm{d}s_1\mathrm{d}s_2\mathrm{d}s_2 \tag{35}$$

$$-\int\frac{\mathrm{d}(n_j n_k)}{\mathrm{d}s_1}\iint\widetilde{T}_{ij}\mathrm{d}s_1\mathrm{d}s_2\mathrm{d}s_1 \tag{36}$$

$$+\iint\frac{\mathrm{d}^2(n_j n_k)}{\mathrm{d}s_1\mathrm{d}s_2}\iint\widetilde{T}_{ij}\mathrm{d}s_1\mathrm{d}s_2\mathrm{d}s_1\mathrm{d}s_2. \tag{37}$$

To keep the expression readable, the dependence of $\widetilde{\boldsymbol{T}}$ and $\boldsymbol{n}_0$ on s_1 and s_2 has been omitted, as well as the index 0 and the partition number index. One can see that each summand contains $\int_{\partial\Omega_i}\widetilde{\boldsymbol{T}}_i\mathrm{d}A_0$ as a factor. This factor is because of Eq. (27) equal to zero, making the whole expression Eq. (33) vanish. Thus, the choice $\delta\dot{\boldsymbol{u}}_i(\boldsymbol{x}_{0i}) = \alpha\tilde{\boldsymbol{t}}_i(\boldsymbol{x}_{0i})$ is always in accordance with Eq. (24).

In conclusion, we must have $\tilde{\boldsymbol{t}}_i = \boldsymbol{o}$ on $\partial\Omega_i$. Then, using three linear independent surface normals on $\partial\Omega_i$ in Eq. (28) and comparing coefficients shows that

$$\boldsymbol{T}_i(\boldsymbol{x}_{0i}) = \overline{\boldsymbol{T}}_i, \tag{38}$$

holds on $\partial\Omega_i$. When taking $k = 1$, i.e., no surface partitioning at all, the equivalence of homogeneous stress BC to the kinematic minimal BC is implied. If $\partial\Omega_i$ does not contain three linear independent surface normals, we are restricted to the part of $\boldsymbol{T}_i$ that is projected from the right handside into the subspace spanned by the linear independent surface orientations. However, only surface normals from $\partial\Omega_i$ are multiplied from the right to $\boldsymbol{T}_i$, i.e., the missing part does not enter the argumentation.

Because of Eq. (38), one can pull $\overline{\boldsymbol{T}}_i$ out of the integral in Eq. (20), and it remains

$$0 = \sum_{i=1,n}\overline{\boldsymbol{T}}_i \cdot\cdot \left[\int_{\partial\Omega_i}\dot{\boldsymbol{u}}_i(\boldsymbol{x}_{0i})\otimes\mathrm{d}\boldsymbol{A}_0 - \dot{\overline{\boldsymbol{H}}}_i\int_{\partial\Omega_i}\boldsymbol{x}_0\otimes\mathrm{d}\boldsymbol{A}_0\right]. \tag{39}$$

We notice that the expression in the squared brackets is zero due to the premise that Eq. (1) holds on all $\partial\Omega_i$, which means that the Hill–Mandel-condition is fulfilled.

References

[1] T. Böhlke, F. Fritzen, K. Jöchen, R. Tsotsova, International Journal of Material Forming 2 (2009) 915–917.
[2] E.W.C. Coenen, V.G. Kouznetsova, M.G.D. Geers, International Journal for Numerical Methods in Engineering 90 (2012) 1–21.
[3] J. Fish, R. Fan, International Journal for Numerical Methods in Engineering 76 (2008) 1044–1064.
[4] R. Glüge, M. Weber, A. Bertram, Computational Material Science 63 (2012) 91–104.
[5] R. Hill, Proceedings of the Royal Society of London A 65 (1952) 349–354.
[6] H. Inglis, P. Geubelle, K. Matous, Philosophical Magazine 88 (16) (2008) 2373–2397.
[7] J. Kreikemeier, Technische Mechanik 32 (6) (2012) 658–666.
[8] C. Miehe, Computer Methods in Applied Mechanics and Engineering 192 (2003) 559–591.
[9] C. Miehe, J. Schotte, M. Lambrecht, Journal of the Mechanics and Physics of Solids 50 (10) (2002) 2123–2167.
[10] S. Nemat-Nasser, Mechanics of Materials 31 (1999) 493–523.
[11] M. Ortiz, E. Repetto, Journal of the Mechanics and Physics of Solids 47 (1999) 397–462.
[12] M. Ortiz, L. Stainier, Computer Methods in Applied Mechanics and Engineering 171 (3–4) (1999) 419–444.
[13] C. Pelissou, J. Baccou, Y. Monrie, F. Perales, International Journal of Solids and Structures 46 (2009) 2842–2855.
[14] P. Suquet, Homogenization Techniques for Composite Media, Lectures Delivered at the CISM International Center for Mechanical Sciences Udine, Italy, July 1–5, 1985. Lecture Notes in Physics, vol. 272, Springer-Verlag, Berlin, 1987 (Chapter Averages, Boundary conditions).
[15] W. Drugan, J. Willis, Journal of the Mechanics and Physics of Solids 44 (4) (1996) 497–524.
[16] T. Kanit, S. Forest, I. Galliet, V. Mounoury, D. Jeulin, International Journal of Solids and Structures 40 (2003) 3647–3679.
[17] R. Glüge, M. Weber, A. Bertram, Computational Material Science 63 (2012) 91–104.
[18] R. Hill, Journal of the Mechanics and Physics of Solids 11 (5) (1963) 357–372.
[19] Z. Hashin, Journal of Applied Mechanics 50 (1983) 481–505.

In R. Glüge und J. Kalisch (2014). **The effective stiffness and stress concentrations of a multi-layer laminate**. In: *Composite Structures* 111, S. 580–586

- wurde ein kompakter Ausdruck für die effektive Laminatsteifigkeit mit beliebig vielen anisotropen Konstituenten hergeleitet,
- wurden kompakte Ausdrücke für die Spannungs- und Dehnungskonzentrationstensoren hergeleitet,
- wurde ein ausführlicher Vergleich zu isotropen und anisotropen Lösungen der klassischen Laminattheorie und zu isotropen dreidimensionalen Lösungen vollzogen,
- wurde festgestellt, dass die klassische Laminattheorie vollständig als Spezialfall in der 3D Homogenisierung enthalten ist.

Composite Structures 111 (2014) 580–586

Contents lists available at ScienceDirect

Composite Structures

journal homepage: www.elsevier.com/locate/compstruct

The effective stiffness and stress concentrations of a multi-layer laminate

Rainer Glüge *, Jan Kalisch

Otto-von-Guericke-University Magdeburg, Universitätsplatz 2, D-39106, Germany

ARTICLE INFO

Article history:
Available online 5 February 2014

Keywords:
Laminate
Jump balance
Anisotropy
Effective stiffness
Stress concentration

ABSTRACT

Using the jump conditions for the geometrically linearized strains and the Cauchy stresses and assuming homogeneous strain and stress fields inside the layers, we determine the effective stiffness tetrad of a laminate consisting of linearly elastic layers. From a two-layer reference solution, an explicit solution for the multi-layer case is derived. Unlike classical methods, the present approach applies to any loading case and an arbitrary number of layers with arbitrary stiffness tetrads, and can be considered as the explicit analytical solution of the multi-layer homogenization in linear elasticity.

1. Introduction

Laminates are widely used in industrial applications and aeronautics (see, e.g., [18]), because their properties can be controlled by choosing different material combinations, volume fractions, fiber orientations, etc. Thus, one can design laminates adjusted to ones needs, e.g., a high mass-specific strength in aeronautics, low cost plates in mass productions, and fiber reinforcement that is optimized for specific loading cases.

In order to accelerate simulations for composite materials, a reliable prediction of its effective elastic properties is required. Also, for the design of laminates with specific elastic properties, analytical estimates are needed. The optimization problems that arise in this context are still subject to performance improvement (e.g. [11]). A recent comparison of different analytical models for estimating the effective stiffness due to a wavy fiber alignment can be found in Nik et al. [17]. A comparison of an analytical, semi-analytical and numerical estimates can be found in Rodríguez-Ramos [20].

In the present paper, we present the analytical effective stiffness of a multi-layer laminate with arbitrary anisotropic stiffness tetrads and volume fractions. The concentration tensors for calculating the partial stresses and strains from the effective stresses and strains and are obtained as well. The partial stresses are usually needed for predicting failure of the laminate (e.g. [12]). The result is obtained by considering the *jump balances of stresses and strains* and presuming *piecewise homogeneous stress and strain fields* in the individual layers. A similar proceeding has been employed by Martínez et al. [16], who considered the isostrain condition parallel and the isostress condition perpendicular to the interface to estimate the delamination resistance. Likewise, the jump conditions have been used by Idiart [10] to give expressions for the effective stress and strain potentials of infinite-rank laminates of two phases, where the laminates at the different scales have different orientations. Here we are concerned with arbitrary many layers, but only one interface orientation. However, the rank-1 case in Idiart [10] corresponds to the double-layer laminate in this work.

The engineers approach is to consider specific loading cases, like tension/compression parallel and perpendicular to the laminate normal, shearing parallel and perpendicular to the laminate, with specific material symmetries and a symmetric alignment of the anisotropy axes. For each of theses loading cases, specific rules of mixture apply to specific elastic constants. For example, in a tension test parallel to an interface of a laminate of isotropic constituents, the effective Young's modulus is given by the Voigt average, i.e. the arithmetic mean of the Young's moduli. However, this approach works only for special layer arrangements [5], for which the notion of the effective laminate behavior is obvious.

The analytical effective stiffness of a double layer composite with arbitrary layer stiffnesses has been given already by Francfort and Murat [6] (see Section 4.1). This work is, however, mainly concerned with bounds, and extremely mathematical, so it is hard to extract explicit results for engineering applications.[1] The present

* Corresponding author. Tel.: +49 391 67 52592; fax: +49 391 67 12863.
E-mail addresses: gluege@ovgu.de (R. Glüge), jan.kalisch@ovgu.de (J. Kalisch).

[1] For example, the restriction to the three-dimensional space comes after the analytical homogenization of the double layer laminate.

http://dx.doi.org/10.1016/j.compstruct.2014.01.027
0263-8223/

article lays out a more conventional proceeding, with nevertheless quite general but also practical results. We find explicit symbolic expressions for the effective stiffness of a m-layer laminate. The explicit expression for a two-layer composite can already be extracted from Francfort and Murat [6], while the explicit expression for the multi-layer case appears to be new.

1.1. Jump balances

In the context of linear elasticity, the jump balances have been exploited by, e.g., Laws [13], Gemperlová et al. [7], and Dvorak [5]. The principle result is that the jump of the stresses and strains can be calculated using only the stiffness tetrads on both sides and the stresses and strains on one side of the interface. However, the focus is on stress concentration factors rather than effective stiffness tetrads. The jump balances have firstly been used by Francfort and Murat [6] to determine the effective laminate stiffness, but the method remained somewhat unnoticed.

1.2. Piecewise homogeneous stress and strain fields

The assumption of homogeneous stresses and strains inside the lamellae is quite common [2]. Here, it is tacitly implied by the rule of mixture for the stresses and strains. The assumption is particularly reasonable for thin layers: fluctuations are energetically unfavorable, i.e., in the absence of microscopic perturbations (other than the interfaces), the stress and strain fields are homogeneous in each layer. If the lamellae thickness is similar to that of the whole laminate, the homogeneity is rendered unrealistic by bending moments. This corresponds to the well-known loss of scale separation between the microscale and the macroscale [8]. In this case, the layers need to be considered explicitly in the engineering problem. Particular methods have been developed to this end, see, e.g., Makeev and Armanios [15].

1.3. Outline

First, we give the general solution for the effective stiffness tetrad, the stress concentrations, and the strain concentrations in the two-layer case. Then, we investigate two examples in more detail: (a) two isotropic layers and (b) two transversely isotropic layers of equal stiffness and volume fraction but different fiber direction. Next, we consider the multi-layer case. Based on the two-layer-solution, we derive an explicit expression for the effective stiffness tetrad. Finally, we compare our result to other approaches.

1.4. Notation

A direct notation is preferred. Vectors are denoted as bold minuscules (like $\boldsymbol{a}$), second-order tensors as bold majuscules or bold greek letters (like $\boldsymbol{A}, \varepsilon, \sigma$), and fourth-order tensors as super bold majuscules (like $\mathbb{A}$). The dyadic product and single scalar contractions are denoted like $(\boldsymbol{a}\otimes\boldsymbol{b}\otimes\boldsymbol{c})\cdot\cdot(\boldsymbol{d}\otimes\boldsymbol{e}) = (\boldsymbol{b}\cdot\boldsymbol{d})(\boldsymbol{c}\cdot\boldsymbol{e})\boldsymbol{a}$, with $\cdot$ being the usual scalar product between vectors. The upper index T denotes the transpose of a second-order tensor, $(\boldsymbol{a}\otimes\boldsymbol{b})^T := \boldsymbol{b}\otimes\boldsymbol{a}$. The upper index S is used to define symmetric parts for second- and fourth-order tensors,

$$\boldsymbol{A}^S := \frac{1}{2}(\boldsymbol{A}+\boldsymbol{A}^T), \tag{1}$$

$$\mathbb{A}^S := \frac{1}{4}(A_{ijkl}+A_{jikl}+A_{ijlk}+A_{jilk})\boldsymbol{e}_i\otimes\boldsymbol{e}_j\otimes\boldsymbol{e}_k\otimes\boldsymbol{e}_l. \tag{2}$$

Components are given w.r.t. orthonormalized bases $\{\boldsymbol{e}_i\}$ or $\{\boldsymbol{E}_I\}$, where

$$\begin{aligned}
\boldsymbol{E}_1 &:= \boldsymbol{e}_1\otimes\boldsymbol{e}_1, & \boldsymbol{E}_4 &:= \sqrt{2}(\boldsymbol{e}_2\otimes\boldsymbol{e}_3)^S,\\
\boldsymbol{E}_2 &:= \boldsymbol{e}_2\otimes\boldsymbol{e}_2, & \boldsymbol{E}_5 &:= \sqrt{2}(\boldsymbol{e}_3\otimes\boldsymbol{e}_1)^S,\\
\boldsymbol{E}_3 &:= \boldsymbol{e}_3\otimes\boldsymbol{e}_3, & \boldsymbol{E}_6 &:= \sqrt{2}(\boldsymbol{e}_1\otimes\boldsymbol{e}_2)^S.
\end{aligned}$$

We make use of Einstein's summation convention with implicit summation from 1 to 3 and 1 to 6 for minuscule and majuscule indices that appear pairwise in a product, e.g., the second order identity tensor is given by

$$\boldsymbol{I} = \boldsymbol{e}_i\otimes\boldsymbol{e}_i = \boldsymbol{E}_1+\boldsymbol{E}_2+\boldsymbol{E}_3. \tag{3}$$

Within this paper, all relevant fourth-order tensors possess the left and right subsymmetry, i.e., $A_{ijkl} = A_{jikl} = A_{ijlk} = A_{jilk}$. The inverse of such fourth-order tensors satisfies $\mathbb{A}\cdot\cdot\mathbb{A}^{-1} = \mathbb{I}^S$, where

$$\mathbb{I}^S = \frac{1}{2}(\boldsymbol{e}_i\otimes\boldsymbol{e}_j\otimes\boldsymbol{e}_i\otimes\boldsymbol{e}_j + \boldsymbol{e}_i\otimes\boldsymbol{e}_j\otimes\boldsymbol{e}_j\otimes\boldsymbol{e}_i) = \boldsymbol{E}_I\otimes\boldsymbol{E}_I \tag{4}$$

denotes the fourth order identity tensor on symmetric second-order tensors.

2. Solution for a two-layer laminate

For a two-layer laminate, we have to consider only one interface with normal $\boldsymbol{n}$. The quantities on different sides of the interface are distinguished by upper indices $+$ and $-$. The jump balances for the Cauchy stresses (σ) and the strains (ε) and the volume average of these quantities are given by

$$\varepsilon^+ - \varepsilon^- = (\boldsymbol{a}\otimes\boldsymbol{n})^S, \tag{5}$$

$$(\sigma^+ - \sigma^-)\cdot\boldsymbol{n} = \boldsymbol{o}, \tag{6}$$

$$V := V^+ + V^-, \tag{7}$$

$$V^\pm \geqslant 0, \tag{8}$$

$$\varepsilon := \frac{1}{V}(V^+\varepsilon^+ + V^-\varepsilon^-), \tag{9}$$

$$\sigma := \frac{1}{V}(V^+\sigma^+ + V^-\sigma^-), \tag{10}$$

where $\boldsymbol{a}\otimes\boldsymbol{n}$ is the jump of the deformation gradient at the interface. Inside the layers we assume Hooke's law,

$$\sigma^\pm = \mathbb{C}^\pm\cdot\cdot\varepsilon^\pm, \tag{11}$$

with the stiffness tetrads $\mathbb{C}^\pm$. Subsequently, we will use abbreviations to denote volume fractions, the difference of stiffness tetrads and the Voigt average

$$v^\pm := \frac{V^\pm}{V}, \tag{12}$$

$$\Delta\mathbb{C} := \mathbb{C}^+ - \mathbb{C}^-, \tag{13}$$

$$\mathbb{C}^V := v^+\mathbb{C}^+ + v^-\mathbb{C}^-. \tag{14}$$

Next, we seek an explicit expression for $\mathbb{C}$ in $\sigma = \mathbb{C}\cdot\cdot\varepsilon$. Inserting the constitutive equations (Eq. 11) into the jump balance of the stresses (Eq. 6) gives

$$(\mathbb{C}^+\cdot\cdot\varepsilon^+ - \mathbb{C}^-\cdot\cdot\varepsilon^-)\cdot\boldsymbol{n} = \boldsymbol{o}. \tag{15}$$

Using the jump balance for the strains (Eq. 5), we can eliminate either ε^+ or ε^-, thus

$$(\mathbb{C}^+\cdot\cdot(\boldsymbol{a}\otimes\boldsymbol{n})^S + \Delta\mathbb{C}\cdot\cdot\varepsilon^-)\cdot\boldsymbol{n} = \boldsymbol{o}, \tag{16}$$

$$(\mathbb{C}^-\cdot\cdot(\boldsymbol{a}\otimes\boldsymbol{n})^S + \Delta\mathbb{C}\cdot\cdot\varepsilon^+)\cdot\boldsymbol{n} = \boldsymbol{o}. \tag{17}$$

Since the stiffness tetrads possess the sub-symmetries, we can drop the symmetrization of $\boldsymbol{a}\otimes\boldsymbol{n}$ and rewrite these equations

$$\boldsymbol{A}^+\cdot\boldsymbol{a} = -(\Delta\mathbb{C}\cdot\cdot\varepsilon^-)\cdot\boldsymbol{n}, \tag{18}$$

$$\boldsymbol{A}^-\cdot\boldsymbol{a} = -(\Delta\mathbb{C}\cdot\cdot\varepsilon^+)\cdot\boldsymbol{n}. \tag{19}$$

The so-called acoustic tensors $\boldsymbol{A}^{\pm}$ are associated to the stiffness tetrads where $A_{ik} := C_{ijkl} n_j n_l$ are the components w.r.t. an orthonormal basis. Multiplying the latter equations with the volume fractions v^- and v^+, respectively, their sum becomes

$$(v^- \boldsymbol{A}^+ + v^+ \boldsymbol{A}^-) \cdot \boldsymbol{a} = -(\Delta\mathbb{C} \cdot\cdot\, \varepsilon) \cdot \boldsymbol{n}, \tag{20}$$

where the rule of mixture for the strains (Eq. 9) has been used. This equation can be used to determine $\boldsymbol{a}$. For convenience, we define the tensors $\boldsymbol{Z}$ and $\mathbb{Z}$ via

$$\boldsymbol{Z} := (v^- \boldsymbol{A}^+ + v^+ \boldsymbol{A}^-)^{-1}, \tag{21}$$

$$\mathbb{Z} := \boldsymbol{n} \otimes \boldsymbol{Z} \otimes \boldsymbol{n}, \tag{22}$$

which renders a compact expression for $\boldsymbol{n} \otimes \boldsymbol{a}$

$$\boldsymbol{n} \otimes \boldsymbol{a} = -\mathbb{Z} \cdot\cdot\, \Delta\mathbb{C} \cdot\cdot\, \varepsilon. \tag{23}$$

With the stiffness tetrads being positive definite, the acoustic tensors are positive definite, too, and so is their weighted sum. Thus $\boldsymbol{Z}$ exists and is positive definite. The intermediate fourth-order tensor $\mathbb{Z}$ possesses neither the major symmetry nor one of the subsymmetries. With the subsymmetries of $\mathbb{C}^{\pm}$ and the symmetrization of $\boldsymbol{n} \otimes \boldsymbol{a}$ we can impose the subsymmetries without loss of generality, thus replacing $\mathbb{Z}$ by $\mathbb{Z}^S$. Then, due to the symmetry of $\boldsymbol{Z}$, $\mathbb{Z}^S$ also possesses the major symmetry. The strain jump is conveniently rewritten as

$$(\boldsymbol{a} \otimes \boldsymbol{n})^S = -\mathbb{Z}^S \cdot\cdot\, \Delta\mathbb{C} \cdot\cdot\, \varepsilon. \tag{24}$$

On the other hand, combining the constitutive equations (Eq. 11) and the rule of mixture for the stresses (Eq. 10), we find the effective stresses,

$$\sigma = v^+ \mathbb{C}^+ \cdot\cdot\, \varepsilon^+ + v^- \mathbb{C}^- \cdot\cdot\, \varepsilon^-. \tag{25}$$

By means of the jump balance of the strains (Eq. 5), we can remove either ε^- or ε^+,

$$\sigma = (v^+ \mathbb{C}^+ + v^- \mathbb{C}^-) \cdot\cdot\, \varepsilon^+ + v^- \mathbb{C}^- \cdot\cdot\, (\boldsymbol{a} \otimes \boldsymbol{n})^S, \tag{26}$$

$$\sigma = (v^+ \mathbb{C}^+ + v^- \mathbb{C}^-) \cdot\cdot\, \varepsilon^- - v^+ \mathbb{C}^+ \cdot\cdot\, (\boldsymbol{a} \otimes \boldsymbol{n})^S. \tag{27}$$

The first term on either right hand side contains the Voigt average. Again, multiplying the latter equations by v^+ and v^-, their sum provides the effective stiffness $\mathbb{C}$

$$\sigma = \mathbb{C} \cdot\cdot\, \varepsilon, \tag{28}$$

$$\mathbb{C} := \mathbb{C}^V - v^+ v^- \Delta\mathbb{C} \cdot\cdot\, \mathbb{Z}^S \cdot\cdot\, \Delta\mathbb{C}, \tag{29}$$

where Eqs. (9) and (24) have been used. The result is reasonable: As expected, $\mathbb{C}$ is invariant under a change of the phase indices $+ \leftrightarrow -$ and inherits the major symmetry and both subsymmetries from $\mathbb{C}^{\pm}$. It is also invariant under a scaling or a change of sign of $\boldsymbol{n}$. For the extremal cases $\mathbb{C}^+ = \mathbb{C}^-$, $v^+ = 0$ or $v^- = 0$, we obtain the stiffness tetrad of a homogeneous medium. The second summand in Eq. (29) is negative semi-definite, thus the Voigt bound cannot be exceeded. Further plausibility tests are postponed to Section 2.2, where isotropic phases are considered.

2.1. Concentration tensors

Using Eqs. (9), (5), and (24) defining the $\mathbb{K}$- and $\mathbb{L}$-tensors by

$$\mathbb{K}^{\pm} := \mathbb{I}^S \mp v^{\mp} \mathbb{Z}^S \cdot\cdot\, \Delta\mathbb{C}, \tag{30}$$

$$\mathbb{L}^{\pm} := \mathbb{C}^{\pm} \cdot\cdot\, \mathbb{K}^{\pm} \cdot\cdot\, \mathbb{C}^{-1}, \tag{31}$$

we can express the partial strains and stresses in terms of the effective strains and stresses, respectively,

$$\varepsilon^{\pm} = \mathbb{K}^{\pm} \cdot\cdot\, \varepsilon, \tag{32}$$

$$\sigma^{\pm} = \mathbb{L}^{\pm} \cdot\cdot\, \sigma. \tag{33}$$

This concept is due to Hill [9]. The non-dimensional concentration tensors fulfill

$$\mathbb{I}^S = v^+ \mathbb{K}^+ + v^- \mathbb{K}^-, \tag{34}$$

$$\mathbb{I}^S = v^+ \mathbb{L}^+ + v^- \mathbb{L}^-. \tag{35}$$

In like vein, we can relate the partial stresses and the effective strains via $\mathbb{M}$-tensors

$$\mathbb{M}^{\pm} := \mathbb{C}^{\pm} \cdot\cdot\, \mathbb{K}^{\pm}, \tag{36}$$

$$\sigma^{\pm} = \mathbb{M}^{\pm} \cdot\cdot\, \varepsilon, \tag{37}$$

$$\mathbb{C} = v^+ \mathbb{M}^+ + v^- \mathbb{M}^-, \tag{38}$$

as has been done first by Laws [13] (Eqs. (28) and (29) there). All concentration tensors exhibit both subsymmetries but not the major symmetry, in general. The partial stresses are required for estimating the strength of a laminate. With the partial stresses at hand, one can evaluate a flow or failure criterion inside the layers, or calculate the normal traction and shear stresses at the interface. The latter is needed to predict the delamination resistance, see, e.g., Zou et al. [21] and Diaz Diaz and Caron [4].

2.2. Example 1: isotropic layers

Let us consider two isotropic stiffness tetrads, given in terms of the fourth-order isotropic projectors $\mathbb{P}_1$ and $\mathbb{P}_2$,

$$\mathbb{C}^{\pm} = 3K^{\pm} \mathbb{P}_1 + 2G^{\pm} \mathbb{P}_2, \tag{39}$$

$$\mathbb{P}_1 := \frac{1}{3} \boldsymbol{I} \otimes \boldsymbol{I}, \tag{40}$$

$$\mathbb{P}_2 := \mathbb{I}^S - \frac{1}{3} \boldsymbol{I} \otimes \boldsymbol{I}. \tag{41}$$

For the subsequent sections, the following abbreviations come in handy,

$$A^{\pm} := C^{\pm}_{11} = K^{\pm} + \frac{4}{3} G^{\pm}, \quad 3K^{\pm} = A^{\pm} + 2B^{\pm}, \tag{42}$$

$$B^{\pm} := C^{\pm}_{12} = K^{\pm} - \frac{2}{3} G^{\pm}, \quad 2G^{\pm} = A^{\pm} - B^{\pm}. \tag{43}$$

A and B correspond to $k + m$ and $k - m$, with the moduli k and m as used by Hill [9].

Furthermore, the following combinations (difference, Voigt average, mixed average, Reuss average) will appear frequently in subsequent sections,

$$\Delta X := X^+ - X^-, \tag{44}$$

$$X^V := v^+ X^+ + v^- X^-, \tag{45}$$

$$X^M := v^+ X^- + v^- X^+, \tag{46}$$

$$X^R := \left(v^+ (X^+)^{-1} + v^- (X^-)^{-1} \right)^{-1}, \tag{47}$$

$$= X^V - v^+ v^- \frac{\Delta X^2}{X^M}, \tag{48}$$

$$= \frac{X^+ X^-}{X^M}, \tag{49}$$

where $X \in \{A, B, G, K, \boldsymbol{A}, \mathbb{C}\}$. W.r.t. the basis $\{\boldsymbol{E}_I \otimes \boldsymbol{E}_J\}$, the components are

$$\mathbb{C}^{\pm} = \begin{bmatrix} C^{\pm}_{11} & C^{\pm}_{12} & C^{\pm}_{12} & & & \\ C^{\pm}_{12} & C^{\pm}_{11} & C^{\pm}_{12} & & & \\ C^{\pm}_{12} & C^{\pm}_{12} & C^{\pm}_{11} & & & \\ & & & C^{\pm}_{11} - C^{\pm}_{12} & & \\ & & & & C^{\pm}_{11} - C^{\pm}_{12} & \\ & & & & & C^{\pm}_{11} - C^{\pm}_{12} \end{bmatrix}. \tag{50}$$

The effective stiffness tetrad becomes transversely isotropic w.r.t. the interface normal $\boldsymbol{n}$. For $\boldsymbol{n}=\boldsymbol{e}_3$, the non-zero components of $\mathbb{C}$ w.r.t. $\{\boldsymbol{E}_I\otimes\boldsymbol{E}_J\}$ are given by

$$\mathbb{C}=\begin{bmatrix} C_{11} & C_{12} & C_{13} & & & \\ C_{12} & C_{11} & C_{13} & & & \\ C_{13} & C_{13} & C_{33} & & & \\ & & & C_{44} & & \\ & & & & C_{44} & \\ & & & & & C_{11}-C_{12} \end{bmatrix}, \tag{51}$$

where

$$C_{11}=A^V-v^-v^+\frac{\Delta B^2}{A^M}, \tag{52}$$

$$C_{12}=B^V-v^-v^+\frac{\Delta B^2}{A^M}, \tag{53}$$

$$C_{13}=B^V-v^-v^+\frac{\Delta A\Delta B}{A^M}, \tag{54}$$

$$C_{33}=A^R, \tag{55}$$

$$C_{44}=2G^R, \tag{56}$$

$$C_{66}=C_{11}-C_{12}=2G^V. \tag{57}$$

$2G^V$ and $2G^R$ are double eigenvalues of $\mathbb{C}$. The corresponding eigendeformations $\varepsilon^{V/R}$ are given by arbitrary linear combinations (with coefficients $l_i^{V/R}$)

$$\varepsilon^V=l_1^V\boldsymbol{E}_6+l_2^V\frac{1}{\sqrt{2}}(\boldsymbol{E}_1-\boldsymbol{E}_2), \tag{58}$$

$$\varepsilon^R=l_1^R\boldsymbol{E}_4+l_2^R\boldsymbol{E}_5. \tag{59}$$

Thus, depending on whether a shear deformation $\boldsymbol{F}=\boldsymbol{I}+\gamma\boldsymbol{d}\otimes\boldsymbol{s}$ has either $\boldsymbol{d}$ or $\boldsymbol{s}$ parallel and the other one perpendicular to the interface (Reuss case) or both $\boldsymbol{d}$ and $\boldsymbol{s}$ parallel to the interface (Voigt case), one obtains the correct shear modulus, i.e., the lamellae appear in sequence or parallel w.r.t. the shear deformation. These eigendeformations are independent on $K^\pm$ and $G^\pm$.

The remaining two eigendeformations depend on $K^\pm$ and $G^\pm$,

$$\varepsilon_5^\alpha=\frac{\cos\alpha}{\sqrt{2}}(\boldsymbol{E}_1+\boldsymbol{E}_2)+\sin\alpha\boldsymbol{E}_3, \tag{60}$$

$$\varepsilon_6^\alpha=-\frac{\sin\alpha}{\sqrt{2}}(\boldsymbol{E}_1+\boldsymbol{E}_2)+\cos\alpha\boldsymbol{E}_3, \tag{61}$$

where the parameter α is determined by

$$\cot 2\alpha=\frac{(v^+)^2B^+A^-+(v^-)^2B^-A^++v^+v^-(\Delta A^2-2\Delta B^2+A^+B^++A^-B^-)}{2\sqrt{2}(v^+B^+A^-+v^-B^-A^+)}. \tag{62}$$

In the event of $G^+=G^-$, the laminate stiffness becomes isotropic. This is an example for the fundamental result of Hill [9], who found that any microstructure of two isotropic materials with equal shear rigidity is isotropic, irrespective of the geometry of the microstructure.

For the concentration tensors $\mathbb{K}^+$ and $\mathbb{L}^+$, we find the following components w.r.t. $\boldsymbol{E}_I\otimes\boldsymbol{E}_J$,

$$\mathbb{K}^\pm=\begin{bmatrix} 1 & 0 & 0 & & & \\ 0 & 1 & 0 & & & \\ K_{31}^\pm & K_{31}^\pm & K_{33}^\pm & & & \\ & & & K_{44}^\pm & & \\ & & & & K_{44}^\pm & \\ & & & & & 1 \end{bmatrix}, \tag{63}$$

$$\mathbb{L}^\pm=\begin{bmatrix} L_{11}^\pm & L_{12}^\pm & L_{13}^\pm & & & \\ L_{12}^\pm & L_{11}^\pm & L_{13}^\pm & & & \\ 0 & 0 & 1 & & & \\ & & & 1 & & \\ & & & & 1 & \\ & & & & & L_{11}^\pm-L_{12}^\pm \end{bmatrix}, \tag{64}$$

where

$$K_{31}^+=-v^-\frac{\Delta B}{A^M},\quad L_{11}^+=\frac{G^+}{G^V}\left(1+\frac{v^-G^-(A^-B^+-A^+B^-)}{3(v^-G^-K^-A^++v^+G^+K^+A^-)}\right), \tag{65}$$

$$K_{33}^+=\frac{A^-}{A^M},\quad L_{12}^+=\frac{G^+}{G^V}\frac{v^-G^-(A^-B^+-A^+B^-)}{3(v^-G^-K^-A^++v^+G^+K^+A^-)}, \tag{66}$$

$$K_{44}^+=\frac{G^-}{G^M},\quad L_{13}^+=-v^-\frac{(A^+)^2B^--(A^-)^2B^++B^+B^-(\Delta A-2\Delta B)}{6(v^-G^-K^-A^++v^+G^+K^+A^-)}, \tag{67}$$

$$\text{and}\qquad L_{66}^+=L_{11}^+-L_{12}^+=\frac{G^+}{G^V}. \tag{68}$$

The counterparts $\mathbb{K}^-$ and $\mathbb{L}^-$ are easily determined by virtue of Eqs. (34) and (35), respectively.

2.2.1. Comparison to other results

2.2.1.1. Classical laminate theory. In the classical laminate theory (CLT), a plane stress state is usually presumed, i.e. there are only three non-zero in-plane stress components (σ_{11},σ_{22} and σ_{12} when $\boldsymbol{e}_3$ is the laminate normal), coupled by a Q_{ij}-matrix to the three independent strain components $\varepsilon_{11},\varepsilon_{22}$ and ε_{12} [3]. Thus, Hooke's matrix is reduced to an effective 3×3 matrix Q_{ij} for a plane stress state, which is obtained by adding the individual plane-stress Hooke matrices $Q_{ij}^\pm$ of the individual materials, weighted by the layer thickness fraction. Considering this special case, we found full agreement with the CLT approach by applying a plane stress state to the inverse of $\mathbb{C}$ (given in Section 2.2, Eq. 51), inverting the relations of the independent strain components and extracting the reduced plane strain stiffness.

2.2.1.2. Liu et al. [14]. The work of Liu et al. [14] follows the proceeding outlined in the introduction: for isotropic phases, the effective transversally isotropic laminate stiffness is presumed, and for some characteristic in-plane and normal-to-plane tests the corresponding kinematic and dynamic equivalences are exploited to derive the compliance constants. We found all given effective compliances (Eqs. (21), (22), (29), (30), (35), and (36) in Liu et al. [14]) in agreement with our results.

2.3. Example 2: two transversely isotropic layers, orthotropic laminate

Another important case is the stacking of unidirectionally reinforced layers. These layers exhibit a transversely isotropic stiffness tetrad with the fiber direction and symmetry axis $\boldsymbol{d}$,

$$\begin{aligned}\mathbb{C}^t(\boldsymbol{d}) :=\ & C_{12}^t\boldsymbol{I}\otimes\boldsymbol{I}+(C_{11}^t-C_{12}^t)\mathbb{I}^S \\ & +2(C_{12}^t-C_{11}^t+C_{44}^t)(\boldsymbol{d}\otimes\boldsymbol{I}\otimes\boldsymbol{d})^S \qquad (69)\\ & +(C_{13}^t-C_{12}^t)(\boldsymbol{I}\otimes\boldsymbol{d}\otimes\boldsymbol{d}+\boldsymbol{d}\otimes\boldsymbol{d}\otimes\boldsymbol{I}) \\ & +(C_{11}^t+C_{33}^t-2C_{13}^t-2C_{44}^t)\boldsymbol{d}\otimes\boldsymbol{d}\otimes\boldsymbol{d}\otimes\boldsymbol{d}. \qquad (70)\end{aligned}$$

For $\boldsymbol{d}=\boldsymbol{e}_3$, the components w.r.t. the basis $\{\boldsymbol{E}_I\otimes\boldsymbol{E}_J\}$ are given by

$$\mathbb{C}^t(\boldsymbol{e}_3) = \begin{bmatrix} C^t_{11} & C^t_{12} & C^t_{13} & & & \\ C^t_{12} & C^t_{11} & C^t_{13} & & & \\ C^t_{13} & C^t_{13} & C^t_{33} & & & \\ & & & C^t_{44} & & \\ & & & & C^t_{44} & \\ & & & & & C^t_{11} - C^t_{12} \end{bmatrix} \boldsymbol{E}_I \otimes \boldsymbol{E}_J. \tag{71}$$

The components after a change of the symmetry axis from $\boldsymbol{e}_3$ to $\boldsymbol{e}_1$ are obtained by interchanging the first with the third and the fourth with the sixth rows and columns.

We consider the most common case: both layers consist of the same material but differ by the fiber direction. For both layers the fiber direction is parallel to the interface, i.e., $\boldsymbol{d}^{\pm} \cdot \boldsymbol{n} = 0$. Both layers have a volume fraction of 50%. In order not to conceal the symmetries of the effective stiffness tetrad, we choose an orthonormalized basis $\{\boldsymbol{e}_i\}$ w.r.t. which

$$\boldsymbol{d}^{\pm} = \cos\phi \boldsymbol{e}_1 \pm \sin\phi \boldsymbol{e}_2, \tag{72}$$

$$\boldsymbol{n} = \boldsymbol{e}_3. \tag{73}$$

Thus, the directions enclose an angle of 2ϕ, see Fig. 1. The effective stiffness tetrad is orthotropic w.r.t. the basis $\{\boldsymbol{e}_i\}$, and w.r.t. the basis $\{\boldsymbol{E}_I \otimes \boldsymbol{E}_J\}$, its components are given by

$$\mathbb{C} = \begin{bmatrix} C_{11} & C_{12} & C_{13} & & & \\ C_{12} & C_{22} & C_{23} & & & \\ C_{13} & C_{23} & C_{33} & & & \\ & & & C_{44} & & \\ & & & & C_{55} & \\ & & & & & C_{66} \end{bmatrix}, \tag{74}$$

where

$$C_{11} = C^t_{11}\sin^2\phi + C^t_{33}\cos^2\phi - x\cos^2\phi\sin^2\phi, \tag{75}$$

$$C_{22} = C^t_{11}\cos^2\phi + C^t_{33}\sin^2\phi - x\cos^2\phi\sin^2\phi, \tag{76}$$

$$C_{33} = C^t_{11}, \tag{77}$$

$$C_{12} = C^t_{13} + x\cos^2\phi\sin^2\phi, \tag{78}$$

$$C_{13} = C^t_{12}\sin^2\phi + C^t_{13}\cos^2\phi, \tag{79}$$

$$C_{23} = C^t_{12}\cos^2\phi + C^t_{13}\sin^2\phi, \tag{80}$$

$$C_{44} = \frac{(C^t_{11} - C^t_{12})C^t_{44}}{(C^t_{11} - C^t_{12})\sin^2\phi - C^t_{44}\cos^2\phi}, \tag{81}$$

$$C_{55} = \frac{(C^t_{11} - C^t_{12})C^t_{44}}{(C^t_{11} - C^t_{12})\cos^2\phi - C^t_{44}\sin^2\phi}, \tag{82}$$

$$C_{66} = C^t_{44} + 2\left(x - \frac{(C^t_{13} - C^t_{12})^2}{C^t_{11}}\right)\cos^2\phi\sin^2\phi, \tag{83}$$

$$x := C^t_{11} + C^t_{33} - 2(C^t_{13} + C^t_{44}). \tag{84}$$

If the angle is an integer multiple of $\frac{\pi}{2}$, the fiber directions coincide (up to the sign), and the original stiffness tetrad is recovered, albeit with a different axis of transversal isotropy.

2.3.1. Comparison to other results

Similar to the proceeding in Section 2.2.1.1, the CLT-estimate is given by averaging the plane-stress stiffnesses of the individual layers. We found complete agreement, independent on the angle ϕ and the volume fractions. The plane-stress elastic law is then given by the matrix–vector product

$$\begin{bmatrix} \sigma_{11} \\ \sigma_{22} \\ \sigma_{12} \end{bmatrix} = \frac{1}{8C^t_{11}} \begin{bmatrix} Q_{11} & Q_{12} & Q_{13} \\ & Q_{22} & Q_{23} \\ \text{sym} & & Q_{33} \end{bmatrix} \cdot \begin{bmatrix} \varepsilon_{11} \\ \varepsilon_{22} \\ \varepsilon_{12} \end{bmatrix}, \tag{85}$$

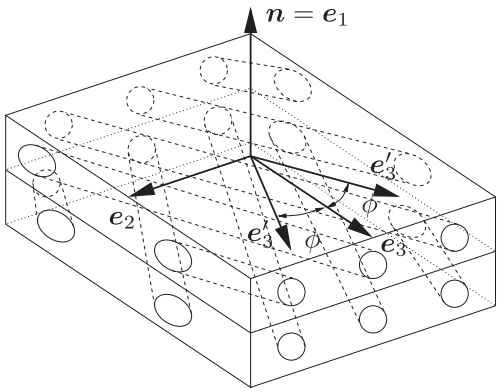

Fig. 1. Two transversely isotropic layers with equal stiffness tetrads and volume fractions.

with

$$Q_{11} = 3C^{t2}_{11} - 3C^{t2}_{12} + 2C^t_{11}C^t_{13} - 2C^t_{12}C^t_{13} - 3C^{t2}_{13} + 3C^t_{11}C^t_{33} + 2C^t_{11}C^t_{44} - 4(C^{t2}_{11} - C^{t2}_{12} + C^{t2}_{13} - C^t_{11}C^t_{33})\cos 2\phi + (C^{t2}_{11} - (C^t_{12} - C^t_{13})^2 + C^t_{11}(C^t_{33} - 2C^t_{13} - 2C^t_{44}))\cos 4\phi, \tag{86}$$

$$Q_{12} = C^{t2}_{11} - C^{t2}_{12} - C^t_{13}(6C^t_{12} + C^t_{13}) + C^t_{11}(6C^t_{13} + C^t_{33} - 2C^t_{44}) + ((C^t_{12} - C^t_{13})^2 - C^{t2}_{11} + C^t_{11}(2C^t_{13} - C^t_{33} + 2C^t_{44})) \times \cos 4\phi, \tag{87}$$

$$Q_{22} = 3C^{t2}_{11} - 3C^{t2}_{12} + 2C^t_{11}C^t_{13} - 2C^t_{12}C^t_{13} - 3C^{t2}_{13} + 3C^t_{11}C^t_{33} + 2C^t_{11}C^t_{44} + 4(C^{t2}_{11} - C^{t2}_{12} + C^{t2}_{13} - C^t_{11}C^t_{33})\cos 2\phi + (C^{t2}_{11} - (C^t_{12} - C^t_{13})^2 + C^t_{11}(C^t_{33} - 2C^t_{13} - 2C^t_{44}))\cos 4\phi, \tag{88}$$

$$Q_{33} = 2[C^{t2}_{11} - (C^t_{12} - C^t_{13})^2 + C^t_{11}(C^t_{33} - 2C^t_{13} + 2C^t_{44}) + ((C^t_{12} - C^t_{13})^2 - C^{t2}_{11} + C^t_{11}(2C^t_{13} - C^t_{33} + 2C^t_{44})) \times \cos 4\phi], \tag{89}$$

independent of the volume fractions and

$$Q_{13} = 4\Delta\nu(C^{t2}_{12} - C^{t2}_{11} - C^{t2}_{13} + C^t_{11}C^t_{33} + (C^{t2}_{11} - (C^t_{12} - C^t_{13})^2 + C^t_{11}(C^t_{33} - 2C^t_{13} - 2C^t_{44}))\cos 2\phi)\sin 2\phi, \tag{90}$$

$$Q_{23} = 4\Delta\nu(C^{t2}_{12} - C^{t2}_{11} - C^{t2}_{13} + C^t_{11}C^t_{33} - (C^{t2}_{11} - (C^t_{12} - C^t_{13})^2 + C^t_{11}(C^t_{33} - 2C^t_{13} - 2C^t_{44}))\cos 2\phi)\sin 2\phi, \tag{91}$$

where $\nu_{\pm}$ are the volume fractions of the layers that are rotated by $\pm\phi$ around the $\boldsymbol{e}_3$-axis.

3. Arbitrary many layers

Subsequently, we encounter only double contractions among fourth and second order tensors. For the sake of simplicity, we drop the respective symbol $\cdot\cdot$ in the remainder.

In the two-layer case, there is only one interface, i.e. one can assign all quantities from the two-layer case to the interface. In order to extend the two-layer solution to the multi-layer solution, we supplement all quantities by an interface index i and can apply the two-layer solution to any two layers that are adjoint to the same interface. For an m-layer composite, the indexing fulfills

$$X^+_i = X^-_{i+1} \quad \text{modulo} \quad m, \quad X \in \{V, \varepsilon, \sigma, \boldsymbol{A}, \mathbb{C}\}. \tag{92}$$

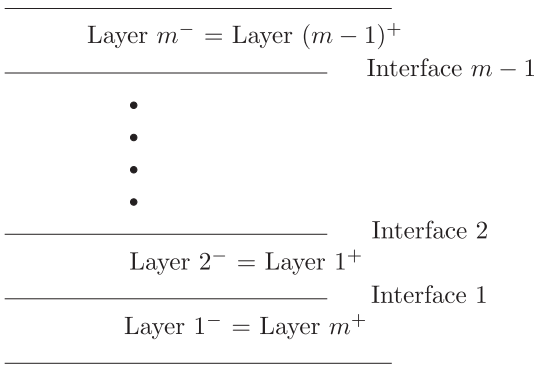

Fig. 2. Indexing of the multi-layer.

For an illustration of the indexing, see Fig. 2. The effective stiffness of the multi-layer laminate is constructed by means of the stiffness tetrads and concentration tensors (which themselves are defined in terms of stiffness tetrads, volume fractions and the interface normal). Using these, we define $\mathbb{A}$- and $\mathbb{B}$-tensors

$$\mathbb{A}_i^- := \mathbb{K}_i^+ (\mathbb{K}_i^-)^{-1}, \tag{93}$$
$$\mathbb{B}_i^- := \mathbb{C}_{i+1}^- \mathbb{A}_i^- \mathbb{C}_i^{--1}, \tag{94}$$

and find the recurrence relations for the partial strains

$$\begin{aligned} \varepsilon_{i+1}^- &= \varepsilon_i^+ && (95)\\ &= \mathbb{K}_i^+ \varepsilon_i && (96)\\ &= \mathbb{K}_i^+ (\mathbb{K}_i^-)^{-1} \varepsilon_i^- && (97)\\ &= \mathbb{A}_i^- \varepsilon_i^-, && (98) \end{aligned}$$

and the partial stresses

$$\begin{aligned} \sigma_{i+1}^- &= \mathbb{C}_{i+1}^- \varepsilon_{i+1}^- && (99)\\ &= \mathbb{C}_{i+1}^- \mathbb{A}_i^- \varepsilon_i^- && (100)\\ &= \mathbb{C}_{i+1}^- \mathbb{A}_i^- (\mathbb{C}_i^-)^{-1} \sigma_i^- && (101)\\ &= \mathbb{B}_i^- \sigma_i^-. && (102) \end{aligned}$$

The inverse of $\mathbb{K}_i^-$ exists in general. Otherwise we would have a decoupling of the strains of adjoint layers, i.e., we would not consider a proper laminate.

With the conventions $\mathbb{A}_0 := \mathbb{I}^S$ and $\mathbb{B}_0 := \mathbb{I}^S$, any partial strain or stress is easily rewritten as a function of only one partial strain or stress (here: ε_1^- or σ_1^-, respectively)

$$\varepsilon_{i+1}^- = \left(\prod_{k=0}^{i} \mathbb{A}_k^- \right) \varepsilon_1^-, \tag{103}$$
$$\sigma_{i+1}^- = \left(\prod_{k=0}^{i} \mathbb{B}_i^- \right) \sigma_1^-. \tag{104}$$

where the product consists of double contractions. Thus, the effective strains and stresses are recast as a function of only ε_1^- and σ_1^-, respectively. The effective strains and stresses are given by

$$V := \sum_{i=1}^{m} V_i^{\pm}, \tag{105}$$
$$\varepsilon := \frac{1}{V} \sum_{i=1}^{m} V_i^{\pm} \varepsilon_i^{\pm}, \tag{106}$$
$$\sigma := \frac{1}{V} \sum_{i=1}^{m} V_i^{\pm} \sigma_i^{\pm}. \tag{107}$$

Considering the $-$-part of these definitions and using Eqs. (103) and (104), the effective stresses are compactly rewritten as

$$\varepsilon = \frac{1}{V} \mathbb{E}_1^- \varepsilon_1^-, \tag{108}$$
$$\sigma = \frac{1}{V} \mathbb{S}_1^- \sigma_1^-. \tag{109}$$

where

$$\mathbb{E}_1^- := \sum_{k=1}^{m} V_k^- \prod_{n=0}^{k-1} \mathbb{A}_n^-, \tag{110}$$
$$\mathbb{S}_1^- := \sum_{k=1}^{m} V_k^- \prod_{n=0}^{k-1} \mathbb{B}_n^-. \tag{111}$$

Finally, invoking Hooke's law for the $-$-phase of interface 1, we find

$$\begin{aligned} \sigma &= \frac{1}{V} \mathbb{S}_1^- \sigma_1^- && (112)\\ &= \frac{1}{V} \mathbb{S}_1^- \mathbb{C}_1^- \varepsilon_1^- && (113)\\ &= \mathbb{S}_1^- \mathbb{C}_1^- (\mathbb{E}_1^-)^{-1} \varepsilon, && (114) \end{aligned}$$

which renders the effective stiffness tetrad

$$\mathbb{C} = \mathbb{S}_1^- \mathbb{C}_1^- (\mathbb{E}_1^-)^{-1}. \tag{115}$$

The explicit expression for $\mathbb{C}$ is quite lengthy when all intermediate quantities are inserted. However, it is easily calculated step by step from the stiffness tetrads $\mathbb{C}_{1\ldots m}$, volume fractions $v_{1\ldots m}$ and the interface normal $\boldsymbol{n}$. Again, the Voigt and Reuss averaging of the shear moduli of isotropic layers are recovered for shears parallel or perpendicular to the interfaces.

A Mathematica notebook that performs this task is provided in the articles supplementary material. To obtain $\mathbb{C}$, one could also use the two-layer solution to summarize successively all layers of a multi-layer. One may also feed the linear system for $\boldsymbol{a}_{1\ldots m-1}$ directly to a computer algebra system. However, for an algorithmic implementation, the explicit expression (115) may prove useful.

For the sake of completeness, we also note that the same procedure can be started from any interface other than 1^-, as well as from the plus side of any interface.

It is noteworthy that an interchanging of two layers of a multi-layer does not affect the effective stiffness. This is clear because of the invariance of the effective stiffness of the two-layer solution under interchanging the indices. Interchanging any two layers in the multi-layer case can be regarded as a sequence of interchanges of two adjoint layers.

The closure that comes through considering the periodic arrangement does not affect the solution. Adding the jump $\varepsilon_1 - \varepsilon_m = (\boldsymbol{a}_m \otimes \boldsymbol{n})^S$ allows to sum up all strain jumps from ε_1 to ε_1, which gives $\sum_{i=1}^{m} (\boldsymbol{a}_i \otimes \boldsymbol{n})^S = \boldsymbol{O}$. This implies $\sum_{i=1}^{m} \boldsymbol{a}_n = \boldsymbol{o}$, which allows to remove one of the $\boldsymbol{a}_i$ immediately. In terms of $\mathbb{A}$- and $\mathbb{B}$-tensors, this closure corresponds to

$$\prod_{k=1}^{m} \mathbb{A}_k = \mathbb{I}^S, \tag{116}$$
$$\prod_{k=1}^{m} \mathbb{B}_k = \mathbb{I}^S. \tag{117}$$

4. Summary and outlook

Using the jump balances for the stresses and strains, Hooke's law for each layer and the assumption of homogeneity inside each layer, we derived the effective elastic stiffness of a laminate with m layers. An explicit expression for the elastic stiffness tetrad is provided. For the two-layer case, two typical examples are given, namely isotropic layers of different volume fractions and

transversely isotropic layers of equal volume fractions and stiffness tetrads but different orientations. The result passes different tests of plausibility, most importantly, the compliance with the classical laminate theory is given. It turns out that the classical laminate theory provides identically the plane-stress part of the analytical effective stiffness.

However, the analysis of the jump balances provides the full effective stiffness tetrad in a straightforward manner, using the volume fractions, the individual stiffness tetrads and the interface orientation. No restrictions regarding the stress or strain state, the symmetry class or the alignment of anisotropy axes are necessary. Nevertheless, for the sake of scale separation, the approach is only applicable when the individual layers are much thinner than the overall laminate.

The given methodology allows to easily extract all partial stresses for a given effective strain or stress. This is an important information for an estimation of the laminate strength. It may also serve for the modeling of the effective plastic behavior of laminates, since one can check the flow condition layer-wise. Further, since the full effective stiffness is given, this analytical homogenization result may serve for higher order estimates by sequential homogenization [1]. One could regard the effective stiffness of a double layer laminate as an interface stiffness, and estimate effective properties of a heterogeneous two-phase material by an interface orientation average, in the sense of Richeton and Berbenni [19]. A somewhat similar proceeding has been presented by Idiart [10], who superimposed laminates with different orientations at different scales to obtain an explicit expression for the effective strain potential of a two-phase composite, where also an interface orientation distribution is used.

Appendix A. Supplementary data

Supplementary data associated with this article can be found, in the online version, at http://dx.doi.org/10.1016/j.compstruct.2014.01.027.

References

[1] Agoras M, Ponte-Castañeda P. Homogenization estimates for multi-scale nonlinear composites. Euro J Mech A/Solids 2011;30(6):828–43.
[2] Anderson DL. Elastic wave propagation in layered anisotropic media. J Geophys Res 1961;66(9):2953–63.
[3] Berthelot J-M. Classical laminate theory. In: Composite materials, Mechanical engineering series. New York: Springer; 1999. p. 287–311.
[4] Diaz Diaz A, Caron J-F. Prediction of the onset of mode {III} delamination in carbon-epoxy laminates. Compos Struct 2006;72(4):438–45.
[5] Dvorak G. Micromechanics of composite materials. Springer; 2013.
[6] Francfort G, Murat F. Homogenization and optimal bounds in linear elasticity. Arch Rat Mech Anal 1986;94(4):307–34.
[7] Gemperlová J, Paidar V, Kroupa F. Compatibility stresses in deformed bicrystals. Czech J Phys B 1989;39(4):427–46.
[8] Hashin Z. Analysis of composite materials – a survey. J Appl Mech 1983;50:481–505.
[9] Hill R. Elastic properties of reinforced solids: some theoretical principles. J Mech Phys Solids 1963;11(5):357–72.
[10] Idiart MI. Modeling the macroscopic behavior of two-phase nonlinear composites by infinite-rank laminates. J Mech Phys Solids 2008;56(8):2599–617.
[11] Javidrad F, Nouri R. A simulated annealing method for design of laminates with required stiffness properties. Compos Struct 2011;93(3):1127–35.
[12] Ko C, Lin C, Chin H. Prediction for delamination initiation around holes in symmetric laminates. Compos Struct 1992;22(4):187–91.
[13] Laws N. On interfacial discontinuities in elastic composites. J Elast 1975;5(3–4):227–35.
[14] Liu B, Feng X, Zhang S. The effective young's modulus of composites beyond the voigt estimation due to the poisson effect. Compos Sci Technol 2009;69(13):2198–204.
[15] Makeev A, Armanios E. An iterative method for solving elasticity problems for composite laminates. J Appl Mech 1999;67:96–104.
[16] Martínez X, Oller S, Barbero E. Mechanical response of composites. Computational methods in applied sciences, vol. 10. Springer; 2008 [Ch. Study of Delamination in Composites by Using the Serial/Parallel Mixing Theory and a Damage Formulation].
[17] Nik MA, Fayazbakhsh K, Pasini D, Lessard L. A comparative study of metamodeling methods for the design optimization of variable stiffness composites. Compos Struct 2014;107(0):494–501.
[18] Niu M. Composite airframe structures: practical design information and data. Conmilit Press; 1992.
[19] Richeton T, Berbenni S. From bicrystals to spherical inclusions: a superposition method to derive analytical expressions of stress fields in presence of plastic strain gradients. Int J Solids Struct 2014;51(3–4):794–807.
[20] Rodríguez-Ramos R, de Medeiros R, Guinovart-Díaz R, Bravo-Castillero J, Otero JA, Tita V. Different approaches for calculating the effective elastic properties in composite materials under imperfect contact adherence. Compos Struct 2013;99(0):264–75.
[21] Zou Z, Reid S, Li S, Soden P. Application of a delamination model to laminated composite structures. Compos Struct 2002;56(4):375–89.

In J. Kalisch und R. Glüge (2015). **Analytical homogenization of linear elasticity based on the interface orientation distribution – a complement to the self-consistent approach**. In: *Composite Structures* 126, S. 398–416 wurde ein analytischer Ansatz zur Approximation der elastischen Steifigkeit von Kompositen vorgeschlagen. Dieser beruht auf der Reduktion der statistischen Eigenschaften des Komposits auf die Grenzflächenorientierungsverteilung. Der Ansatz erlaubt

- die analytische Abschätzung der effektiven elastischen Steifigkeit
- einschließlich der morphologieinduzierten Anisotropie.

Weiterhin hat die vorgeschlagene Abschätzung folgende Eigenschaften:

- Die Abschätzung liegt für isotrope Materialien und beliebige Grenzflächenorientierungsverteilungen innerhalb der Hashin-Shtrikman-Grenzen.
- Die Abschätzung ist komplementär zum selbstkonsistenten Ansatz.

Letztere Eigenschaft zeigt sich bei extremen Volumenfraktionen, bei welchen der Grenzflächenansatz und der selbstkonsistente Ansatz jeweils an die Hashin-Shtrikman-Grenze mit dem größeren und dem kleineren Anstieg anschmiegt. Dies ist eine Konsequenz der konträren Annahmen über die Phasenverteilung in beiden Fällen. Die selbstkonsistenten Ansätze gehen von einer Matrix-Einschluss-Struktur aus, der Grenzflächenansatz nimmt beide Phasen als gleichberechtigt an. Daher eignet sich der Grenzflächenansatz für Mikrostrukturen die

- reich an Grenzflächen sind,
- eine Matrix-Einschluss-Struktur aufweisen, bei welcher die Matrixphase die kleinere Volumenfraktion hat oder
- eine gleichartige Verteilung beider Phasen aufweisen (also sich durchdringende Phasen).

Dies konnte anhand eines Vergleichs des Grenzflächenansatzes zu RVE-Rechnungen bestätigt werden.

Composite Structures 126 (2015) 398–416

Contents lists available at ScienceDirect

Composite Structures

journal homepage: www.elsevier.com/locate/compstruct

Analytical homogenization of linear elasticity based on the interface orientation distribution – A complement to the self-consistent approach

Jan Kalisch *, Rainer Glüge *

Otto von Guericke University Magdeburg, Universitätsplatz 2, D-39106 Magdeburg, Germany

ARTICLE INFO

Article history:
Available online 6 March 2015

Keywords:
Homogenization
Self-consistent
Interface orientation distribution

ABSTRACT

We combine a laminate-based approach and an interface orientation average. For linear elasticity, we obtain analytical expressions for the effective stiffness of mixtures of two isotropic phases with isotropic, transversely isotropic, hexahedral and octahedral interface orientation distributions (IOD). The estimates are in accordance with well-established analytical results such as the Hashin–Shtrikman bounds and Hill's findings for phases with equal shear moduli.

For isotropic and transversely isotropic IODs, this approach is compared to the Hashin–Shtrikman bounds and the inclusion-based self-consistent approach. At extremal volume fractions, both approaches coincide up to first order with complementary and mixed Hashin–Shtrikman-bounds. Thus, our approach provides an alternative to the self-consistent approach.

Moreover, the effective stiffness inherits any symmetry of the IOD. Therefore, it captures basic features of the morphology-induced anisotropy.

For the hexahedral and octahedral IOD, the approach is compared to RVE simulations. To assess the impact of morphological features beyond the IOD, we consider RVEs with different microstructures but equal IOD. Comparing similar microstructures, the error attains a local minimum close to the point of equal arrangement of phases. Further, we find a reasonable agreement if the shear moduli are of the same order of magnitude or if both phases percolate the material.

1. Introduction

Context. Determining the effective macro-scale constitutive equations for microstructured materials is a challenge for both engineers and material scientists and there is a persistent demand for accurate and efficient homogenization methods.

Many authors are concerned with accelerating the numerical homogenization by the representative volume element (RVE) method (e. g., [37]), which allows for the incorporation of more complex microstructures or a macro–micro-coupling by the FE^2 method [15]. In addition, analytical methods are developed and refined. While nonlinear micro-scale material laws and complicated microstructures still require a (semi-) numerical approach, quite efficient methods have been developed for the linearly elastic setting when only volume fractions are taken into account, and for some idealized microstructures. A survey is given by, e. g., [13].

However, the main issues of the analytical homogenization are large strains, complex material behavior and complex morphologies, which render analytical estimates or even closed-form solutions to the homogenization problem complex if not impossible. First, the large strain setting and complex material behavior induce a nonlinearity that hampers analytical approaches and, second, complex microstructures induce local fluctuations of the stress and strain field that are difficult to account for. Analytical results thus are available only for idealized structures like laminates [16], ellipsoidal inclusions [14] or a unidirectional fiber alignment [27] (see [36] for more examples), whereas real microstructures are often more complex (e. g., [32]). From the results for idealized microstructures, semi-empirical models like the Halpin–Tsai model [22] have been developed.

However, we aim for an approach that is applicable to arbitrary microstructures of piecewise homogeneous phase mixtures. This approach is based on two observations:

- Most microstructures consist of piecewise homogeneous phase mixtures. The morphology is then completely described by the interface arrangement between the phases.

* Corresponding authors.
E-mail addresses: jan.kalisch@ovgu.de (J. Kalisch), gluege@ovgu.de (R. Glüge).

http://dx.doi.org/10.1016/j.compstruct.2015.02.072
0263-8223/

- At the interface, the effective material behavior can be estimated. For example, [21] gives an interface stiffness that depends on the curvature. Also, the jump balances for stresses and strains allow for a connection of the interface orientation with the constitutive equations.

The second point is a considerable advantage over the description of the microstructure by n-point correlation functions. There are only few higher-order bounds and estimates that include higher-order correlation functions, e. g., [12,31,46,42], which are also restricted to specific morphologies (e. g., perfectly disordered, [31]). Thus, it may pay off to consider alternative microstructure descriptors that are more easily connected to material properties. For example, estimates that involve the jump balances have been used already by [34,33,38,44]. The present approach consists of an interface reference solution of a two-phase laminate depending on the interface normal and an orientation average w. r. t. the interface normal. The latter involves the concept of an interface orientation distribution (IOD), hence the name of the approach. A similar approach is employed by [40].

As a first step, the methodology is examined for the effective elastic material behavior. The most interesting features of this approach become apparent already in the small strain and linearly elastic setting, where competing theories are abundant. Our approach is similar to the sequential/iterated homogenization approach by [5,11,10,30,1,39,2,29], which takes advantage of the simple homogenization of lamellar microstructures.

In the context of this work, the laminate stiffness is an auxiliary quantity within the homogenization procedure, a tool by means of which the stresses and strains in the vicinity of an interface are approximated. Clearly, this corresponds to a violation of the scale separation in the aforementioned interpretations. Therefore, the IOD approach is necessarily an approximation. Nevertheless, it is a step that goes beyond pure volume fractions, and it can be easily applied to any two-phase microstructure with sharp interfaces. To assess the quality of this approach, we compute estimates for different IODs and compare these to other analytical estimates and numerical results.

- **Comparison to other analytical estimates.** In the IOD approach, both phases are treated equally – in contrast to the ellipsoidal-inclusion based self-consistent (SC) approach[1] [8], which implies that the phase with the smaller volume fraction is the inclusion phase. Consequently, the IOD approach may serve in case of more equitable microstructures than a matrix-inclusion morphology. A thorough comparison to the SC approach shows in fact that the IOD estimates are, within the Hashin–Shtrikman bounds, opposite to the SC approach. In effect, we obtain estimates that are suitable for microstructures in which both phases percolate the material. These estimates thus complement the well-known self-consistent estimates.
- **Comparison to numerically obtained effective elasticities.** The reduction of the microstructure to the IOD involves a severe loss of information of the microstructures morphology. Specifically, the spatial arrangement of the interfaces in a representative volume of the microstructure is lost. Thus, to quantify this loss of information in terms of a deviation from the true effective material law, we consider different microstructures with equal IOD and volume fraction. For hexahedral microstructures, a reasonable agreement is found for equitable microstructures.

[1] We shall use the term *self-consistent* only with reference to this approach. Elsewhere, it is also used for homogenization approaches such as the Aleksandrov or geometric mean, see Appendix E.

Outline. We collect the ingredients for the IOD approach, namely the effective stiffness of a two-layer laminate (Section 1.1), the IOD itself (Section 1.2) and the orientation averages (Section 1.3). Focussing on the morphological aspects, we consider a mixture of two isotropic phases and apply the IOD approach to isotropic (Section 2), transversely isotropic (Section 3), and hexahedral IODs (Section 4). In Section 2 and Section 3, the IOD approach is compared to well-established analytical estimates, while in Section 4, it is compared to RVE simulations with different microstructures. In Section 5, we highlight the most important qualitative findings.

Notation. A direct notation is preferred. If the index notation is required, we will make use of Einstein's summation convention with implicit summation over pairs of indices from 1 to 3. Vectors are denoted as bold minuscules (like $\mathbf{a}$), second-order tensors as bold majuscules or bold Greek letters (like $\mathbf{A}, \varepsilon, \sigma$), and fourth-order tensors as double-stroke majuscules (like $\mathbb{A}$). Groups are denoted by italic letters, such as, e. g., $\mathcal{SO}_3$, the group of proper rotations in three-dimensional space. The dyadic product and single scalar contractions are denoted like $(\mathbf{a}\otimes\mathbf{b}\otimes\mathbf{c})\cdot\cdot(\mathbf{d}\otimes\mathbf{e}) = (\mathbf{b}\cdot\mathbf{d})(\mathbf{c}\cdot\mathbf{e})\mathbf{a}$, with $\cdot$ and $\otimes$ being the usual scalar and dyadic product between vectors, respectively. The upper index T denotes the transpose of a second-order tensor, $(\mathbf{a}\otimes\mathbf{b})^T := \mathbf{b}\otimes\mathbf{a}$. Components are given w. r. t. orthonormal bases $\{\mathbf{e}_i\}$. The symmetric parts of second and fourth order tensors are denoted as

$$\mathbf{A}_S := \frac{1}{2}(\mathbf{A}+\mathbf{A}^T), \tag{1}$$

$$\mathbb{A}_S := \mathbb{I}_S\cdot\cdot\mathbb{A}\cdot\cdot\mathbb{I}_S, \tag{2}$$

$$\mathbb{I}_S := \frac{1}{2}(\mathbf{e}_i\otimes\mathbf{e}_j\otimes\mathbf{e}_i\otimes\mathbf{e}_j + \mathbf{e}_i\otimes\mathbf{e}_j\otimes\mathbf{e}_j\otimes\mathbf{e}_i), \tag{3}$$

for second- and fourth-order tensors, respectively, where $\mathbb{I}_S$ denotes the identity on symmetric second-order tensors. Within this paper, all relevant fourth-order tensors possess the left and right subsymmetry, i. e. $A_{ijkl} = A_{jikl} = A_{ijlk} = A_{jilk}$. The inverse of such fourth-order tensors satisfies $\mathbb{A}\cdot\cdot\mathbb{A}^{-1} = \mathbb{I}_S$.

Two phases are distinguished by the upper index + or −. The interface orientation is denoted by $\mathbf{n}$, pointing into the + phase. In order to distinguish the various approaches to homogenization – Voigt, Reuss, Aleksandrov, self-consistent, Hashin–Shtrikman, Walpole -, we use lower capital indices V, R, A, SC, HS, and W respectively. Moreover, the following abbreviations for the difference, the Voigt, Reuss, Aleksandrov and mixed mean of a generic quantity Z come in handy,

$$\Delta Z := Z^+ - Z^-, \tag{4}$$

$$Z_V := v^+Z^+ + v^-Z^-, \tag{5}$$

$$Z_R := \left(v^+(Z^+)^{-1} + v^-(Z^-)^{-1}\right)^{-1}, \tag{6}$$

$$Z_A := \exp\left(v^+\ln Z^+ + v^-\ln Z^-\right), \tag{7}$$

$$Z_M := v^-Z^+ + v^+Z^-, \tag{8}$$

where the volume fractions v^- and v^+ are constrained by $v^- + v^+ = 1$ and $v^\pm \geqslant 0$. Among these expressions, the following relations hold for scalar quantities Z,

$$Z_V - Z_M = \Delta v\,\Delta Z, \tag{9}$$

$$Z_V + Z_M = Z^- + Z^+, \tag{10}$$

$$Z_R Z_M = Z^-Z^+, \tag{11}$$

$$(Z_R + Z_V)Z_M = 2Z^-Z^+ + v^-v^+\Delta Z^2, \tag{12}$$

$$(Z_R - Z_V)Z_M = -v^-v^+\Delta Z^2. \tag{13}$$

For quick reference, all variables and their first appearance are collected in the following list.

a	interface area per unit volume (Eq. (160))
$\mathbf{a}$	part of the jump of the strains at an interface (Eq. (15))
A, B, E, H	auxiliary quantities, combinations of K and G (Eqs. (49)–(51), (101))
$\tilde{\mathbb{B}}_I, \mathbb{B}_I$	(non-) orthogonal basis for transversely isotropic tetrads (Eqs. (181) and (186))
C_I	component of a transversely isotropic stiffness tetrad w. r. t. $\mathbb{B}_I$. (Eq. (192))
$C_{r/s/t}$	combinations of $C_1, \ldots, C_5$ (Eqs. (57)–(59))
$\mathbb{C}$	auxiliary quantity, effective stiffness of the two-phase laminate (Eq. (20))
$\mathbb{C}^{\pm}$	stiffness tetrads of the phases + and − (Eq. (16))
$\mathbb{C}_{V/R/A}$	effective stiffness tetrads according to the elementary Voigt, Reuss, and Aleksandrov mean (Eqs. (32)–(34)), where interface effects are not taken into account
$\overline{\mathbb{C}}^{x}_{X}$	effective stiffness tetrads, the upper index refers to the IOD, the lower index to the type of mean value (Eq. (44))
$\mathbf{d}$	axis of transversal isotropy (Eq. (119))
$f(\mathbf{n})$	interface orientation distribution (IOD), assigns to each interface normal $\mathbf{n}$ its fraction of the total interface
$\mathbb{F}$	auxiliary quantity, orientation average of $g(\mathbb{C}(\mathbf{n}))$ supplemented by the IOD $f(\mathbf{n})$ (Eq. (213))
$g(\cdot)$	generalized mean (Eq. (29)–(31))
G, K	isotropic shear and compression moduli (Eq. (35))
k, l, m, n, p	Hill moduli for transversely isotropic stiffness tetrads (Eqs. (111)–(115))
$\mathbf{n}$	normal vector of the interface between the + and − phase (Eq. (15))
$\mathbb{P}_{\alpha}$	αth projector, the upper index refers to the symmetry (Eq. (35))
$\mathbf{R}$	orthogonal tensor (Eq. (41))
v	volume fraction (Eq. (5))
x	characteristic length of microstructure (Eq. (160))
Z	generic quantity (Eqs. (4)–(8))
$\mathbb{Z}$	auxiliary quantity (Eq. (21))
$x/i/t/h/o$	indicates generic, isotropic, transversely isotropic, hexahedral, or octahedral symmetry (or IOD)
$X/V/R/A$	indicates generic, Voigt, Reuss, or Aleksandrov mean
γ, κ	non-dimensional combinations of A, B, E, G, K (Eqs. (53) and (52))
$\delta_{\parallel}(\cdot)$	Dirac distribution (Eq. (148))
$\delta_{\perp}(\cdot)$	confined Dirac distribution (Eq. (119))
Δ	error (difference of IOD approach to RVE simulation, Eq. (167)) or difference (Eq. (4))
$\boldsymbol{\varepsilon}$	effective strain tensor of the two-phase laminate (Eq. (17))
$\boldsymbol{\varepsilon}^{\pm}$	strains in the laminate layers (Eq. (15))
ϕ, θ	spherical coordinates (Eq. (120))
λ_{α}	αth eigenvalue of a stiffness tetrad (Eq. (61))
ρ	non-dimensional combination of C_5 and C_r (Eq. (60))
$\boldsymbol{\sigma}$	effective stess tensor of the two-phase laminate (Eq. (18))
$\boldsymbol{\sigma}^{\pm}$	stresses in the laminate layers (Eq. (14))
Ω	unit sphere in a three-dimensional space (Eq. (23))
ζ	parameter in the spectral decomposition of a transversely isotropic tetrad (Eq. (194))

1.1. Effective stiffness of a two-layer laminate

The analytical effective stiffness of a two-layer laminate with arbitrary layer stiffnesses is well-known and can be found, e. g., in [16] (Section 4.1), [4,36,7] (Eqs. (24) and (25)). It has been generalized from Tartar's approach [43] to the homogenization of the thermal conductivity of two-phase laminates [36]. In [18], we have reproduced this result for the multi-layer case with anisotropic constituents. We recall the solution here in due brevity.

We obtain the solution by invoking the jump balances of stresses and strains at an interface and by presuming homogeneous stress and strain fields on either side. The latter assumption can only be justified for very fine laminates. Thus, the resulting stiffness corresponds to that of a fine two-phase laminate.

The jump balance for the Cauchy stresses $\boldsymbol{\sigma}$ and the strains, $\boldsymbol{\varepsilon}$, the elastic laws on both sides of the interface and the volume averages of the stresses and the strains are given by

$$(\sigma^{+} - \sigma^{-}) \cdot \mathbf{n} = \mathbf{o}, \tag{14}$$

$$\varepsilon^{+} - \varepsilon^{-} = (\mathbf{a} \otimes \mathbf{n})_S, \tag{15}$$

$$\sigma^{\pm} = \mathbb{C}^{\pm} \cdot\cdot\, \varepsilon^{\pm}, \tag{16}$$

$$\varepsilon := v^{+}\varepsilon^{+} + v^{-}\varepsilon^{-}, \tag{17}$$

$$\sigma := v^{+}\sigma^{+} + v^{-}\sigma^{-}, \tag{18}$$

respectively. Across an interface with orientation $\mathbf{n}$, the displacement field $\mathbf{u}$ is in general only C^0-continuous. Thus, its gradient generally has a jump in direction of $\mathbf{n}$ which, by virtue of the strain displacement relation $\boldsymbol{\varepsilon} = (\mathbf{u} \otimes \nabla_0)_S$, induces the jump balance Eq. (15). The vector $\mathbf{a}$ is the jump of the directional derivative of $\mathbf{u}$ in direction of $\mathbf{n}$. The jump balance for the stresses is given by the principle of sections $\mathbf{t}^{+} + \mathbf{t}^{-} = \mathbf{o}$ where, according to Cauchy's theorem, $\mathbf{t}^{\pm} = \boldsymbol{\sigma}^{\pm} \cdot \mathbf{n}^{\pm}$ and $\mathbf{n}^{-} = -\mathbf{n}^{+}$. This linear system (Eqs. (14)–(18)) gives rise to the laminate stiffness tetrad $\mathbb{C}$, which satisfies

$$\boldsymbol{\sigma} = \mathbb{C} \cdot\cdot\, \boldsymbol{\varepsilon}, \tag{19}$$

$$\mathbb{C} := \mathbb{C}_V - v^{-}v^{+}\Delta\mathbb{C} \cdot\cdot\, \mathbb{Z}$$

With $\mathbb{C}^{\pm}$ positive definite, $\mathbb{C}_V$ and $\mathbb{C}_M$ (see Eqs. (5) and (8)) are positive definite, too, and so is $\mathbf{n} \cdot \mathbb{C}_M \cdot \mathbf{n}$. The intermediate fourth-order tensor $\mathbb{Z}$ possesses neither major symmetry nor subsymmetries. However, we can impose the subsymmetries without loss of generality, since on both sides of $\mathbb{Z}$ in Eq. (20), the double contractions involve the subsymmetric tensor $\Delta\mathbb{C}$. Upon imposing both subsymmetries, $\mathbb{Z} \to \mathbb{Z}_S$, we find that $\mathbb{Z}_S$ also possesses the major symmetry.

For the extremal cases corresponding in effect to a single phase composite, i. e. $\mathbb{C}^{+} = \mathbb{C}^{-}$, $v^{+} = 0$ or $v^{-} = 0$, the laminate stiffness equals that of the corresponding homogeneous medium. Also, scaling $\mathbf{n}$ does not affect the result. In particular, the laminate stiffness displays a head–tail symmetry,

$$\mathbb{C}(-\mathbf{n}) = \mathbb{C}(\mathbf{n}), \tag{22}$$

Due to this symmetry, neither phase is a priori distinguished in the IOD approach.

1.2. Interface orientation distributions

The set of all possible interface normals $\mathbf{n}$ is the unit sphere Ω (surface of a ball) in a three-dimensional space. We introduce the surface element $\mathrm{d}\Omega$ of normalized integration such that

$$\int_{\Omega} \mathrm{d}\Omega = 1. \tag{23}$$

The interface orientation distribution f (IOD) is non-negative and normalized,

$$f(\mathbf{n}) \geqslant 0, \tag{24}$$

$$\int_\Omega f(\mathbf{n})\,\mathrm{d}\Omega = 1. \tag{25}$$

1.3. Generalized mean

1.3.1. Properties

The IOD approach is given by a combination of the laminate stiffness (Eqs. (20) and (21)) and the distribution of the interface normal. Choosing $v := v^+$ as the independent volume fraction (and then $v^- = 1 - v$), the laminate stiffness tetrad becomes a function of $\mathbf{n}$ and v, while $\mathbb{C}^-$ and $\mathbb{C}^+$ are considered as parameters for the time being. The effective stiffness estimate is a functional depending on the IOD f and the type of mean value, indicated by the function g. It is defined via

$$\overline{\mathbb{C}}[f,g](v) := g^{-1}\left(\int_\Omega f(\mathbf{n})\, g(\mathbb{C}(v,\mathbf{n}))\,\mathrm{d}\Omega\right), \tag{26}$$

where g^{-1} denotes the inverse function of g (not its reciprocal).

1.3.2. Homogeneity

A common feature of any homogenization approach discussed hereafter is the homogeneity of the effective stiffness tetrad w. r. t. the individual tetrads (which are otherwise considered as mere parameters and thus suppressed in the list of arguments)

$$\forall \alpha \in \mathbb{R}: \quad \overline{\mathbb{C}}(\alpha\mathbb{C}^-, \alpha\mathbb{C}^+) = \alpha\,\overline{\mathbb{C}}(\mathbb{C}^-, \mathbb{C}^+) \tag{27}$$

This requirement is due to the fact that the estimate should not depend on the physical units of $\mathbb{C}^\pm$. It imposes a constraint on the choice of g which is met by, e. g., $g(x) = x^p$ for $p \in \mathbb{R}$ and $g(x) = \ln x$ (thus in particular for the Voigt, Reuss and Aleksandrov mean, see [3]).

1.3.3. Derivative

Interestingly, the derivative of the effective stiffness w. r. t. the volume fraction v is at extremal volume fractions independent of g (proven in Appendix D), and given by

$$\left.\frac{\mathrm{d}\overline{\mathbb{C}}[f,g]}{\mathrm{d}v}\right|_{\frac{1}{2}\mp\frac{1}{2}} = \int_\Omega \left.\frac{\partial\mathbb{C}}{\partial v}\right|_{\frac{1}{2}\mp\frac{1}{2}} f(\mathbf{n})\,\mathrm{d}\Omega. \tag{28}$$

1.4. Voigt, Reuss, and Aleksandrov mean

Subsequently, we shall investigate the Voigt (V, arithmetic), Reuss (R, harmonic) and Aleksandrov (A, geometric) mean in more detail. These are defined, respectively, via

$$g_V(x) := x, \tag{29}$$

$$g_R(x) := x^{-1}, \tag{30}$$

$$g_A(x) := \ln x. \tag{31}$$

Using these functions, we can define well-known elementary estimates without considering the IOD

$$\mathbb{C}_V := v^-\,\mathbb{C}^- + v^+\,\mathbb{C}^+, \tag{32}$$

$$\mathbb{C}_R := \left(v^-\,(\mathbb{C}^-)^{-1} + v^+\,(\mathbb{C}^+)^{-1}\right)^{-1}, \tag{33}$$

$$\mathbb{C}_A := \exp\left(v^-\,\ln\mathbb{C}^- + v^+\,\ln\mathbb{C}^+\right). \tag{34}$$

1.5. Isotropic phases

Since our focus is on the effect of the interface arrangement (morphology of the microstructure) rather than on the anisotropy of the phases, we consider two isotropic phases with stiffness tetrads $\mathbb{C}^\pm$ given in terms of the fourth-order isotropic projectors (see Appendix B) and the compression and shear modulus

$$\mathbb{C}^\pm = 3K^\pm\,\mathbb{P}_1^i + 2G^\pm\,\mathbb{P}_2^i. \tag{35}$$

The essential parts of the laminate stiffness $\mathbb{C}$ (Eq. (20)) are thus given by

$$\mathbb{C}_V = 3K_V\,\mathbb{P}_1^i + 2G_V\,\mathbb{P}_2^i, \tag{36}$$

$$\Delta\mathbb{C} = 3\Delta K\,\mathbb{P}_1^i + 2\Delta G\,\mathbb{P}_2^i, \tag{37}$$

$$\mathbb{Z}_S = Z_1\,(\mathbf{n}\otimes\mathbf{I}\otimes\mathbf{n})_S + Z_2\,\mathbf{n}\otimes\mathbf{n}\otimes\mathbf{n}\otimes\mathbf{n}, \tag{38}$$

$$Z_1 := (G_M)^{-1}, \tag{39}$$

$$Z_2 := \left(K_M + \frac{4}{3}G_M\right)^{-1} - (G_M)^{-1}. \tag{40}$$

This reference solution, which is fundamental to the following considerations, is transversely isotropic w. r. t. the interface normal $\mathbf{n}$.

1.5.1. Microstructural symmetries

For isotropic phases (see Eq. (35) or (41)), the only source of anisotropy of the effective stiffness that remains is the IOD. Then the rotational symmetries of the IOD, forming the symmetry group $\mathcal{G}^x \subseteq \mathcal{SO}_3$, also apply to the effective stiffness (see Appendix C),

$$\mathbf{R} * \mathbb{C}^\pm = \mathbb{C}^\pm \qquad \forall \mathbf{R} \in \mathcal{SO}_3, \tag{41}$$

$$\wedge f(\mathbf{R}^x\mathbf{n}) = f(\mathbf{n}) \quad \forall \mathbf{R}^x \in \mathcal{G}^x \forall \mathbf{n} \in \Omega, \tag{42}$$

$$\Rightarrow \mathbf{R}^x * \overline{\mathbb{C}} = \overline{\mathbb{C}} \qquad \forall \mathbf{R}^x \in \mathcal{G}^x. \tag{43}$$

By the latter, one can conclude that the IOD approach predicts for any arrangement of isotropic phases with isotropic IOD an isotropic effective stiffness. For example, this holds for any arrangement of spherical inclusions, although their arrangement may be anisotropic. Clearly, this indicates the approximate sense and the loss of information due to the IOD approach. For brevity, we keep the indices for any combination of IOD f^x and type of mean g_X, thus

$$\overline{\mathbb{C}}_X^x := \overline{\mathbb{C}}[f^x, g_X]. \tag{44}$$

The bar is used to distinguish these tetrads from the respective elementary mean values (Eqs. (32)–(34)).

1.5.2. A note on material directions

From the previous considerations, we can deduce that for isotropic phases the effective stiffness tetrads are determined by the tensors (see Eqs. (38))

$$\int_\Omega f(\mathbf{n})\,\mathbf{n}\otimes\mathbf{n}\,\mathrm{d}\Omega, \tag{45}$$

$$\int_\Omega f(\mathbf{n})\,\mathbf{n}\otimes\mathbf{n}\otimes\mathbf{n}\otimes\mathbf{n}\,\mathrm{d}\Omega. \tag{46}$$

As a byproduct, we may identify material directions as eigenvectors or eigentensors of this second- or fourth-order tensor, respectively. However, these contain only a very small part of the information that is condensed in the IOD.

1.5.3. Exact solution for equal shear moduli

We note that only for $\Delta G = 0$, thus $G := G^+ = G^- = G_V = G_R = G_M$, the resulting laminate stiffness tetrad is isotropic and the IOD contribution to Voigt's approach is purely volumetric

$$\mathbb{C}_H := \mathbb{C}|_{G^+=G^-} = \left(K_V - v^-\,v^+\,\frac{\Delta K^2}{K_M + \frac{4}{3}G}\right)3\,\mathbb{P}_1^i + 2G\,\mathbb{P}_2^i. \tag{47}$$

The stiffness tetrad has been given first by [25]. He has shown that it is the exact solution for any microstructure of isotropic phases

with equal shear moduli. $\mathbb{C}_H$ is isotropic, i. e. independent of $\mathbf{n}$. From Eq. (26) we conclude that for any type of mean value and any IOD (thus any microstructure), $\mathbb{C}_H$ is at the same time the effective stiffness according to the IOD approach

$$G^- = G^+ \Rightarrow \overline{\mathbb{C}}^x_X = \mathbb{C}_H. \tag{48}$$

Thus, the IOD approach provides the exact solution for this particular case.

1.5.4. Useful abbreviations

For the subsequent sections, the following moduli-like abbreviations (capital Latin letters) come in handy,

$$A_X := K_X + \frac{4}{3} G_X, \tag{49}$$

$$B_X := K_X - \frac{2}{3} G_X, \tag{50}$$

$$E_X := K_X + 2 G_X, \tag{51}$$

where $X \in \{V, R, A, M\}$. In like vein, the respective individual moduli and differences are defined, e. g., $E^\pm := K^\pm + 2G^\pm$ and $\Delta E := \Delta K + 2\Delta G$ etc. Further, the following non-dimensional abbreviations (minuscule Greek letters) will be used

$$\kappa_X := \frac{\Delta K}{A_X}, \tag{52}$$

$$\gamma_X := \frac{2\Delta G E_X}{5 A_X G_X}, \tag{53}$$

where $X \in \{V, R, A, M\}$. W. r. t. the basis given in Appendix A (Eqs. (186)–(190)), $\{C_1, \ldots, C_5\}$ represent the components of the transversely isotropic laminate stiffness tetrad (Eqs. (20), (35)–(40))

$$C_{1/2} = 2 G_{V/R}, \tag{54}$$

$$C_{3/4} = \frac{1}{2}\left(A_V \mp A_R + B_V - v^- v^+ \frac{2\Delta B^2}{A_M}\right), \tag{55}$$

$$C_5 = -\sqrt{2}\left(B_V - v^- v^+ \frac{\Delta A \Delta B}{A_M}\right). \tag{56}$$

The following combinations of these will appear frequently

$$C_r := \sqrt{C_3^2 + C_4^2}, \tag{57}$$

$$C_s := \sqrt{C_5^2 - C_r^2}, \tag{58}$$

$$C_t := \frac{1}{3}(2\sqrt{2} C_3 - C_4), \tag{59}$$

$$\rho := \sqrt{\frac{C_5 + C_r}{C_5 - C_r}}. \tag{60}$$

The eigenvalues of $\mathbb{C}$ are given by

$$\lambda^t_{1/2} = C_{1/2}, \tag{61}$$

$$\lambda^t_{3/4} = C_5 \pm C_r. \tag{62}$$

Since $\mathbb{C}$ is positive definite, we conclude that $0 \leqslant C_r < C_5$, thus C_s is real and ρ is positive.

1.6. Content of subsequent sections

Using the results of previous sections, we will evaluate the IOD approach for the Voigt, Reuss and Aleksandrov mean and for isotropic, transversely isotropic, and hexahedral IODs in Section 2–4.

For the isotropic and transversely isotropic IOD, isotropic and transversely isotropic stiffnesses (similar to [23]) are obtained, and we can compare the IOD approach to well-established approaches, such as the self-consistent approach and the Hashin–Shtrikman bounds. In particular, we consider the elastic moduli and their derivatives w. r. t. the volume fraction at extremal volume fractions.

For the hexahedral IOD, we compare the predictions of the IOD approach to numerical results from RVE simulations. In particular, we consider the elastic moduli of different microstructures, many of which have the same volume fractions and IOD. Thus, we determine for which types of microstructure (morphology) the IOD approach is most suitable.

2. Comparison for isotropic IOD

Well-ordered materials. Subsequently, we consider well-ordered materials (where $K^+ > K^-$ and $G^+ > G^-$), because this restriction is used in many theories that feature in the comparison. However, the IOD approach itself is not restricted to well-ordered materials.

2.1. Interface approach

2.1.1. Isotropic IOD

We consider the isotropic IOD (upper index i), which is simply given by

$$f^i(\mathbf{n}) := 1. \tag{63}$$

According to Eq. (43), the respective effective stiffness is isotropic.

2.1.2. Elastic moduli

2.1.2.1. Voigt mean. For the isotropic IOD, the shear and bulk moduli of the Voigt mean of the laminate stiffness are given by

$$\overline{\mathbb{C}}^i_V = 3\overline{K}_V \mathbb{P}^i_1 + 2\overline{G}_V \mathbb{P}^i_2, \tag{64}$$

$$\overline{K}_V = K_V - v^- v^+ \Delta K \kappa_M, \tag{65}$$

$$\overline{G}_V = G_V - v^- v^+ \Delta G \gamma_M, \tag{66}$$

or, equivalently,

$$3\overline{K}_V = C_5 - C_t, \tag{67}$$

$$2\overline{G}_V = \frac{1}{5}(2(C_1 + C_2) + C_5 + C_t) \tag{68}$$

2.1.2.2. Reuss mean. For the isotropic IOD, the shear and bulk moduli of the Reuss mean of the laminate stiffness are given by

$$\overline{\mathbb{C}}^i_R = 3\overline{K}_R \mathbb{P}^i_1 + 2\overline{G}_R \mathbb{P}^i_2, \tag{69}$$

$$\overline{K}_R = \frac{v^- G^- K^- A^+ + v^+ G^+ K^+ A^-}{G_V K_M + 4 G^+ G^-/3}, \tag{70}$$

$$\overline{G}_R = G_V\left(1 + v^- v^+ \frac{2\Delta G^2}{5 G^- G^+} \frac{v^- G^- K^- E^+ + v^+ G^+ K^+ E^-}{v^- G^- K^- A^+ + v^+ G^+ K^+ A^-}\right)^{-1}, \tag{71}$$

or, equivalently,

$$3\overline{K}_R = \frac{C_s^2}{C_5 + C_t}, \tag{72}$$

$$2\overline{G}_R = \frac{5 C_1 C_2 C_s^2}{2(C_1 + C_2) C_s^2 + C_1 C_2 (C_5 - C_t)}. \tag{73}$$

2.1.2.3. Aleksandrov mean. For the Aleksandrov mean, the expressions for the shear and bulk moduli become quite lengthy. Therefore, we only the give their compact form in terms of the components of the laminate stiffness (see Eqs. (54)–(60)),

$$\overline{\mathbb{C}}_A^i = 3\overline{K}_A\,\mathbb{P}_1^i + 2\overline{G}_A\,\mathbb{P}_2^i, \tag{74}$$

$$3\overline{K}_A = C_s\,\rho^{-C_t/C_r}, \tag{75}$$

$$2\overline{G}_A = \left(C_1^2 C_2^2 C_s\right)^{1/5}\rho^{C_t/(5C_r)}. \tag{76}$$

2.1.3. Derivatives at extremal volume fractions

The remainder of this section is dedicated to calculating and comparing the derivatives of effective quantities with respect to the volume fractions at extremal volume fractions. For the IOD approach, we have shown the derivatives to be independent of the type of mean g (see Eqs. (29)–(31) and Appendix D). To determine the derivatives, the volume fractions are replaced by $v^+ = v$ and thus $v^- = 1 - v$. Note that at extremal volume fractions we have for a generic quantity Z (see Eqs. (4)–(8))

$$Z_V\left(\frac{1}{2}\mp\frac{1}{2}\right) = Z_R\left(\frac{1}{2}\mp\frac{1}{2}\right) = Z_A\left(\frac{1}{2}\mp\frac{1}{2}\right) = Z^{\mp}, \tag{77}$$

$$Z_M\left(\frac{1}{2}\mp\frac{1}{2}\right) = Z^{\pm}, \tag{78}$$

$$\frac{\mathrm{d}Z_V}{\mathrm{d}v} = \Delta Z, \tag{79}$$

$$\frac{\mathrm{d}}{\mathrm{d}v}\left(v(1-v)Z(v)\right)_{\frac{1}{2}\mp\frac{1}{2}} = \pm Z\left(\frac{1}{2}\mp\frac{1}{2}\right), \tag{80}$$

These relations simplify the calculation considerably. Evaluating the derivatives at $v = 0$ and $v = 1$ provides

$$\left.\frac{\mathrm{d}\overline{K}_X}{\mathrm{d}v}\right|_{\frac{1}{2}\mp\frac{1}{2}} = \Delta K\left(1\mp\kappa^{\pm}\right), \tag{81}$$

$$\left.\frac{\mathrm{d}\overline{G}_X}{\mathrm{d}v}\right|_{\frac{1}{2}\mp\frac{1}{2}} = \Delta G\left(1\mp\gamma^{\pm}\right), \tag{82}$$

where $X \in \{V, R, A\}$.

2.2. Inclusion-based self-consistent approach

2.2.1. Elastic moduli

For two isotropic phases, the effective shear and bulk moduli K_{SC} and G_{SC} of the self-consistent approach result from solving (see [20])

$$\left(K_{\mathrm{SC}} - K^+\right)\left(K_{\mathrm{SC}} - K^-\right) = \left(K_{\mathrm{SC}} + \frac{4}{3}G_{\mathrm{SC}}\right)\left(K_{\mathrm{SC}} - K_{\mathrm{V}}\right), \tag{83}$$

$$2\left(K_{\mathrm{SC}} + 2G_{\mathrm{SC}}\right)\left(G_{\mathrm{SC}} - G^+\right)\left(G_{\mathrm{SC}} - G^-\right) = \left(K_{\mathrm{SC}} + \frac{4}{3}G_{\mathrm{SC}}\right) \times \left(G_{\mathrm{SC}} - G_{\mathrm{V}}\right)5G_{\mathrm{SC}}. \tag{84}$$

These equations have an explicit solution for K_{SC} and G_{SC}, which involves the root of a fourth-order polynomial. However, we can determine the derivatives without reference to this root.

2.2.2. Derivatives at extremal volume fractions

Upon differentiating Eqs. (83) and (84) w. r. t. v, we use

$$K_{\mathrm{SC}}\left(\frac{1}{2}\mp\frac{1}{2}\right) = K_{\mathrm{V}}\left(\frac{1}{2}\mp\frac{1}{2}\right) = K^{\mp}, \tag{85}$$

$$G_{\mathrm{SC}}\left(\frac{1}{2}\mp\frac{1}{2}\right) = G_{\mathrm{V}}\left(\frac{1}{2}\mp\frac{1}{2}\right) = G^{\mp}, \tag{86}$$

and Eq. (79). This provides the decoupled linear system

$$\mp\Delta K\left.\frac{\mathrm{d}K_{\mathrm{SC}}}{\mathrm{d}v}\right|_{\frac{1}{2}\mp\frac{1}{2}} = \left(K^{\mp} + \frac{4}{3}G^{\mp}\right)\left(\left.\frac{\mathrm{d}K_{\mathrm{SC}}}{\mathrm{d}v}\right|_{\frac{1}{2}\mp\frac{1}{2}} - \Delta K\right), \tag{87}$$

$$\mp 2\Delta G E^{\mp}\left.\frac{\mathrm{d}G_{\mathrm{SC}}}{\mathrm{d}v}\right|_{\frac{1}{2}\mp\frac{1}{2}} = \left(K^{\mp} + \frac{4}{3}G^{\mp}\right)\left(\left.\frac{\mathrm{d}G_{\mathrm{SC}}}{\mathrm{d}v}\right|_{\frac{1}{2}\mp\frac{1}{2}} - \Delta G\right)5G^{\mp}, \tag{88}$$

which is easily solved for the slopes

$$\left.\frac{\mathrm{d}K_{\mathrm{SC}}}{\mathrm{d}v}\right|_{\frac{1}{2}\mp\frac{1}{2}} = \Delta K(1\pm\kappa^{\mp})^{-1}, \tag{89}$$

$$\left.\frac{\mathrm{d}G_{\mathrm{SC}}}{\mathrm{d}v}\right|_{\frac{1}{2}\mp\frac{1}{2}} = \Delta G(1\pm\gamma^{\mp})^{-1}. \tag{90}$$

2.3. Hashin–Shtrikman bounds

2.3.1. Elastic moduli

If our knowledge of the microstructure is restricted to the volume fractions, the Hashin–Shtrikman bounds (HSBs) are the narrowest possible bounds [20] and given by

$$K_{\mathrm{HS}}^{\pm} = K^{\pm} \mp v^{\mp}\Delta K\left(1\mp v^{\pm}\kappa^{\pm}\right)^{-1}, \tag{91}$$

$$= K_{\mathrm{V}} - v^- v^+ \Delta K\,\frac{\kappa^{\pm}}{1\mp v^{\pm}\kappa^{\pm}}, \tag{92}$$

$$G_{\mathrm{HS}}^{\pm} = G^{\pm} \mp v^{\mp}\Delta G\left(1\mp v^{\pm}\gamma^{\pm}\right)^{-1}, \tag{93}$$

$$= G_{\mathrm{V}} - v^- v^+ \Delta G\,\frac{\gamma^{\pm}}{1\mp v^{\pm}\gamma^{\pm}}. \tag{94}$$

2.3.2. Derivatives at extremal volume fractions

These derivatives can be calculated directly

$$\left.\frac{\mathrm{d}K_{\mathrm{HS}}^{+}}{\mathrm{d}v}\right|_{\frac{1}{2}\mp\frac{1}{2}} = \Delta K\left(1-\kappa^{+}\right)^{\pm 1}, \tag{95}$$

$$\left.\frac{\mathrm{d}K_{\mathrm{HS}}^{-}}{\mathrm{d}v}\right|_{\frac{1}{2}\mp\frac{1}{2}} = \Delta K\left(1+\kappa^{-}\right)^{\mp 1}, \tag{96}$$

$$\left.\frac{\mathrm{d}G_{\mathrm{HS}}^{+}}{\mathrm{d}v}\right|_{\frac{1}{2}\mp\frac{1}{2}} = \Delta G\left(1-\gamma^{+}\right)^{\pm 1}, \tag{97}$$

$$\left.\frac{\mathrm{d}G_{\mathrm{HS}}^{-}}{\mathrm{d}v}\right|_{\frac{1}{2}\mp\frac{1}{2}} = \Delta G\left(1+\gamma^{-}\right)^{\mp 1}. \tag{98}$$

2.4. Walpole bounds

2.4.1. Elastic moduli

The bounds suggested by [45] are given by

$$K_{\mathrm{W}}^{\pm} := K_{\mathrm{V}} - v^- v^+ \Delta K^2\left(K_M + \frac{4}{3}G^{\pm}\right)^{-1}, \tag{99}$$

$$G_{\mathrm{W}}^{\pm} := G_{\mathrm{V}} - v^- v^+ \Delta G^2\left(G_M + H^{\pm}\right)^{-1}, \tag{100}$$

$$H^{\pm} := \frac{3}{2}\left(\frac{1}{G^{\pm}} + \frac{10}{9K^{\pm} + 8G^{\pm}}\right)^{-1} = \frac{G^{\pm}\left(9K^{\pm} + 8G^{\pm}\right)}{6E^{\pm}}, \tag{101}$$

thus

$$G^{\pm} + H^{\pm} = \frac{5G^{\pm}A^{\pm}}{2E^{\pm}} = \frac{\Delta G}{\gamma^{\pm}}. \tag{102}$$

In fact, upon replacing $G^{\pm} \to G_M$ and $H^{\pm} \to H_M$, these bounds coincide with the IOD approach for the Voigt mean, i. e. $\overline{K}_V$ and $\overline{G}_V$ (see Eqs. (65) and (66)).

2.4.2. Derivatives at extremal volume fractions

The derivatives are easily calculated. Rearranging these by means of the previous abbreviations, we find

$$\left.\frac{\mathrm{d}K_{\mathrm{W}}^{+}}{\mathrm{d}v}\right|_{\frac{1}{2}\mp\frac{1}{2}} = \Delta K\left(1-\kappa^{+}\right)^{\pm 1}, \tag{103}$$

$$\left.\frac{\mathrm{d}K_{\mathrm{W}}^{-}}{\mathrm{d}v}\right|_{\frac{1}{2}\mp\frac{1}{2}} = \Delta K\left(1+\kappa^{-}\right)^{\mp 1}, \tag{104}$$

$$\left.\frac{\mathrm{d}G_{\mathrm{W}}^{+}}{\mathrm{d}\nu}\right|_{\frac{1}{2}^{\mp}\frac{1}{2}} = \Delta G(1-\gamma^{+})^{\pm 1}, \tag{105}$$

$$\left.\frac{\mathrm{d}G_{\mathrm{W}}^{-}}{\mathrm{d}\nu}\right|_{\frac{1}{2}^{\mp}\frac{1}{2}} = \Delta G(1+\gamma^{-})^{\mp 1}, \tag{106}$$

all of which coincide with the slopes of the Hashin–Shtrikman bounds.

2.5. Summary

The previous results (Eqs. (81), (82), (89), (90), (95) to (98)) imply

$$\left.\frac{\mathrm{d}K_X}{\mathrm{d}\nu}\right|_0 = \left.\frac{\mathrm{d}K_{\mathrm{HS}}^{+}}{\mathrm{d}\nu}\right|_0 \quad \left.\frac{\mathrm{d}K_{\mathrm{SC}}}{\mathrm{d}\nu}\right|_1 = \left.\frac{\mathrm{d}K_{\mathrm{HS}}^{+}}{\mathrm{d}\nu}\right|_1, \tag{107}$$

$$\left.\frac{\mathrm{d}K_{\mathrm{SC}}}{\mathrm{d}\nu}\right|_0 = \left.\frac{\mathrm{d}K_{\mathrm{HS}}^{-}}{\mathrm{d}\nu}\right|_0 \quad \left.\frac{\mathrm{d}K_X}{\mathrm{d}\nu}\right|_1 = \left.\frac{\mathrm{d}K_{\mathrm{HS}}^{-}}{\mathrm{d}\nu}\right|_1, \tag{108}$$

and likewise

$$\left.\frac{\mathrm{d}G_{\mathrm{SC}}}{\mathrm{d}\nu}\right|_0 = \left.\frac{\mathrm{d}G_{\mathrm{HS}}^{-}}{\mathrm{d}\nu}\right|_0 \quad \left.\frac{\mathrm{d}G_X}{\mathrm{d}\nu}\right|_1 = \left.\frac{\mathrm{d}G_{\mathrm{HS}}^{-}}{\mathrm{d}\nu}\right|_1, \tag{109}$$

$$\left.\frac{\mathrm{d}G_X}{\mathrm{d}\nu}\right|_0 = \left.\frac{\mathrm{d}G_{\mathrm{HS}}^{+}}{\mathrm{d}\nu}\right|_0 \quad \left.\frac{\mathrm{d}G_{\mathrm{SC}}}{\mathrm{d}\nu}\right|_1 = \left.\frac{\mathrm{d}G_{\mathrm{HS}}^{+}}{\mathrm{d}\nu}\right|_1, \tag{110}$$

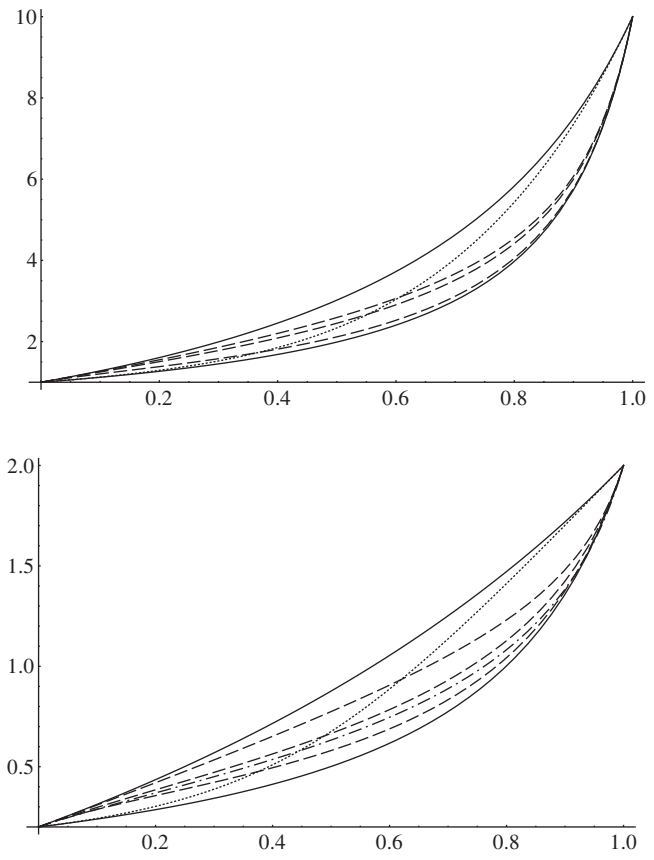

Fig. 1. Effective compression moduli K (top) and bulk moduli G (bottom) over ν^{+} for different estimates, with the phase moduli satisfying $G^{+}/G^{-} = K^{+}/K^{-} = 10, K^{\pm} = 5G^{\pm}$ and normalized to $K^{-} = 1$. The HS bounds are depicted as solid lines, the self-consistent approach is depicted as dotted line, the Voigt (arithmetic), Aleksandrov (geometric) and Reuss (harmonic) isotropic orientation-averages are drawn as dashed lines, where $K_V \geqslant K_A \geqslant K_R$ and $G_V \geqslant G_A \geqslant G_R$ hold. For the bulk moduli, the approximation $\sqrt{G_R G_V}$ has been added (dashed-dotted), which is close to the Aleksandrov mean, but much simpler to calculate.

i. e. the elastic moduli, as predicted by the IOD and SC approach, coincide with mixed and complementary pairs of the HSBs at extremal volume fractions, see Fig. 1. The IOD approach tends to the steeper of the Hashin–Shtrikman bounds at extremal volume fractions (Eq. (81) and 82), opposite to the self-consistent scheme (Eqs. (89) and (90)).

3. Comparison for transversely isotropic IOD

Again, theories for well-ordered materials are used for comparison. Also note that for $\nu = 0$ and $\nu = 1$, the composite becomes a single phase material. Since either phase is assumed isotropic (in this paper), these limits are isotropic, too.

According to [26], this implies universal relations among the five components, reducing the number of independent components to three. Consequently, we restrict our considerations to Hill's moduli m, k, p and skip the remaining moduli l, n. For the pure - isotropic - phases, Hill's moduli are related to shear and bulk modulus via

$$k^{\pm} = K^{\pm} + \frac{1}{3}G^{\pm}, \tag{111}$$

$$l^{\pm} = K^{\pm} - \frac{2}{3}G^{\pm}, \tag{112}$$

$$m^{\pm} = G^{\pm}, \tag{113}$$

$$n^{\pm} = K^{\pm} + \frac{4}{3}G^{\pm}, \tag{114}$$

$$p^{\pm} = G^{\pm}. \tag{115}$$

We give preference to the symbols m, k, p subsequently in order to reduce the number of different symbols in the equations.

Hill's parameters. With $\mathbf{d} = \mathbf{e}_3$ being the axis of transversal isotropy, Hill's parameters $\overline{m}, \overline{k}, \overline{p}$ are related to the components of the transversely isotropic *effective* stiffness via

$$\overline{m} = \frac{1}{2}\overline{C}_1, \tag{116}$$

$$\overline{k} = \frac{1}{2}(\overline{C}_4 + \overline{C}_5), \tag{117}$$

$$\overline{p} = \frac{1}{2}\overline{C}_2. \tag{118}$$

3.1. Interface approach

3.1.1. Transversely isotropic IOD

We consider a transversely isotropic IOD (upper index t)

$$f^{t}(\mathbf{n}) := \delta_{\perp}(\mathbf{n}, \mathbf{d}), \tag{119}$$

where $\delta_{\perp}$ denotes the Dirac distribution confined to the equatorial plane perpendicular to $\mathbf{d}$, the axis of transversal isotropy. Given a generic function h, the distribution $\delta_{\perp}$ acts as follows

$$\int_{\Omega} \delta_{\perp}(\mathbf{n}, \mathbf{e}_3)\, h(\mathbf{n})\, \mathrm{d}\Omega = \frac{1}{2\pi}\int_0^{2\pi} h(\cos\phi\, \mathbf{e}_1 + \sin\phi\, \mathbf{e}_2)\, \mathrm{d}\phi. \tag{120}$$

3.1.2. Elastic moduli

3.1.2.1. Voigt mean. The elastic moduli are given by

$$\overline{m}_V = m_V - \nu^{-}\nu^{+}\frac{\Delta m^2}{m_M}\frac{k_M + 2m_M}{2(k_M + m_M)}, \tag{121}$$

$$\overline{k}_V = k_V - \nu^{-}\nu^{+}\frac{\Delta k^2}{k_M + m_M}, \tag{122}$$

$$\overline{p}_V = \frac{1}{2}(p_R + p_V). \tag{123}$$

3.1.2.2. Reuss and Aleksandrov mean. The expressions become quite lengthy but details of the calculations are given in Appendix B.

3.1.3. Derivatives at extremal volume fractions

Again, the derivatives at extremal volume fractions are the same for Voigt, Reuss and Aleksandrov mean. Thus, we can use the comparatively simple formulae for the Voigt mean to obtain the derivatives. Thus, for $X \in \{V, R, A\}$ we find

$$\left.\frac{\mathrm{d}\overline{m}_X}{\mathrm{d}v}\right|_{\frac{1}{2}\mp\frac{1}{2}} = \frac{2m^- m^+ + k^\pm(m^- + m^+)}{2m^\pm(k^\pm + m^\pm)}\Delta m, \tag{124}$$

$$\left.\frac{\mathrm{d}\overline{k}_X}{\mathrm{d}v}\right|_{\frac{1}{2}\mp\frac{1}{2}} = \frac{k^\mp + m^\pm}{k^\pm + m^\pm}\Delta k, \tag{125}$$

$$\left.\frac{\mathrm{d}\overline{p}_X}{\mathrm{d}v}\right|_{\frac{1}{2}\mp\frac{1}{2}} = \frac{p^- + p^+}{2p^\pm}\Delta p. \tag{126}$$

3.2. Self-consistent approach

The self-consistent approach for long fiber–matrix composites is summarized in Section 7.1.2 of [13].

3.2.1. Elastic moduli

The elastic modulus m_{SC} is given implicitly,

$$\frac{v^- k^-}{k^- + m_{\mathrm{SC}}} + \frac{v^+ k^+}{k^+ + m_{\mathrm{SC}}} = 2\left(\frac{v^- m^+}{m^+ - m_{\mathrm{SC}}} + \frac{v^+ m^-}{m^- - m_{\mathrm{SC}}}\right). \tag{127}$$

Next, knowing $m_{\mathrm{SC}}, k_{\mathrm{SC}}$ is determined from

$$\frac{1}{k_{\mathrm{SC}} + m_{\mathrm{SC}}} = \frac{v^-}{k^- + m_{\mathrm{SC}}} + \frac{v^+}{k^+ + m_{\mathrm{SC}}}, \tag{128}$$

and p_{SC} is the positive root of

$$\frac{v^-}{p_{\mathrm{SC}} - p^+} + \frac{v^+}{p_{\mathrm{SC}} - p^-} = \frac{1}{2p_{\mathrm{SC}}}. \tag{129}$$

3.2.2. Derivatives at extremal volume fractions

As for the isotropic case, upon differentiating we obtain linear equations in the derivatives. Using

$$m_{\mathrm{SC}}\left(\frac{1}{2}\mp\frac{1}{2}\right) = m^\mp, \tag{130}$$

$$k_{\mathrm{SC}}\left(\frac{1}{2}\mp\frac{1}{2}\right) = k^\mp, \tag{131}$$

$$p_{\mathrm{SC}}\left(\frac{1}{2}\mp\frac{1}{2}\right) = p^\mp, \tag{132}$$

we find

$$\left.\frac{\mathrm{d}m_{\mathrm{SC}}}{\mathrm{d}v}\right|_{\frac{1}{2}\mp\frac{1}{2}} = \frac{2m^\mp(k^\mp + m^\mp)}{2m^- m^+ + k^\mp(m^- + m^+)}\Delta m, \tag{133}$$

$$\left.\frac{\mathrm{d}k_{\mathrm{SC}}}{\mathrm{d}v}\right|_{\frac{1}{2}\mp\frac{1}{2}} = \frac{k^\mp + m^\mp}{k^+ + m^\mp}\Delta k, \tag{134}$$

$$\left.\frac{\mathrm{d}p_{\mathrm{SC}}}{\mathrm{d}v}\right|_{\frac{1}{2}\mp\frac{1}{2}} = \frac{2p^\mp}{p^- + p^+}\Delta p \tag{135}$$

3.3. Hashin–Shtrikman bounds

For the long-fiber microstructure, the second-order bounds for Hill's moduli m, k, and p are summarized in [24] (Eqs. 4.25–4.28, 5.12, 5.13) and [13] (Section 6.4.1).

3.3.1. Elastic moduli

The elastic moduli are given by

$$m^\pm_{\mathrm{HS}} = m^\pm + \frac{v^\mp}{(m^\mp - m^\pm)^{-1} + v^\pm\frac{k^\pm + 2m^\pm}{2m^\pm(k^\pm + m^\pm)}}, \tag{136}$$

$$k^\pm_{\mathrm{HS}} = k^\pm + \frac{v^\mp}{(k^\mp - k^\pm)^{-1} + v^\pm(k^\pm + m^\pm)^{-1}}, \tag{137}$$

$$p^\pm_{\mathrm{HS}} = p^\pm + \frac{v^\mp}{(p^\mp - p^\pm)^{-1} + v^\pm(2p^\pm)^{-1}}, \tag{138}$$

where

$$m^-_{\mathrm{HS}}\left(\frac{1}{2}\mp\frac{1}{2}\right) = m^+_{\mathrm{HS}}\left(\frac{1}{2}\mp\frac{1}{2}\right) = m^\mp, \tag{139}$$

$$k^-_{\mathrm{HS}}\left(\frac{1}{2}\mp\frac{1}{2}\right) = k^+_{\mathrm{HS}}\left(\frac{1}{2}\mp\frac{1}{2}\right) = k^\mp, \tag{140}$$

$$p^-_{\mathrm{HS}}\left(\frac{1}{2}\mp\frac{1}{2}\right) = p^+_{\mathrm{HS}}\left(\frac{1}{2}\mp\frac{1}{2}\right) = p^\mp. \tag{141}$$

3.3.2. Derivatives at extremal volume fractions

The twelve derivatives of the six Hashin–Shtrikman bounds for m, k, and p correspond to the six derivatives of the self-consistent estimate and the six derivatives of the IOD approach, again in a complementary fashion. Thus, the same discussion as for the isotropic interface distribution applies.

$$\left.\frac{\mathrm{d}k^-_{\mathrm{HS}}}{\mathrm{d}v}\right|_{\frac{1}{2}\mp\frac{1}{2}} = \left(\frac{k^- + m^-}{k^+ + m^-}\right)^{\pm1}\Delta k, \tag{142}$$

$$\left.\frac{\mathrm{d}k^+_{\mathrm{HS}}}{\mathrm{d}v}\right|_{\frac{1}{2}\mp\frac{1}{2}} = \left(\frac{k^- + m^+}{k^+ + m^+}\right)^{\pm1}\Delta k, \tag{143}$$

$$\left.\frac{\mathrm{d}m^-_{\mathrm{HS}}}{\mathrm{d}v}\right|_{\frac{1}{2}\mp\frac{1}{2}} = \left(\frac{2m^-(k^- + m^-)}{2m^- m^+ + k^-(m^- + m^+)}\right)^{\pm1}\Delta m, \tag{144}$$

$$\left.\frac{\mathrm{d}m^+_{\mathrm{HS}}}{\mathrm{d}v}\right|_{\frac{1}{2}\mp\frac{1}{2}} = \left(\frac{2m^- m^+ + k^+(m^- + m^+)}{2m^+(k^+ + m^+)}\right)^{\pm1}\Delta m, \tag{145}$$

$$\left.\frac{\mathrm{d}p^-_{\mathrm{HS}}}{\mathrm{d}v}\right|_{\frac{1}{2}\mp\frac{1}{2}} = \left(\frac{2p^-}{p^- + p^+}\right)^{\pm1}\Delta p, \tag{146}$$

$$\left.\frac{\mathrm{d}p^+_{\mathrm{HS}}}{\mathrm{d}v}\right|_{\frac{1}{2}\mp\frac{1}{2}} = \left(\frac{p^- + p^+}{2p^+}\right)^{\pm1}\Delta p. \tag{147}$$

3.4. Summary

The very same conclusions as in the isotropic case apply. Hill's moduli as predicted by the IOD and SC estimate, approach complementary and mixed Hashin–Shtrikman bounds at extremal volume fractions. Again, the IOD approach coincides always with the bound that has the steeper slope. The effective moduli are plotted for an example material combination in Fig. 2.

4. Comparison for hexahedral and octahedral IODs

In this chapter we compare the predictions by the IOD approach to numerical results obtained from RVE simulations. To assess the significance of the IOD for the effective stiffness and the quality of the IOD approach, we have designed different microstructures, all of which exhibit cubic symmetry and the hexahedral IOD.

4.1. Interface approach

4.1.1. Hexahedral IOD

The aforementioned microstructures correspond to an IOD with cubic symmetry which in turn relates to the six faces of a regular hexahedron or cube (upper index h) with normals $\{\mathbf{n}_i^h\}$ and is therefore called hexahedral IOD,

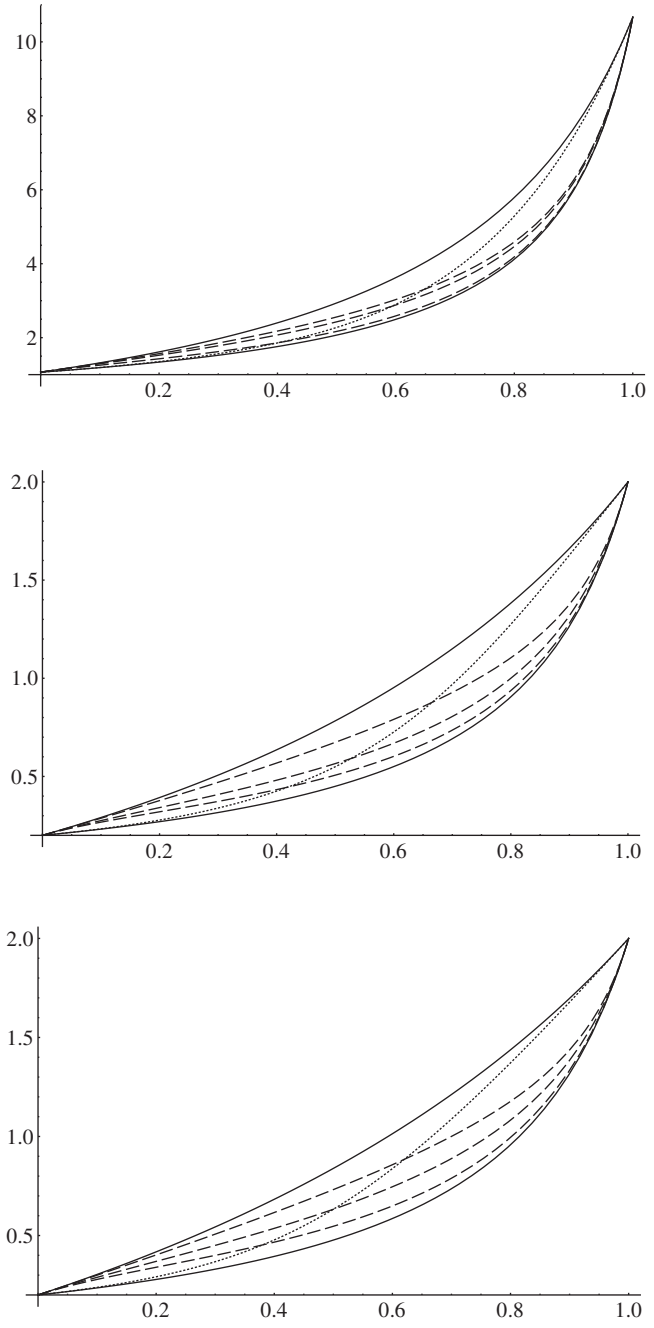

Fig. 2. Effective Hill moduli k (top), m (middle) and p (bottom) over ν^+ for different estimates, with the phase moduli satisfying $G^+/G^- = K^+/K^- = 10$, $K^\pm = 5G^\pm$ and normalized to $K^- = 1$. The HS bounds are depicted as solid lines, the self-consistent approach is depicted as dotted line, the Voigt (arithmetic), Aleksandrov (geometric) and Reuss (harmonic) transversely isotropic orientation-averages are drawn as dashed lines, where $\{k,m,p\}_V \geqslant \{k,m,p\}_A \geqslant \{k,m,p\}_R$ hold.

$$f^h(\mathbf{n}) := \frac{1}{6}\sum_{i=1}^{6}\delta_\parallel(\mathbf{n},\mathbf{n}_i^h), \tag{148}$$

where $\delta_\parallel(\mathbf{n},\mathbf{n}_0)$ is a distribution centered at $\mathbf{n}_0$ which acts as follows on a generic function h,

$$\int_\Omega \delta_\parallel(\mathbf{n},\mathbf{n}_0)\,h(\mathbf{n})\,\mathrm{d}\Omega = h(\mathbf{n}_0). \tag{149}$$

According to Eq. (43), both IODs yield effective stiffness tetrads with cubic symmetry. These are conveniently described by three eigenvalues $\{\lambda^h_{X,\alpha}\}$ and projectors $\{\mathbb{P}^h_\alpha\}$ given in full detail in Appendix B,

$$\overline{\mathbb{C}}^h_X = \sum_{\alpha=1}^{3}\lambda^h_{X,\alpha}\,\mathbb{P}^h_\alpha. \tag{150}$$

4.1.2. Elastic moduli

4.1.2.1. Voigt mean. Recalling the abbreviations introduced in (54)–(60), the elastic moduli for f^h are given by

$$\lambda^h_{V,1} = C_5 - C_t, \tag{151}$$

$$\lambda^h_{V,2} = \frac{1}{2}(C_1 + C_5 + C_t), \tag{152}$$

$$\lambda^h_{V,3} = \frac{1}{3}(C_1 + 2C_2). \tag{153}$$

4.1.2.2. Reuss mean. The elastic moduli for f^h are given by

$$\lambda^h_{R,1} = \frac{C_s^2}{C_5 + C_t}, \tag{154}$$

$$\lambda^h_{R,2} = \frac{2C_1C_s^2}{C_1(C_5 - C_t) + C_s^2}, \tag{155}$$

$$\lambda^h_{R,3} = \frac{3C_1C_2}{2C_1 + C_2}. \tag{156}$$

4.1.2.3. Aleksandrov mean. The elastic moduli for f^h are given by

$$\lambda^h_{A,1} = C_s\,\rho^{-C_t/C_r}, \tag{157}$$

$$\lambda^h_{A,2} = (C_1C_s)^{1/2}\,\rho^{C_t/(2C_r)}, \tag{158}$$

$$\lambda^h_{A,3} = \left(C_1C_2^2\right)^{1/3}. \tag{159}$$

The details of the calculation are given in Appendix B.

4.2. RVE simulations

Averaging the results of full field simulations of the loaded microstructure [48] provides a versatile tool to assess the quality of the estimate. Since we consider different microstructures with equal cubic IOD, our microstructure as well as the external loading is well represented by a single cubical unit cell and periodic boundary conditions.

4.2.1. Hexahedral microstructures

In accordance with the IOD described above, we consider the following hexahedral microstructures, where a and v denote the interface area (per unit volume) and the volume fraction in terms of a parameter x describing the microstructure.

4.2.1.1. Cubic inclusions (CI). The RVE consists of a cube (material '−') within which another cube (material '+') is centered (see Fig. 3). This is a matrix-inclusion microstructure. While increasing the edge length x of the inner cube, we also increase the volume

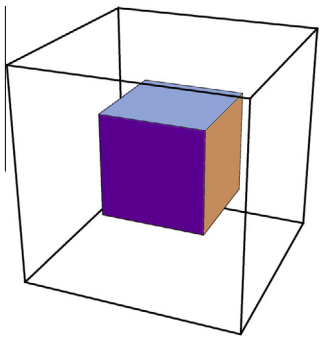

Fig. 3. Cubic inclusion in a cubic RVE.

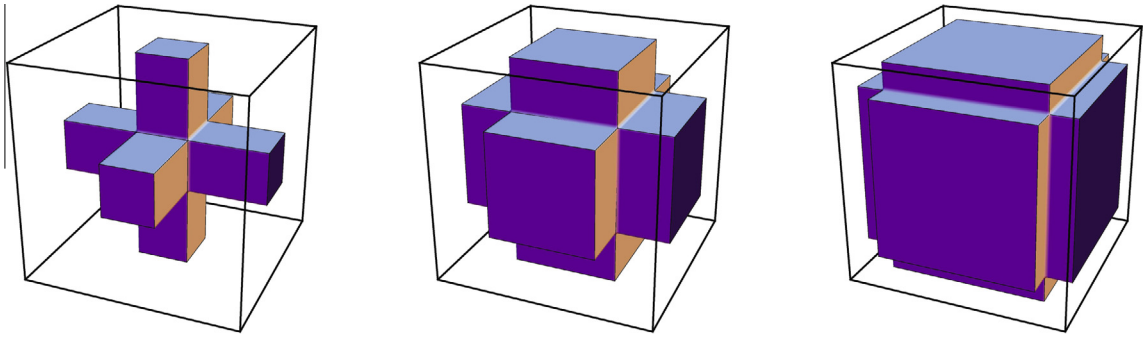

Fig. 4. Mutually penetrating lattices with one lattice thickness being 1/4 (left), 1/2 (center), and 3/4 (right) of the RVE size.

fraction v. We also consider the inverse arrangement, since, according to the IOD approach, the effective stiffness should be the same for either arrangement provided the volume fraction is the same.

$$a_{CI} = 6x^2 \quad \text{for} \quad x \in [0,1[\tag{160}$$

$$v_{CI}^{+} = x^3 \quad \text{for} \quad x \in [0,1] \tag{161}$$

$$v_{CI}^{-} = 1 - x^3 \quad \text{for} \quad x \in [0,1] \tag{162}$$

Here, the upper indices + and − denote the inclusion phase.

4.2.1.2. Mutually penetrating lattices (MPL). The RVE consists of a cube, with one material (+) located at its edges and vertices, the other (−) filling the remaining inner part of the cube (see Fig. 4). By extending this microstructure periodically in all directions, it becomes apparent that it consists of two mutually penetrating lattices. Here, x denotes the lattice thickness of the + material. This is not a matrix-inclusion microstructure, but rather an equitable one.

$$a_{MPL} = 12x(1-x) \quad \text{for} \quad x \in [0,1] \tag{163}$$

$$v_{MPL} = x^2(3-2x) \quad \text{for} \quad x \in [0,1] \tag{164}$$

4.2.1.3. Alternating cubic inclusions (ACI). Placing a cube with edge length $0 \leqslant x \leqslant 1$ on each of the six face centers of the unit cell (with edge length 2) defines the alternating cubic inclusion microstructure (see Fig. 5). This arrangement allows to consider volume fractions $0 \leqslant v \leqslant \frac{1}{2}$. To consider $\frac{1}{2} \leqslant v \leqslant 1$, we swap the ±-assignment. In general, this is a matrix-inclusion microstructure, however, for $v = \frac{1}{2}$, it is similar to the MPL in that it is an equitable arrangement of phases.

$$a_{ACI} = \begin{cases} \frac{9}{2}x^2 & \text{if} \quad 0 \leqslant x < 1 \\ \frac{9}{2}(2-x)^2 & \text{if} \quad 1 \leqslant x \leqslant 2 \end{cases} \tag{165}$$

$$v_{ACI} = \begin{cases} \frac{1}{2}x^3 & \text{if} \quad 0 \leqslant x < 1 \\ 1 - \frac{1}{2}(2-x)^3 & \text{if} \quad 1 \leqslant x \leqslant 2. \end{cases} \tag{166}$$

4.2.2. Details of the RVE implementation

The simulations have been carried out using the finite element system Abaqus. Upon generating a single cubical unit cell, we have applied an average strain by periodic boundary conditions, and then have extracted the average stresses. Details of the implementation can be found in [19,17]. We have used a regular meshing, with 40^3 hexahedral elements with quadratic shape functions (element type C3D20 in Abaqus), resulting in approximately 800,000 degrees of freedom in the finite element model. The microstructures' interfaces are easily accounted for by a regular, microstructure-conformal meshing.

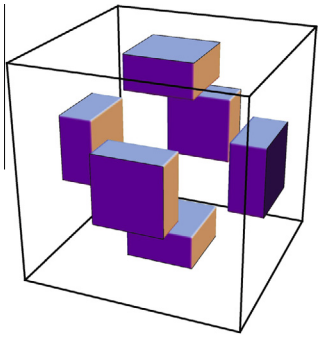

Fig. 5. Alternating cubic inclusions with the inclusion thickness being 1/3 of the RVE size.

Since the effective stiffness tetrad is cubic, and the orientation of the axes of anisotropy is known a priori, the three independent eigenvalues can be determined in two tests with very small strains, e. g., an elongation test in direction of $\mathbf{e}_1$ with confined lateral straining, extracting σ_{11} and $\sigma_{22}(=\sigma_{33})$, and a shear test with the shear direction $\mathbf{e}_1$ and the shear plane normal $\mathbf{e}_2$, extracting σ_{12}. The tests can actually be carried out superimposed in only one simulation, due to the fact that their stress–strain responses are decoupled.

4.2.3. Definition of the error

In order to quantify the deviation of the IOD approach from the reference stiffness (provided by the RVE), we maximize the relative error in terms of the Cauchy stress over the domain of all strains

$$\Delta_X := \max_{\varepsilon} \frac{\|\overline{\boldsymbol{\sigma}}_X - \overline{\boldsymbol{\sigma}}_{RVE}\|}{\|\overline{\boldsymbol{\sigma}}_{RVE}\|}, \tag{167}$$

where $X \in \{V, R, A\}$. As shown in Appendix F, for the microstructures considered here this definition is equivalent to

$$\Delta_X = \max_{\alpha} \frac{|\lambda^h_{\alpha,X} - \lambda^h_{\alpha,RVE}|}{\lambda^h_{\alpha,RVE}}. \tag{168}$$

Since we consider different mean values (Voigt, Reuss, Aleksandrov), there are in fact three different errors for any microstructure. However, we have found their qualitative behavior to be very similar.

4.3. Comparison

4.3.1. Survey of numerical results

First, let us give an impression of the effect of morphology. There are four microstructures with the same – hexahedral – IOD, namely the two variants of CI and the ACI and MPL. We find that, given the same parameters, the same volume fraction and

the same IOD, the minimum and maximum eigenvalues are always attained by the ACI and at least one variant of the CI microstructures, while the MPL is usually in between. This holds for all of the qualitatively different parameter sets involved in Fig. 6.

4.3.2. Effect of the parameters

Knowing that the IOD approach is correct for any microstructure of isotropic phases with equal shear moduli (see Section 1.5 and Eq. (47)), we have investigated various combinations of shear moduli with $G^- \neq G^+$. For the sake of simplicity, we consider the special case of equal bulk moduli, $K^- = K^+$, first. Then, the error depends on the ratio G^+/G^-. Depending on the microstructure, we find a reasonable agreement ($\Delta \lesssim 0.1$) with the IOD approach for $1/4 \lesssim G^+/G^- \lesssim 4$. Considering a fixed ratio $G^+ = 4G^-$, the effect of varying the common K on any type of error (V, R, A which are collected in columns of figures) is quantitatively insignificant (compare curves within one and the same diagram) and depends qualitatively on the type of microstructure (compare diagrams in the same row in Fig. 7). Thus, for $K^- \neq K^+$, the error is still comparable to that for the case $K^\pm = K$.

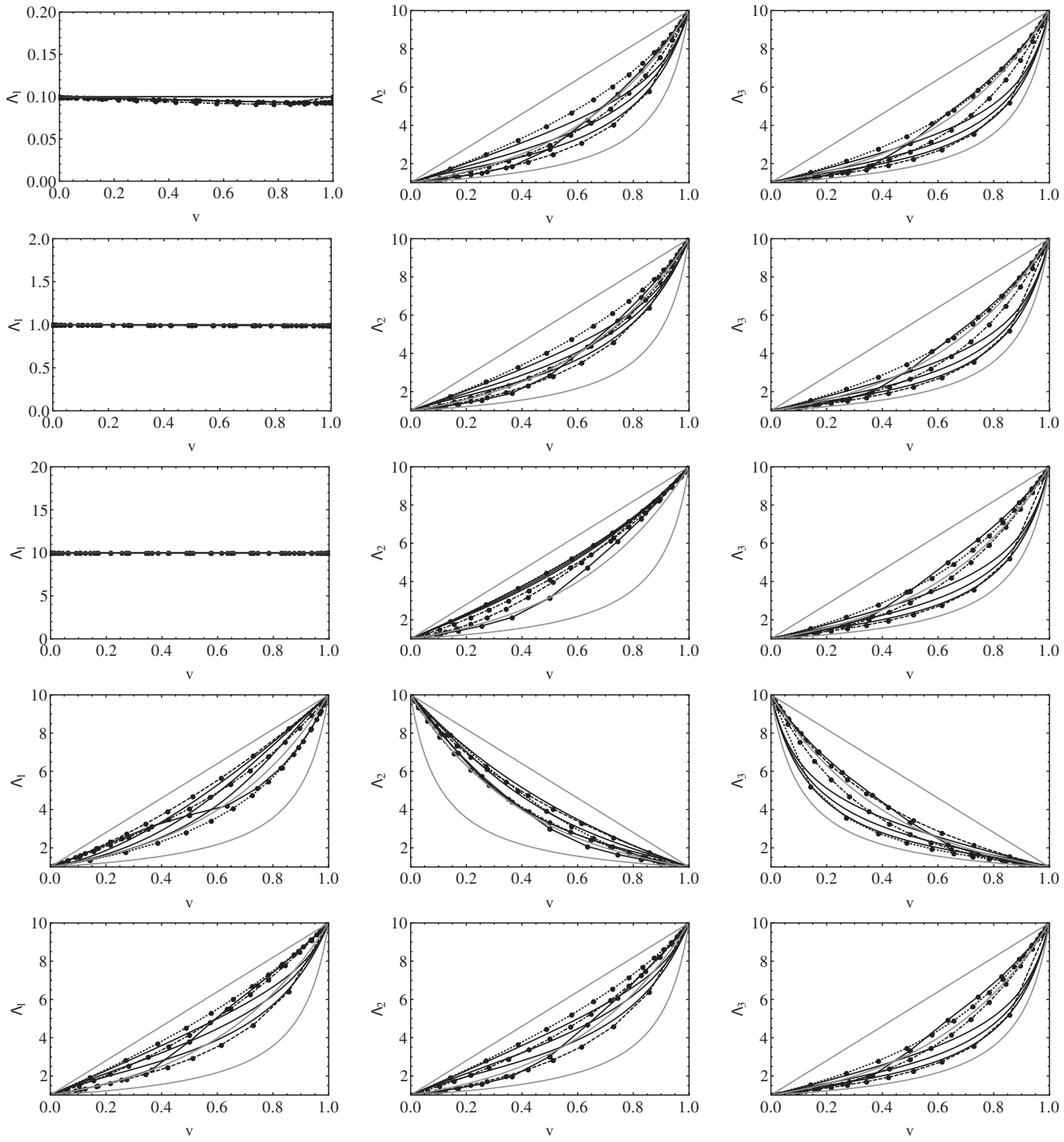

Fig. 6. The effect of morphology: The three eigenvalues of the effective stiffness tetrad for different hexahedral microstructures (same IOD): MPL (dot-dashed), CI (dotted, dashed), ACI (continuous) and elementary mean values (gray), IOD (black). Qualitatively different sets of parameters (from top to bottom): $(3K^-, 2G^-, 3K^+, 2G^+) \in \{(0.1, 1, 0.1, 10), (1, 1, 1, 10), (10, 1, 10, 10), (1, 10, 10, 1), (1, 1, 10, 10)\}$.

$K^{\pm} = K.$

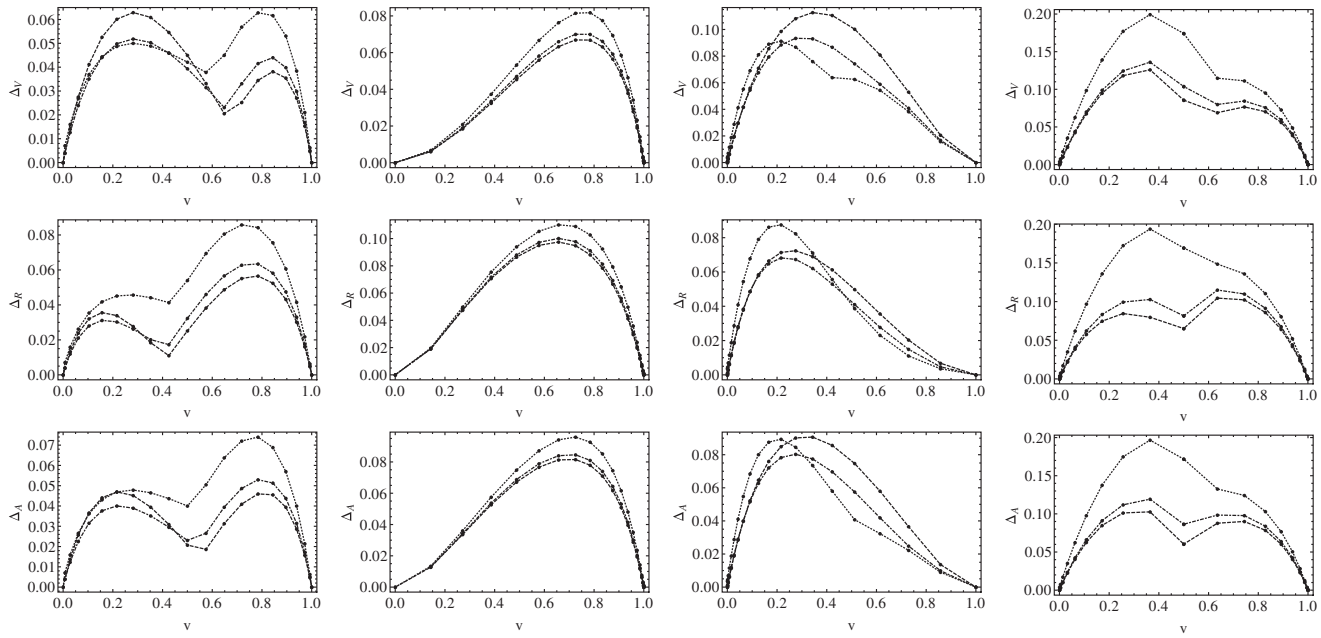

Fig. 7. The effect of varying the common $K = K^{+} = K^{-}$ for $G^{+} = 4G^{-}$ (and $2G^{-} = 1$) on the error: error for different $3K \in \{0.1, 1, 10\}$ (dashed, dot-dashed, dotted) w. r. t. the Voigt-IOD approach (top), Reuss-IOD approach (middle), Aleksandrov-IOD approach (bottom) and different microstructures (MPL - left, two CIs - center, ACI - right).

4.3.3. Effect of the morphology

In terms of morphology, there are two fundamentally different classes of microstructures, namely the matrix-inclusion microstructures and those microstructures in which the phases are arranged in a more equitable manner. The matrix-inclusion microstructures include both variants of CIs and the ACI for $v \neq \frac{1}{2}$. The equitable microstructures are represented by the MPL, and the ACI for $v = \frac{1}{2}$.

For a phase contrast of factor 2 in G and of factor 10 in K, we have found that the error is least for the MPL structure (well below 8%). Further, for the equitable microstructures (MPL, ACI at $v = 1/2$) we have found a local minimum of the error Δ close to $v = \frac{1}{2}$, i. e. close to that volume fraction, where the arrangement of phases is symmetric and thus most equitable. Since the IOD approach does not distinguish any phase a priori - recall the head–tail symmetry of the stiffness tetrad (Eq. (22)), – this minimum is in accordance with our expectations.

For the equitable microstructures, the point $v = \frac{1}{2}$ also maximizes the interface area a (per unit volume), and we could be tempted to attribute the local minimum of error to this fact, stating that in this case much of the material is close to some interface. However, comparing MPL and ACI for $v = \frac{1}{2}$, we find

$$\Delta_{ACI} > \Delta_{MPL}, \tag{169}$$

$$a_{ACI} > a_{MPL}, \tag{170}$$

which contradicts this conjecture. However, in the ACI microstructure, the domains of the same phase are in contact only by the edges of the cubes. The edges form a set of measure zero in terms of area, i. e. the ACI is equitable but still close to a matrix inclusion microstructure – unlike the MPL.

In contrast, the error for the CI microstructure has no local minimum. The maximum is drawn to one side of the diagram (see Fig. 7 middle columns). This is due to the fact that small cubical inclusions are badly represented by the IOD approach, while large cubical inclusions result in a microstructure similar to three orthogonal laminates, which complies well with the presumptions of the IOD approach.

4.3.4. Conclusion

Combining the concepts underlying the IOD approach and the numerical results of RVE simulations, we expect that the IOD approach gives reasonable predictions whenever.

1. the microstructure is close to a single phase
2. the shear moduli are of the same magnitude

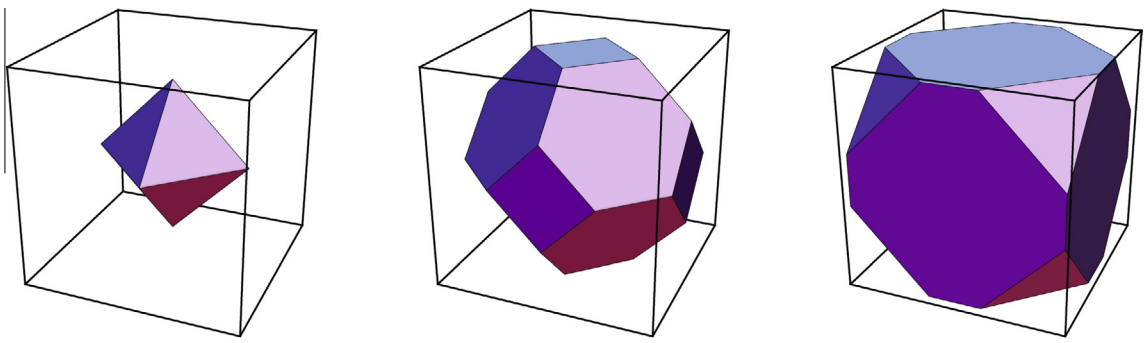

Fig. 8. (Truncated) octahedral inclusion with a distance of opposite vertices of the octahedron being 3/4 (left), 3/2 (center), 9/4 (right) of the RVE size.

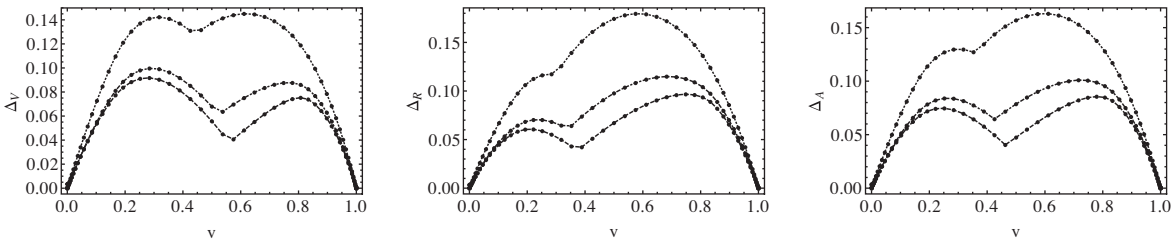

Fig. 9. The effect of varying the common $K = K^+ = K^-$ for $G^+ = 4G^-$ on the error for the octahedral inclusion microstructure: Error for different $3K \in \{0.1, 1, 10\}$ (dashed, dot-dashed, dotted) w. r. t. the Voigt-IOD approach (left), Reuss-IOD approach (center), Aleksandrov-IOD approach (right). Similar to ACI and MPL, there is always a local minimum of the error close to $\nu = \frac{1}{2}$.

3. both phases form the microstructure in an equitable manner – in contrast to matrix-inclusion microstructures.

4.3.5. Further validation by means of octahedral inclusions

In order to validate our conjectures, we have designed an additional type of microstructure which combines all previously discussed types.

The respective RVE consists of a cube (material '–') within which an octahedral inclusion (material '+') is centered (see Fig. 8(a)). Upon increasing the size of the inclusion, the tips of the octahedron penetrate the cube's faces. We proceed with cutting these tips, which yields a microstructure that resembles the MPL to some extent, however now consisting of truncated octahedra (see Fig. 8(b)). Upon further enlarging the inclusion, we find a microstructure similar to the initial one–but with swapped phases and one eighth of an octahedron located at each vertex of the cube (see Fig. 8(c)). Thus, there is transition from a matrix-inclusion microstructure (at $\nu = \frac{1}{6}$) to an equitable arrangement of phases (with a substantial contact zone) and then back to a matrix-inclusion microstructure (at $\nu = \frac{5}{6}$).

The respective octahedral IOD f^o is given by

$$f^o(\mathbf{n}) := \frac{1}{8}\sum_{i=1}^{8}\delta_{\|}(\mathbf{n}, \mathbf{n}_i^o), \tag{171}$$

where $\{\mathbf{n}_i^o\}$ denote the normals of the octahedral faces. Again, the IOD yields an effective stiffness tetrad with cubic symmetry, and we refer to the same projectors, $\mathbb{P}_\alpha^o = \mathbb{P}_\alpha^h$, and to Appendix B for details of the calculation. Interestingly, for all mean values certain eigenvalues coincide with those from the hexahedral IOD.

4.3.5.1. Voigt mean. The elastic moduli for f^o are given by

$$\lambda_{V,1}^o = \lambda_{V,1}^h, \tag{172}$$
$$\lambda_{V,2}^o = \lambda_{V,3}^h, \tag{173}$$
$$\lambda_{V,3}^o = \frac{1}{9}(4C_1 + 2C_2 + 3(C_5 + C_t)). \tag{174}$$

4.3.5.2. Reuss mean. The elastic moduli for f^o are given by

$$\lambda_{R,1}^o = \lambda_{R,1}^h, \tag{175}$$
$$\lambda_{R,2}^o = \lambda_{R,3}^h, \tag{176}$$
$$\lambda_{R,3}^o = \frac{9C_1C_2C_s^2}{(2C_1 + 4C_2)C_s^2 + 3C_1C_2(C_5 - C_t)}. \tag{177}$$

4.3.5.3. Aleksandrov mean. The elastic moduli for f^o are given by

$$\lambda_{A,1}^o = \lambda_{A,1}^h, \tag{178}$$
$$\lambda_{A,2}^o = \lambda_{A,3}^h, \tag{179}$$
$$\lambda_{A,3}^o = \left(C_1^4C_2^2C_s^3\right)^{1/9}\rho^{C_t/(3C_r)}. \tag{180}$$

Though quantitatively the error of the octahedral inclusions, by and large, exceeds that of the MPL, we find the same qualitative behavior, i. e. a reasonable agreement for shear moduli of the same magnitude and a local minimum of the error close to the most equitable microstructure at $\nu = \frac{1}{2}$, see Fig. 9.

5. Summary, discussion, and outlook

5.1. Summary

We have used the well-known effective stiffness for an infinitely fine two-layer composite as a reference solution for averaging over (a) an isotropic, (b) a transversely isotropic, and (c) hexahedral interface orientation distribution (IOD). In either case, isotropic constituents have been assumed. The results are explicit relations for (a) the effective bulk and shear modulus in the isotropic and (b) effective Hill's moduli in the transversely isotropic case, as well as for the three eigenvalues in (c).

For (a) and (b), a comparison to the existing self-consistent estimate shows the opposite behavior. Both approximations tend to opposing Hashin–Shtrikman bounds when extremal volume fractions are considered.

For (c), the emphasis has been on the comparison of different microstructures with the same IOD (and volume fraction). Since the IOD approach provides the same predictions for these microstructures, the comparison to RVE simulations allows us to determine its range of applicability. In doing so, we find a significant reduction in the error (difference between IOD approach and RVE simulations), whenever the microstructure is close to an equitable one. We also find, that the IOD approach provides reasonable estimates whenever the shear moduli are of the same magnitude.

5.2. Discussion

The matrix inclusion-based self-consistent approach relies on the ellipsoidal inclusion solution by Eshelby [8]. The notion of self-consistency is due to the assumption that the elastic moduli of the aggregate remain equal, to the first order, to those of the surrounding effective medium, when the perturbation between the embedded element and the effective medium is minimized [13]. As a result, the curves $K_{SC}(\nu)$ and $G_{SC}(\nu)$ exhibit the smallest possible absolute slope at the extremal volume fractions. Thus, the stiffening or softening effect of the smaller volume fraction is underestimated for extremal volume fractions. This behavior is well-known, see, e. g., [20,13].

The IOD approach behaves conversely to the self-consistent approach. For extremal volume fractions, the elastic moduli take the largest possible absolute slope, i. e. they approach the HSB with the larger absolute slope. We have shown this result to be independent of the particular mean value. Thus, the IOD approach overestimates the stiffening or softening effect of the smaller volume fraction.

Fig. 10. Examples for matrix-inclusion microstructures with a stiffer matrix phase that has a lower volume fraction and for an interface-rich microstructure. Left: an open-cell foam [9]. Center: micrograph of a hypereutectic steel with perlite grains and cementite surrounding [6]. Right: an amorphous polymer structure with no specific matrix-inclusion assignment of the phases. Courtesy of Frans Holthuysen [28].

Apparently, the SC and IOD approach encompass converse assumptions regarding the microstructure. The SC approach necessarily considers the phase with the smaller volume fraction as the inclusion phase. Consequently, the phase with the larger volume fraction percolates through the material and carries the loading, and therefore controls the change of stiffness when the volume fractions change. Therefore, a change of the volume fraction has the lowest possible effect at extremal volume fractions. In the IOD approach, both phases are treated equal. The latter implies that both phases percolate the material. Therefore the stiffer material carries the loading. Consequently, replacing one material by the other has the largest possible effect at extremal volume fractions.

We can decide which of the two approaches suits better by considering the microstructure's morphology. For example, in closed-cell foams, or for polycrystals with a precipitation phase at the grain boundaries, the smaller phase is not the matrix phase, but percolates through the material (see Fig. 10). Thus, we would rather use the IOD approach in such a case. Other potential applications are microstructures without matrix inclusion structure, i. e. structures in which both phases percolate through the sample. For example, an irregular long fiber reinforcement, or an amorphous polymer mixture come close to such a structure. Consequently, we may consider the IOD approach as a reasonable complement to the SC approach for those microstructures where the latter fails to give appropriate predictions. This finding is supported by further evidence from the RVE simulations. Designing sequences of different anisotropic microstructures with equal IOD, we find that within a sequence of similar microstructures, the difference between the IOD approach and RVE results attains a local minimum close to those volume fraction which corresponds to the most equitable microstructure. This is also in accordance with the head–tail symmetry of the laminate stiffness which in turn arises from the equitable treatment of both phases. Comparing different microstructures with the same volume fraction and IOD also provides an estimate of the influence of morphological characteristics beyond volume fractions and IOD.

In addition, as the IOD approach includes Hill's special case of equal shear moduli, the error of the IOD approach is generally acceptable whenever the shear moduli are of the same magnitude.

Other potential applications of the approach are materials with fine-scaled microstructures, for which the interface properties are more important than the bulk properties [41].

Most importantly, the IOD approach includes the morphology-induced anisotropy in an approximate sense, while the (possibly numerical) evaluation of the weighted orientation integral remains relatively simple.

5.3. Outlook

The interface orientation distribution provides only a first approximation to the morphology of the microstructure. Future work on more sophisticated approaches should address the following problems:

- Consider an RVE with a matrix material and some non-overlapping inclusions. For any other non-overlapping configuration of these inclusions, the IOD approach predicts the same effective stiffness.
- For equal volume fractions, $v^- = v^+ = \frac{1}{2}$, switching the phases in the microstructure does not affect the predictions by the IOD approach, but most certainly the results of the respective RVE simulations.
- Similar to the cubic microstructures that have been considered here, isotropic distributions of fibers or platelets both exhibit isotropic IOD but different effective elasticities [22,47].
- The orientation averaging of a reference solution could be extended to other problems, e. g., closed-cell foams.

Apart from the cubic microstructures considered in this work, we can construct other microstructures with equal IOD but otherwise different morphology. For either microstructure the effective stiffness as determined from RVE simulations will fall within the Hashin–Shtrikman bounds, as does the prediction by the IOD approach.

Yet, since two-phase microstructures are completely determined by the interface alignment, it may be possible to improve upon the present results by virtue of additional geometrical information of the microstructure morphology, e. g., a distribution of the two principal curvatures of the interface.

The key problem is to connect the geometrical information to material laws. We would need, for example, higher-order jump balances. Higher-order estimates might be constructed using the work on the stiffness of curved interfaces [21].

Acknowledgment

We would like to thank the reviewer for a careful and thorough revision and valuable comments.

Appendix A. Transversely isotropic tetrads

A.1. Base tensors

Any fourth-order transversely isotropic tensor $\mathbb{C}^t$ with major and left and right minor symmetries can be written in terms of the following basis

$$\tilde{\mathbb{B}}_1 := \mathbf{I} \otimes \mathbf{I}, \tag{181}$$

$$\tilde{\mathbb{B}}_2 := \mathbb{I}_S, \tag{182}$$

$$\tilde{\mathbb{B}}_3 := (\mathbf{n} \otimes \mathbf{I} \otimes \mathbf{n})_S, \tag{183}$$

$$\tilde{\mathbb{B}}_4 := \mathbf{n} \otimes \mathbf{n} \otimes \mathbf{I} + \mathbf{I} \otimes \mathbf{n} \otimes \mathbf{n}, \tag{184}$$

$$\tilde{\mathbb{B}}_5 := \mathbf{n} \otimes \mathbf{n} \otimes \mathbf{n} \otimes \mathbf{n}. \tag{185}$$

However, for the subsequent calculations, the following choice provides a more suitable base,

$$\mathbb{B}_1 := \tilde{\mathbb{B}}_2 - 2\,\tilde{\mathbb{B}}_3 - \frac{1}{2}\,(\tilde{\mathbb{B}}_1 - \tilde{\mathbb{B}}_4 - \tilde{\mathbb{B}}_5), \tag{186}$$

$$\mathbb{B}_2 := 2\,(\tilde{\mathbb{B}}_3 - \tilde{\mathbb{B}}_5), \tag{187}$$

$$\mathbb{B}_3 := \frac{1}{\sqrt{2}}\,(2\,\tilde{\mathbb{B}}_5 - \tilde{\mathbb{B}}_4), \tag{188}$$

$$\mathbb{B}_4 := \frac{1}{2}\,(\tilde{\mathbb{B}}_1 - \tilde{\mathbb{B}}_4 - \tilde{\mathbb{B}}_5), \tag{189}$$

$$\mathbb{B}_5 := \frac{1}{2}\,(\tilde{\mathbb{B}}_1 - \tilde{\mathbb{B}}_4 + 3\,\tilde{\mathbb{B}}_5). \tag{190}$$

This base is orthogonal and normalized to length $\sqrt{2}$, thus the components $\{C_1, \dots, C_5\}$ of $\mathbb{C}^t$ are easily obtained

$$\mathbb{B}_I \cdot \cdots \cdot \mathbb{B}_J = 2\,\delta_{IJ}, \tag{191}$$

$$C_I = \frac{1}{2}\,\mathbb{C}^t \cdot \cdots \cdot \mathbb{B}_I. \tag{192}$$

A.2. Eigenvalues and projectors

Depending on the circumstances, we need to know the tetrad in terms of components $\{C_1, \dots, C_5\}$ and base tensors $\{\mathbb{B}_1, \dots, \mathbb{B}_5\}$ or eigenvalues $\{\lambda_1^t, \dots, \lambda_4^t\}$ and projectors $\{\mathbb{P}_1^t, \dots, \mathbb{P}_4^t\}$

$$\mathbb{C}^t = \sum_{I=1}^{5} C_I\,\mathbb{B}_I \tag{193}$$

$$= \sum_{\alpha=1}^{4} \lambda_\alpha^t\,\mathbb{P}_\alpha^t(\zeta). \tag{194}$$

The four (different) eigenvalues of $\mathbb{C}^t$ are related to its five components via

$$\lambda_{1/2}^t = C_{1/2}, \tag{195}$$

$$\lambda_{3/4}^t = C_5 \pm C_r, \tag{196}$$

$$C_r := \sqrt{(C_3)^2 + (C_4)^2}. \tag{197}$$

The relation between the four projectors and five base tensors involves the parameter ζ as the fifth degree of freedom in the projector decomposition

$$\mathbb{P}_{1/2}^t := \mathbb{B}_{1/2}, \tag{198}$$

$$\mathbb{P}_{3/4}^t := \frac{1}{2}\,(\mathbb{B}_5 \pm (\cos\zeta\,\mathbb{B}_3 + \sin\zeta\,\mathbb{B}_4)) \tag{199}$$

$$= \frac{1}{2}\left(\mathbb{B}_5 \pm \frac{1}{C_r}\,(C_3\,\mathbb{B}_3 + C_4\,\mathbb{B}_4)\right), \tag{200}$$

$$\cos\zeta = \frac{C_3}{C_r}, \tag{201}$$

$$\sin\zeta = \frac{C_4}{C_r}. \tag{202}$$

For the sake of completeness, we note that

$$\mathbb{I}_S = \sum_{\alpha=1}^{4} \mathbb{P}_\alpha^t \tag{203}$$

$$= \mathbb{B}_1 + \mathbb{B}_2 + \mathbb{B}_5. \tag{204}$$

A.3. Functions

Applying a function g to a tetrad $\mathbb{C}$

$$\mathbb{C} = \sum_\alpha \lambda_\alpha\,\mathbb{P}_\alpha, \tag{205}$$

is defined in terms of the eigenvalues and projectors of $\mathbb{C}$,

$$g(\mathbb{C}) := \sum_\alpha g(\lambda_\alpha)\,\mathbb{P}_\alpha. \tag{206}$$

For a transversely isotropic tetrad, the function is rewritten in terms of components and base tensors by virtue of Eqs. (195)–(202)

$$g(\mathbb{C}^t(\mathbf{n})) = \sum_{\alpha=1}^{4} g(\lambda_\alpha^t)\,\mathbb{P}_\alpha^t(\zeta, \mathbf{n}) \tag{207}$$

$$= \sum_{I=1}^{5} g_I^t(C_1, \dots, C_5)\,\mathbb{B}_I(\mathbf{n}) \tag{208}$$

where the auxiliary functions $\{g_1^t, \dots, g_5^t\}$ are defined via

$$g_{1/2}^t := g(C_{1/2}), \tag{209}$$

$$g_{3/4}^t := \frac{g(C_5 + C_r) - g(C_5 - C_r)}{2}\,\frac{C_{3/4}}{C_r}, \tag{210}$$

$$g_5^t := \frac{g(C_5 + C_r) + g(C_5 - C_r)}{2}. \tag{211}$$

Appendix B. Computing the effective stiffness tetrad

For the examples considered here, the effective stiffness tetrads can be computed analytically. To start with, we recall the definition of the effective stiffness tetrad

$$\overline{\mathbb{C}}[f, g] := g^{-1}\left(\int_\Omega f(\mathbf{n})\,g(\mathbb{C}(\mathbf{n}))\,\mathrm{d}\Omega\right). \tag{212}$$

For a microstructure consisting of two isotropic phases, the laminate stiffness is transversely isotropic, $\mathbb{C} = \mathbb{C}^t$. Thus, in order to compute $g(\mathbb{C})$, we can make use of Eq. (208). In the next step, we perform the integration

$$\mathbb{F}[f, g] := \int_\Omega f(\mathbf{n})\,g(\mathbb{C}^t(\mathbf{n}))\,\mathrm{d}\Omega \tag{213}$$

$$= \int_\Omega f(\mathbf{n}) \sum_{I=1}^{5} g_I^t(C_1, \dots, C_5)\,\mathbb{B}_I(\mathbf{n})\,\mathrm{d}\Omega \tag{214}$$

$$= \sum_{I=1}^{5} g_I^t(C_1, \dots, C_5)\,\mathbb{F}_I[f], \tag{215}$$

$$\mathbb{F}_I[f] := \int_\Omega f(\mathbf{n})\,\mathbb{B}_I(\mathbf{n})\,\mathrm{d}\Omega. \tag{216}$$

In Appendix C, we prove that $\mathbb{F}_I[f]$ inherits the rotational symmetries of f (see Eq. (261)). W. r. t. the aforementioned base, the components of the laminate stiffness are given by

$$C_{1/2} = 2\,G_{V/R}, \tag{217}$$

$$C_{3/4} = \frac{1}{2}\left(A_V \mp A_R + B_V - v^-\,v^+\,\frac{2\Delta B^2}{A_M}\right), \tag{218}$$

$$C_5 = -\sqrt{2}\left(B_V - v^-\,v^+\,\frac{\Delta A\,\Delta B}{A_M}\right). \tag{219}$$

The auxiliary tetrads $\{\mathbb{F}_1, \dots, \mathbb{F}_5\}$ inherit the rotational symmetries of f. This is due to the rotational symmetries of f and the fact that the base tensors $\mathbb{B}_I(\mathbf{n})$ are isotropic tensor functions in $\mathbf{n}$. For a proof see Appendix C, Eq. (261). For the isotropic, hexahedral and

octahedral IOD, all auxiliary tetrads can be given in terms of isotropic and cubic projectors, respectively,

$$\mathbb{F}_I[f^{i/h/o}] = \sum_{\alpha=1}^{2/3/3} F_{I\alpha}^{i/h/o}\, \mathbb{P}_\alpha^{i/h/o}, \tag{220}$$

while for the transversely isotropic IOD (with $\mathbf{d}$ as axis of transversal isotropy), they are given in terms of the transversely isotropic base tensors

$$\mathbb{F}_I[f^t] = \sum_{J=1}^{5} F_{IJ}^t\, \mathbb{B}_J(\mathbf{d}). \tag{221}$$

Combining these decompositions with Eq. (215), we find

$$\mathbb{F}[f^{i/h/o}, g] = \sum_{I=1}^{5} g_I^t(C_1,\dots,C_5)\, \mathbb{F}_I[f^{i/h/o}] \tag{222}$$

$$= \sum_{I=1}^{5} g_I^t(C_1,\dots,C_5) \sum_{\alpha=1}^{2/3/3} F_{I\alpha}^{i/h/o}\, \mathbb{P}_\alpha^{i/h/o} \tag{223}$$

$$= \sum_{\alpha=1}^{2/3/3} F_\alpha^{i/h/o}\, \mathbb{P}_\alpha^{i/h/o}, \tag{224}$$

$$F_\alpha^{i/h/o} := \sum_{I=1}^{5} g_I^t(C_1,\dots,C_5)\, F_{I\alpha}^{i/h/o}, \tag{225}$$

$$\mathbb{F}[f^t, g] = \sum_{I=1}^{5} g_I^t(C_1,\dots,C_5)\, \mathbb{F}_I[f^t] \tag{226}$$

$$= \sum_{I=1}^{5} g_I^t(C_1,\dots,C_5) \sum_{J=1}^{5} F_{IJ}^t\, \mathbb{B}_J(\mathbf{d}) \tag{227}$$

$$= \sum_{J=1}^{5} F_J^t\, \mathbb{B}_J(\mathbf{d}), \tag{228}$$

$$F_J^t := \sum_{I=1}^{5} g_I^t(C_1,\dots,C_5)\, F_{IJ}^t. \tag{229}$$

The final step in either case consists of applying the inverse function to $\mathbb{F}$

$$\overline{\mathbb{C}}[f, g] = g^{-1}(\mathbb{F}[f, g]). \tag{230}$$

For the isotropic and hexahedral IODs we recall the definition of a function of a tetrad (Eq. (206)) and obtain

$$\mathbb{C}[f^{i/h/o}, g] = g^{-1}\left(\mathbb{F}[f^{i/h/o}, g]\right) \tag{231}$$

$$= g^{-1}\left(\sum_{\alpha=1}^{2/3/3} F_\alpha^{i/h/o}\, \mathbb{P}_\alpha^{i/h/o}\right) \tag{232}$$

$$= \sum_{\alpha=1}^{2/3/3} g^{-1}\left(F_\alpha^{i/h/o}\right) \mathbb{P}_\alpha^{i/h/o}, \tag{233}$$

while for the transversely isotropic IOD, we employ Eq. (208) once more, however substituting $g \to g^{-1}$

$$\mathbb{C}[f^t, g] = g^{-1}\left(\mathbb{F}[f^t, g]\right) \tag{234}$$

$$= \sum_{I=1}^{5} (g^{-1})_I^t(F_1^t,\dots,F_5^t)\, \mathbb{B}_I(\mathbf{d}). \tag{235}$$

For the sake of completeness, we provide the F-matrices first used in Eq. (220) and (221)

$$F^i = \begin{pmatrix} 0 & \frac{2}{5} \\ 0 & \frac{2}{5} \\ -\frac{2\sqrt{2}}{3} & \frac{2\sqrt{2}}{15} \\ \frac{1}{3} & -\frac{1}{15} \\ 1 & \frac{1}{5} \end{pmatrix}, \quad F^h = \begin{pmatrix} 0 & \frac{1}{2} & \frac{1}{3} \\ 0 & 0 & \frac{2}{3} \\ -\frac{2\sqrt{2}}{3} & \frac{\sqrt{2}}{3} & 0 \\ \frac{1}{3} & -\frac{1}{6} & 0 \\ 1 & \frac{1}{2} & 0 \end{pmatrix},$$

$$F^o = \begin{pmatrix} 0 & \frac{1}{3} & \frac{4}{9} \\ 0 & \frac{2}{3} & \frac{2}{9} \\ -\frac{2\sqrt{2}}{3} & 0 & \frac{2\sqrt{2}}{9} \\ \frac{1}{3} & 0 & -\frac{1}{9} \\ 1 & 0 & \frac{1}{3} \end{pmatrix}, \tag{236}$$

$$F^t = \begin{pmatrix} \frac{1}{8} & \frac{1}{2} & \frac{1}{2\sqrt{2}} & -\frac{1}{8} & \frac{3}{8} \\ \frac{1}{2} & \frac{1}{2} & 0 & 0 & 0 \\ \frac{1}{2\sqrt{2}} & 0 & \frac{1}{2} & -\frac{1}{2\sqrt{2}} & -\frac{1}{2\sqrt{2}} \\ -\frac{1}{8} & 0 & -\frac{1}{2\sqrt{2}} & -\frac{3}{8} & \frac{1}{8} \\ \frac{3}{8} & 0 & -\frac{1}{2\sqrt{2}} & \frac{1}{8} & \frac{5}{8} \end{pmatrix}. \tag{237}$$

To determine these matrices, we need the isotropic and cubic projectors,

$$\mathbb{P}_1^i := \frac{1}{3}\mathbf{I}\otimes\mathbf{I}, \tag{238}$$

$$\mathbb{P}_2^i := \mathbb{I}_S - \frac{1}{3}\mathbf{I}\otimes\mathbf{I}, \tag{239}$$

and

$$\mathbb{P}_1^{h/o} := \frac{1}{3}\mathbf{I}\otimes\mathbf{I}, \tag{240}$$

$$\mathbb{P}_2^{h/o} := \sum_{i=1}^{3} \mathbf{e}_i\otimes\mathbf{e}_i\otimes\mathbf{e}_i\otimes\mathbf{e}_i - \frac{1}{3}\mathbf{I}\otimes\mathbf{I}, \tag{241}$$

$$\mathbb{P}_3^{h/o} := \mathbb{I}_S - \sum_{i=1}^{3} \mathbf{e}_i\otimes\mathbf{e}_i\otimes\mathbf{e}_i\otimes\mathbf{e}_i, \tag{242}$$

respectively, and the following elementary integrals

$$\int_\Omega \mathbf{n}\otimes\mathbf{n}\,\mathrm{d}\Omega = \frac{1}{3}\mathbf{I}, \tag{243}$$

$$\int_\Omega \mathbf{n}\otimes\mathbf{n}\otimes\mathbf{n}\otimes\mathbf{n}\,\mathrm{d}\Omega = \frac{1}{15}(\mathbf{I}\otimes\mathbf{I} + 2\,\mathbb{I}_S), \tag{244}$$

$$\int_\Omega \delta_\perp(\mathbf{n},\mathbf{d})\,\mathbf{n}\otimes\mathbf{n}\,\mathrm{d}\Omega = \frac{1}{2}(\mathbf{I} - \mathbf{d}\otimes\mathbf{d}), \tag{245}$$

$$\begin{aligned}&\int_\Omega \delta_\perp(\mathbf{n},\mathbf{d})\,\mathbf{n}\otimes\mathbf{n}\otimes\mathbf{n}\otimes\mathbf{n}\,\mathrm{d}\Omega \\ &= \frac{1}{8}(\mathbf{I}\otimes\mathbf{I} + 2\,\mathbb{I}_S + 3\,\mathbf{d}\otimes\mathbf{d}\otimes\mathbf{d}\otimes\mathbf{d} \\ &\quad - \left(4\,(\mathbf{d}\otimes\mathbf{I}\otimes\mathbf{d})_S + \mathbf{d}\otimes\mathbf{d}\otimes\mathbf{I} + \mathbf{I}\otimes\mathbf{d}\otimes\mathbf{d}\right)).\end{aligned} \tag{246}$$

The latter are determined easily by parametrizing $\mathbf{n}$ with spherical coordinates,

$$\mathbf{n}(\theta,\phi) = \sin\theta\cos\phi\,\mathbf{e}_1 + \sin\theta\sin\phi\,\mathbf{e}_2 + \cos\theta\,\mathbf{e}_3, \tag{247}$$

$$(\theta,\phi) \in [0,\pi]\times[0,2\pi[, \tag{248}$$

with the element $\mathrm{d}\Omega$ of normalized integration

$$\mathrm{d}\Omega = \frac{1}{4\pi}\sin\theta\,\mathrm{d}\theta\,\mathrm{d}\phi \tag{249}$$

such that for any function h

$$\int_\Omega h(\mathbf{n})\,\mathrm{d}\Omega = \frac{1}{4\pi}\int_0^{2\pi}\int_0^{\pi} h(\mathbf{n}(\theta,\phi))\sin\theta\,\mathrm{d}\theta\,\mathrm{d}\phi. \tag{250}$$

Appendix C. Inheritance of symmetries

Subsequently we give the proof for the implication Eq. (43). To begin with, we note that $\mathbb{C}(\mathbf{n})$ for isotropic phases (Eqs. (35)–(41)) and $g(\mathbb{C})$ and $g^{-1}(\mathbb{F})$ in general are isotropic tensor functions in their respective argument, i. e.

$$\mathbb{C}(\mathbf{R}\cdot\mathbf{n}) = \mathbf{R}*\mathbb{C}(\mathbf{n}) \quad \forall \mathbf{R}\in\mathcal{SO}_3, \tag{251}$$
$$g(\mathbf{R}*\mathbb{C}) = \mathbf{R}*g(\mathbb{C}) \quad \forall \mathbf{R}\in\mathcal{SO}_3, \tag{252}$$
$$g^{-1}(\mathbf{R}*\mathbb{F}) = \mathbf{R}*g^{-1}(\mathbb{F}) \quad \forall \mathbf{R}\in\mathcal{SO}_3, \tag{253}$$

where $\mathcal{SO}_3$ is the group of proper orthogonal second-order tensors and $*$ denotes the Rayleigh product,

$$\mathbf{R}*\mathbb{C} := C_{ijkl}\,(\mathbf{R}\cdot\mathbf{e}_i)\otimes(\mathbf{R}\cdot\mathbf{e}_j)\otimes(\mathbf{R}\cdot\mathbf{e}_k)\otimes(\mathbf{R}\cdot\mathbf{e}_l). \tag{254}$$

For the latter two functions this is an immediate consequence of their definition in terms of eigenvalues and projectors which we have used extensively in Appendix B. By virtue of Eqs. (251) and (252) and the symmetry of the IOD $\mathbf{R}^x$ (recall Eq. (42)), we find

$$\mathbf{R}^x*\mathbb{F} = \mathbf{R}^x*\int_\Omega g(\mathbb{C}(\mathbf{n}))f(\mathbf{n})\,\mathrm{d}\Omega \tag{255}$$
$$= \int_\Omega \mathbf{R}^x*g(\mathbb{C}(\mathbf{n}))f(\mathbf{n})\,\mathrm{d}\Omega \tag{256}$$
$$= \int_\Omega g(\mathbf{R}^x*\mathbb{C}(\mathbf{n}))f(\mathbf{n})\,\mathrm{d}\Omega \tag{257}$$
$$= \int_\Omega g(\mathbb{C}(\mathbf{R}^x\cdot\mathbf{n}))f(\mathbf{n})\,\mathrm{d}\Omega \tag{258}$$
$$= \int_\Omega g(\mathbb{C}(\mathbf{R}^x\cdot\mathbf{n}))f(\mathbf{R}^x\cdot\mathbf{n})\,\mathrm{d}\Omega \tag{259}$$
$$= \int_\Omega g(\mathbb{C}(\mathbf{n}))f(\mathbf{n})\,\mathrm{d}\Omega \tag{260}$$
$$= \mathbb{F}, \tag{261}$$

where, from Eq. (259) to (260), we have made use of the invariance of the domain of integration under arbitrary rotations. Using Eq. (261), the remainder of the proof becomes straightforward,

$$\mathbf{R}^x*\overline{\mathbb{C}} = \mathbf{R}^x*\left(g^{-1}(\mathbb{F})\right) \tag{262}$$
$$= g^{-1}(\mathbf{R}^x*\mathbb{F}) \tag{263}$$
$$= g^{-1}(\mathbb{F}) \tag{264}$$
$$= \overline{\mathbb{C}}. \tag{265}$$

Appendix D. Derivative of the generalized mean at extremal volume fractions

We seek to prove Eq. (28). Again, we use $v^+ = v$ and $v^- = 1-v$. For convenience, we rewrite the essential parts of $\mathbb{C}$,

$$\Delta\mathbb{C} = \mathbb{C}^+ - \mathbb{C}^-, \tag{266}$$
$$\mathbb{C}_V(v) = \mathbb{C}^- + v\Delta\mathbb{C}, \tag{267}$$
$$\mathbb{C}_M(v) = \mathbb{C}^+ - v\Delta\mathbb{C}, \tag{268}$$
$$\mathbb{Z}_S(v,\mathbf{n}) = (\mathbf{n}\otimes(\mathbf{n}\cdot\mathbb{C}_M(v)\cdot\mathbf{n})^{-1}\otimes\mathbf{n})_S, \tag{269}$$
$$\mathbb{C}(v,\mathbf{n}) = \mathbb{C}_V(v) - v(1-v)\Delta\mathbb{C}\cdot\cdot\mathbb{Z}_S(v,\mathbf{n})\cdot\cdot\Delta\mathbb{C}. \tag{270}$$

Thus

$$\mathbb{C}\left(\frac{1}{2}\mp\frac{1}{2},\mathbf{n}\right) = \mathbb{C}^\mp. \tag{271}$$

and

$$\left.\frac{\partial\mathbb{C}}{\partial v}\right|_{\frac{1}{2}\mp\frac{1}{2}} = \Delta\mathbb{C}\mp\Delta\mathbb{C}\cdot\cdot\mathbb{Z}_S\left(\frac{1}{2}\mp\frac{1}{2},\mathbf{n}\right)\cdot\cdot\Delta\mathbb{C}. \tag{272}$$

Next, we consider the orientation average of a generic function g of $\mathbb{C}$

$$\mathbb{F}(v) := \int_\Omega g(\mathbb{C}(v,\mathbf{n}))f(\mathbf{n})\,\mathrm{d}\Omega. \tag{273}$$

At extremal volume fractions, this average and its derivative w. r. t. the volume fraction are given by

$$\mathbb{F}\left(\frac{1}{2}\mp\frac{1}{2}\right) = \int_\Omega g\left(\mathbb{C}\left(\frac{1}{2}\mp\frac{1}{2},\mathbf{n}\right)\right)f(\mathbf{n})\,\mathrm{d}\Omega \tag{274}$$
$$= \int_\Omega g(\mathbb{C}^\mp)f(\mathbf{n})\,\mathrm{d}\Omega \tag{275}$$
$$= g(\mathbb{C}^\mp), \tag{276}$$

and

$$\left.\frac{\mathrm{d}\mathbb{F}}{\mathrm{d}v}\right|_{\frac{1}{2}\mp\frac{1}{2}} = \left.\frac{\mathrm{d}}{\mathrm{d}v}\int_\Omega g(\mathbb{C}(v,\mathbf{n}))f(\mathbf{n})\,\mathrm{d}\Omega\right|_{\frac{1}{2}\mp\frac{1}{2}} \tag{277}$$
$$= \int_\Omega \left.\frac{\partial g(\mathbb{C}(v,\mathbf{n}))}{\partial v}\right|_{\frac{1}{2}\mp\frac{1}{2}} f(\mathbf{n})\,\mathrm{d}\Omega \tag{278}$$
$$= \int_\Omega \left.\frac{\mathrm{d}g(\mathbb{C})}{\mathrm{d}\mathbb{C}}\right|_{\mathbb{C}^\mp}\cdot\cdot\cdot\left.\frac{\partial\mathbb{C}(v,\mathbf{n})}{\partial v}\right|_{\frac{1}{2}\mp\frac{1}{2}} f(\mathbf{n})\,\mathrm{d}\Omega \tag{279}$$
$$= \left.\frac{\mathrm{d}g(\mathbb{C})}{\mathrm{d}\mathbb{C}}\right|_{\mathbb{C}^\mp}\cdot\cdot\cdot\int_\Omega \left.\frac{\partial\mathbb{C}(v,\mathbf{n})}{\partial v}\right|_{\frac{1}{2}\mp\frac{1}{2}} f(\mathbf{n})\,\mathrm{d}\Omega, \tag{280}$$

respectively. Recalling the definition of the generalized mean of $\mathbb{C}$,

$$\overline{\mathbb{C}}(v) := g^{-1}\left(\int_\Omega g(\mathbb{C}(v,\mathbf{n}))f(\mathbf{n})\,\mathrm{d}\Omega\right) \tag{281}$$
$$= g^{-1}(\mathbb{F}(v)) \tag{282}$$

we further deduce

$$\left.\frac{\mathrm{d}\overline{\mathbb{C}}}{\mathrm{d}v}\right|_{\frac{1}{2}\mp\frac{1}{2}} = \left.\frac{\mathrm{d}g^{-1}(\mathbb{F})}{\mathrm{d}\mathbb{F}}\right|_{\mathbb{F}(\frac{1}{2}\mp\frac{1}{2})}\cdot\cdot\cdot\left.\frac{\mathrm{d}\mathbb{F}}{\mathrm{d}v}\right|_{\frac{1}{2}\mp\frac{1}{2}} \tag{283}$$
$$= \left.\frac{\mathrm{d}g^{-1}(\mathbb{F})}{\mathrm{d}\mathbb{F}}\right|_{g(\mathbb{C}^\mp)}\cdot\cdot\cdot\left(\left.\frac{\mathrm{d}g(\mathbb{C})}{\mathrm{d}\mathbb{C}}\right|_{\mathbb{C}^\mp}\cdot\cdot\cdot\int_\Omega\left.\frac{\partial\mathbb{C}}{\partial v}\right|_{\frac{1}{2}\mp\frac{1}{2}} f(\mathbf{n})\,\mathrm{d}\Omega\right) \tag{284}$$
$$= \left(\left.\frac{\mathrm{d}g^{-1}(\mathbb{F})}{\mathrm{d}\mathbb{F}}\right|_{g(\mathbb{C}^\mp)}\cdot\cdot\cdot\left.\frac{\mathrm{d}g(\mathbb{C})}{\mathrm{d}\mathbb{C}}\right|_{\mathbb{C}^\mp}\right)\cdot\cdot\cdot\int_\Omega\left.\frac{\partial\mathbb{C}}{\partial v}\right|_{\frac{1}{2}\mp\frac{1}{2}} f(\mathbf{n})\,\mathrm{d}\Omega \tag{285}$$
$$= \int_\Omega\left.\frac{\partial\mathbb{C}}{\partial v}\right|_{\frac{1}{2}\mp\frac{1}{2}} f(\mathbf{n})\,\mathrm{d}\Omega \tag{286}$$

In the last step we have made use of the multidimensional generalization of $\frac{\mathrm{d}y}{\mathrm{d}x}\frac{\mathrm{d}x}{\mathrm{d}y} = 1$. The final expression is independent of g which concludes the proof.

Appendix E. Consistency of the geometric mean

The geometric mean has been suggested first by [3], but actually used by [35]. It is distinguished in that it preserves the relation of stiffness and compliance, $\mathbb{S} = \mathbb{C}^{-1}$, along the process of homogenization

$$\mathbb{S}_A[f] := \exp\left(\int_\Omega f(\mathbf{n})\,\ln\mathbb{S}(\mathbf{n})\,\mathrm{d}\Omega\right) \tag{287}$$
$$= \exp\left(\int_\Omega f(\mathbf{n})\,\ln\mathbb{C}^{-1}(\mathbf{n})\,\mathrm{d}\Omega\right) \tag{288}$$
$$= \exp\left(-\int_\Omega f(\mathbf{n})\,\ln\mathbb{C}(\mathbf{n})\,\mathrm{d}\Omega\right) \tag{289}$$
$$= \left(\exp\left(\int_\Omega f(\mathbf{n})\,\ln\mathbb{C}(\mathbf{n})\,\mathrm{d}\Omega\right)\right)^{-1} \tag{290}$$
$$= (\mathbb{C}_A[f])^{-1} \tag{291}$$

In that sense it can be considered as self-consistent, and the result is known to lie between the Voigt and Reuss estimate. The latter are associated with the extremal assumption of homogeneous strains (and non-equilibrated stresses) and homogeneous stresses (and incompatible strains), respectively.

Appendix F. Equivalence of different errors

To begin with, we maximize the relative error in terms of the Cauchy stress over the domain of all strains

$$\Delta_X := \max_{\varepsilon} \frac{\|\overline{\boldsymbol{\sigma}}_X - \overline{\boldsymbol{\sigma}}_{RVE}\|}{\|\overline{\boldsymbol{\sigma}}_{RVE}\|}, \tag{292}$$

where $X \in \{V, R, A\}$. Upon introducing

$$\overline{\boldsymbol{\sigma}}_X = \overline{\mathbb{C}}_X \cdot\cdot \overline{\varepsilon}, \tag{293}$$

$$\overline{\boldsymbol{\sigma}}_{RVE} = \overline{\mathbb{C}}_{RVE} \cdot\cdot \overline{\varepsilon} \tag{294}$$

and expanding the Euclidean norm, we obtain

$$\Delta_X = \left(\max_{\overline{\varepsilon}\cdot\cdot\overline{\varepsilon}=1} \frac{\overline{\varepsilon} \cdot\cdot \left(\overline{\mathbb{C}}_X - \overline{\mathbb{C}}_{RVE}\right)^2 \cdot\cdot \overline{\varepsilon}}{\overline{\varepsilon} \cdot\cdot \left(\overline{\mathbb{C}}_{RVE}\right)^2 \cdot\cdot \overline{\varepsilon}} \right)^{1/2}. \tag{295}$$

The restriction to $\overline{\varepsilon} \cdot\cdot \overline{\varepsilon} = 1$ is justified by the homogeneity of degree zero of the – therefore relative – error in the norm of $\overline{\varepsilon}$.

In our examples, all stiffness tetrads can be represented in terms of the same projectors. Using this representation,

$$\overline{\mathbb{C}}_X = \sum_{\alpha=1}^{A} \lambda_{\alpha,X}\, \mathbb{P}_\alpha, \tag{296}$$

$$\overline{\mathbb{C}}_{RVE} = \sum_{\alpha=1}^{A} \lambda_{\alpha,RVE}\, \mathbb{P}_\alpha, \tag{297}$$

we find numerator and denominator to be linear combinations of non-negative expressions

$$\overline{\varepsilon} \cdot\cdot \mathbb{P}_\alpha \cdot\cdot \overline{\varepsilon} \;\geqslant 0, \tag{298}$$

the sum of which is

$$1 = \overline{\varepsilon} \cdot\cdot \overline{\varepsilon} \tag{299}$$

$$= \overline{\varepsilon} \cdot\cdot \mathbb{I}_S \cdot\cdot \overline{\varepsilon} \tag{300}$$

$$= \overline{\varepsilon} \cdot\cdot \sum_{\alpha=1}^{A} \mathbb{P}_\alpha \cdot\cdot \overline{\varepsilon} \tag{301}$$

$$= \sum_{\alpha=1}^{A} \overline{\varepsilon} \cdot\cdot \mathbb{P}_\alpha \cdot\cdot \overline{\varepsilon}. \tag{302}$$

The non-negative expressions can be substituted by squares of real expressions ε_α

$$\varepsilon_\alpha^2 = \overline{\varepsilon} \cdot\cdot \mathbb{P}_\alpha \cdot\cdot \overline{\varepsilon} \tag{303}$$

Then, the problem is reduced to maximizing a function on the unit-sphere in the A-dimensional space of $\{\varepsilon_\alpha\}$.

In both numerator and denominator, the coefficients of the linear combination are non-negative and positive, respectively,

$$\left(\lambda_{\alpha,X}^{h/o} - \lambda_{\alpha,RVE}^{h/o}\right)^2 \;\geqslant 0 \tag{304}$$

$$\left(\lambda_{\alpha,RVE}^{h/o}\right)^2 \;> 0 \tag{305}$$

Let us restate the problem with less indices

$$\Delta^2 = \max_{\sum_\alpha \varepsilon_\alpha^2 = 1} \frac{\sum_\alpha \varepsilon_\alpha^2 n_\alpha}{\sum_\alpha \varepsilon_\alpha^2 d_\alpha}, \tag{306}$$

$$n_\alpha := \left(\lambda_{\alpha,X}^{h/o} - \lambda_{\alpha,RVE}^{h/o}\right)^2 \geqslant 0, \tag{307}$$

$$d_\alpha := \left(\lambda_{\alpha,RVE}^{h/o}\right)^2 > 0. \tag{308}$$

This expression is maximized for any pure strain state with components $\{0, \ldots, \varepsilon_{\alpha^*}, 0, \ldots, 0\}$, where

$$\frac{n_{\alpha^*}}{d_{\alpha^*}} = \max_\alpha \frac{n_\alpha}{d_\alpha}. \tag{309}$$

There can be more than one α^* maximizing this expression. In this case, any (normalized) linear combination of the respective strains maximizes Δ, but the actual value of the maximum is the same as for any of the pure maximizing states, thus

$$\Delta^2 = \max_\alpha \frac{n_\alpha}{d_\alpha}, \tag{310}$$

and finally

$$\Delta_X = \max_\alpha \frac{\left|\lambda_{\alpha,X}^{h/o} - \lambda_{\alpha,RVE}^{h/o}\right|}{\lambda_{\alpha,RVE}^{h/o}}. \tag{311}$$

References

[1] Agoras M, Ponte-Castañeda P. Homogenization estimates for multi-scale nonlinear composites. Eur J Mech A/Solids 2011;30(6):828–43.
[2] Agoras M, Ponte-Castañeda P. Multi-scale homogenization-based modeling of semi-crystalline polymers. Philos Mag 2012;92(8):925–58.
[3] Aleksandrov KS, Aisenberg L. Method of calculating physical constants of polycrystalline metals. Sov Phys Dokl 1966;11(3):323–5.
[4] Allaire G. Shape optimization by the homogenization method. Applied mathematical sciences, vol. 146. Springer; 2002.
[5] Braides A, Lukkassen D. Reiterated homogenization of integral functionals. Math Models Methods Appl Sci 2000;10(1):47–71.
[6] Callister W, Rethwisch D. Materialwissenschaften und Werkstofftechnik. Wiley-VCH Verlag; 2012.
[7] Cherkaev A. Approaches to nonconvex variational problems of mechanics. In: Ponte-Castañeda P, Telega J, Gambin B, editors. Nonlinear homogenization and its applications to composites. Polycrystals and smart materials, NATO science series II: mathematics, physics and chemistry, vol. 170. Springer; 2005. p. 65–105.
[8] Christensen R. A critical evaluation for a class of micro-mechanics models. J Mech Phys Solids 1990;38(3):379–404.
[9] Dannemann K, Lankford JJ. High strain rate compression of closed-cell aluminium foams. Mater Sci Eng A 2000;293(1-2):157–64.
[10] deBotton G. Transversely isotropic sequentially laminated composites in finite elasticity. J Mech Phys Solids 2005;53(6):1334–61.
[11] deBotton G, Hariton I. High-rank nonlinear sequentially laminated composites and their possible tendency towards isotropic behavior. J Mech Phys Solids 2002;50:2577–95.
[12] Dederichs P, Zeller R. Variational treatment of the elastic constants of disordered materials. Z Phys 1973;259:103–16.
[13] Dvorak G. Micromechanics of composite materials. Springer; 2013.
[14] Eshelby J. The determination of the elastic field of an ellipsoidal inclusion, and related problems. Proc R Soc London Ser A: Math Phys Eng Sci 1957;241:376–96.
[15] Feyel F, Chaboche J-L. FE^2 multiscale approach for modelling the elastoviscoplastic behaviour of long fibre SiC/Ti composite materials. Comput Methods Appl Mech Eng 2000;183:309–30.
[16] Francfort G, Murat F. Homogenization and optimal bounds in linear elasticity. Arch Ration Mech Anal 1986;94(4):307–34.
[17] Glüge R. Generalized boundary conditions on representative volume elements and their use in determining the effective material properties. Comput Mater Sci 2013;79:408–16.
[18] Glüge R, Kalisch J. The effective stiffness and stress concentrations of a multi-layer laminate. Compos Struct 2014;111(0):580–6.
[19] Glüge R, Weber M, Bertram A. Comparison of spherical and cubical statistical volume elements with respect to convergence, anisotropy, and localization behavior. Comput Mater Sci 2012;63:91–104.
[20] Gross D, Seelig T. Fracture mechanics with an introduction to micromechanics. 2nd ed. Springer; 2011.
[21] Gurtin M, Murdoch I. Surface stress in solids. Int J Solids Struct 1978;14(6):431–40.
[22] Halpin J, Kardos J. Halpin-Tsai equations: a review. Polym Eng Sci 1976;16(5):344–52.
[23] Harrison I, deBotton G. The nearly isotropic behaviour of high-rank nonlinear sequentially laminated composites. Proc R Soc London Ser A: Math Phys Eng Sci 2003;459(2029):157–74.
[24] Hashin Z. On elastic behaviour of fibre reinforced materials of arbitrary transverse phase geometry. J Mech Phys Solids 1965;13(3):119–34.
[25] Hill R. Elastic properties of reinforced solids: some theoretical principles. J Mech Phys Solids 1963;11(5):357–72.

[26] Hill R. Theory of mechanical properties of fibre-strengthened materials: I. Elastic behaviour. J Mech Phys Solids 1964;12(4):199–212.
[27] Hill R. Theory of mechanical properties of fibre-strengthened materials: III. Self-consistent model. J Mech Phys Solids 1965;13(4):189–98.
[28] Holthuysen F. Zebra's eye, The 46th international conference on electron, ion and photon beam technology and nanofabrication: bizarre/beautiful micrograph contest; 2002.
[29] Idiart M, Ponte-Castañeda P. Estimates for two-phase nonlinear conductors via iterated homogenization. Proc R Soc London Ser A: Math Phys Eng Sci 2013;469(2153):1583–604.
[30] Idiart MI. Modeling the macroscopic behavior of two-phase nonlinear composites by infinite-rank laminates. J Mech Phys Solids 2008;56(8):2599–617.
[31] Kröner E. Bounds for the effective elastic moduli of disordered materials. J Mech Phys Solids 1977;25:137–55.
[32] Lapeyronnie P, Le Grognec P, Binétruy C, Boussu F. Homogenization of the elastic behavior of a layer-to-layer angle-interlock composite. Compos Struct 2011;93(11):2795–807.
[33] Lee B, Argon A, Parks D, Ahzi S, Bartczak Z. Simulation of large strain plastic deformation and texture evolution in high density polyethylene. Polymer 1993;34(17):3555–75.
[34] Lee B, Parks D, Ahzi S. Micromechanical modeling of large plastic deformation and texture evolution in semi-crystalline polymers. J Mech Phys Solids 1993;41(10):1651–87.
[35] Matthies S, Humbert M. On the principle of a geometric mean of even-rank symmetric tensors for textured polycrystals. J Appl Crystal 1995;28(3):254–66.
[36] Milton G. The theory of composites. Cambridge University Press; 2002.
[37] Orlik J. Asymptotic homogenization algorithm for reinforced metal-matrix elasto-plastic composites. Compos Struct 2010;92(7):1581–90.
[38] Ortiz M, Repetto E, Stainier L. A theory of subgrain dislocation structures. J Mech Phys Solids 2000;48(10):2077–114.
[39] Ponte-Castañeda P. Bounds for nonlinear composites via iterated homogenization. J Mech Phys Solids 2012;60:1583–604.
[40] Richeton T, Berbenni S. From bicrystals to spherical inclusions: a superposition method to derive analytical expressions of stress fields in presence of plastic strain gradients. Int J Solids Struct 2014;51(3–4):794–807.
[41] Shen L, Li J. Homogenization of a fibre/sphere with an inhomogeneous interphase for the effective elastic moduli of composites. Proc R Soc London Ser A: Math Phys Eng Sci 2005;461(2057):1475–504.
[42] Talbot D. Bounds which incorporate morphological information for a nonlinear composite dielectric. Proc R Soc London Ser A: Math Phys Eng Sci 1999;455(1990):3617–28.
[43] Tartar L. Estimations fines des coefficients homogénéisés. In: Krée P, editor. Ennio di Giorgi Colloquium: Papers presented at a colloquium held at the H. Poincaré institute in Nov. 1983. Pitman Publishing Ltd; 1985. p. 168–87.
[44] van Dommelen J, Parks D, Boyce M, Brekelmans W, Baaijens F. Micromechanical modeling of the elasto-viscoplastic behavior of semi-crystalline polymers. J Mech Phys Solids 2003;51(3):519–41.
[45] Walpole L. The analysis of the overall elastic properties of composite materials. Cambridge: Cambridge University Press; 1985.
[46] Willis J. Advances in applied mechanics, vol. 21. New York: Academic Press; 1981. Ch. Variational and related methods for the overall properties of composites, pp. 1–78.
[47] Zahr Viñuela J, Pérez-Castellanos J. A particular implementation of the modified secant homogenization method for particle reinforced metal matrix composites. Compos Struct 2014;109(0):260–7.
[48] Zhang X, Xiao B, Andrä H, Ma Z. Homogenization of the average thermo-elastoplastic properties of particle reinforced metal matrix; 2014.